University of Kentucky
UKnowledge

Theses and Dissertations--Chemical and Materials Engineering

Chemical and Materials Engineering

2011

UNDERSTANDING AND IMPROVING LITHIUM ION BATTERIES THROUGH MATHEMATICAL MODELING AND EXPERIMENTS

Rutooj D. Deshpande
University of Kentucky, rutooj.dehpande@uky.edu

Right click to open a feedback form in a new tab to let us know how this document benefits you.

Recommended Citation
Deshpande, Rutooj D., "UNDERSTANDING AND IMPROVING LITHIUM ION BATTERIES THROUGH MATHEMATICAL MODELING AND EXPERIMENTS" (2011). *Theses and Dissertations--Chemical and Materials Engineering*. 4.
https://uknowledge.uky.edu/cme_etds/4

This Doctoral Dissertation is brought to you for free and open access by the Chemical and Materials Engineering at UKnowledge. It has been accepted for inclusion in Theses and Dissertations--Chemical and Materials Engineering by an authorized administrator of UKnowledge. For more information, please contact UKnowledge@lsv.uky.edu.

STUDENT AGREEMENT:

I represent that my thesis or dissertation and abstract are my original work. Proper attribution has been given to all outside sources. I understand that I am solely responsible for obtaining any needed copyright permissions. I have obtained and attached hereto needed written permission statements(s) from the owner(s) of each third-party copyrighted matter to be included in my work, allowing electronic distribution (if such use is not permitted by the fair use doctrine).

I hereby grant to The University of Kentucky and its agents the non-exclusive license to archive and make accessible my work in whole or in part in all forms of media, now or hereafter known. I agree that the document mentioned above may be made available immediately for worldwide access unless a preapproved embargo applies.

I retain all other ownership rights to the copyright of my work. I also retain the right to use in future works (such as articles or books) all or part of my work. I understand that I am free to register the copyright to my work.

REVIEW, APPROVAL AND ACCEPTANCE

The document mentioned above has been reviewed and accepted by the student's advisor, on behalf of the advisory committee, and by the Director of Graduate Studies (DGS), on behalf of the program; we verify that this is the final, approved version of the student's dissertation including all changes required by the advisory committee. The undersigned agree to abide by the statements above.

Rutooj D. Deshpande, Student

Prof. Yang-Tse Cheng, Major Professor

Dr. Stephen Rankin, Director of Graduate Studies

UNDERSTANDING AND IMPROVING LITHIUM ION BATTERIES THROUGH MATHEMATICAL MODELING AND EXPERIMENTS

DISSERTATION

A dissertation submitted in partial fulfillment of the
requirements for the degree of Doctor of Philosophy in the
College of Engineering
at the University of Kentucky

By
Rutooj D. Deshpande

Lexington, Kentucky

Directors : Prof. Yang-Tse Cheng, Professor of Chemical and Materials Engineering,
University of Kentucky, Lexington, Kentucky

Dr. Mark W. Verbrugge, Director, Chemical and Materials Laboratory,
General Motors R & D, Warren, Michigan

2011

Copyright © Rutooj D. Deshpande 2011

ABSTRACT OF DISSERTATION

UNDERSTANDING AND IMPROVING LITHIUM ION BATTERIES THROUGH MATHEMATICAL MODELING AND EXPERIMENTS

There is an intense, worldwide effort to develop durable lithium ion batteries with high energy and power densities for a wide range of applications, including electric and hybrid electric vehicles. For improvement of battery technology understanding the capacity fading mechanism in batteries is of utmost importance. Novel electrode material and improved electrode designs are needed for high energy- high power batteries with less capacity fading. Furthermore, for applications such as automotive applications, precise cycle-life prediction of batteries is necessary.

One of the critical challenges in advancing lithium ion battery technologies is fracture and decrepitation of the electrodes as a result of lithium diffusion during charging and discharging operations. When lithium is inserted in either the positive or negative electrode, there is a volume change associated with insertion or de-insertion. Diffusion-induced stresses (DISs) can therefore cause the nucleation and growth of cracks, leading to mechanical degradation of the batteries. With different mathematical models we studied the behavior of diffusion induces stresses and effects of electrode shape, size, concentration dependent material properties, pre-existing cracks, phase transformations, operating conditions etc. on the diffusion induced stresses. Thus we develop tools to guide the design of the electrode material with better mechanical stability for durable batteries.

Along with mechanical degradation, chemical degradation of batteries also plays an important role in deciding battery cycle life. The instability of commonly employed electrolytes results in solid electrolyte interphase (SEI) formation. Although SEI formation contributes to irreversible capacity loss, the SEI layer is necessary, as it passivates the electrode-electrolyte interface from further solvent decomposition. SEI layer and diffusion induced stresses are inter-dependent and affect each-other. We study coupled chemical-mechanical degradation of electrode materials to understand the capacity fading of the battery with cycling. With the understanding of chemical and mechanical degradation, we develop a simple phenomenological model to predict battery life.

On the experimental part we come up with a novel concept of using liquid metal alloy as a self-healing battery electrode. We develop a method to prepare thin film liquid gallium electrode on a conductive substrate. This enabled us to perform a series of electrochemical and characterization experiments which certify that liquid electrode undergo liquid-solid-liquid transition and thus self-heals the cracks formed during de-insertion. Thus the mechanical degradation can be avoided. We also perform ab-initio calculations to understand the equilibrium potential of various lithium-gallium phases.

KEYWORDS: Lithium ion batteries, diffusion induced stresses, self-healing electrode, coupled chemical and mechanical degradation, life-prediction model.

Rutooj D Deshpande

09/28/2011

UNDERSTANDING AND IMPROVING LITHIUM ION BATTERIES THROUGH MATHEMATICAL MODELING AND EXPERIMENTS

By

Rutooj D. Deshpande

Prof. Yang-Tse Cheng
Director of Dissertation

Dr. Mark W. Verbrugge
Director of Dissertation

Dr. Stephen Rankin
Director of Graduate Studies

Date

Saluting a 'Free Flight'… unrestrained… with the wings of random thoughts…beyond the dreams...!

ACKNOWLEDGEMENTS

Thou hast made me endless, such is thy pleasure.

This frail vessel thou emptiest again and again, and fillest it ever with fresh life

This little flute of a reed thou hast carries over hills and dales,

And hast breathed through it melodies eternally new.

- **'Little Flute' by Rabindranath Tagore**

First of all, with all my sincerity I wish to thank God for blessing me with this dreamy period in my journey of life! All the different fragrances of life I could savor here are from Thou! Without You I am nothing.

I dedicate this 'Doctorate degree' to my parents, my Aai (Mom) and Baba (Dad) -the real 'Sculptors' as I see them, who sweat day and night to carve me into a presentable shape. Their never ending love and affection provide me strength and keep me strong to surpass all the hurdles in my way. I am grateful to my brother for all the flowery moments of childhood we shared and whom I always looked up to throughout my childhood. He is always among the strongest pillars of my support system. I am grateful to my late grandparents (Aaji and Ajoba) who graced me with their unconditional love and left with me an everlasting bank of memories and teachings. I am grateful to my uncle (Vilaskaka) and aunt (Kaku) for the beautiful stories they told; the light moments they shared with me always sprinkle happiness in my loneliness. I sincerely thank all my relatives, my teachers, mentors and childhood friends who taught me the various fundamentals of science and life.

I am grateful to my undergraduate school UDCT where I built my educational and social fundamentals. Special acknowledgements go to my UD friends (Sotu, Babban, Banny and Dadda). Thinking of them even for a moment makes me happy.

With all my heart I would like to thank YT (Professor Y T Cheng) who guided me with fatherly affection throughout my PhD. With his charm, difficulties and tensions would melt down in minutes before I realize. His kind and encouraging words, always kept my spirits high, no matter if the results were good or bad. Along with technical and mathematical skills, he taught the tricks of life, which made the way easier and helped me improve my personality. I feel fortunate that I got an opportunity to 'HAVE FUN' (it was never 'WORK') in YT's lab. I also wish to express my most sincere gratitude and appreciation to Mark (Dr Mark Verbrugge, Big Boss, General Motors) who guided me toward industrial research. In spite of him being busy in driving the research of the whole automotive industry, he took out his precious time for guiding my little flight (of my research) whenever I needed it. His 'Midas touch' to my research always boosted my confidence and kept me motivated. I also thank my Ph.D. committee members: Drs. Dibakar Bhattacharyya, Stephen Rankin, Fuqian Yang, and Michel Jabbour who helped me shape this work with the helpful discussions and knowledgeable inputs. Special gratitude goes to all the other faculties and staff at University of Kentucky whose support in various capacities ensured the completion of my studies.

I wish to express my thanks to my group members J C Li, Ilona Hofmann and Yunchao Li and undergrad colleagues Nisha and Lena. The time spent with them while working in the lab, in the conferences, in trips and in dinner parties was fun.

I am thankful to them for every small and ‘interesting’ discussion we had in the lab which has a special place in my memory book.

I would also like to thank Yue Qi, Stephen Harris, Xingcheng Xiao, Adam Timmons, Misle tessema, Mike Balough, Anil Sachdev and my other colleagues at GM who with their valuable inputs and thoughtful discussions helped me understanding the batteries in more detail and taught me ‘ABC of research’. Special thanks to Yue Qi, Xingcheng and Steve Harris for their immense support in and beyond research.

They say achievements are of no use if you do not get to enjoy life. Thanks to all of my friends here in Lexington who made my stay of three and half years at UK so much fun. Be it day, night, weekdays, weekends, festivities, moments of tensions, anxiety or relaxing moments, smiles or tears, everything was enlivened here due to presence of my friends. My sincere gratitude to senior-cum-friends Abhay, Hari, Nitin, Abhijit, Jeevan, Sarita, Kamalika, Archisman, Ranjana and Paritosh for their help and support to get adjusted in this country and make it feel homely. I would like to thank *Gazzete Janata* (Suvid, Amit, Sumesh, Pratik, Sonam, Shrusti, Anwesha, Venu, Deepai and Swagata) with whom I had immense fun, some magical moments to cherish and with whom I learnt leading a balanced life. I would like to thank Shweta for her sisterly affection and support whenever it was needed. I would like to thank Venkat, Sonal for the pleasing memories we share. Thanks to Priyanka and Sucharita for the warm friendship we have. I would like to thank my roommates Nikhil and Abhijit for their ‘behind the curtains’ support in all my activities.

Special acknowledgement goes to to Bappa (Saket), Nisha, ‘Va’ (Raghav), Bhadukali (Prachi) who rejuvenated ‘*Bhavra*’ with the elixir of their selfless friendship. They helped me in keeping my energies high all the time. I am grateful to Pasha (Vikas Marwaha), Mate (Pranit Metakar), KC (Kiran Chaudhari), Shailu for their love and help in every aspect of life.

And finally, my special thanks to the God sent best friend, Yedi (Sonam Chaurasia) who patiently listened to my random (often whimsical) dreams, believed in them more than I did and resonated with my madness. This warmhearted friendship always brings a wide smile on my face!

I would like to thank NSF (CMMI #1000726) and General Motors for the financial support for this thesis research. Also Acknowledgements go to General Motors for Summer Internships 2009 and 2011.

TABLE OF CONTENTS

ACKNOWLEDGEMENTS iii

LIST OF TABLES xvi

LIST OF FIGURES xvii

CHAPTER 1 1

INTRODUCTION 1

1.1 Dissertation overview 5

1.2 References 9

CHAPTER 2 11

BACKGROUND 11

2.1 Lithium ion batteries 11

2.2 Negative electrodes 15

2.2.1 Alloying active-inactive material: 15

2.2.2 Nanoparticles and porous material: 16

2.2.3 Artificial SEI/ coating and conductive additives: 16

2.3 Mathematical models: 17

2.3.1 Mechanical degradation modeling: 18

2.3.2 Chemical degradation modeling:..... 18

2.3.3 Cycle life prediction models:..... 19

2.3.4 Ab-initio calculation tools: 20

2.4 Background summary: 20

2.5 Reference: 22

CHAPTER 3 35

MODELING DIFFUSION-INDUCED STRESS IN NANOWIRE ELECTRODE STRUCTURES..... 35

3.1 Summary 35

3.2 Introduction 36

3.3 Stress modeling..... 39

3.4 Diffusion in a cylinder: potentiostatic operation..... 44

3.5 Strain energy..... 50

3.6 Stress and strain energy analysis for the galvanostatic operation: 54

3.7 Conclusions 61

3.8 List of symbols 63

3.9 References 66

CHAPTER 4 90

DESIGNING NANOTUBES AS DURABLE LITHIUM-ION BATTERY NEGATIVE ELECTRODES WITH TIO2 NANOTUBES AS AN EXAMPLE 90

4.1 Summary 90

4.2 Introduction 91

4.3 Experimental section 92

4.4 Analysis of the fracture tendency for tubular electrode 93

4.5 Designing tubular electrodes based on DIS and fracture tendency 99

4.6 Results and discussion 103

4.7 References 105

CHAPTER 5 111

EFFECT OF CONCENTRATION-DEPENDENT ELASTIC MODULOUS ON DIFFUSION INDUCED STRESSES FOR BATTERY APPLICATIONS 111

5.1 Summary 111

5.2 Introduction 112

5.3 Methods 115

5.3.1 Mechanics 115

5.3.2 Diffusion in a cylinder 117

5.3.3 Effects of concentration-dependent Young's modulus on DIS 118

5.4 Results and discussions 119

5.4.1 Stress evolution 119

5.4.2 Tendency of fracture 122

5.5 Conclusion 125

5.6 List of symbols 126

5.7 References 128

CHAPTER 6 138

DIFFUSION INDUCED STRESSES AND STRAIN ENERGY IN A PHASE-TRANSFORMING SPHERICAL ELECTRODE PARTICLE 138

6.1 Summary 138

6.2 Introduction 139

6.3 Core-shell model 141

6.4 Mathematical analysis 141

6.4.1. Mechanics 141

6.4.2. Diffusion in spherical core-shell 145

6.5 Results and discussions 147

6.6 Strain energy calculations 151

6.7 Summery and conclusions 153

6.8 List of symbols 156

6.9 References 158

CHAPTER 7 172

EFFECT OF MESOPORES INSIDE ELECTRODE PARTICLES ON DIFFUSION INDUCED STRESS 172

7.1 Summary 172

7.2 Introduction 173

7.3 Experimental procedure 175

7.4 Results 175

7.5 Analysis for diffusion induced stress (DIS) 177

7.6 Discussion and conclusions 182

7.7 List of symbols 186

7.8 References 188

CHAPTER 8 194

EFFECTS OF SOLID-ELECTROLYTE INTERPHASE (SEI) ON THE COUPLED MECHANICAL-CHEMICAL DEGRADATION OF LITHIUM ION BATTERY ELECTRODES 194

8.1 Summary 194

8.2 Introduction 195

8.3 Mathematical analysis: 196

8.3.1. Mechanics: 197

8.3.2. Diffusion in a spherical core-shell: 200

8.4 Results and discussion 206

8.5 Strain energy calculations 210

8.6 Conclusions 211

8.7 List of symbols 214

8.8 Reference: 216

CHAPTER 9 232

BATTERY CYCLE LIFE PREDICTION WITH COUPLED CHEMICAL DEGRADATION AND FATIGUE MECHANICS 232

9.1 Summary 232

9.2 Introduction 233

9.3 Theory 235

9.4 Experimental 236

9.5 Experimental results and discussion: 237

9.6 Mathematical model: 239

9.6.1 Loss of lithium due to SEI formation on the new surface formed due to crack propagation 240

9.6.2 Lithium loss due to increase in the thickness ($LSEI$) of the initial SEI layer…... 245

9.6.3 Lithium loss due to increase in the thickness (L_{SEI}) of the initial SEI layer…… 245

9.6.4 Loss of lithium due to growth of SEI thickness in the cracked area.. 246

9.6.5 Total lithium loss after formation cycles 247

9.7 First cycle SEI formation lithium loss and estimation of L_{SEI}^{0} 250

9.8 Parameters and assumptions: 251

9.9 Modeling results and discussions:..... 252

9.10 Conclusions: 254

9.11 References: 255

CHAPTER 10 267

LIQUID METAL ALLOYS AS SELF-HEALING NEGATIVE ELECTRODES FOR LITHIUM ION BATTERIES 267

10.1 Summary 267

10.2 Introduction 268

10.3 Experimental..... 270

10.4 Results and discussion..... 271

10.5 Conclusions..... 274

10.6 References..... 275

CHAPTER 11 283

IN SITU XRD OF LIQUID GALLIUM ELECTRODE AND AB-INITIO STUDY OF LITHIUM-GALLIUM PHASES 283

11.1 Summary 283

11.2 Introduction 284

11.3 Computational methods 286

11.4 Experimental 287

11.5 Cell design 288

11.6 Simulations results and discussions 288

11.7 Experimental results and discussions 293

11.8 Conclusion 295

11.9 References 296

CHAPTER 12 309

CONCLUSIONS 309

BIBLIOGRAPHY 319

VITA 334

LIST OF TABLES

Table 5.1: Fracture tendency at *Tp*, which is the dimensionless time at which radial stress reaches maximum during insertion 131

Table 11.1: The optimized lattice parameters of the different crystalline Li–Ga phases obtained from our calculations are summarized 301

Table 11.2: The calculation of Relative volume expansion of liquid Ga on lithiation using the densities calculated from the ab initio calculation 302

LIST OF FIGURES

Figure 1.1: Schematic representation of a lithium ion battery 10

Figure 2.1: The state of charge (SOC) variation of an electrode particle during electrochemical cycling 34

Figure 3.1: Lithium ion concentration (Eq. 3.20) inside an electrode at different radial locations and times for the potentiostatic insertion condition. 71

Figure 3.2: Radial stress (Eq. 3.23) inside an electrode at different radial locations at different time. This is for generalized plane strain condition. 72

Figure 3.3: Radial stress inside an electrode at different radial locations and times. This is for the potentiostatic charging of the battery. 73

Figure 3.4: Tangential stress (Eq. 3.24) inside an electrode at radial locations and times. This is for generalized plane strain condition. This is for the potentiostatic charging of the battery.. 74

Figure 3.5: Tangential stress (Eq. 3.24) inside an electrode at different radial locations and times. This is for the potentiostatic charging of the battery. Solid lines represent plane stress condition. Dashed lines represent generalized plane strain condition. No surface effects are considered. 75

Figure 3.6: Axial stress (Eq. 3.25) inside an electrode at radial locations and times. This is for the potentiostatic charging of the battery. Solid lines represent plane strain condition. Dashed lines represent generalized plane strain condition. No surface effects are considered. 76

Figure 3.7: Radial stress at a dimensionless time T = 0.076 for electrodes with different diameters. The results are for plane strain and generalized plane strain conditions. This is for the potentiostatic charging of the battery. 77

Figure 3.8: Tangential stress at dimensionless time T = 0.076 for electrodes with different diameters. The results are for plane strain and generalized plane strain conditions. This is for the potentiostatic charging of the battery. 78

Figure 3.9: Bulk strain energy, surface strain energy, total strain energy with time for a 5-nm electrode subject to the generalized plane strain condition. This is for the potentiostatic charging of the battery. 79

Figure 3.10: Total strain energy variation with time for a 5-nm electrode. All the three loading conditions are taken investigated, and it is clear that the total strain energy stored varies with the axial loading condition. This is for the potentiostatic charging of the battery 80

Figure 3.11: A schematic illustration of contributions to strain-energy. 81

Figure 3.12: Lithium ion concentration (Eq. 3.41) inside an electrode at different radial locations and times for the galvanostatic insertion condition. 82

Figure 3.13: Radial stress (Eq. 3.44) inside an electrode at different radial locations at different time. This is for the galvanostatic charging of the battery. This is for plane strain and generalized plane strain condition. Solid lines represents stresses in large electrode i.e. no surface effects are considered (S_1 = 1, S_2 = 0). Dashed lines represent stresses in 5 nm diameter nanowire electrodes 83

Figure 3.14: Tangential stress (Eq. 3.45) inside an electrode at radial locations and times. This is for the galvanostatic charging of the battery. Solid lines represents stresses in large electrode i.e. no surface effects are considered (S_1 = 1, S_2 = 0). Dashed lines represent stresses in 5 nm diameter nanowire electrodes 84

Figure 3.15: Radial stress (Eq. 3.44) inside an electrode at different radial locations and times. This is for the galvanostatic charging of the battery. 85

Figure 3.16: Tangential stress (Eq. 3.45) inside an electrode at different radial locations and times. This is for the galvanostatic charging of the battery. 86

Figure 3.17: Axial stress (Eq. 3.46) inside an electrode at radial locations and times. This is for the galvanostatic charging of the battery. 87

Figure 3.18: Bulk strain energy, surface strain energy, total strain energy with time for a 5-nm electrode subject to the generalized plane strain condition. This is for the galvanostatic charging of the battery. 88

Figure 3.19: Total strain energy variation with time for a 5-nm electrode. All the three loading conditions are taken investigated, and it is clear that the total strain energy stored varies with the axial loading condition. This is for the galvanostatic charging of the battery. 89

Figure 4.1**:** Comparison between the maximum stress that the tubular electrode experiences (a) in the radial direction during delithiation (lithium extraction), and (b) in the tangential direction during lithiation (lithium insertion) and (c, d, e, and f) delithiation. The ratio of inner radius to outer radius of tube a/R for curves (a, b, and f) = 0.3, for curve (e) 0.4, for curve (d) 0.5, and for curve (c) 0.6. 107

Figure 4.2**:** Schematic illustrating tubular electrode undergoing axial and tangential fracture during charge/discharge operation. 108

Figure 4.3: Fracture tendency as a function of the ratio of the inner radius to outer radius of tubes (*a/R*) assuming current density $I = 1\ mA\ cm^{-2}$ and (a) height of the tube fixed at $h = 300\ nm$ or (b) radius of the tube fixed at $R = 50\ nm$. 109

Figure 4.4: Fracture tendency as a function of current density for a given set of dimensions of the tube (height h =351 nm, radius r=50 nm and a/R=0.5). The solid line represent tangential fracture tendency and the dashed line represent axial fracture tendency. 110

Figure 5.1: Lithium ion concentration inside an electrode at different radial locations at time T=0.01 and T=0.076 for insertion and de-insertion conditions. 132

Figure 5.2: Radial stress inside an electrode at different radial locations at time $T = 0.01$ for insertion and de-insertion for different k' values. 133

Figure 5.3: Radial stress inside an electrode at different radial locations at time $T = 0.076$ for insertion and de-insertion for different k' values. 134

Figure 5.4: Tangential stress inside an electrode at different radial locations at time $T = 0.01$ for insertion and de-insertion for different k' values. 135

Figure 5.5: Tangential stress inside an electrode at different radial locations at time $T = 0.076$ for insertion and de-insertion for different k' values. 136

Figure 5.6: Variation of maximum stress normalized with strength, and strain energy normalized with fracture energy with *k'* value 137

Figure 6.1: A cartoon diagram indicating that, initially, before lithium removal the electrode is completely β Phase (a), which convert to a two phase system with β core and α shell (b), and finally the whole particle is α phase (c). 163

Figure 6.2: A plot of the lithium ion concentration inside an electrode particle at different radial locations and times for during lithium removal $C_\beta/C_\alpha = 2$. At the interface there is sharp jump in concentration. Here the magnitude of the jump in concentration is decided by the ratio of C_β/C_α between the two phases. 164

Figure 6.3: A plot of the interface location along the radius at different times $C_\beta/C_\alpha = 2$. As the lithium removal proceeds, β phase transforms into α phase, and the interface moves towards the particle center. After a certain period of lithium removal, β phase completely diminishes and the particle becomes a single phase particle. 165

Figure 6.4: A plot of the radial stress inside an electrode particle at different radial locations at different times. 166

Figure 6.5: A plot of the tangential stress inside an electrode particle at radial locations and times 167

Figure 6.6: A plot of the maximum stress jump (tangential) at the interface as a function of C_β/C_α assuming the same material properties for both phases. If the material properties such as partial molar volume and Young's modulus of both phases are the same, as $C_\beta/C_\alpha \to 1$, then stress discontinuity at the interface vanishes. 168

Figure 6.7: A plot of the maximum stress jump (tangential) at the interface as a function of the relative partial molar volume of two phases $\Omega_\beta/\Omega_\alpha$ for different values of relative Young's modulus E_β/E_α of the two phases, for $C_\beta/C_\alpha = 2$..... 169

Figure 6.8: Variation of strain energy with time in an electrode particle. Different curves represent strain energy variation for different magnitudes of $\Omega_\beta/\Omega_\alpha$. For these curves, $E_\beta/E_\alpha = 1$ and $C_\beta/C_\alpha = 2$. 170

Figure 6.9: Peak strain energy variation with different values of E_β/E_α. The different curves represent such a variation in peak strain energy for different C_β/C_α ratios. Here $\Omega_\beta/\Omega_\alpha = 1$..... 171

Figure 7.1: Li-concentration profiles and the radial stress distribution inside the particle subject to two different boundary conditions, (*i*) solid electrode particle (*ii*) an electrode particle with a pre-existing pore accessible to the electrolyte 191

Figure 7.2: Dimensionless tangential stress at different radial location at different time (a) for solid homogeneous electrode, (b) for an electrode with a pre-existing pore accessible to the electrolyte during de-insertion. 192

Figure 7.3: Strain energy evolution with diffusion time for a homogeneous particle (dotted line) and an electrode particle with a pre-existing pore accessible to the electrolyte..... 193

Figure 8.1: A schematic diagram indicating that, initially, before lithiation particle/ SEI layer makes a shell surrounding the active material core. 220

Figure 8.2: a. A plot showing the interface concentration (shell side) of the solute during de-insertion at a time $\tau = 0.4$ for different SEI thicknesses calculated using COMSOL, approximate solution and pseudo steady solution 221

Figure 8.2: b. A plot showing the interface concentration (shell side) of the solute during de-insertion as a function of time for different SEI thicknesses calculated using COMSOL, approximate solution and pseudo steady solution..... 222

Figure 8.3: A plot of the radial stress during lithiation inside an electrode particle at different radial locations at different times in presence of SEI 223

Figure 8.4: A plot of the tangential stress during de-lithiation inside an electrode particle at radial locations and times in presence of SEI. There is a jump in the stress at the interface between SEI and active core. 224

Figure 8.5: A plot of the maximum tangential stress inside an electrode particle during delithiation as a function of change in SEI thickness for different values of relative equilibrium concentration of SEI (K). 225

Figure 8.6: A plot of the maximum radial stress inside an electrode particle during lithiation as a function of change in SEI stiffness..... 226

Figure 8.7: A plot of the maximum tangential stress inside an active core part of the electrode particle during delithiation as a function of change in SEI stiffness for different values of relative diffusion coefficient of SEI (ξ)..... 227

Figure 8.8: A plot of the fracture tendency inside SEI layer part of the electrode particle during lithiation as a function of change in SEI stiffness. 228

Figure 8.9: Variation of dimensionless strain energy stored with time during lithiation in presence of SEI. 229

Figure 8.10: A plot of peak strain energy variation with different values of relative thickness (t/R) of SEI (dotted red line). Also, a plot of strain energy stored at the end of lithiation variation with different values of relative thickness (t/R) of SEI (blue line). 230

Figure 8.11: A plot of peak strain energy variation with different values of relative stiffness (E_{SEI}/E_{α}) of SEI (dotted red line). Also, a plot of strain energy stored at the end of lithiation variation with different values of relative thickness (t/R) of SEI (blue line). 231

Figure 9.1: A cartoon diagram representing the schematics of the lithium loss as proposed. As a result of diffusion induced stresses (DISs), the cracks at the particle surface propagate with cycling, a new surface is exposed to electrolyte and results in SEI formation. 260

Figure 9.2: The solid curves are the plots potential vs. state of charge (SOD) curves for the individual electrodes of a commercial A123 battery. The dotted curves are the plots of dV /d(SOC) against SOC for the individual electrodes. We find that the negative electrode dV/d(SOC) curve (Blue symbols) shows peaks for the graphite staging at the same time dV/d(SOC) curve for $FePO_4$ have fairly constant and does not show any variation (Red symbols). In both plots, we use blue color for the negative electrode and red color for the positive electrode. 261

Figure 9.3: Plots of the measured voltage against the capacity for A123 battery at 45^0C at cycle numbers 2, 436 and 963..... 262

Figure 9.4: Plot of experimentally obtained differential voltages of the full cell against the cell capacity (Ah) for A123 battery at 45^0C at cycle numbers 2, 436 and 963. 263

Figure 9.5: A plot of the capacity fading of the cell as a function of number of cycles for different temperatures. The dots represent the experimental data of the capacity of the cell and the solid lines represent the calculated capacity using the model. 264

Figure 9.6: Plots of voltage (V) vs. capacity(Ah) at different number of cycles for the data calculated using the model. We degenerate the voltage cell voltage in to the voltage profiles for the individual electrode voltages against the cell capacity for different cycle numbers. 265

Figure 9.7: Plots of differential voltages (dV/dQ) against the Capacity (Ah) for different cycle numbers obtained using the proposed model for different cycle numbers. 266

Figure 10.1: Galvanostatic voltage-capacity profile of Ga at 40 °C. The cycling rate was C/50. The numbers (1) – (7) correspond to different states for the XRD results in Fig. 10.2. 279

Figure 10.2: Ex-situ XRD results of the Ga electrode during electrochemical cycling. The numbers (1) – (7) refer to different states of Ga in a lithiation and delithiation cycle depicted in Fig. 10.1. The stainless steel substrate peaks are indicated with 'S'. 280

Figure 10.3: (a) A capillary cell with (b) its conceptual picture. (c) Magnified view of the surface near Ga electrode before lithiation and (d) after partial lithiation. The lithiated part is gray and delithiated part is glossy. 281

Figure 10.4: Schematic of morphology changes in liquid electrode during cycling. (a) Liquid metal electrode on a solid substrate before electrochemical cycling. (b) Liquid solidifies and expands during lithiation. (c) Cracking occurs in solid mainly during delithiation. (d) Electrode returns to the liquid state during delithiation. Cracks are self-healed by the solid-to-liquid phase transformation. 282

Figure 11.1: The exploded view of a cell for the in-situ study of liquid gallium electrode 303

Figure 11.2: Optimized crystal structure different possible phases of the lithium-gallium system at equilibrium 304

Figure 11.3: Voltage vs. SOC of liquid gallium electrode. The symbols are experimental data and solid lines are from MD calculations. 305

Figure 11.4: A plot of relative volume expansion (RVE) of different Li-Ga phases against the moles of lithium per cc of liquid gallium in those phases. 306

Figure 11.5: The experimental setup for the in-situ x-ray diffraction study of liquid gallium with heating arrangement. 307

Figure 11.6: *In-situ* X-ray diffraction of lithiation and delithiation of Li_2Ga_7 (a) 2D peak intensity map as we lithiate and delithiate the Li_2Ga_7. (b) 1D peaks after integration at different time period. 308

CHAPTER 1

INTRODUCTION

With rapidly growing energy demands, there is a large increase in demand for more efficient and renewable energy resources. Today, we rely on fossil fuels for most of our energy needs. Combustion of fossil fuels leads to the emission of greenhouse gases into the atmosphere. Global warming is a direct consequence of the accumulation of greenhouse gases. Internal combustion engines are a major source of CO_2 emission and hence alternative energy sources for automotive propulsion applications is one of the prime focuses of research throughout the world. The renewable sources such as solar energy and wind energy are "green" sources of energy but these are intermittent sources. For a continuous use, storage of energy is necessary. Batteries are electrochemical storage devices with which we can store energy in the form of chemical potential difference and use it whenever and wherever it is needed. (*1, 2*)

With a large number of applications in portable electronics such as mobile phones, laptops and other electronic gadgets and potential applications for automobile purpose, lithium ion batteries have gained a lot of attention from researchers worldwide. Hybrid electric vehicles (HEV), plug in hybrid vehicles (PHEV), purely electric vehicles (EV) developments have been the focus of the research of most of the automotive companies. The recent launch of the 'extended range electric vehicle – Chevy Volt' from General Motors has a catalytic effect to the battery research, since the Chevy Volt is completely driven on a lithium ion battery pack. For the automotive applications lithium ion batteries are limited by volumetric and gravimetric energy density, as well as with cycle life.

With better engineering of the electrode size, shape and mechanical properties, there is a lot of room for improvement (*1, 2*). The focus of the current project is to understand the capacity fading in the lithium ion batteries and improve the battery electrodes to have more capacity and a longer cycle life.

A battery is composed of a negative electrode and a positive electrode. These electrodes are separated by an electrolyte which has a finite ionic conductivity and negligible electronic conductivity (Figure 1.1). The potential difference between the two electrodes drives the ions from one electrode to the other. The current collectors transfer the electrons through the external circuit.

Among the various presently available battery technologies such as lead-acetate battery, metal-hydride battery, nickel-cadmium battery, lithium ion battery *etc.* lithium based batteries are known to have the highest gravimetric and volumetric energy storage capacity (*1, 3*).

The commercially available lithium ion batteries commonly contain graphite as a negative electrode material. At the same time, lithium iron phosphate, lithium cobalt oxide, spinel or their derivatives are commonly used positive electrode material. A typical electrolyte is 1:1 by volume mixture of ethylene-carbonate (EC) and dimethyl-carbonate (DMC) with 1M $LiPF_6$ salt. Poly-olefins have proven stable over time and are universally used in lithium ion cells as separators.

The functioning of a lithium ion battery is based on the insertion mechanism. While discharging, a lithium atom leaves the negative electrode leaving an electron behind and enters the electrolyte in the ionic form.

This lithium ion travels through the electrolyte towards the positive electrode where it gains an electron and thus is converted back to the atomic state. This atomic lithium is inserted and stored in the positive electrode material. The electron travels through the external electrical circuit and thus we get external current. Before discharge, two electrodes are at different chemical potentials. When we connect two electrodes electrically with the external circuit, the system will minimize the potential difference between the electrodes. This drives the ions to diffuse from one electrode to the other electrode through the electrolyte. In case of charging, the current and ions are forced to flow in the opposite direction and thus we create a potential difference between two electrodes. Thus we store electrical energy in the form of chemical potential.

If 'B' is the charge carrying specie ('Li' in case of lithium ion batteries), A is one of the electrode (say negative electrode) and C is the other electrode (say positive electrode), then during discharge, B migrates from electrode 'A' to 'C' with simultaneous transfer of electrons through the external circuit. This can be represented with the following equations;

$AB \rightleftarrows A + B^{n+} + ne^{-}$ (oxidation)

$C + B^{n+} + ne^{-} \rightleftarrows BC$ (reduction)

$AB + C \rightleftarrows A + B^{n+} + ne^{-} + C \rightleftarrows A + BC$ (redox reaction)

$\Delta G = -nFE$

Here, ΔG is the Gibb's free energy difference between two electrodes. E is the potential difference between two electrodes. n is the number of positive charges the ions carry and F is Faraday's constant.

When lithium ions reach the negative electrode they gain the electron at the surface of the electrode and are converted back to the atomic lithium state from the ionic state. The lithium atoms on the surface of the electrode diffuse inside the electrode due to the concentration difference inside. Thus we can assume that it follows Fick's law of diffusion. Upon electrochemical cycling, lithium ions move back and forth from one electrode to the other electrode. This mechanism is called the 'rocking chair' mechanism (*2*).

The capacity of lithium ion batteries fades as the battery ages or as we cycle the battery (*4*). It is important to understand the fundamental causes of the capacity fading and come up with improved designs for batteries with longer cycle life. Different degradation mechanisms such as chemical degradation, mechanical degradation, electrochemical shocks *etc.* are known to degrade the batteries. This dissertation focuses on:

a) Understanding the causes of the mechanical degradation at the electrode particle level;

b) Developing mathematical tools to improve the electrode design and optimize the electrode material properties for longer battery life;

c) Understanding the inter-dependence of chemical and mechanical degradation and coupling them to develop a tool to predict battery life;

d) Developing novel electrode materials for improved battery life; and

e) Developing experimental and simulation techniques for a fundamental study of the different electrode materials.

1.1 Dissertation overview

The specific research objectives of this dissertation can be summarized as

- To understand the mechanical degradation of electrode particles as a result of diffusion induced stresses (DISs) with use of available mathematical tools. Analyzing the effect of size, shape, charging and discharging conditions, material properties of electrode material on diffusion induced stresses.
- To develop mathematical tools to describe different processes inside the lithium ion batteries and use them for improving the electrode design to minimize the electrode degradation and thus prolong the cycle life of the batteries with high capacity.
- To use the understanding of mechanical degradation coupled with chemical degradation of batteries to develop the model for predicting cycle life of commercial batteries. Check the validity of model, comparing the predictions with the experimental data from the commercial batteries.
- To develop a new electrode material and with different experimental tools understand the stability of the electrode. Validate the concept of liquid electrode and confirming the liquid-solid-liquid transition on electrochemical cycling thus avoiding mechanical degradation.
- To develop a method for in-situ X-ray diffraction studies of the lithium ion battery electrode.
- To use the Vienna ab-initio simulation package (VASP) for understanding the different phases formed upon lithiation of gallium and calculate the voltage vs. state of charge (SOC) curves.

In chapter 3, we examine the nature of DISs during the electrochemical charging and discharging to understand the mechanical degradation of electrodes. We keep our focus on studying DISs in cylindrical electrode elements such as nanowires. We analyze the effects of size of the nanowires, different boundary conditions and different charging conditions such as potentiostatic and galvanostatic charging on DISs. We optimize the electrode size to minimize the diffusion induced stresses.

Along with the electrode particle sizes and shapes, porosity also affects the stress behavior in a lithium ion battery electrode. In Chapter 4, we develop a model to understand the diffusion induced stress behavior for a tubular electrode structure. We optimize the dimensions of tubes to minimize the fracture tendency of the electrodes. Under the guidelines of the model titania nanotube electrodes were prepared and the cycling performance was evaluated. In accordance with the prediction, the tubes were found to be mechanically stable upon electrochemical cycling.

The models above assume that the material properties of the electrode material do not change during lithiation. In fact, some of the electrode materials are shown to have a drastic change their mechanical properties with changing lithium concentration. In Chapter 5, we investigate effects of this change in properties of the electrode material during lithiation and delithiation on the diffusion induces stress behavior and the fracture tendency of electrode materials.

Some of the electrode materials are known to undergo phase transformation upon lithiation and delithiation. These materials show one or more plateaus on the voltage *vs*. charge curve, exhibiting co-existence of the two phases.

Lithiation or delithiation of such a particle can be represented as a shrinking core model with a sharp jump in the lithium concentration at the interface. In Chapter 6, we examine the stress behavior in such a particle, more specifically, the stress behavior at the interface and degradation of such an electrode particle

The models we developed in the chapters above, assume that the electrode particles are homogeneous and isotropic. In a real electrode particle, a large number of pre-existing pores are observed. In Chapter 7, we study the effect of pre-existing pores on the diffusion induced stresses and show that even a single pre-existing pore can have a significant effect on the diffusion induced stress behavior. This model establishes the significance of fundamental understanding of microstructure and its incorporation in the stress and transport models.

The operating voltage (vs. a lithium reference electrode) of the commonly used negative electrodes is lower than the lower limit of the stability voltage window of the commonly used electrolytes (*5, 6*). Hence, the electrolytes undergo reduction on the negative electrode surface forming solid electrolyte interphase (SEI) on the surface of electrode. SEI formations results in capacity fading of the battery. The SEI layer on the electrode particle affects the diffusion behavior or concentration profile of lithium atoms inside the host particle which eventually changes the stress behavior. Different artificial SEI materials/coatings are used on the electrode particle in attempt to enhance the life of electrode.

In Chapter 8, we mathematically correlate the SEI properties with the diffusion induced stresses and thus optimize the design of artificial SEI. The chemical degradation or mechanical degradation or both of the degradation mechanisms in combination can result in capacity fading of the lithium ion batteries. For automotive applications prediction of battery life is of utmost importance. With our understanding of mechanical and chemical degradation, in Chapter 9, we develop a model that combines chemical and mechanical degradation capacity fading mechanism for commercial batteries to predict battery life at different temperatures and compare this with the cycling data on the commercial cells.

To minimize the mechanical degradation and improve the energy density, in Chapter 10 we propose a novel concept of using a liquid metal electrode as a self-healing electrode. With various techniques such as XRD, optical observation and electrochemistry we show the reversibility of liquid-solid-liquid transition of the liquid metal electrode upon electrochemical cycling.

To further investigate the crystallographic changes in liquid metal electrode, in Chapter 11 we develop a method for *in-situ* X-ray diffraction study of such an electrode. With such a technique, the different phase transformations that the electrode material undergoes during lithiation and delithiation can be observed. Using *in-situ* XRD we validate the liquid-solid-liquid transition in liquid electrode upon lithiation and delithiation. The technique developed for *in-situ* X-ray diffraction study can be used for other possible liquid metal electrodes. To get the crystal structure understanding of the different phases formed during lithiation of a gallium electrode, we performed the density function theory (DFT) calculations on the different equilibrium phases of Li-Ga system.

We optimize the crystal energies of different possible phases of Li-Ga system which we use to construct the equilibrium potential vs. state of charge (SOC) curve for the gallium-lithium system.

In chapter 12 we summarize the different mathematical models we developed and the experiments we performed for understanding and improvement of the lithium ion batteries. We also suggest different ways in which the presented work can be used and developed for further improvement of lithium ion batteries.

1.2 References

1. J. B. Goodenough, "Basic energy needs for electrical energy storage- Report of the Basic Energy Sciences Workshop for Electrical Energy Storage" (July, 2007).
2. R. A. Huggins, *Advanced Batteries: Materials Science Aspects*. (Springer, 2009).
3. J. M. Tarascon, M. Armand, Issues and challenges facing rechargeable lithium batteries. *Nature* **414**, 359 (2001).
4. R. Huggins, W. Nix, Decrepitation Model For Capacity Loss During Cycling of Alloys in Rechargeable Electrochemical Systems. *Ionics* **6**, 57 (2000).
5. D. Aurbach, Review of selected electrode-solution interactions which determine the performance of Li and Li ion batteries. *Journal of Power Sources* **89**, 206 (2000).
6. E. Markervich, G. Salitra, M. Levi, D. Aurbach, Capacity fading of lithiated graphite electrodes studied by a combination of electroanalytical methods, Raman spectroscopy and SEM. *Journa of Power Sources* **146**, 146 (2005).

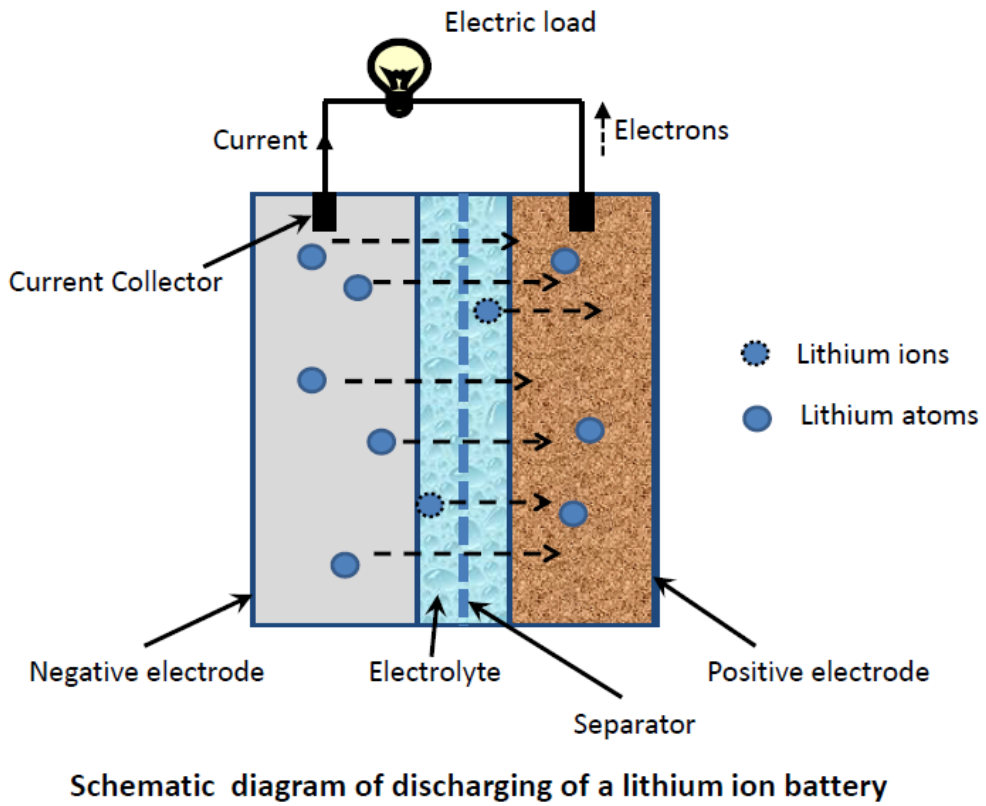

Figure 1.1: Schematic representation of a lithium ion battery

CHAPTER 2

BACKGROUND

2.1 Lithium ion batteries

Potential applications for automotive purposes have attracted the attention of researchers worldwide to lithium ion batteries. The commercially available lithium ion batteries have energy density of 320 WhL^{-1} (135 $Whkg^{-1}$). This is much higher than the other currently available battery technologies such as Pb/ PbO_2 (90 Wh L^{-1}), Cd/Ni (130 Wh L^{-1}), Hydride/Ni (215 Wh L^{-1}).(*1*) There is intense research for increasing the volumetric and gravimetric energy density of lithium ion batteries. The energy density of the battery system is determined by the amount of lithium that can be stored inside the electrode. Currently graphite is used as an anode material which has a capacity of 372 mAh gm^{-1}. Apart from graphite, there are several materials available which are active in lithium storage. Lithium forms intermetallic phases (Li_xM) with numerous metals M (M=Mg, Ca, Al, Si, Ge, Sn, Pb, As, Sb, Bi, Pt, Ag, Au, Zn, Cd, Hg, etc.) at room temperature with sufficient electrochemical conditions such as potential difference and availability of lithium ions. (*2*) This alloying is mostly reversible and can be represented as following;

$$Li_xM \rightleftarrows xLi^+ + xe^- + M$$

Most of these metals can potentially be used as negative electrodes for rechargeable lithium ion batteries. Materials such as Si and Sn have much larger lithium storage capacities than currently used graphite electrodes (*1, 3*).

The automobile industry is looking forward for batteries and capacitors as energy sources for propulsion purposes. General Motors recently launched the 'Chevy Volt' which is an extended range electric vehicle completely driven on a large lithium ion battery pack. To meet the automobile requirements, the battery pack has to have high power density (fast charge and discharge) and high energy density (large storage capacity). Materials such as Si and Sn have larger lithium storing ability than the commercially used carbon electrodes, and thus hold a great potential as future anode materials (*4*).

One of the critical challenges in advancing lithium ion battery technologies is that the battery capacity tends to fade upon electrochemical cycling. Fracture and decrepitation of the electrodes is observed as a result of lithium diffusion during the charging and discharging operations. During the battery operation, when lithium is inserted into (or extracted from) the active materials of both positive and negative electrodes, volume expansion (and contraction) occurs (*1*). For example, graphite, the most common negative electrode for Li-ion batteries, expands 10% of its volume when Li intercalates between the graphite sheets (*5*). Compared to graphite, Si can store ~10 times more Li, but is associated with massive volume expansion, of the order of 300% (*6*). The large volume expansion and the associated stress within electrodes can lead to fracture and failure of the electrodes, causing capacity loss of batteries (*7*). The diffusion induced stresses inside the electrode particle on charging and discharging have a variation proportional to the state of charge (SOC) of the particle. The SOC of a particle has a sinusoidal variation with the electrochemical cycling (Figure 2.1). The electrode material properties and electrode morphology might decide the way mechanical failure would occur as a result of diffusion induced stresses.

Atomic diffusion is observed and used in various applications in the research community. Stresses induced during diffusion can cause dislocation generation which may be desirable for some applications such as surface hardening, improving mechanical properties of steel (*8*) or may have undesired effects in some applications such as degrading the electric properties of semiconductor devices (*9*). In manufacturing of different materials such as semiconductors and alloys and in different applications such as fuel cells, batteries etc. atomic diffusion plays an important role. Hence, atomic diffusion and its effects have been topics of investigation for different applications. Experiments by Dunand (*10, 11*) have demonstrated that cycles of hydrogen alloying and dealloying induce internal stress plasticity in titanium (*12*). Yang *et al*. (*13*) showed diffusion of hydrogen in metals can introduce hydrogen induced cracking and hydrogen enhanced plasticity. This effect is also observed to result in cracking of hydrogenation reactor with crack initiation at the fusion surface between welding overlay and base metal (*14*). Lee and coworkers studied diffusion induced stresses in solid oxide fuel cells (SOFC) (*9*). Diffusion induced bending can be useful in microelectromechanical systems (MEMS) for hydrogen sensing applications (*15*).

In lithium ion battery applications, the electrode might undergo fracture, delamination from the substrate, gradual cracking, change in morphology or change in surface topology resulting in mechanical failure of the electrode, as a consequence of diffusion induced stresses. Such mechanical degradation of the electrode material results in the capacity loss of lithium ion batteries. The mechanical stresses are related to the diffusion of lithium atoms in/out of the electrode particles and are thus related to the electrochemical cycling of batteries.

Apart from mechanical degradation, there is a loss of active lithium content from the system due to chemical reactions at the electrode operating potentials. Capacity of the battery fades with time even if the battery is not operating. Chemical degradation occurs due to the instability of commonly used electrolytes such as ethylene carbonates and propylene carbonates at the operating potentials of the commonly used negative electrodes, resulting in a solid electrolyte interphase (SEI) formation (*16, 17*). The formation of the SEI consumes active material and thus causes irreversible loss in the stored lithium. In spite of this, the SEI formation is important since it passivates further reduction of the electrolyte and thus stabilizes the system (*18*). Several groups are studying SEI to unveil its formation mechanism and its mechanical and transport properties (*19, 20*). Tasaki *et al*. (*21, 22*) studied in detail the major components of SEI and their solubility in the electrolyte. There is still ambiguity about the exact SEI composition. Also, different studies in the literature report different SEI thicknesses and there is no consensus among the researchers about the SEI thickness. At the same time, it is now well accepted that the SEI consists of a dense inorganic layer near the particle surface followed by a porous organic layer (*1*). The calendar life of a battery is associated with the chemical degradation of the battery.

The capacity fading of the battery upon electrochemical cycling may be a result of the chemical degradation or the mechanical degradation or both the degradation mechanisms in combination. The cracks on the electrode surface propagate due to DISs and a new surface area is exposed to the electrolyte. This new surface area would finally be covered with a new SEI layer and more irreversible capacity loss occurs.

Thus cycle life of the battery is determined by the coupled chemical and mechanical degradation. For the application purpose, including automotive applications, it is important to have batteries with long cycle life.

2.2 Negative electrodes

Currently graphite is used as a negative electrode in the commercial Li ion batteries. There is ongoing effort to increase the capacity of carbon. Different chemical and mechanical preparation and modification methods, such as paralytic processes, mechanical milling *etc.* are employed on the carbon negative electrodes for improving their electrochemical performances. The capacities of 450 mAh g^{-1}(*23*) are now achievable, as compared to conventionally used graphite which has a practical capacity of 350 mA h g^{-1} (theoretically 372 mA h g^{-1} for the end compound LiC_6)(*24*).

Different strategies such as alloying the Li-active materials with inactive elements, building nano-structural/ nano-porous electrodes, coating or having electrolyte additives for a stable SEI etc. are commonly used by different studies focusing on improving electrode durability in the past 15 years.

2.2.1 Alloying active-inactive material:

Alloying Li-active with inactive materials has shown to improve the battery cycle life significantly as compared to the pure active material. For example alloying Sn with Cu (*25*) , Co (*26, 27*), or Ni (*28*) has shown improved electrode performance. Even ternary alloys such as Si-Sb-Co and Sn-Sb-Ag are shown to have good electrochemical performance as negative electrode materials (*29, 30*). Winter *et al*. (*2*) give a nice review on the efforts to use the tin-based metallic alloys as negative electrodes for the LIBs.

Inactive material acts as a buffer for the active material expansion on lithiation. Such alloy materials have shown improvement in mechanical stability as compared to a pure material (*2*). At the same time, alloying results in the lower energy density of the electrode as compared to a pure active material electrode.

2.2.2 Nanoparticles and porous material:

Apart from alloying, optimizing the size of electrode particles has been an area of widespread attention. Nano-structural electrodes show improved mechanical stability compared with their bulk counterparts (*24, 31, 32*). Thin-film Si (*33*), Si nano-particles (*34*), Si nanowires (*35*) and TiO_2 nanowires (*36*), as well as porous transition metal oxides (*37, 38*), show improvements in the cycle life performance as compared to their bulk-material counterparts. A porous material can accommodate the expansion of the electrode material on lithiation and thus is more stable than the bulk counterparts (*39, 40*). A nanostructure electrode provides a shorter diffusion path length which is advantageous for high power batteries as well. The disadvantage with the nano-materials is the high surface area, which results in large first cycle irreversible loss. At the same time, with nano-particles the packing density of the electrode is low which results in the lower volumetric energy density.

2.2.3 Artificial SEI/ coating and conductive additives:

The electrode durability also depends on the stability of SEI. There have been attempts to make a more stable artificial SEI layer/ coating layers on the electrode particles, which show significant improvement in the mechanical and chemical stability of electrodes (*41, 42*).

SEI stabilizers and electrolyte additives such as vinylene carbonate and vinyl ethylene carbonate can be used to form a more stable SEI (*43*). Recently atomic layer deposition of Al_2O_3 on the electrode particles has been shown to improve electrode stability (*44*, *45*). Zhang *et al*. (*46*) explained the effect of different possible additives on SEI stabilization. Surface modifications and surface coatings of materials such as metals, metal oxides and conducting polymers have been shown to improve the battery performance (*47*). Moreover, conducting additives and chemical binders, such as carbon black and polyvinylidene fluoride (PVDF), are shown to improve the battery cycle life at the cost of extra mass and volume occupied by the additives (*48*, *49*).

As we observe, efforts have been made in different directions to obtain improved stability of electrode material. With the understanding of degradation mechanisms and the help of mathematical tools the improved electrodes might be achieved. New Li active materials or new combinations of active-active, active-inactive alloys or newer structures are needed for improvement of the battery electrodes.

2.3 Mathematical models:

A substantial body of literature in battery research is devoted to the modeling of different aspects of lithium ion batteries. Through mathematical modeling we can correlate different physical processes in the battery. This can help us garner a better understanding of some of the complex processes and design improved batteries (*1*). A large number of articles in the literature are devoted to the modeling of lithium ion batteries using volume-averaged (macro-homogeneous) methods to characterize simultaneously the liquid and solid phase phenomena (*50-57*).

Porous electrode models describe transport and conduction in an electrolyte and a solid along a macro-length scale and describe diffusion in a solid along a micro-length scale (*50, 51*).

2.3.1 Mechanical degradation modeling:

Following early work of Huggins and Nix (*7*), several recent theoretical studies have modeled internal stresses induced during insertion and removal of Li into electrode particles (*58-60*). Christensen and Newman (*59, 61*) and Zhang *et al.*(*58, 62*) simulated intercalation induced stresses within single particles to capture salient features of the governing electrochemistry and solid mechanics taking place in lithium ion batteries. One of the objectives of these studies is to explain particle fracture, which is sometimes observed in degraded electrodes (*17, 63-65*). These calculations have generally used the shrinking core model (*66, 67*) to predict intra-particle Li concentration profiles and the associated stress fields.

Cheng and Verbrugge (*68-71*) have developed several mathematical models relating the diffusion induced stresses (DISs) with lithium concentration in the electrode material, electrode geometry and charging condition.

2.3.2 Chemical degradation modeling:

Along with the mechanical degradation, the chemical degradation is widely recognized as a major cause of loss of active material (*16, 17, 72*). Molecular dynamics simulations have been used to get a fundamental understanding of SEI (*73*). Ning *et al.* (*74*) developed a computer simulation based on the solvent reduction on the electrode-electrolyte interface as a major source of lithium loss.

Many of the other models in the literature consider the chemical degradation as a major source of capacity fading and thus predict the calendar life of the battery (*75-82*). For example, Broussely *et al.* (*83*) focused on identifying the capacity loss of batteries at different temperatures during controlled experiments and put forward a simple mathematical model which predicts the calendar life. Spotnitz *et al.* (*84*) gives a nice review of different capacity fading experiments and the models predicting calendar life of a battery. Some of the models such as proposed in Bloom *et al.* (*85*) are purely empirical and might not describe the physics behind the degradation.

2.3.3 Cycle life prediction models:

Prediction of the cycle life of lithium ion batteries is of utmost importance for the automobile industry. Safari *et al*. (*76, 77*) used a new approach of accounting fatigue mechanics into battery life prediction. Ramadass *et al.* (*86*) developed a capacity fade prediction model for Li-ion cells based on a semi-empirical approach. Santhanagopalan *et al.* (*87*) gives a nice review on life prediction models.

Most of the battery life models consider chemical degradation as a major source of capacity loss. Along with the chemical degradation, mechanical degradation is also a major aspect of capacity fading which is not paid enough attention by the published life prediction models. As discussed earlier, mechanical degradation of the batteries occur due to diffusion induced stresses as a result of charging and discharging the battery. A large number of articles in the literature study the mechanical stresses in single electrode particles. (*58, 59, 61, 62*).

We recently proposed several models to understand the effects of different operating conditions, different electrode particle sizes, particle shapes, phase transformations (*68, 71, 88-90*) *etc.* on the stresses induced in the electrode particles during battery charging and discharging. A phenomenological model combining the mechanical degradation with chemical degradation to predict battery cycle life is needed.

2.3.4 Ab-initio calculation tools:

Molecular dynamics simulation tools have also been used to understand different aspects of lithium ion batteries. Ceder *et al.* (*91-94*) has done rigorous ab-initio calculations to identify and understand different positive electrode material and their lithium conducting and storage properties. Recently Qi *et al.* (*95, 96*) has used density functional theory calculations to understand the softening or stiffening of the electrode material due to lithiation and delithiation. A detailed molecular level understanding of the mechanism by which an ion intercalated or reacts at the liquid-solid interface and the crystal transformations between different phases during intercalation and de-intercalation is needed (*97*).

2.4 Background summary:

Based on the detailed background, the following conclusions are made:

a. Lithium ion batteries have the highest energy and power density among all the currently available batteries. Yet, the commercially available lithium ion batteries need further improvement for efficient use in propulsion of vehicles.

b. The commercially available batteries use graphite as a negative electrode. Sn, Si and some other metals and alloys can store much more lithium than the currently used graphite and are the potential electrode materials for high energy batteries.

c. Capacity fading upon electrochemical cycling is one of the major issues that the lithium ion battery technology is currently facing.

d. Understanding different capacity fading mechanisms such as the chemical degradation and mechanical degradation is important. Such an understanding can be used to develop tools to predict the battery life accurately.

e. Novel electrode materials with newer designs are needed to decrease the chemical and mechanical degradation for improved battery technology.

f. The development of mathematical models and molecular dynamic simulation tools along with different electrochemical and characterization techniques is important to provide insights into the complex battery processes. The combination of experiments and modeling can lead to improved batteries with high energy density and longer battery life.

2.5 Reference:

1. R. A. Huggins, *Advanced Batteries: Materials Science Aspects*. (Springer, 2009).
2. M. Winter, J. O. Besenhard, Electrochemical lithiation of tin and tin-based intermetallics and composites. *Electrochimica Acta* **45**, 31 (1999).
3. M. N. Obrovac, L. Christensen, D. Ba Le, J. R. Dahn, Alloy Design for Lithium-Ion Battery Anodes. *Journal of The Electrochemical Society* **154**, A849 (2007).
4. B. A. Boukamp, G. C. Lesh, R. A. Huggins, All-Solid Lithium Electrodes with Mixed-Conductor Matrix. *Journal of The Electrochemical Society* **128**, 725 (1981).
5. J. R. Dahn, Phase diagram of LixC6. *Physical Review B* **44**, 9170 (1991).
6. L. Y. Beaulieu, T. D. Hatchard, A. Bonakdarpour, M. D. Fleischauer, J. R. Dahn, Reaction of Li with Alloy Thin Films Studied by In Situ AFM. *Journal of The Electrochemical Society* **150**, A1457 (2003).
7. R. Huggins, W. Nix, Decrepitation Model For Capacity Loss During Cycling of Alloys in Rechargeable Electrochemical Systems. *Ionics* **6**, 57 (2000).
8. J. Chen-Min Li, Physical chemistry of some microstructural phenomena. *Metallurgical and Materials Transactions A* **9**, 1353 (1978).
9. W. L. Wang, S. Lee, J. R. Chen, Effect of chemical stress on diffusion in a hollow cylinder. *Journal of Applied Physics* **91**, 9584 (2002).
10. P. Zwigl, D. C. Dunand, Internal-stress plasticity in titanium by cyclic alloying/dealloying with hydrogen. *Journal of Materials Processing Technology* **117**, 409 (Nov, 2001).

11. D. C. Dunand, P. Zwigl, Hydrogen-induced internal-stress plasticity in titanium. *Metallurgical and Materials Transactions a-Physical Metallurgy and Materials Science* **32**, 841 (Mar, 2001).

12. C. Schuh, D. C. Dunand, Internal stress plasticity due to chemical stresses. *Acta Mater*. **49**, 3387 (Oct, 2001).

13. F. Q. Yang, Interaction between diffusion and chemical stresses. *Mater. Sci. Eng. A-Struct. Mater. Prop. Microstruct. Process.* **409**, 153 (Nov, 2005).

14. X. L. Zhang, C. Y. Zhou, Study on cracking of welding overlay based on the theory of diffusion-induced stress. *Acta Metall. Sin.-Engl. Lett.* **24**, 75 (Feb, 2011).

15. F. Q. Yang, J. C. M. Li, Diffusion-induced beam bending in hydrogen sensors. *Journal of Applied Physics* **93**, 9304 (Jun, 2003).

16. D. Aurbach, Review of selected electrode-solution interactions which determine the performance of Li and Li ion batteries. *Journal of Power Sources* **89**, 206 (2000).

17. E. Markervich, G. Salitra, M. Levi, D. Aurbach, Capacity fading of lithiated graphite electrodes studied by a combination of electroanalytical methods, Raman spectroscopy and SEM. *Journa of Power Sources* **146**, 146 (2005).

18. E. Peled, D. Golodnitsky, C. Menachem, D. Bar-Tow, An Advanced Tool for the Selection of Electrolyte Components for Rechargeable Lithium Batteries. *Journal of The Electrochemical Society* **145**, 3482 (1998).

19. S. S. Zhang, K. Xu, T. R. Jow, EIS study on the formation of solid electrolyte interface in Li-ion battery. *Electrochimica Acta* **51**, 1636 (2006).

20. V. A. Sethuraman, L. J. Hardwick, V. Srinivasan, R. Kostecki, Surface structural disordering in graphite upon lithium intercalation/deintercalation. *Journal of Power Sources* **195**, 3655 (2010).

21. K. Tasaki *et al.*, Solubility of Lithium Salts Formed on the Lithium-Ion Battery Negative Electrode Surface in Organic Solvents. *Journal of The Electrochemical Society* **156**, A1019 (2009).

22. K. Tasaki, S. J. Harris, Computational Study on the Solubility of Lithium Salts Formed on Lithium Ion Battery Negative Electrode in Organic Solvents. *J. Phys. Chem. C* **114**, 8076 (May, 2010).

23. B. M. Way, J. R. Dahn, THE EFFECT OF BORON SUBSTITUTION IN CARBON ON THE INTERCALATION OF LITHIUM IN LIX(BZC1-Z)6. *Journal of The Electrochemical Society* **141**, 907 (Apr, 1994).

24. J. M. Tarascon, M. Armand, Issues and challenges facing rechargeable lithium batteries. *Nature* **414**, 359 (2001).

25. Y. Y. Xia, T. Sakai, T. Fujieda, M. Wada, H. Yoshinaga, Flake Cu-Sn alloys as Negative Electrode Materials for Rechargeable Lithium Batteries. *Journal of the Electrochemical Society* **148**, A471 (May, 2001).

26. A. D. W. Todd, R. E. Mar, J. R. Dahn, Tin-Transition Metal-Carbon Systems for Lithium-Ion Battery Negative Electrodes. *Journal of the Electrochemical Society* **154**, A597 (2007).

27. J. S. Thorne, R. J. Sanderson, J. R. Dahn, R. A. Dunlap, Combinatorial Study of the Sn-Cu-C System for Li-Ion Battery Negative Electrode Materials. *Journal of The Electrochemical Society* **157**, A1085 (2010).

28. J. Hassoun, S. Panero, B. Scrosati, Electrodeposited Ni-Sn Intermetallic Electrodes for Advanced Lithium Ion Batteries. *Journal of Power Sources* **160**, 1336 (Oct, 2006).

29. T. Tabuchi, N. Hochgatterer, Z. Ogumi, M. Winter, Ternary Sn-Sb-Co alloy film as new negative electrode for lithium-ion cells. *Journal of Power Sources* **188**, 552 (Mar, 2009).

30. M. Wachtler, M. Winter, J. O. Besenhard, Anodic materials for rechargeable Li-batteries. *Journal of Power Sources* **105**, 151 (2002).

31. A. S. Arico, P. Bruce, B. Scrosati, J. M. Tarascon, W. Van Schalkwijk, Nanostructured materials for advanced energy conversion and storage devices. *NATURE MATERIALS* **4**, 366 (May, 2005).

32. R. B. Lewis, A. Timmons, R. E. Mar, J. R. Dahn, In Situ AFM Measurements of the Expansion and Contraction of Amorphous Sn-Co-C Films Reacting with Lithium. *Journal of The Electrochemical Society* **154**, A213 (2007).

33. J. Graetz, C. C. Ahn, R. Yazami, B. Fultz, Highly Reversible Lithium Storage in Nanostructured Silicon. *Electrochem. Solid State Lett.* **6**, A194 (Sep, 2003).

34. H. Kim, M. Seo, M. H. Park, J. Cho, A Critical Size of Silicon Nano-Anodes for Lithium Rechargeable Batteries. *Angew. Chem.-Int. Edit.* **49**, 2146 (2010).

35. C. K. Chan *et al.*, High-Performance Lithium Battery Anodes using Silicon Nanowires. *Nat. Nanotechnol.* **3**, 31 (Jan, 2008).

36. G. Armstrong, A. R. Armstrong, P. G. Bruce, P. Reale, B. Scrosati, TiO_2(B) Nanowires as An Improved Anode Material for Lithium-Ion Batteries Containing

$LiFePO_4$ or $LiNi_{0.5}Mn_{1.5}O_4$ Cathodes and A Polymer Electrolyte. *Adv. Mater.* **18**, 2597 (Oct, 2006).

37. H. C. Shin, J. Dong, M. L. Liu, Porous Tin Oxides Prepared using an Anodic Oxidation Process. *Adv. Mater.* **16**, 237 (Feb, 2004).

38. S. J. Bao, Q. L. Bao, C. M. Li, Z. L. Dong, Novel Porous Anatase TiO_2 Nanorods and their High Lithium Electroactivity. *Electrochemistry Communications* **9**, 1233 (May, 2007).

39. H. C. Shin, M. L. Liu, Three-dimensional porous copper-tin alloy electrodes for rechargeable lithium batteries. *Advanced Functional Materials* **15**, 582 (Apr, 2005).

40. S. C. Zhang *et al.*, A three-dimensional tin-coated nanoporous copper for lithium-ion battery anodes. *Journal of Power Sources* **196**, 6915 (Aug, 2011).

41. S. Menkin, D. Golodnitsky, E. Peled, Artificial solid-electrolyte interphase (SEI) for improved cycleability and safety of lithium-ion cells for EV applications. *Electrochemistry Communications* **11**, 1789 (2009).

42. E. Peled, C. Menachem, D. BarTow, A. Melman, Improved graphite anode for lithium-ion batteries - Chemically bonded solid electrolyte interface and nanochannel formation. *Journal of The Electrochemical Society* **143**, L4 (Jan, 1996).

43. Y. Ein-Eli, A new perspective on the formation and structure of the solid electrolyte interface at the graphite anode of Li-ion cells. *Electrochem. Solid State Lett.* **2**, 212 (May, 1999).

44. Y. S. Jung *et al.*, Enhanced Stability of LiCoO(2) Cathodes in Lithium-Ion Batteries Using Surface Modification by Atomic Layer Deposition. *Journal of The Electrochemical Society* **157**, A75 (2010).

45. Y. S. Jung *et al.*, Ultrathin Direct Atomic Layer Deposition on Composite Electrodes for Highly Durable and Safe Li-Ion Batteries. *Adv. Mater.* **22**, 2172 (May, 2010).

46. S. S. Zhang, A review on electrolyte additives for lithium-ion batteries. *Journal of Power Sources* **162**, 1379 (Nov, 2006).

47. L. J. Fu *et al.*, Surface modifications of electrode materials for lithium ion batteries. *Solid State Sci.* **8**, 113 (Feb, 2006).

48. K. C. Kil *et al.*, Enhanced Electrochemical Properties of LiFePO(4) Electrodes with Carboxylated Poly(vinyl difluoride) in Lithium-Ion Batteries: Experimental and Theoretical Analysis. *J. Phys. Chem. C* **115**, 16242 (Aug, 2011).

49. J. Y. Song, Y. Y. Wang, C. C. Wan, Review of gel-type polymer electrolytes for lithium-ion batteries. *Journal of Power Sources* **77**, 183 (1999).

50. M. Doyle, T. F. Fuller, J. Newman, Modeling of Galvanostatic Charge and Discharge of the Lithium/Polymer/Insertion Cell. *Journal of The Electrochemical Society* **140**, 1526 (1993).

51. T. F. Fuller, M. Doyle, J. Newman, Simulation and Optimization of the Dual Lithium Ion Insertion Cell. *Journal of The Electrochemical Society* **141**, 1 (1994).

52. M. Doyle, J. Newman, A. S. Gozdz, C. N. Schmutz, J.-M. Tarascon, Comparison of Modeling Predictions with Experimental Data from Plastic Lithium Ion Cells. *Journal of The Electrochemical Society* **143**, 1890 (1996).

53. R. Darling, J. Newman, Modeling a Porous Intercalation Electrode with Two Characteristic Particle Sizes. *Journal of The Electrochemical Society* **144**, 4201 (1997).

54. D. R. Baker, M. W. Verbrugge, Temperature and Current Distribution in Thin-Film Batteries. *Journal of The Electrochemical Society* **146**, 2413 (1999).

55. V. Srinivasan, J. Newman, Discharge Model for the Lithium Iron-Phosphate Electrode. *Journal of The Electrochemical Society* **151**, A1517 (2004).

56. S. Devan, V. R. Subramanian, R. E. White, Analytical Solution for the Impedance of a Porous Electrode. *Journal of The Electrochemical Society* **151**, A905 (2004).

57. D. Dees, E. Gunen, D. Abraham, A. Jansen, J. Prakash, Electrochemical Modeling of Lithium-Ion Positive Electrodes during Hybrid Pulse Power Characterization Tests. *Journal of The Electrochemical Society* **155**, A603 (2008).

58. X. Zhang, W. Shyy, A. M. Sastry, Numerical Simulation of Intercalation-Induced Stress in Li-Ion Battery Electrode Particles. *Journal of The Electrochemical Society* **154**, A910 (2007).

59. J. Christensen, J. Newman, A Mathematical Model of Stress Generation and Fracture in Lithium Manganese Oxide. *Journal of The Electrochemical Society* **153**, A1019 (2006).

60. R. E. Garcia, Y.-M. Chiang, W. C. Carter, P. Limthongkul, C. M. Bishop, Microstructural Modeling and Design of Rechargeable Lithium-Ion Batteries. *Journal of The Electrochemical Society* **152**, A255 (2005).

61. J. Christensen, J. Newman, Stress generation and fracture in lithium insertion materials. *Journal of Solid State Electrochemistry* **10**, 293 (2006).

62. X. Zhang, A. M. Sastry, W. Shyy, Intercalation-Induced Stress and Heat Generation within Single Lithium-Ion Battery Cathode Particles. *Journal of The Electrochemical Society* **155**, A542 (2008).

63. H. Gabrisch, J. Wilcox, M. Doeff, TEM Study of Fracturing in Spherical and Plate-like LiFePO4 Particles. *Electrochemical and Solid-State Letters* **11**, A25 (2008).

64. Y. Itou, Y. Ukyo, Performance of LiNiCoO2 materials for advanced lithium-ion batteries. *Journal of Power Sources* **146**, 39 (2005).

65. T. Ohzuku, H. Tamura, K. Sawai, Monitoring of particle fracture by acoustic emission during charge and discharge of Li/MnO2 cells. *Journal of the Electrochemical Society* **144**, (1997).

66. V. Srinivasan, J. Newman, Discharge Model for the Lithium Iron-Phosphate Electrode. *Journal of The Electrochemical Society* **151**, A1517 (2004).

67. V. Srinivasan, J. Newman, Existence of path-dependence in the LiFePO4 electrode. *Electrochemical and Solid-State Letters* **9**, A110 (2006).

68. Y.-T. Cheng, M. W. Verbrugge, The influence of surface mechanics on diffusion induced stresses within spherical nanoparticles. *Journal of Applied Physics* **104**, 083521 (2008).

69. Y.-T. Cheng, M. W. Verbrugge, Evolution of stress within a spherical insertion electrode particle under potentiostatic and galvanostatic operation. *Journal of Power Sources* **190**, 453 (2009).

70. M. W. Verbrugge, Y.-T. Cheng, Stress and Strain-Energy Distributions within Diffusion-Controlled Insertion-Electrode Particles Subjected to Periodic Potential Excitations. *Journal of The Electrochemical Society* **156**, A927 (2009).

71. R. Deshpande, Y.-T. Cheng, M. W. Verbrugge, Modeling diffusion-induced stress in nanowire electrode structures. *Journal of Power Sources* **195**, 5081 (2010).

72. J. Yan *et al.*, Phenomenologically modeling the formation and evolution of the solid electrolyte interface on the graphite electrode for lithium-ion batteries. *Electrochimica Acta* **53**, 7069 (2008).

73. K. Leung, J. L. Budzien, Ab initio molecular dynamics simulations of the initial stages of solid-electrolyte interphase formation on lithium ion battery graphitic anodes. *Physical Chemistry Chemical Physics* **12**, 6583 (2010).

74. G. Ning, R. E. White, B. N. Popov, A generalized cycle life model of rechargeable Li-ion batteries. *Electrochimica Acta* **51**, 2012 (Feb, 2006).

75. J. Christensen, J. Newman, A mathematical model for the lithium-ion negative electrode solid electrolyte interphase. *Journal of The Electrochemical Society* **151**, A1977 (2004).

76. M. Safari, M. Morcrette, A. Teyssot, C. Delacourt, Life-Prediction Methods for Lithium-Ion Batteries Derived from a Fatigue Approach I. Introduction: Capacity-Loss Prediction Based on Damage Accumulation. *Journal of The Electrochemical Society* **157**, A713 (2010).

77. M. Safari, M. Morcrette, A. Teyssot, C. Delacourt, Life Prediction Methods for Lithium-Ion Batteries Derived from a Fatigue Approach II. Capacity-Loss

Prediction of Batteries Subjected to Complex Current Profiles. *Journal of The Electrochemical Society* **157**, A892 (2010).

78. Q. Zhang, R. E. White, Calendar life study of Li-ion pouch cells. *Journal of Power Sources* **173**, 990 (Nov, 2007).

79. Q. Zhang, R. E. White, Calendar life study of Li-ion pouch cells - Part 2: Simulation. *Journal of Power Sources* **179**, 785 (May, 2008).

80. Q. Zhang, R. E. White, Capacity fade analysis of a lithium ion cell. *Journal of Power Sources* **179**, 793 (May, 2008).

81. R. P. Ramasamy, R. E. White, B. N. Popov, Calendar life performance of pouch lithium-ion cells. *Journal of Power Sources* **141**, 298 (2005).

82. R. P. Ramasamy, J.-W. Lee, B. N. Popov, Simulation of capacity loss in carbon electrode for lithium-ion cells during storage. *Journal of Power Sources* **166**, 266 (2007).

83. M. Broussely *et al.*, Main aging mechanisms in Li ion batteries. *Journal of Power Sources* **146**, 90 (Aug, 2005).

84. R. Spotnitz, Simulation of capacity fade in lithium-ion batteries. *Journal of Power Sources* **113**, 72 (Jan, 2003).

85. I. Bloom *et al.*, An accelerated calendar and cycle life study of Li-ion cells. *Journal of Power Sources* **101**, 238 (2001).

86. K. Kumaresan, Q. Z. Guo, P. Ramadass, R. E. White, Cycle life performance of lithium-ion pouch cells. *Journal of Power Sources* **158**, 679 (Jul, 2006).

87. S. Santhanagopalan, Q. Guo, P. Ramadass, R. E. White, Review of models for predicting the cycling performance of lithium ion batteries. *Journal of Power Sources* **156**, 620 (2006).

88. R. Deshpande, Y. Qi, Y.-T. Cheng, Effects of Concentration-Dependent Elastic Modulus on Diffusion-Induced Stresses for Battery Applications. *Journal of The Electrochemical Society* **157**, A967 (2010).

89. S. J. Harris, R. D. Deshpande, Y. Qi, I. Dutta, Y. T. Cheng, Mesopores inside electrode particles can change the Li-ion transport mechanism and diffusion-induced stress. *Journal of Materials Research* **25**, 1433 (Aug, 2010).

90. R. Deshpande, Y.-T. Cheng, M. W. Verbrugge, A. Timmons, Diffusion Induces Stresses and Strain Energy in a Phase Transforming Spherical Electrode Particle. *Journal of The Electrochemical Society* **158**, 1 (2011).

91. M. K. Aydinol, A. F. Kohan, G. Ceder, K. Cho, J. Joannopoulos, Ab initio study of lithium intercalation in metal oxides and metal dichalcogenides. *Physical Review B* **56**, 1354 (Jul, 1997).

92. G. Ceder *et al.*, Identification of cathode materials for lithium batteries guided by first-principles calculations. *Nature* **392**, 694 (Apr, 1998).

93. B. Kang, G. Ceder, Battery materials for ultrafast charging and discharging. *Nature* **458**, 190 (Mar, 2009).

94. K. S. Kang, Y. S. Meng, J. Breger, C. P. Grey, G. Ceder, Electrodes with high power and high capacity for rechargeable lithium batteries. *Science* **311**, 977 (Feb, 2006).

95. V. B. Shenoy, P. Johari, Y. Qi, Elastic softening of amorphous and crystalline Li-Si Phases with increasing Li concentration: A first-principles study. *Journal of Power Sources* **195**, 6825 (Oct, 2010).

96. Y. Qi, H. Guo, J. L. G. Hector, A. Timmons, Threefold Increase in the Young's Modulus of Graphite Negative Electrode during Lithium Intercalation. *Journal of The Electrochemical Society* **157**, A558 (2010).

97. J. B. Goodenough, "Basic energy needs for electrical energy storage- Report of the Basic Energy Sciences Workshop for Electrical Energy Storage" (July, 2007).

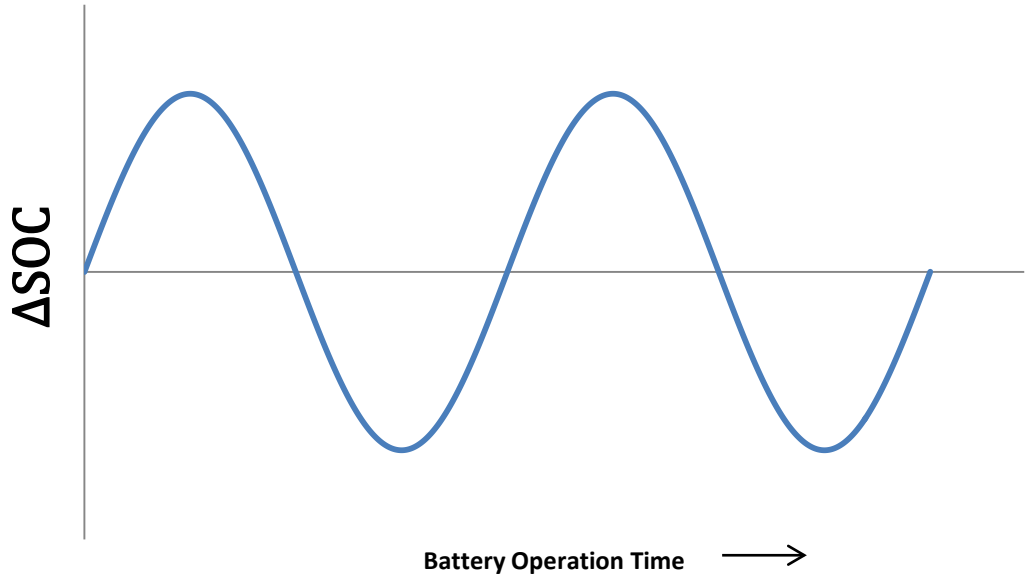

Figure 2.1: The state of charge (SOC) variation of an electrode particle during electrochemical cycling

CHAPTER 3

MODELING DIFFUSION-INDUCED STRESS IN NANOWIRE ELECTRODE STRUCTURES

This chapter is based on work published as:

R. Deshpande, Y.-T. Cheng, M. W. Verbrugge, Modeling diffusion-induced stress in nanowire electrode structures. *Journal of Power Sources* **195**, 5081 (2010).

It's reproduced by permission of The Electrochemical Society.

3.1 Summary

There is an intense, worldwide effort to develop durable lithium ion batteries with high energy and power densities for a wide range of applications, including electric and hybrid electric vehicles. One of the critical challenges in advancing lithium ion battery technologies is fracture and decrepitation of the electrodes as a result of the lithium diffusion during charging and discharging operations. When lithium is inserted in either the positive or negative electrode, a large volume change of the order of a few to several hundred percent, can occur. Diffusion-induced stresses (DISs) can therefore cause the nucleation and growth of cracks, leading to mechanical degradation of the active electrode materials. In this chapter, we develop a mathematical model relating surface energy with diffusion induced stresses in nanowire electrodes. With decreasing size of the electrode, the ratio of surface area to volume increases.

Thus, surface energy and surface stress can play important roles in mitigating DISs in nano-structured electrodes. In this chapter, we establish relationships between the surface energy, surface stress and the magnitude of DISs in nanowires. We find that DISs, especially the tensile stresses, can decrease significantly due to the surface effects. This model also establishes a relationship between the stress and the nanowire radius. We show that, with decreasing size, the electrode material will be less prone to mechanical degradation, leading to an increase in the life of lithium ion batteries, provided other phenomena are unaffected by increased surface area (e.g., chemical degradation reactions). We also show that, in the case of nano-structures, surface strain energy is significant in magnitude compared to bulk strain energy. A mathematical tool to calculate total strain energy is developed that can be used to compare strain energy with the fracture energy of that material in the electrode system.

3.2 Introduction

The lithium diffusion within the host electrodes of lithium ion batteries leads to 'Diffusion Induced Stresses' (DISs), which stimulate mechanical degradation of the electrodes, i.e. pulverization, capacity fading and decrease in battery performance. Recently, Chan *et al.* (*1*), showed that silicon nanowires can accommodate large strain without pulverization. Due to low discharge potential (relative to a lithium reference) and identified high theoretical charge capacity (4,200 $mAh\ g^{-1}$) (*2*), silicon nanowires are of interest for lithium ion battery applications. Several research groups have reported on the use of nanotubes and nanowires of different materials as electrodes in lithium ion batteries.

Chen and co-workers (*3*) have recently shown that CuO nanowires have high reversible capacity. Earlier, Chan and coworkers (*4*) proposed that Ge nanowires can be used to construct a high capacity Li ion battery. With the decreasing size of the active electrode element the surface area to volume ratio increases; as has been recognized in many publications. When the characteristic dimension of a particle falls below tens of nanometers, the number of atoms on the surface of the particle exceeds those of the bulk (*5*), and unusual particle properties often result relative to the bulk material, which has given rise to the term nanotechnology in more recent times. Cuenot *et al.* (*6*) have clarified the influence of nanowire radius on mechanical properties including the apparent stiffness and tensile modulus. Hence, for nano-scale electrode structures, surface energies, and surface stresses can be expected to have a significant impact on the mechanical properties of electrode materials.

A substantial body of literature is devoted to the modeling of lithium ion batteries using volume-averaged (macro-homogeneous) methods to characterize simultaneously the liquid and solid phase phenomena (*7-14*). Prussin (*15*) made an analogy between thermal stress and DIS and analyzed the transverse stresses developed in a thin plate during mass transfer. Lee and co-workers (*16-18*) also studied DIS in various systems including thin plates, hollow cylinders, and composites. García *et al.* (*19*) developed a numerical framework which describes the spatial distribution of electrochemical fields and stress distribution in porous electrode microstructures. Christensen and Newman (*20, 21*), and Zhang *et al.* (*22, 23*) simulated intercalation induced stresses within single particles to capture salient features of the governing electrochemistry and solid mechanics taking place in lithium ion batteries.

At the nano-scale, surface effects mentioned above are prominent, which has prompted the inclusion of surface mechanics within the analysis of DIS of spherical electrode particles (*24*).

In this chapter, we couple the DISs and surface stresses so as to elucidate their combined effects on the mechanical behavior of nanowire electrodes; our approach is similar to that employed for spherical particles (*24*). This chapter provides a mathematical framework for the investigation of nanowire electrodes. In addition to stress effects, surface strain energy also becomes significant relative to that of the bulk at the nano-scale. Strain energy is an important criterion that can be used to determine the mechanical stability of an electrode material. Cheng and Verbrugge (*25*) analyzed strain energy for spherical particles without considering the effects of surface energy. In this work, we perform a complete strain energy analysis showing that surface strain energy contributes significantly to total strain energy for nanowires. Furthermore, the total strain energy can be compared with the fracture energy to derive a condition for crack propagation in electrode materials; the ensuing analysis and approach is new to modeling DIS of nano-scale systems and provides a general framework for the investigation of other nano-scale geometries. The specific results of this analysis should prove helpful in guiding the selection of materials for nanowire electrodes.

3.3 Stress modeling

The surface stress of a material is related to the surface energy and the strain tensor of a particular geometry of the material. This can be expressed with Gibb's equation (*26*)

$$\sigma_{\alpha\beta}^{surf} = \gamma\delta_{\alpha\beta} + \frac{\partial\gamma}{\partial\varepsilon_{\alpha\beta}} \tag{3.1}$$

where, γ is surface energy per unit area, $\varepsilon_{\alpha\beta}$ is a 2×2 surface strain tensor, and $\delta_{\alpha\beta}$ is the Kronecker delta function. For liquids, surface stress and γ have the same value because of the high mobility of atoms in fluids. For solids, surface stress and surface energy are not the same because of the finite elasticity of solid surfaces. Under the assumption that the surface adheres to the bulk without slipping, and in the absence of body forces, the equilibrium and constitutive equations for isotropic case can be summarized as follows (*26*). In the bulk,

$$\sigma_{ij,j}^{bulk} = 0 \tag{3.2a}$$

$$\sigma_{ij}^{bulk} = C_{ijkl}\,\varepsilon_{kl} = \left[\,\lambda\,\delta_{ij}\delta_{kl} + \mu\left(\,\delta_{ik}\delta_{jl} + \delta_{il}\delta_{jk}\right)\right]\varepsilon_{kl}$$

On the surface (or interface),

$$\sigma_{\beta\alpha}^{bulk} n_\beta + \sigma_{\beta\alpha,\beta}^{surface} = 0 \qquad \sigma_{ij}^{bulk} n_j n_i = \sigma_{\alpha\beta}^{surface}\kappa_{\alpha\beta}$$

(3.2b)

$$\sigma_{\alpha\beta}^{surface} = \tau^0\delta_{\beta\alpha} + 2(\mu^s - \tau^0)\delta_{\beta\gamma}\varepsilon_{\gamma\alpha} + (\lambda^s + \tau^0)\varepsilon_{\gamma\gamma}\delta_{\beta\alpha}$$

where, λ and μ are the Lamé constants for the isotropic bulk material. The surface/interface can be characterized by surface Lamé constants λ^s and μ^s, which give deformation dependent surface energy.

Other symbols denote the following (*26*); $\kappa_{\alpha\beta}$ is the curvature tensor of the surface/interface, τ^0 is residual surface tension under unrestrained conditions, n_α is normal vector to surface/ interface, and ε_{ij} is infinitesimal strain tensor. It is noted that only certain strain components appear within the constitutive law for surfaces due to the 2×2 nature of the surface stress tensor (*i.e.* strains normal to the surface are excluded). The Greek indices take on values 1 and 2 while Latin subscripts adopt values 1 through 3. Conventional summation rules apply unless otherwise noted.

For cylindrical structure, *i.e.*, nanowires, we can rewrite this equation as

$$\sigma_\theta = \sigma_{\theta\theta} = \tau^0 + (2\mu^s + \lambda^s - \tau^0)\varepsilon_{\theta\theta} = \tau^0 + K^s\varepsilon_{\theta\theta} \tag{3.3}$$

The bulk of the nanowire will be assumed to be an isotropic, linearly elastic solid. Using the analogy between thermal stresses (*27*, *28*) and DISs, we can write,

$$\varepsilon_{rr} - \frac{\Omega}{3}C = \frac{1}{E}\left(\sigma_r - \nu(\sigma_\theta + \sigma_z)\right) \tag{3.4}$$

Similarly,

$$\varepsilon_{\theta\theta} - \frac{\Omega}{3}C = \frac{1}{E}(\sigma_\theta - \nu(\sigma_r + \sigma_z)) \tag{3.5}$$

where E is the Young's modulus, C is the molar concentration, and Ω is the partial molar volume of the solute. Depending upon the axial stress conditions, the axial strain can have three possibilities.

i. If the electrode is a long wire, the strain in the *z*-direction may be negligible. This is the plane strain condition, *i.e.*, $\varepsilon_{zz} = 0$.

ii. If nanowires are free at the ends, $F_z = \int_0^R 2\pi r\sigma_z dr = 0$. This is the generalized plane strain condition.

iii. If there is no axial stress present, $\sigma_z = 0$. This is the plane stress condition.

We further assume that the physicochemical properties associated with the linear elastic solid are independent of concentration.

In practice, nanowires electrodes are long wires grown on a substrate and thus one of the ends of the wire is always attached to the substrate. The other end is free to expand.

Changes in stress condition at the fixed end have effect on the stress distribution near that end. But according to Saint-Venant's principle (*28*), the effects on stress due by the fixed end are expected to diminish with distance from the fixed end. Since the other end is free to expand, we can assume that long nanowires with a fixed end are under the generalized plane strain condition (i.e., condition ii).

Since atomic diffusion in solids is a much slower process than elastic deformation, mechanical equilibrium is established much faster than that of diffusion. Mechanical equilibrium is, therefore, treated as a static equilibrium problem (*24*). In the absence of any body force, the equation for static mechanical equilibrium in the bulk of a cylinder is

$$\frac{d\sigma_r}{dr} + \frac{\sigma_r - \sigma_\theta}{r} = 0 \tag{3.6}$$

For infinitesimally small deformation, the radial and tangential strain of cylindrical particle can be related to radial displacement u, by the relation,

$$\varepsilon_{rr} = \frac{du}{dr}, \quad \varepsilon_{\theta\theta} = \frac{u}{r} \tag{3.7}$$

There is no displacement at the center, and $u(0) = 0$.

Furthermore, the radial stress σ_r must satisfy mechanical equilibrium at the surface $r = R$ (where, R is the radius of the cylinder) (*26*),

$$\sigma_r \big|_{r=R} = -\frac{\sigma_\theta^{surface}}{R} \tag{3.8}$$

Using these conditions, Equations 3.3 through 3.8, and no further assumptions, we can express the stress components as

$$\sigma_r = \frac{\Omega}{3} E^* \left[\frac{1}{2} \left\{ \frac{1 - \frac{(2\mu^s + \lambda^s - \tau^0)}{ER}(1+\nu)}{1 + \frac{(2\mu^s + \lambda^s - \tau^0)}{ER}\nu^*} \right\} C_{avg}(R) - \frac{1}{2} C_{avg}(r) \right] - \left[\frac{\tau^0/R}{1 + \frac{(2\mu^s + \lambda^s - \tau^0)}{ER}\nu^*} \right] \tag{3.9}$$

$$\sigma_\theta = \frac{\Omega}{3} E^* \left[\frac{1}{2} \left\{ \frac{1 - \frac{(2\mu^s + \lambda^s - \tau^0)}{ER}(1+\nu)}{1 + \frac{(2\mu^s + \lambda^s - \tau^0)}{ER}\nu^*} \right\} C_{avg}(R) + \frac{1}{2} C_{avg}(r) - C(r) \right] - \left[\frac{\tau^0/R}{1 + \frac{(2\mu^s + \lambda^s - \tau^0)}{ER}\nu^*} \right] \tag{3.10}$$

$$\sigma_z = j\left[\frac{\Omega}{3}E^*\left[\left\{q^* + \nu\frac{1-\frac{(2\mu^s+\lambda^s-\tau^0)}{ER}(1+\nu)}{1+\frac{(2\mu^s+\lambda^s-\tau^0)}{ER}\nu^*}\right\}C_{avg}(R) - C(r)\right]\right.$$

$$\left. - 2v\left[\frac{\tau^0/R}{1+\frac{(2\mu^s+\lambda^s-\tau^0)}{ER}\nu^*}\right]\right]$$

(3.11)

where $C_{avg}(r) = (2/r^2)\int_0^r C(r')r'dr'$ is the average concentration inside a cylinder of unit length and radius r. Here,

i. For the plane strain condition:

$$E^* = \frac{E}{(1-\nu)}\ ,\ \ \nu^* = (1-2\nu)(1+\nu),\ q^* = 0,\ j = 1 \tag{3.12}$$

ii. For the generalized plane strain condition:

$$E^* = \frac{E}{(1-\nu)}\ ,\ \ \nu^* = (1-2\nu)(1+\nu),\ \ q^* = (1-\nu)\ ,\ \ j = 1 \tag{3.13}$$

iii. For the plane stress condition:

$$E^* = E\ ,\ \ \nu^* = (1-\nu),\ q^* = (1-\nu)\ ,\ \ j = 0 \tag{3.14}$$

The stress components contain surface energy and surface tension terms, and the following definitions are used to streamline notation:

$$S_1 = \left[\frac{1-\frac{(2\mu^s+\lambda^s-\tau^0)}{ER}(1+\nu)}{1+\frac{(2\mu^s+\lambda^s-\tau^0)}{ER}\ \nu^*}\right]\ ,\qquad S_2 = -\left[\frac{\tau^0/R}{1+\frac{(2\mu^s+\lambda^s-\tau^0)}{ER}\ \nu^*}\right]$$

(3.15)

Note that the quantities μ^s, λ^s and τ^0 multiply onto $C_{avg}(R)$, which is a time-dependent quantity. The term S_2 has dimensions of stress and the negative sign ensures that it is always compressive relative to the radial, tangential, or axial stress. The radius R in the denominator makes clear that as the size of the electrode particle is reduced, S_2 will have a greater effect on the principal stresses. Thus, in nanoscale structures, surface tension can be expected to play an important role in affecting DISs.

3.4 Diffusion in a cylinder: potentiostatic operation

Lithium ions diffuse in or out of the electrode during charging or discharging. For dilute solutes within the cylindrical host material, the solute (lithium ion) concentration is governed by the diffusion equation:

$$\frac{\partial C}{\partial t} = \mathcal{D}\left(\frac{\partial^2 C}{\partial r^2} + \frac{1}{r}\frac{\partial C}{\partial r}\right) \tag{3.16}$$

There are two possible ways of operating a battery:

a. Potentiostatic operation: the electrode is surrounded by a constant lithium ion concentration.
b. Galvanostatic operation: the current, thus the ionic flux at the surface of the electrode, is a constant.

Here, we assume that the electrode surface is surrounded by an invariant lithium ion concentration C_R (reflecting facile electrochemical kinetics and a porous-electrode system dominated by solute-diffusion resistance (*24*, *25*)). The case of galvanostatic charging is discussed in details in the section 3.6.

We assume the initial lithium ion concentration inside the electrode is C_0. In addition, the concentration at the center is finite. The initial and boundary conditions are, therefore,

$$C(r,0) = C_0\,, \qquad for\ 0 \le r \le R$$

$$C(R,t) = C_R\,, \qquad for\ t \ge 0$$

$$C(0,t) = finite, \qquad for\ t \ge 0$$

Equation 3.16 can be made dimensionless with the following:

$$x = \frac{r}{R},\ \ T = \frac{\mathcal{D}t}{R^2},\ \ y = \frac{C - C_0}{C_R - C_0} \tag{3.17}$$

Hence,

$$\frac{\partial y}{\partial T} = \left(\frac{\partial^2 y}{\partial x^2} + \frac{1}{x}\frac{\partial y}{\partial x}\right) \tag{3.18}$$

The initial and boundary conditions can be rewritten in the dimensionless form as

$$y(x,0) = 0, \qquad for\ 0 \le x \le 1$$

$$y(1,T) = 1, \qquad for\ T \ge 0$$

$$y(0,T) = finite, \qquad for\ T \ge 0 \tag{3.19}$$

The analytic solution of this problem is well known and is reproduced here (*27*),

$$y(x,T) = \frac{C(r) - C_0}{C_R - C_0} == 1 - 2\sum_{n=1}^{\infty}\left\{\frac{e^{-\lambda_n^2 T}\ J_0(\lambda_n x)}{\lambda_n\ J_1(\lambda_n)}\right\} \tag{3.20}$$

where, J_0 and J_1 are the Bessel functions of the first kind of order 0 and 1 respectively, and λ_n are the n solutions of equation $J_0(\lambda_n) = 0$. The average concentrations can be written as,

$$y_{avg}(x) = \frac{C_{avg}(r) - C_0}{C_R - C_0} = \left(1 - \frac{4}{x}\sum_{n=1}^{\infty}\left(\frac{e^{-\lambda_n^2 T}\ J_0(\lambda_n x)}{\lambda_n\ J_1(\lambda_n)}\right)\right) \tag{3.21}$$

$$y_{avg}(1) = \frac{C_{avg}(R) - C_0}{C_R - C_0} = \left(1 - 4\sum_{n=1}^{\infty} e^{-\lambda_n^2 T}/\lambda_n^2\right) \tag{3.22}$$

We can now recast the stress components in dimensionless form:

$$\xi_r = \frac{\sigma_r}{[\frac{\Omega}{3}\frac{E}{(1-\nu)}(C_R - C_0)]}$$

$$= \left[\frac{1}{2}\bar{\nu}\left[(S_1 - 1)\left(\frac{C_0}{C_0 - C_R}\right) + S_1\left(1 - 4\sum_{n=1}^{\infty} e^{-\lambda_n^2 T}/\lambda_n^2\right)\right.\right.$$

$$\left.\left. - \left(1 - \frac{4}{x}\sum_{n=1}^{\infty}\left(\frac{e^{-\lambda_n^2 T}\ J_0(\lambda_n x)}{\lambda_n\ J_1(\lambda_n)}\right)\right)\right] + \frac{S_2}{[\frac{\Omega}{3}\frac{E}{(1-\nu)}(C_R - C_0)]}\right]$$

(3.23)

$$\xi_\theta = \frac{\sigma_\theta}{[\frac{\Omega}{3}\frac{E}{(1-\nu)}(C_R - C_0)]}$$

$$= \left[\frac{1}{2}\bar{\nu}\left[(S_1 - 1)\left(\frac{C_0}{C_0 - C_R}\right) + S_1\left(1 - 4\sum_{n=1}^{\infty} e^{-\lambda_n^2 T}/\lambda_n^2\right)\right.\right.$$

$$\left. + \left(1 - \frac{4}{x}\sum_{n=1}^{\infty}\left(\frac{e^{-\lambda_n^2 T}\ J_0(\lambda_n x)}{\lambda_n\ J_1(\lambda_n)}\right)\right)\right] - \bar{\nu}\left(1 - 2\sum_{n=1}^{\infty}\frac{e^{-\lambda_n^2 T}\ J_0(\lambda_n x)}{\lambda_n\ J_1(\lambda_n)}\right)$$

$$\left. + \frac{S_2}{[\frac{\Omega}{3}\frac{E}{(1-\nu)}(C_R - C_0)]}\right]$$

(3.24)

$$\xi_z = \frac{\sigma_z}{\left[\frac{\Omega}{3}\frac{E}{(1-\nu)}(C_R - C_0)\right]}$$

$$= j\left[\left[(q^* + \nu S_1 - 1)\left(\frac{C_0}{C_0 - C_R}\right) + [q^* + \nu S_1]\left(1 - 4\sum_{n=1}^{\infty} e^{-\lambda_n^2 T}/\lambda_n^2\right)\right.\right.$$

$$\left. - \left(1 - 2\sum_{n=1}^{\infty}\frac{e^{-\lambda_n^2 T}\ J_0(\lambda_n x)}{\lambda_n\ J_1(\lambda_n)}\right)\right] + 2\upsilon\frac{S_2}{\left[\frac{\Omega}{3}\frac{E}{(1-\nu)}(C_R - C_0)\right]}\right]$$

(3.25)

For the plane-strain condition, $\bar{\nu} = 1$; for the generalized plane-strain condition, $\bar{\nu} = 1$; and for the plane-stress condition, $\bar{\nu} = (1 - \nu)$. The quantities ξ_r, ξ_z, and ξ_θ represent dimensionless stresses in $r, \theta,$ and z directions, respectively.

On charge, lithium ions will be inserted into the negative electrode and extracted from the positive electrode; the opposite holds true for discharge.

We can plot dimensionless concentration at different radial positions and time using Equation (3.20) as depicted in Figure 3.1. First, we consider a case of an electrode with a large diameter. There will be neither surface tension nor surface energy effects on the stresses. In this case, S_1=1 and S_2=0. We plot dimensionless radial and tangential stresses. We find that radial stresses (solid lines, Figure 3.2), in both plane strain and generalized plane stress conditions are similar. Similarly, tangential stresses (solid lines, Figure 3.4), in these two conditions are identical. We assume that the initial concentration of solute (lithium ion) inside the electrode is $C_0 = 0$. Similarly, we plot radial and tangential stress for plane stress condition for a large diameter electrode.

In all the three cases, the radial stress at the center initially increases, reaches a maximum when $T = \frac{\mathcal{D}t}{R^2} = 0.076$, and then decreases gradually until the electrode reaches saturation concentration. The radial stress is always tensile if there are no surface effects. The tangential stress is tensile at the center and compresssive at the surface. The magnitude of radial and tangential stress are the same at the center. The tangential stress maxima occures at the surface at time zero. At time zero and $r = R, C_{avg}(R) = C_{avg}(r) \cong 0,$ and $C(r) = C_R$. From equation (3.10) & (3.13), for the plane strain and generalized plane strain condition,

$$\left.\frac{\sigma_\theta}{[\frac{\Omega \quad E}{3\,(1-\nu)}C_R]}\right|_{max} \cong -\bar{\nu} + \frac{S_2}{[\frac{\Omega \quad E}{3\,(1-\nu)}C_R]} \tag{3.26}$$

Here, $\bar{v}$ value is same as mentioned in equation (3.25) depending upon axial loading condition. Equation (3.26) gives the maximum tangential stress that the electrode material will be subjected to. The maximum tangential stress will vary depending upon value of S_2 and the axial loading condition. It can be used as an important parameter to design an electrode material.

In the absense of surface effects ($S_1 = 1$ and $S_2 = 0$), the equation system is symmetric, and mirror opposite conclusions hold for the case of deinsertion (i.e., replacing tensile stress by compressive stress). This stress distribution is independent of the particle radius; with proper time and radius scaling, the stress distribution is idential for all particle radii.

We see, from Figures 3.3, 3.5 and 3.6, that all three stresses are dependant on the axial loading condition of the electrode. Furthermore, the radial and tangential stresses for plane strain and generalized plane strain condition are exactly the same. In contrast, the axial stresses are significantly different in the two cases. The plane stress condition leads to different radial and tangential stresses than plane strain conditions (see, Figures 3.3 and 3.5).

We now consider the influence of small electrode diameters and surface effects on stress distribution. For evaluating the surface effects, the parameters values of Reference (*24*) are employed directly, making it straightforward to compare spherical and cylindrical electrodes. Specifically, E = 10 GPa, ν = 0.3, and $(\Omega/3)C_R$ = 0.08. We take surface tension value as 1 Jm^{-2} and $(2\mu^s + \lambda^s)$ is 5 Nm^{-1}, which is of same order of magnitude as surface modulus values of Al and Si (*28*).

With these values, we get $S_1 = 0.9855$ and $\left(S_2 / \left[\frac{\Omega}{3} \frac{E}{(1-\nu)} C_R\right]\right) = -0.0174$. The plots obtained of dimensionless radial and tangential stress vs. radial distance for a 5 nm cylindrical wire are shown in Figures 3.2 and 3.4 (dashed lines). These are for plane strain conditions in axial direction. Similar plots can be obtained for the other two axial boundary conditions. In both the Figures 3.2 and 3.4, by comparing solid lines and dashes lines, it can be observed that at the nanoscale, there is a significant decrease in both radial and tangential stresses.

We plot radial and tangential stress at time T =0.076 for cylindrical electrodes of different diameters in Figures 3.7 and 3.8, respectively. For insertion, the maximum tangential stress is always compressive and its magnitude is increased as the particle radius is decreased.

It can be observed that, as radius decreases, the effect of surface tension becomes much more significant. These results make it clear that when the influence of surface tension is incorporated, smaller (nano-scale) wires see a more compressive stress environment, which would decrease the probability of crack formation due to tensile stress.

3.5 Strain energy

Due to deformation, elastic strain energy is stored in the electrode. This energy is a driving force for crack propagation in the electrode. Reference (*25*) overviews a strain-energy analysis for spherical particles. For nano-scale particles, the surface strain energy also has a significant contribution to total energy. The total strain energy for the particle can be expressed as

$$E_{total} = E_{bulk} + E_{surface} \tag{3.27}$$

From the stresses, we can calculate the bulk strain energy per unit volume or bulk strain energy density $e(r)$ accumulated as a result of the elastic deformation for the isotropically deformed cylinder as (*28*)

$$e(r) = \frac{1}{2E}\left(\sigma_r^2 + \sigma_\theta^2 + \sigma_z^2\right) - \frac{\nu}{E}(\sigma_r\sigma_\theta + \sigma_\theta\sigma_z + \sigma_z\sigma_r) \tag{3.28}$$

The total bulk strain energy can be obtained by integrating the strain energy density over the entire volume. The bulk strain energy per unit length of the wire can be obtained as

$$E_{bulk} = 2\pi \int_0^R e(r) r dr \tag{3.29}$$

$$E_{bulk} = 2\pi \int_0^R [\frac{1}{2E}\left(\sigma_r^2 + \sigma_\theta^2 + \sigma_z^2\right) - \frac{\nu}{E}(\sigma_r\sigma_\theta + \sigma_\theta\sigma_z + \sigma_z\sigma_r)\,] r dr$$

In dimensionless form,

$$\prod_{bulk} = \frac{E_{bulk}}{\pi R^2 E(\frac{\Omega}{3}\frac{(C_R - C_0)}{(1-\nu)})^2} = \int_0^1 [\left(\xi_r^2 + \xi_\theta^2 + \xi_z^2\right) - 2\nu(\xi_r\xi_\theta + \xi_\theta\xi_z + \xi_z\xi_r)\,] x dx$$

(3.30)

Along with bulk strain energy, surface strain energy is also stored in the electrode. To derive an expression for surface strain-energy density, we consider a cylinder of original diameter R that is stretched to a new radius $R + \Delta R$ (cf. Figure 3.11). The surface stress has two parts (see, Equation 3.3). The contribution to the total surface energy as a result of the increase in radius can be expressed as

$$2\pi h(R + \Delta R)\tau^0 - 2\pi h R\tau^0 = 2\pi h \Delta R \tau^0 = 2\pi h R \frac{\Delta R}{R}\tau^0 = 2\pi h R \varepsilon_\theta \tau^0 \tag{3.31}$$

The contribution of the surface tension $\tau^0$to the surface strain energy density is, therefore,

$$\frac{2\pi h(R+\Delta R)\tau^0 - 2\pi Rh\tau^0}{2\pi Rh} = \frac{2\pi h\Delta R\tau^0}{2\pi Rh} = \varepsilon_\theta\ \tau^0 \tag{3.32}$$

We now consider the contribution of $K^s\varepsilon_\theta$ to the surface-strain energy density. With the assistance of Figure 3.11, we note that a force balance yields

$$(\sigma^{surface} - \tau^0)h = K^s\varepsilon_\theta h \tag{3.33}$$

The work is the shaded area in Figure 3.11 and is given by

$$\frac{1}{2}(\sigma^{surface} - \tau^0)hdRd\theta = \frac{1}{2}K^s\varepsilon_\theta hdRd\theta \tag{3.34}$$

The work per unit area is, therefore, given by

$$\frac{\frac{1}{2}(\sigma^{surface} - \tau^0)hdRd\theta}{hdRd\theta} = \frac{\frac{1}{2}K^s\varepsilon_\theta hdRd\theta}{hdRd\theta} = \frac{1}{2}K^s\varepsilon_\theta \tag{3.35}$$

Thus total surface strain energy can be written as,

$$Total\ surface\ strain\ energy\ = 2\pi R(\tau^0\varepsilon_0 + \frac{1}{2}K^s\varepsilon_\theta^2) \tag{3.36}$$

To compare with bulk strain energy, this surface strain energy is normalized with the same quantity,

$$\prod_{surface} = \frac{2\pi R(\tau^0\varepsilon_0 + \frac{1}{2}K^s\varepsilon_\theta^2)}{\pi R^2 E(\frac{\Omega(C_R - C_0)}{3\ \ (1-\nu)})^2} = \frac{2(\tau^0\varepsilon_0 + \frac{1}{2}K^s\varepsilon_\theta^2)}{RE(\frac{\Omega(C_R - C_0)}{3\ \ (1-\nu)})^2} \tag{3.37}$$

Thus total strain energy stored in the electrode due to volumetric expansion is an addition of the bulk and surface strain energies.

Figure 3.9 shows the dimensionless bulk strain energy, surface strain energy, and total strain energy stored in 5 nm cylindrical electrode due to lithium intercalation in generalized plane strain condition. We can see that surface strain energy has a considerable effect on the total strain energy. In addition, it can be inferred that the surface strain energy has a comparable magnitude to the bulk strain energy for the 5 nm electrode in all the three cases. This confirms the fact that for representative parameters values and nano-scale electrode dimensions, the surface effects are considerably strong and can mitigate deleterious effects of DISs in terms of fracture propagation; hence, from a fracture perspective, nano-scale electrodes can be expected to provide higher cycle life than electrodes constructed with large particles. Experiments with nanowire electrodes support this. For example, Chan *et al.* (*1*), showed that silicon nanowires can accommodate large strain without pulverization.

Nanowire structured electrodes of different material like Si, Sn, TiO_2 have been investigated experimentally. These experiments also confirm better behavior of nanowire electrodes than bulk electrodes (*4*, *29-35*). These results depend upon the surface and material properties of the electrode material (*36*), and we have not considered potential deleterious chemical reactions that are enhanced by increased electrode surface area, such as solvent reduction on carbon negatives (*37*). Using this mathematical model, we can select the best possible material for the electrode, in terms of resistance to crack propagation, by comparing this total energy calculated with the surface energy for cracking. Thus at nano-scale, not only bulk strain energy but surface strain energy should be considered for predicting the initiation and propagation of fracture.

Figure 3.10 shows the variation of total strain energy in all the axial loading conditions. The difference in the nature of strain energy profiles in all the three cases is due to the different nature of axial stress. From Figure 3.10 we can see that, in case of the plane stress and generalized plane strain condition, strain energy increases initially, reaches a peak value, and then decreases. On the other hand, in case of the plane strain condition, energy increases initially and then a reaches a steady maximum value. The valley seen in the plane strain curve is consistent with the radial and tangential stress maxima. The increase in total energy afterwards is related to the continuous increase in magnitude of axial stress. The electrode subjected to the plane stress condition exhibits less stored strain energy and is thus less prone to cracking as compared to other two cases.

3.6 Stress and strain energy analysis for the galvanostatic operation:

The battery is charged with a constant current density $'I'$. Hence, the ionic flux at the surface of the electrode is constant. The appropriate boundary and initial conditions to solve the diffusion equation can be written as,

$$C(r,0) = C_0\,, \qquad for\ 0 \le r \le R$$

$$D\left.\frac{dC(r,t)}{dr}\right|_{r=R} = \frac{I}{F}, \quad for\ t \ge 0$$

$$C(0,t) = finite, \qquad for\ t \ge 0 \tag{3.38}$$

where F is Faraday's constant.

The diffusion equation, Equation 3.16, can be normalized using the following dimensionless parameters:

$$x = \frac{r}{R},\ \ T = \frac{\mathcal{D}t}{R^2},\ \ y = [C(r,t) - C_0] * \frac{F\mathcal{D}}{IR} \tag{3.39}$$

The initial and boundary conditions can be rewritten in the dimensionless form as

$$y(x,0) = 0, \qquad for\ 0 \le x \le 1$$

$$\left.\frac{dy(x,T)}{dx}\right|_{x=1} = 1, \qquad for\ T \ge 0$$

$$y(0,T) = finite, \qquad for\ T \ge 0 \tag{3.40}$$

The analytic solution of this problem is well known and is reproduced here (*27*),

$$y(x,T) = -\left\{2T + \frac{x^2}{2} - \frac{1}{4} - 2\sum_{n=1}^{\infty} \frac{e^{-\lambda_n^2 T}\ J_0(\lambda_n x)}{{\lambda_n}^2\ J_0(\lambda_n)}\right\} \tag{3.41}$$

where, J_0 and J_1 are the Bessel functions of the first kind of order 0 and 1 respectively, and λ_n is the *nth* solution of equation $J_1(\lambda_n) = 0$. The average concentrations can be written as,

$$y_{avg}(x) = \frac{C_{avg}(r) - C_0}{\left(\frac{IR}{F\mathcal{D}}\right)} = -\left\{2T + \frac{x^2}{4} - \frac{1}{4} - \frac{4}{x}\sum_{n=1}^{\infty} \frac{e^{-\lambda_n^2 T}\ J_0(\lambda_n x)}{{\lambda_n}^2\ J_0(\lambda_n)}\right\} \tag{3.42}$$

$$y_{avg}(1) = \frac{C_{avg}(R) - C_0}{\left(\frac{IR}{F\mathcal{D}}\right)} = -2T \tag{3.43}$$

We can derive the stress components in dimensionless form:

$$\xi_r = \frac{\sigma_r}{[\frac{\Omega}{3}\frac{E}{(1-\nu)}\frac{IR}{F\mathcal{D}}]}$$

$$= \frac{1}{2}\bar{\nu}\left[(S_1 - 1)\left(\frac{C_0}{\left(\frac{IR}{F\mathcal{D}}\right)}\right) + S_1(-2T)\right.$$

$$\left. + \left\{2T + \frac{x^2}{4} - \frac{1}{4} - \frac{4}{x}\sum_{n=1}^{\infty}\frac{e^{-\lambda_n^2 T}\ J_0(\lambda_n x)}{{\lambda_n}^2\ J_0(\lambda_n)}\right\}\right] + \frac{S_2}{[\frac{\Omega}{3}\frac{E}{(1-\nu)}\frac{IR}{F\mathcal{D}}]}$$

(3.44)

$$\xi_\theta = \frac{\sigma_\theta}{[\frac{\Omega}{3}\frac{E}{(1-\nu)}\left(\frac{IR}{F\mathcal{D}}\right)]}$$

$$= \frac{1}{2}\bar{\nu}\left[(S_1 - 1)\left(\frac{C_0}{\left(\frac{IR}{F\mathcal{D}}\right)}\right) + S_1(-2T)\right.$$

$$\left. - \left\{2T + \frac{x^2}{4} - \frac{1}{4} - \frac{4}{x}\sum_{n=1}^{\infty}\frac{e^{-\lambda_n^2 T}\ J_0(\lambda_n x)}{{\lambda_n}^2\ J_0(\lambda_n)}\right\}\right]$$

$$+ \bar{\nu}\left\{2T + \frac{x^2}{2} - \frac{1}{4} - 2\sum_{n=1}^{\infty}\frac{e^{-\lambda_n^2 T}\ J_0(\lambda_n x)}{{\lambda_n}^2\ J_0(\lambda_n)}\right\} + \frac{S_2}{[\frac{\Omega}{3}\frac{E}{(1-\nu)}\left(\frac{IR}{F\mathcal{D}}\right)]}$$

(3.45)

$$\xi_z = \frac{\sigma_z}{\left[\frac{\Omega}{3}\frac{E}{(1-\nu)}\left(\frac{IR}{F\mathcal{D}}\right)\right]}$$

$$= j\left[\left[(q^* + \nu S_1 - 1)\left(\frac{C_0}{\left(\frac{IR}{F\mathcal{D}}\right)}\right) + [q^* + \nu S_1](-2T)\right.\right.$$

$$\left.\left. + \left\{2T + \frac{x^2}{2} - \frac{1}{4} - 2\sum_{n=1}^{\infty}\frac{e^{-\lambda_n^2 T}\ J_0(\lambda_n x)}{{\lambda_n}^2\ J_0(\lambda_n)}\right\}\right] + 2\upsilon\frac{S_2}{\left[\frac{\Omega}{3}\frac{E}{(1-\nu)}\left(\frac{IR}{F\mathcal{D}}\right)\right]}\right]$$

(3.46)

For the plane-strain condition, $\bar{\nu} = 1$; for the generalized plane-strain condition, $\bar{\nu} = 1$; and for the plane-stress condition, $\bar{\nu} = (1-\nu)$. The quantities ξ_r, ξ_z, and ξ_θ represent dimensionless stresses in r, z and θ directions, respectively.

On charging, lithium ions will be inserted into the negative electrode and extracted from the positive electrode; the opposite holds true for discharging.

Similar to the potentiostatic case we calculate bulk strain energy, surface strain energy, and total strain energy for all the three cases. We also compare the total strain energies of the three cases as shown in Figure 3.19

$$\prod_{bulk} = \frac{E_{bulk}}{\pi R^2 E(\frac{\Omega}{3(1-\nu)}\frac{IR}{F\mathcal{D}})^2} = \int_0^1 [\left(\xi_r^2 + \xi_\theta^2 + \xi_z^2\right) - 2\nu(\xi_r\xi_\theta + \xi_\theta\xi_z + \xi_z\xi_r)\ ]xdx$$

(3.47)

$$\prod_{surface} = \frac{2\pi R(\tau^0\varepsilon_0 + \frac{1}{2}K^S\varepsilon_\theta^2)}{\pi R^2 E(\frac{\Omega}{3(1-\nu)}\frac{IR}{F\mathcal{D}})^2} = \frac{2(\tau^0\varepsilon_0 + \frac{1}{2}K^S\varepsilon_\theta^2)}{RE(\frac{\Omega}{3(1-\nu)}\frac{IR}{F\mathcal{D}})^2}$$

(3.48)

We can also calculate,

$$\prod_{total} = \prod_{bulk} + \prod_{surface} \tag{3.49}$$

We plot dimensionless concentration at different radial positions and time using Equation (3.39) in Figure 3.12. We should note that, after a time *T~ 0.4*, the concentration at the surface reaches maximum possible concentration. After this point constant current operation does not hold true. First, we consider a case of an electrode with a large diameter for which we can neglect surface tension and surface energy effects. In this case, S_1=1 and S_2=0. We plot dimensionless radial and tangential stresses. We find that radial stresses (solid lines) in both plane strain and generalized plane stress conditions are similar. Likewise, tangential stresses in these two conditions are identical. We assume that the initial concentration of solute (lithium ion) inside the electrode is $C_0 = 0$. Similarly, we plot radial and tangential stress for plane stress condition for a large diameter electrode. In all the three cases, the radial stress at the center initially increases, reaches a maximum when $T = \frac{\mathcal{D}t}{R^2} = 0.35$, and then remain constant until the electrode reaches the saturation concentration. The radial stress is always tensile if there are no surface effects. The tangential stress is tensile at the center and compresssive at the surface. The magnitudes of radial and tangential stress are the same at the center. The tangential stress maxima occurs at the surface at time zero. At time zero and r=R, we have $C_{avg}(R) = C_{avg}(r) \cong 0$, and $C(r) = C_R$. From Equation (3.45), we obtrain, for the plane strain and generalized plane strain condition,

$$\left.\frac{\sigma_\theta}{\left[\frac{\Omega}{3}\frac{E}{(1-\nu)}\frac{IR}{F\mathcal{D}}\right]}\right|_{max} \cong -\bar{\nu}\cdot y(1) + \frac{S_2}{\left[\frac{\Omega}{3}\frac{E}{(1-\nu)}\frac{IR}{F\mathcal{D}}\right]} \tag{3.50}$$

Here, $\bar{\nu}$ value is same as that in Equation (3.46) depending upon the axial loading condition. Eq (3.50) gives the maximum tangential stress that the electrode material experiences. The maximum tangential stress varies depending upon the value of S_2 and the axial loading condition. It can be used as an important parameter to design an electrode material.

In the absense of surface effects ($S_1 = 1$ and $S_2 = 0$), the equation system is symmetric with respect to insertion and deinsertion, and mirror opposite conclusions hold for the case of deinsertion (i.e., replacing tensile stress by compressive stress). This stress distribution is independent of the wire radius; with proper time and radius scaling, the stress distribution is idential for all wire radii.

From Figures 3.15, 3.16 and 3.17, we see that, all the three stresses depend on the axial loading condition of the electrode.

We note that the radial and tangential stresses for plane strain and generalized plane strain condition are exactly the same. On the other hand, from Figure 3.16, the axial stresses are significantly different in the two cases. The plane stress condition has altogether different radial and tangential stresses than the plane strain conditions.

We now consider the influence of small electrode diameters and surface effects on stress distribution. For evaluating the surface effects, the parameters values of Reference (*24*) are employed, making it straightforward to compare spherical and cylindrical electrodes. Specifically, E = 10 GPa, ν = 0.3, and $(\Omega/3)C_R$ = 0.08.

We take surface tension value as 1 Jm^{-2} and $(2\mu^s + \lambda^s)$ is 5 Nm^{-1}, which is of same order of magnitude as surface modulus values for Al and Si (*28*). With these values, we obtain $S_1 = 0.9855$ and $\left(S_2 / \left[\frac{\Omega}{3} \frac{E}{(1-\nu)} \frac{IR}{F\mathcal{D}}\right]\right) = -0.0174$.

The plots for dimensionless radial and tangential stress vs. radial distance of a 5 nm cylindrical wire are shown in Figures 3.13 and 3.14. These are for plane strain conditions in the axial direction. Similar plots can be obtained for the other two axial boundary conditions. In both Figures 3.13 and 3.14, by comparing the solid and dashes lines, we observe that, at the nano-scale, there is a significant decrease in both radial and tensile stresses.

For insertion, the maximum tangential stress is always compressive and its magnitude increases as the particle radius decreases. It can be observed that, as the radius decreases, the effect of surface tension becomes more significant.

These results shows that when the influence of surface tension is incorporated, smaller (nano-scale) wires experience a more compressive stress environment, which would decrease the probability of crack formation due to tensile stresses.

Figure 3.18 shows the dimensionless bulk strain energy, surface strain energy, and total strain energy stored in 5 nm cylindrical electrodes due to lithium intercalation under the generalized plane strain condition. We can see that the surface strain energy has a considerable effect on the total strain energy. In addition, the surface strain energy has a comparable magnitude to the bulk strain energy for the 5 nm electrode in all the three cases.

This confirms that for representative surface parameters, the surface effects are considerably strong and can mitigate deleterious efforts of DISs in terms of fracture propagation for nano-scale electrodes. Hence, from a fracture perspective, nano-scale electrodes should provide longer cycle life than large electrodes. These results also depend upon the surface and material properties of the electrode material (*36*).

Using this mathematical model, we can select the best possible material for the electrode in terms of resistance to crack propagation by comparing this total energy calculated with the surface energy for cracking. Thus at nano-scale, not only bulk strain energy but surface strain energy should be considered for predicting the initiation and propagation of fracture.

Figure 3.19 shows that variation of total strain energy in all the axial loading conditions. The difference in the nature of strain energy profiles in all the three cases is due to the different nature of axial stresses.

From Figure 3.19 we can see that, the electrode subjected to the plane stress condition exhibits less stored strain energy and is thus less prone to cracking as compared to the other two cases.

3.7 Conclusions

1. There can be a significant decrease in the diffusion induced stress due to surface effects. Furthermore, we find in some cases that the tensile stress is converted to compressive stress, which will inhibit crack formation and in turn reduce mechanical degradation. The results clearly indicate that below a certain wire diameter, the surface effect plays an important role.

2. The importance of the contribution of surface strain energy to the total strain energy is established. This leads to a conclusion that for nano-structured materials, the fracture energy should be compared to total strain energy that includes both bulk and surface strain energies. Surface strain energy analyses have not been incorporated in previous studies.
3. A mathematical tool is developed for the analysis of stress, strain, and strain energy in cylindrical nano-structured electrodes, which can be employed for materials with known properties. This model can be used to optimize the cylindrical electrode size depending upon the properties to maximize battery life. It may also be used as a tool for battery life prediction.

3.8 List of symbols

r, θ, z	cylindrical coordinates
γ	surface energy per unit area $(J\ m^{-2})$
$\delta_{\alpha\beta}$	Kroneker delta function
$\sigma_{\alpha\beta}^{surf}$	surface stress $(N\ m^{-1})$
$\lambda\ and\ \mu$	Lamé constants for isotropic bulk material $(N\ m^{-2})$
$\lambda^s\ and\ \mu^s$,	surface Lamé constants $(N\ m^{-1})$
$\kappa_{\alpha\beta}$	curvature tensor of the surface $(\ m^{-1})$
τ^0	residual surface tension under unrestrained conditions (Nm)
n_α	normal vector
ε_{ij}	infinitesimal strain tensor
Ω	partial molar volume of the solute $(mol\ m^{-3})$
R	radius of the cylindrical electrode (m)
ν	Poisson's ratio
E	Young's modulus $(N\ m^{-2})$
u	radial displacement (m)

σ_r	radial stress $(N\ m^{-2})$
σ_θ	tangential stress $(N\ m^{-2})$
σ_z	axial stress $(N\ m^{-2})$
ε_{rr}	radial strain
$\varepsilon_{\theta\theta}$	tangential strain
ε_{zz}	axial strain
$C(r,t)$	solute concentration at radius r at time t $(mol\ m^{-3})$
$C_{avg}(r)$	average concentration in the area of radius r $(mol\ \ m^{-3})$
$C_{avg}(R)$	average concentration in the area of radius R $(molm^{-3})$
D	diffusion coefficient of the solute $(m^2 sec^{-1})$
t	time (sec)
x	dimensionless radius
T	dimensionless time
y	dimensionless concentration
$J_0\ and\ J_1$	Bessel's function of first kind of order 0 and 1 respectively
ξ_r	dimensionless radial stress

ξ_θ	dimensionless tangential stress
ξ_z	dimensionless axial stress
E_{Total}	total elastic energy stored in the cylinder of radius R and height h (J)
E_{bulk}	strain energy stored due to bulk deformation (J)
$E_{surface}$	strain energy stored due to surface deformation (J)
$\ell(r)$	strain energy density (Jm^{-3})
$\prod_{bulk}$	dimensionless bulk strain energy
$\prod_{surface}$	Dimensionless surface strain energy

3.9 References

1. C. K. Chan *et al.*, High-performance lithium battery anodes using silicon nanowires. *Nat Nano* **3**, 31 (2008).
2. B. A. Boukamp, G. C. Lesh, R. A. Huggins, All-Solid Lithium Electrodes with Mixed-Conductor Matrix. *Journal of The Electrochemical Society* **128**, 725 (1981).
3. L. B. Chen, N. Lu, C. M. Xu, H. C. Yu, T. H. Wang, Electrochemical performance of polycrystalline CuO nanowires as anode material for Li ion batteries. *Electrochimica Acta* **54**, 4198 (2009).
4. M.-H. Park *et al.*, Silicon Nanotube Battery Anodes. *Nano Letters* **9**, 3844 (2009).
5. C. Herring, *Structure and properties of solid surface*. R. Gomer, C. S. Smith, Eds., (University of Chicago press, Chicago, 1953).
6. S. Cuenot, C. Frétigny, S. Demoustier-Champagne, B. Nysten, Surface tension effect on the mechanical properties of nanomaterials measured by atomic force microscopy. *Physical Review B* **69**, 165410 (2004).
7. M. Doyle, T. F. Fuller, J. Newman, Modeling of Galvanostatic Charge and Discharge of the Lithium/Polymer/Insertion Cell. *Journal of The Electrochemical Society* **140**, 1526 (1993).
8. T. F. Fuller, M. Doyle, J. Newman, Simulation and Optimization of the Dual Lithium Ion Insertion Cell. *Journal of The Electrochemical Society* **141**, 1 (1994).
9. M. Doyle, J. Newman, A. S. Gozdz, C. N. Schmutz, J.-M. Tarascon, Comparison of Modeling Predictions with Experimental Data from Plastic Lithium Ion Cells. *Journal of The Electrochemical Society* **143**, 1890 (1996).

10. R. Darling, J. Newman, Modeling a Porous Intercalation Electrode with Two Characteristic Particle Sizes. *Journal of The Electrochemical Society* **144**, 4201 (1997).

11. D. R. Baker, M. W. Verbrugge, Temperature and Current Distribution in Thin-Film Batteries. *Journal of The Electrochemical Society* **146**, 2413 (1999).

12. V. Srinivasan, J. Newman, Discharge Model for the Lithium Iron-Phosphate Electrode. *Journal of The Electrochemical Society* **151**, A1517 (2004).

13. S. Devan, V. R. Subramanian, R. E. White, Analytical Solution for the Impedance of a Porous Electrode. *Journal of The Electrochemical Society* **151**, A905 (2004).

14. D. Dees, E. Gunen, D. Abraham, A. Jansen, J. Prakash, Electrochemical Modeling of Lithium-Ion Positive Electrodes during Hybrid Pulse Power Characterization Tests. *Journal of The Electrochemical Society* **155**, A603 (2008).

15. S. Prussin, Generation and Distribution of Dislocations by Solute Diffusion. *Journal of Applied Physics* **32**, 1876 (1961).

16. W. L. Wang, S. Lee, J. R. Chen, Effect of chemical stress on diffusion in a hollow cylinder. *Journal of Applied Physics* **91**, 9584 (2002).

17. S. Lee, W. L. Wang, J. R. Chen, Diffusion-induced stresses in a hollow cylinder:: Constant surface stresses. *Materials Chemistry and Physics* **64**, 123 (2000).

18. S.-C. Ko, S. Lee, Y. T. Chou, Chemical stresses in a square sandwich composite. *Materials Science and Engineering: A* **409**, 145 (2005).

19. R. E. Garcia, Y.-M. Chiang, W. C. Carter, P. Limthongkul, C. M. Bishop, Microstructural Modeling and Design of Rechargeable Lithium-Ion Batteries. *Journal of The Electrochemical Society* **152**, A255 (2005).

20. J. Christensen, J. Newman, A Mathematical Model of Stress Generation and Fracture in Lithium Manganese Oxide. *Journal of The Electrochemical Society* **153**, A1019 (2006).

21. J. Christensen, J. Newman, Stress generation and fracture in lithium insertion materials. *Journal of Solid State Electrochemistry* **10**, 293 (2006).

22. X. Zhang, A. M. Sastry, W. Shyy, Intercalation-Induced Stress and Heat Generation within Single Lithium-Ion Battery Cathode Particles. *Journal of The Electrochemical Society* **155**, A542 (2008).

23. X. Zhang, W. Shyy, A. M. Sastry, Numerical Simulation of Intercalation-Induced Stress in Li-Ion Battery Electrode Particles. *Journal of The Electrochemical Society* **154**, A910 (2007).

24. Y.-T. Cheng, M. W. Verbrugge, The influence of surface mechanics on diffusion induced stresses within spherical nanoparticles. *Journal of Applied Physics* **104**, 083521 (2008).

25. Y.-T. Cheng, M. W. Verbrugge, Evolution of stress within a spherical insertion electrode particle under potentiostatic and galvanostatic operation. *Journal of Power Sources* **190**, 453 (2009).

26. P. Sharma, S. Ganti, N. Bhate, Erratum: ``Effect of surfaces on the size-dependent elastic state of nano-inhomogeneities" [Appl. Phys. Lett. [bold 82], 535 (2003)]. *Applied Physics Letters* **89**, 049901 (2006).

27. H. S. Carslaw, J. C. Jaeger, *Conduction of heat in solids*. J. C. Jaeger, Ed., (Clarendon Press, Oxford, ed. second, 1959).

28. S. Timoshenko, J. N. Goodier, *Theory of elasticity, by S. Timoshenko and J.N. Goodier*. (New York, McGraw-Hill, 1951).

29. C. K. Chan, X. F. Zhang, Y. Cui, High Capacity Li Ion Battery Anodes Using Ge Nanowires. *Nano Letters* **8**, 307 (2007).

30. L.-F. Cui, R. Ruffo, C. K. Chan, H. Peng, Y. Cui, Crystalline-Amorphous Core−Shell Silicon Nanowires for High Capacity and High Current Battery Electrodes. *Nano Letters* **9**, 491 (2008).

31. H. Kim, J. Cho, Superior Lithium Electroactive Mesoporous Si@Carbon Core−Shell Nanowires for Lithium Battery Anode Material. *Nano Letters* **8**, 3688 (2008).

32. L.-F. Cui, Y. Yang, C.-M. Hsu, Y. Cui, Carbon−Silicon Core−Shell Nanowires as High Capacity Electrode for Lithium Ion Batteries. *Nano Letters* **9**, 3370 (2009).

33. Y. Li, X. Lv, J. Li, High performance binderless TiO[sub 2] nanowire arrays electrode for lithium-ion battery. *Applied Physics Letters* **95**, 113102 (2009).

34. E. Hosono, T. Kudo, I. Honma, H. Matsuda, H. Zhou, Synthesis of Single Crystalline Spinel LiMn2O4 Nanowires for a Lithium Ion Battery with High Power Density. *Nano Letters* **9**, 1045 (2009).

35. E. Hosono *et al.*, Synthesis of single crystalline electro-conductive Na0.44MnO2 nanowires with high aspect ratio for the fast charge-discharge Li ion battery. *Journal of Power Sources* **182**, 349 (2008).

36. R. E. Miller, V. B. Shenoy, Size-dependent elastic properties of nanosized structural elements. *Nanotechnology* **11**, 139 (2000).

37. D. Aurbach, Review of selected electrode-solution interactions which determine the performance of Li and Li ion batteries. *Journal of Power Sources* **89**, 206 (2000).

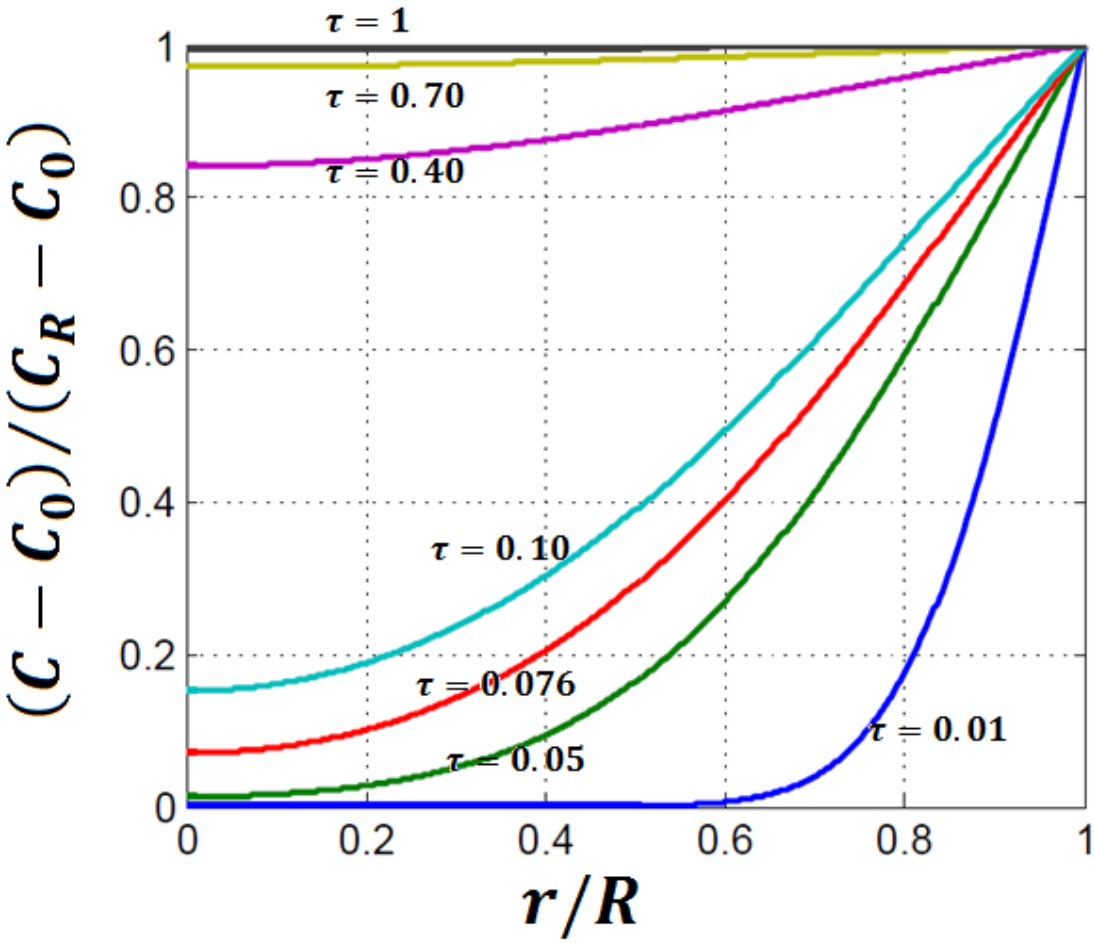

Figure 3.1: Lithium ion concentration (Eq. 3.20) inside an electrode at different radial locations and times for the potentiostatic insertion condition.

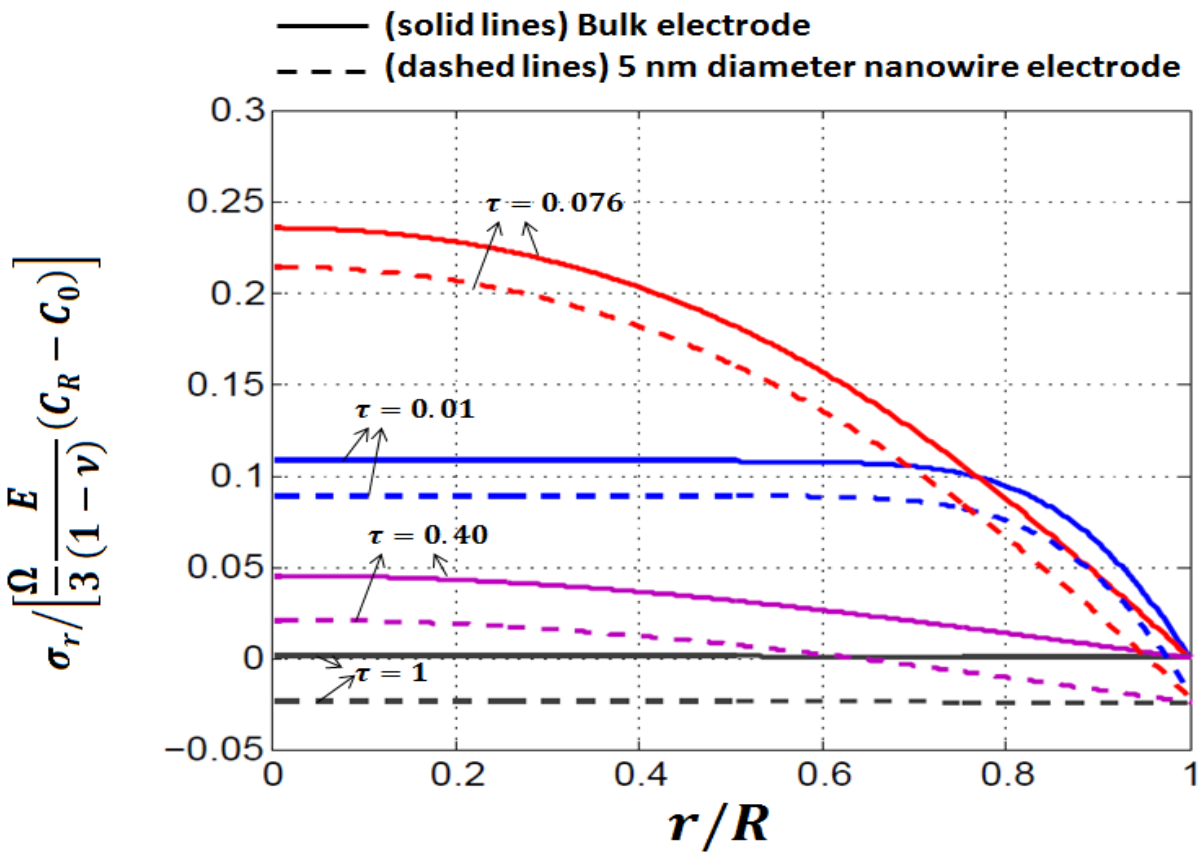

Figure 3.2: Radial stress (Eq. 3.23) inside an electrode at different radial locations at different time. This is for generalized plane strain condition. Solid lines represents stresses in large electrode i.e.no surface effects are considered (S_1 = 1, S_2 = 0). Dashed lines represent stresses in 5 nm diameter nanowire electrodes i.e. surface effect is significant ($S_1 = 0.9855$ and $\left(S_2 / \left[\frac{\Omega}{3}\frac{E}{(1-\nu)} C_R\right]\right) = -0.0174$). This is for the potentiostatic charging of the battery.

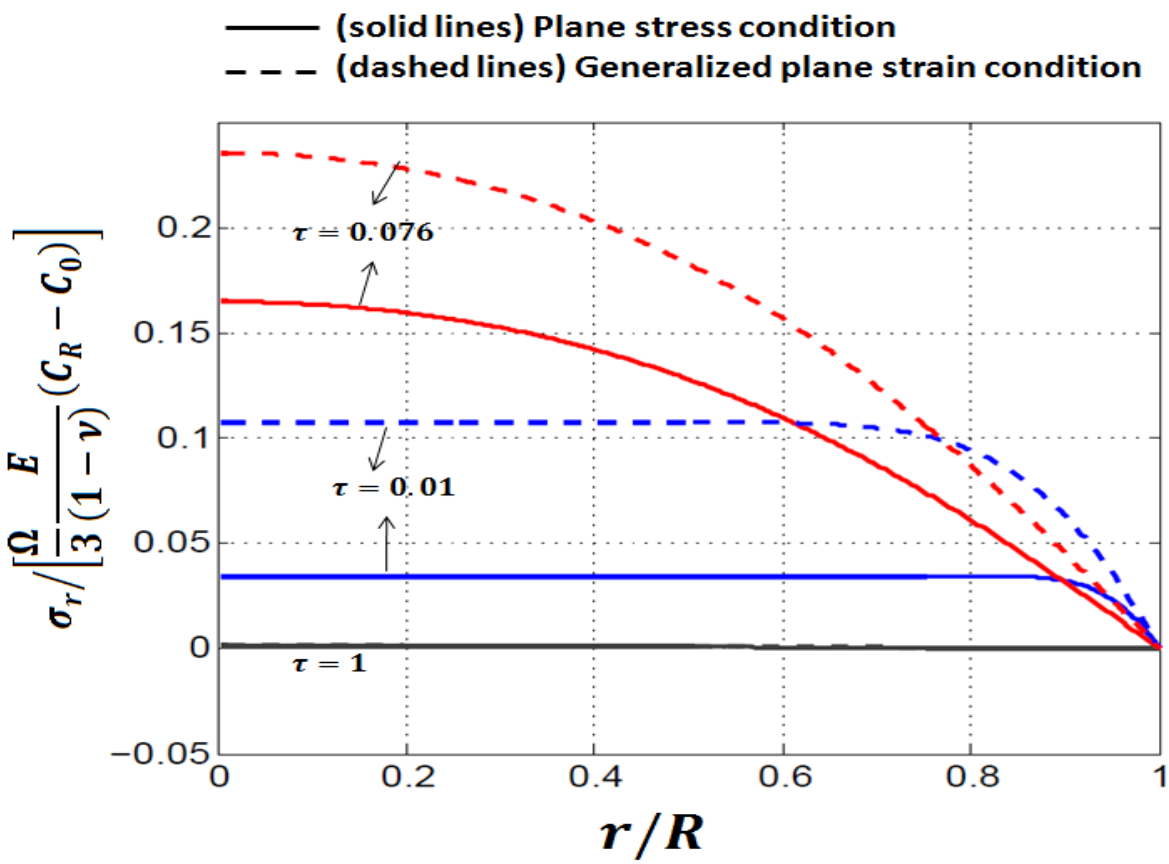

Figure 3.3: Radial stress inside an electrode at different radial locations and times. This is for the potentiostatic charging of the battery. Solid lines represent plane stress condition. Dashed lines represent generalized plane strain condition. No surface effects are considered.

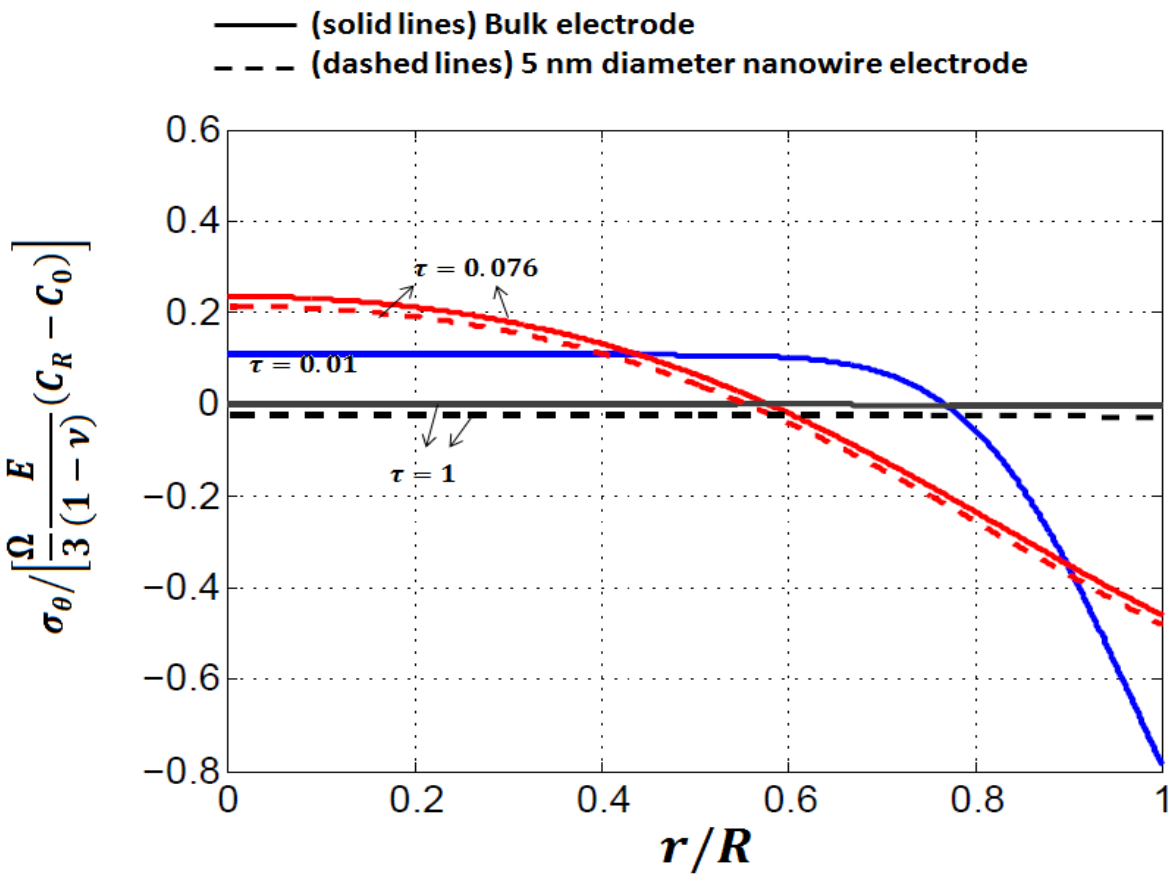

Figure 3.4: Tangential stress (Eq. 3.24) inside an electrode at radial locations and times. This is for generalized plane strain condition. This is for the potentiostatic charging of the battery. Solid lines represents stresses in large electrode i.e. no surface effects are considered (S_1 = 1, S_2 = 0). Dashed lines represent stresses in 5 nm diameter nanowire electrodes i.e. surface effect is significant ($S_1 = 0.9855$ and $\left(S_2 / \left[\frac{\Omega}{3}\frac{E}{(1-\nu)} C_R\right]\right) = -0.0174$).

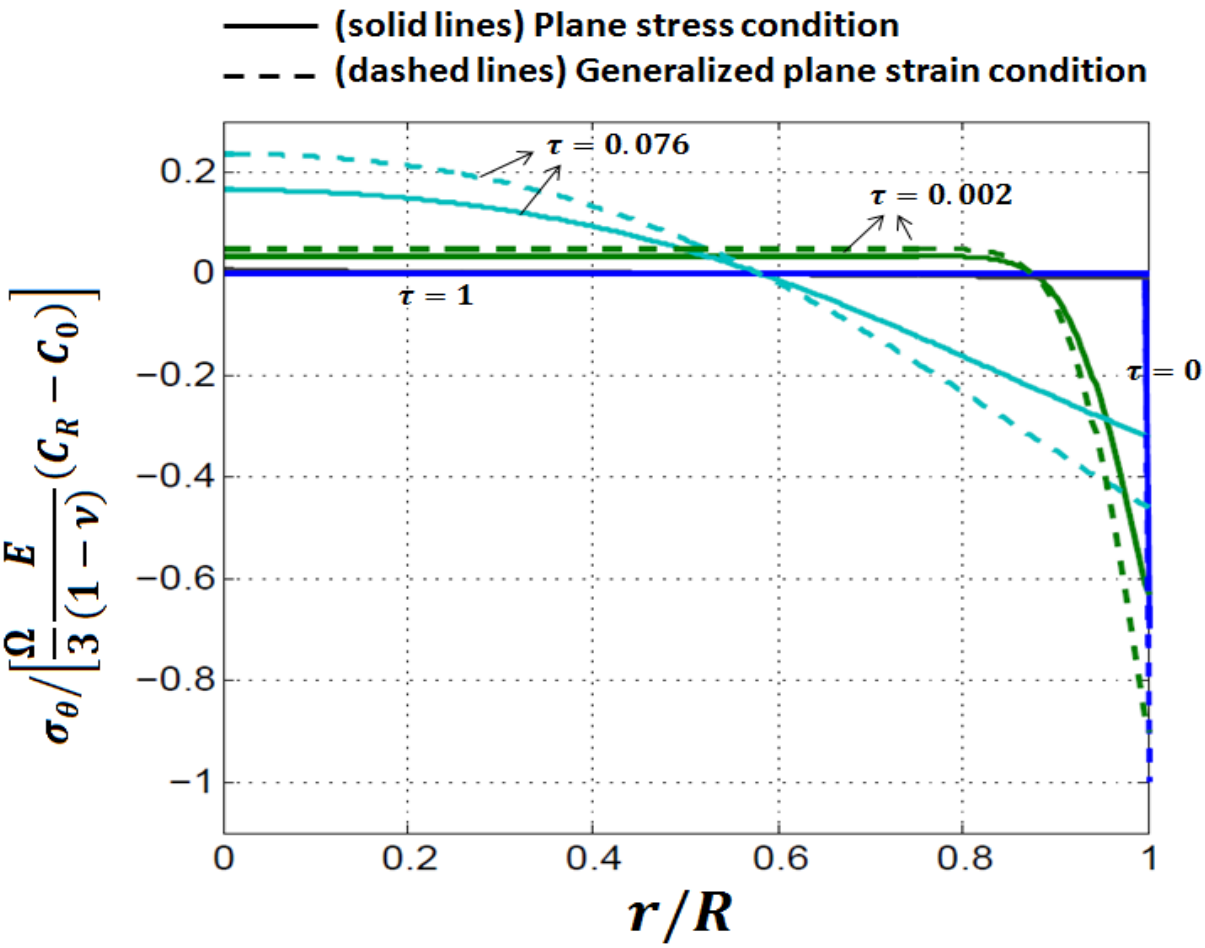

Figure 3.5: Tangential stress (Eq. 3.24) inside an electrode at different radial locations and times. This is for the potentiostatic charging of the battery. Solid lines represent plane stress condition. Dashed lines represent generalized plane strain condition. No surface effects are considered.

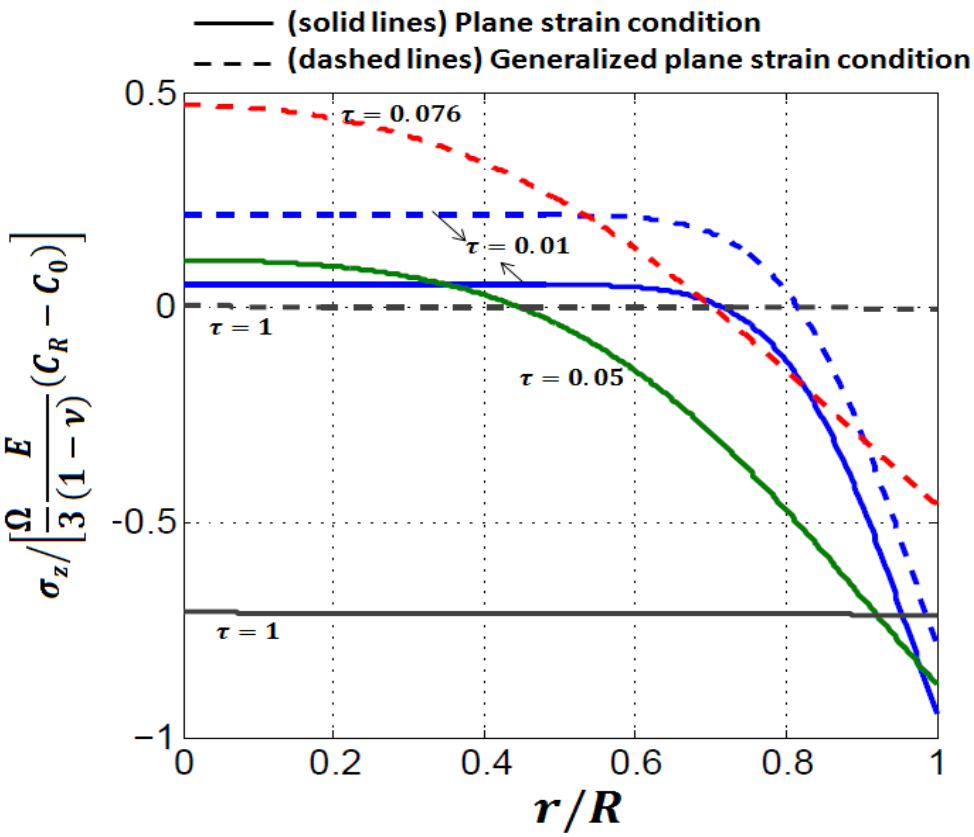

Figure 3.6: Axial stress (Eq. 3.25) inside an electrode at radial locations and times. This is for the potentiostatic charging of the battery. Solid lines represent plane strain condition. Dashed lines represent generalized plane strain condition. No surface effects are considered.

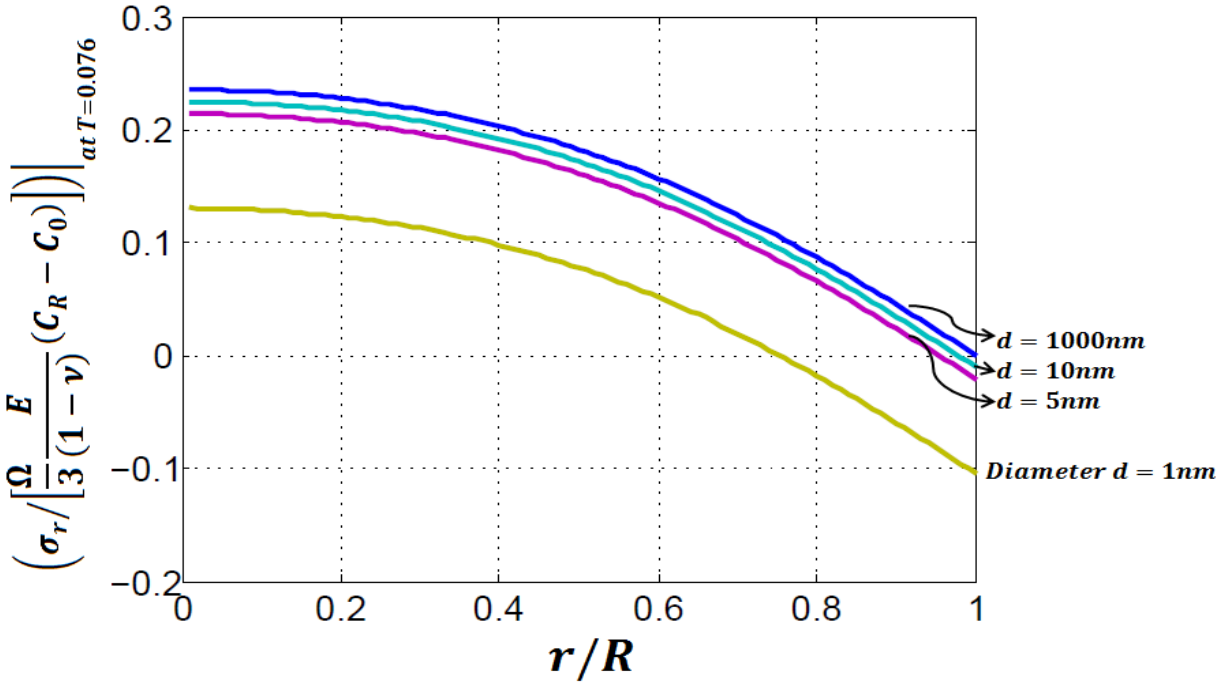

Figure 3.7: Radial stress at a dimensionless time T = 0.076 for electrodes with different diameters. The results are for plane strain and generalized plane strain conditions. This is for the potentiostatic charging of the battery.

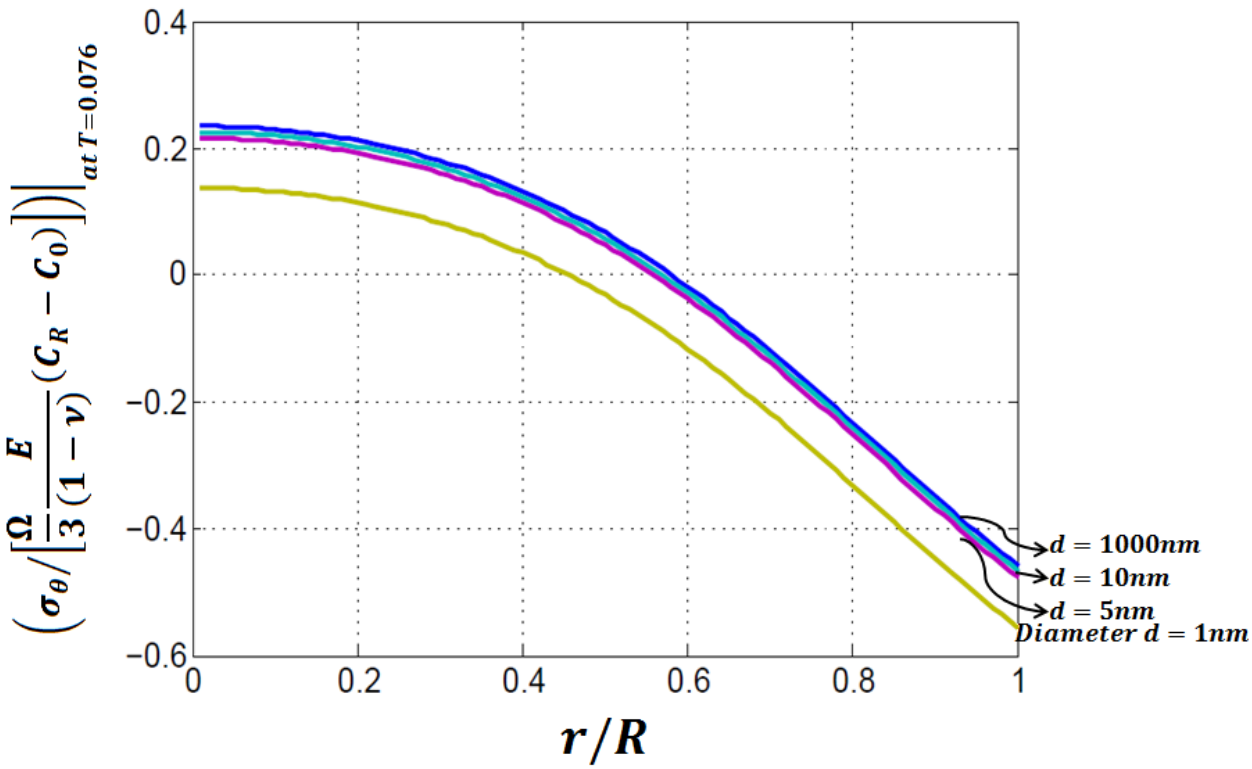

Figure 3.8: Tangential stress at dimensionless time T = 0.076 for electrodes with different diameters. The results are for plane strain and generalized plane strain conditions. This is for the potentiostatic charging of the battery.

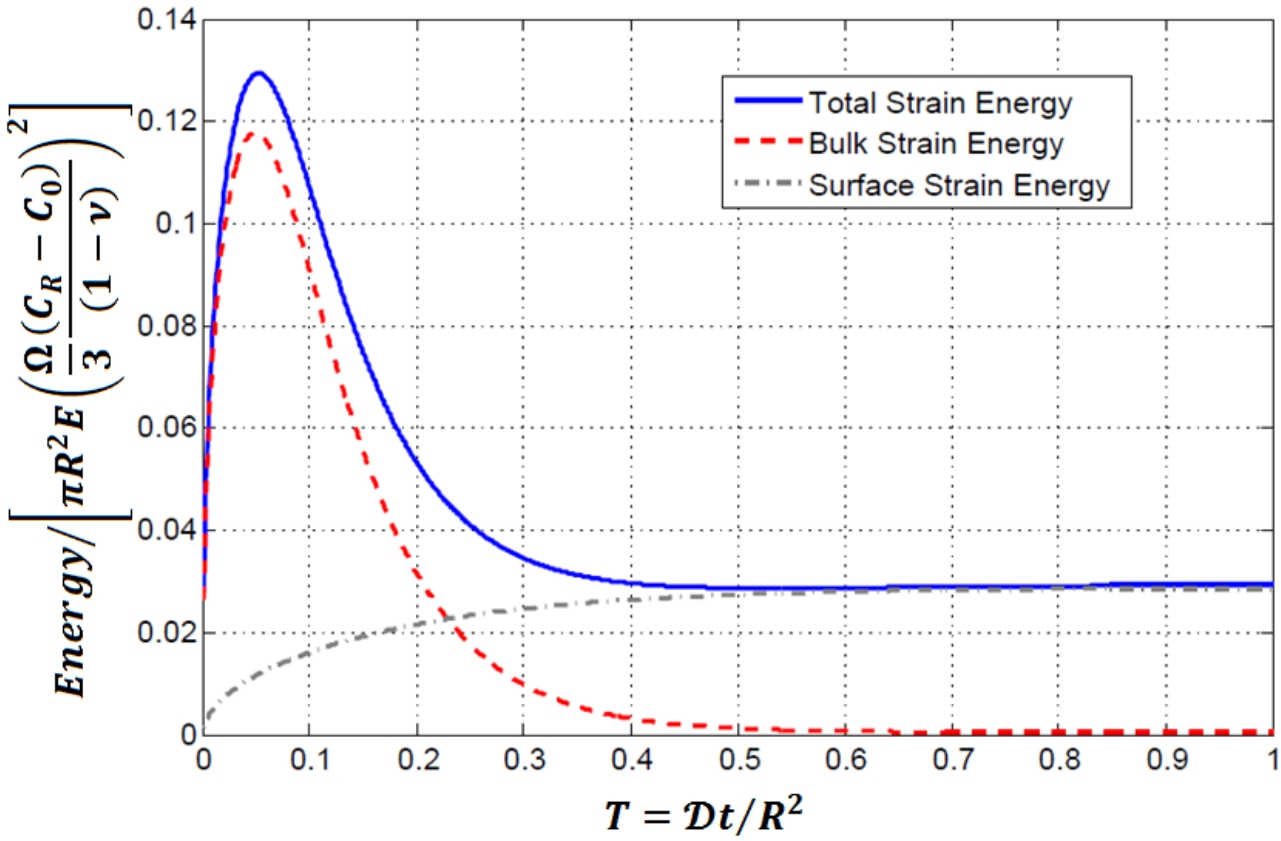

Figure 3.9: Bulk strain energy, surface strain energy, total strain energy with time for a 5-nm electrode subject to the generalized plane strain condition. This is for the potentiostatic charging of the battery.

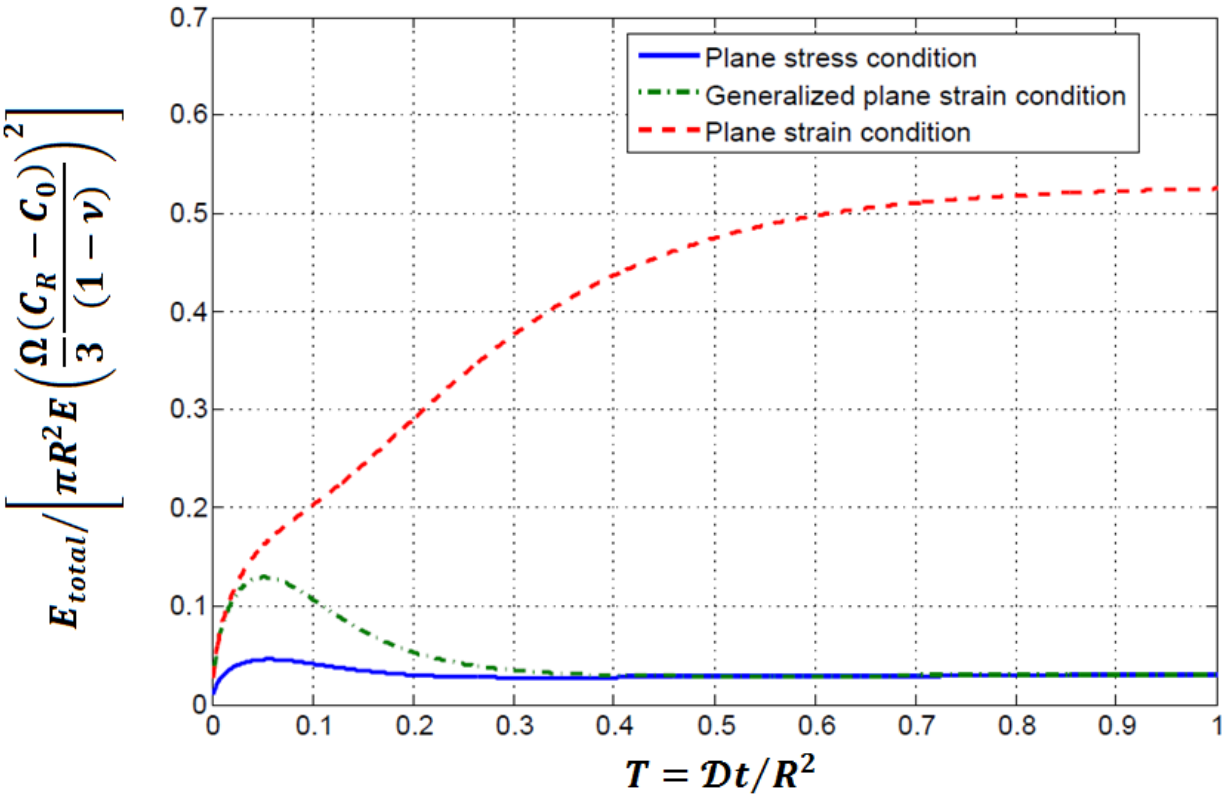

Figure 3.10: Total strain energy variation with time for a 5-nm electrode. All the three loading conditions are taken investigated, and it is clear that the total strain energy stored varies with the axial loading condition. This is for the potentiostatic charging of the battery

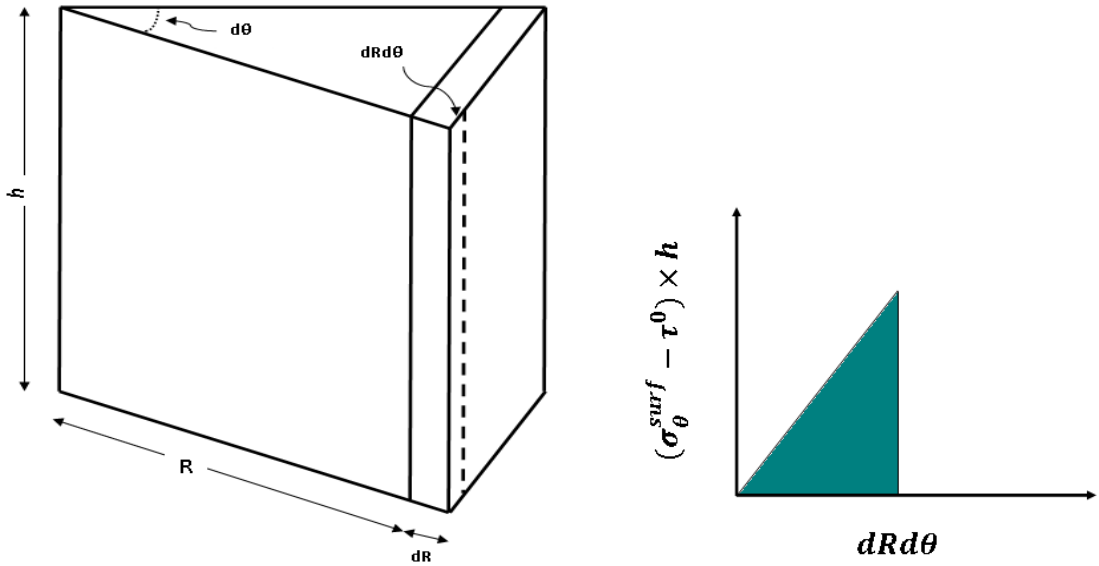

Figure 3.11: A schematic illustration of contributions to strain-energy.

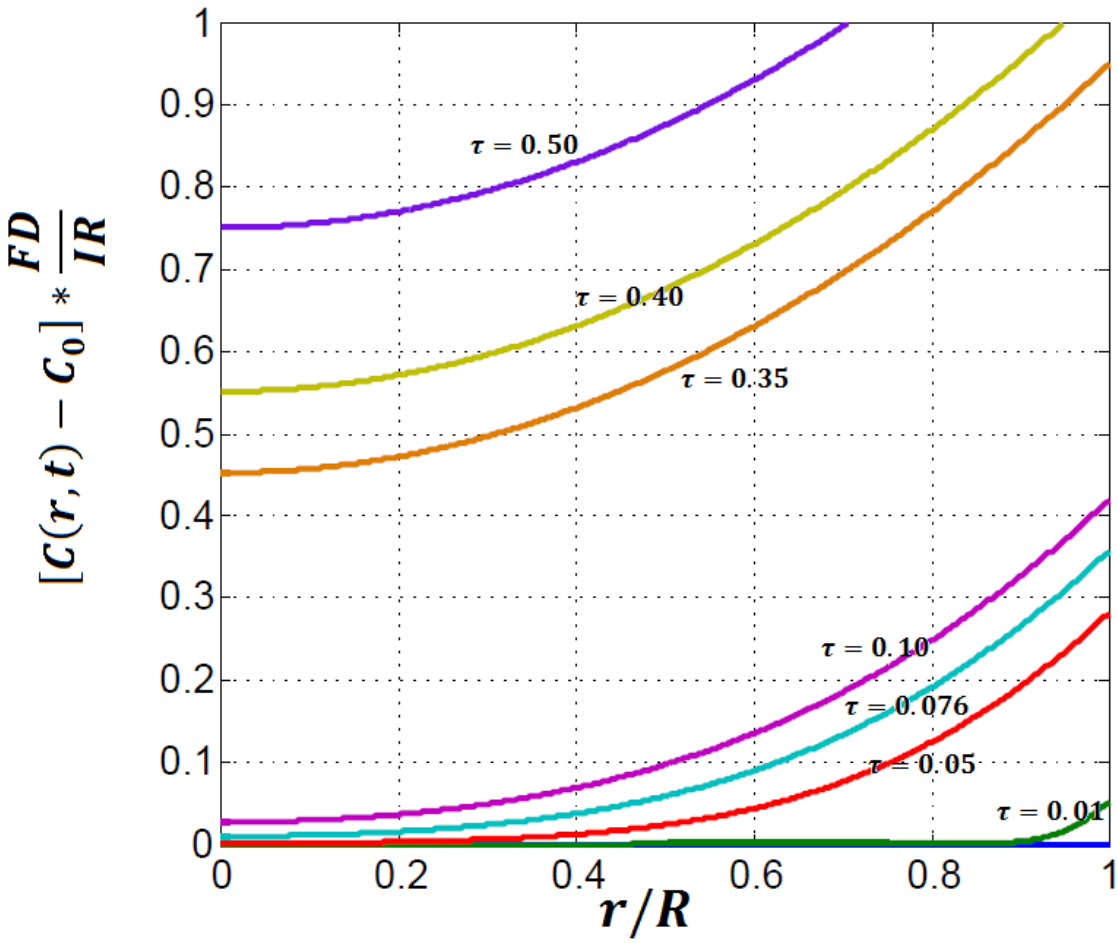

Figure 3.12: Lithium ion concentration (Eq. 3.41) inside an electrode at different radial locations and times for the galvanostatic insertion condition.

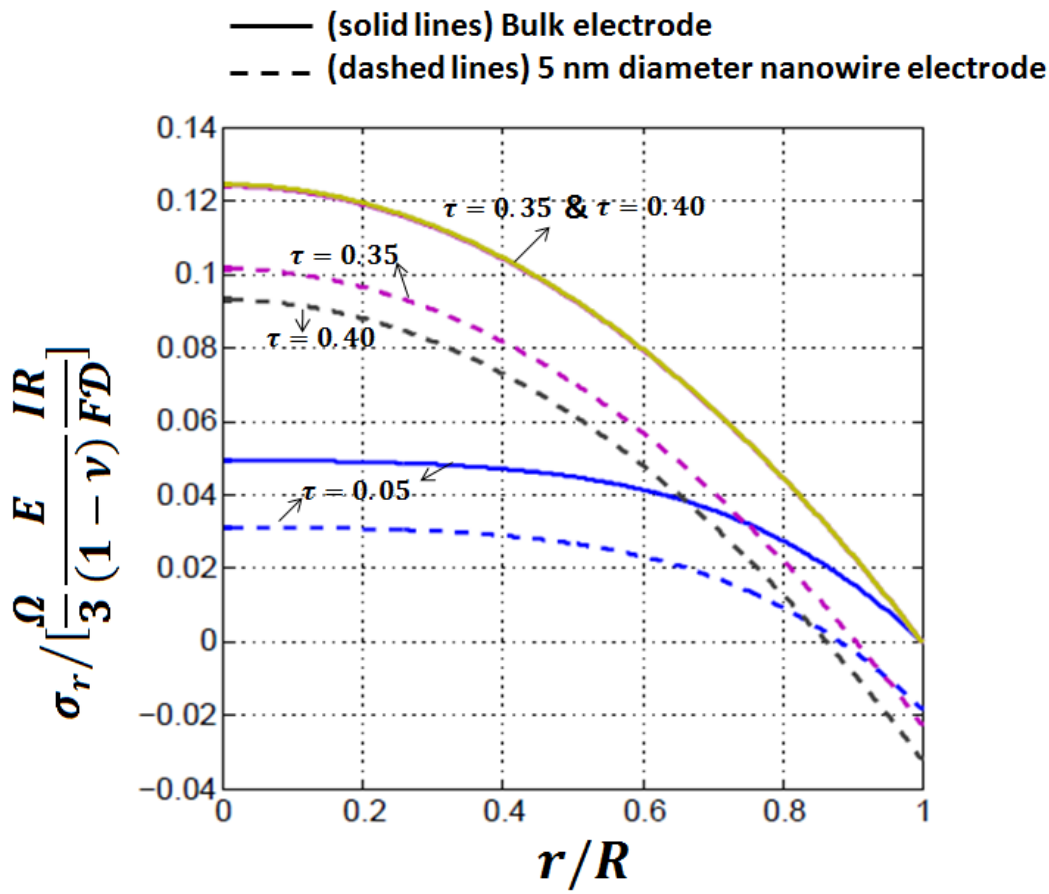

Figure 3.13: Radial stress (Eq. 3.44) inside an electrode at different radial locations at different time. This is for the galvanostatic charging of the battery. This is for plane strain and generalized plane strain condition. Solid lines represents stresses in large electrode i.e. no surface effects are considered (S1 = 1, S2 = 0). Dashed lines represent stresses in 5 nm diameter nanowire electrodes i.e. surface effect is significant ($S_1 = 0.9855$ and $\left(S_2 / \left[\frac{\Omega}{3}\frac{E}{(1-\nu)}\frac{IR}{FD}\right]\right) = -0.0174$).

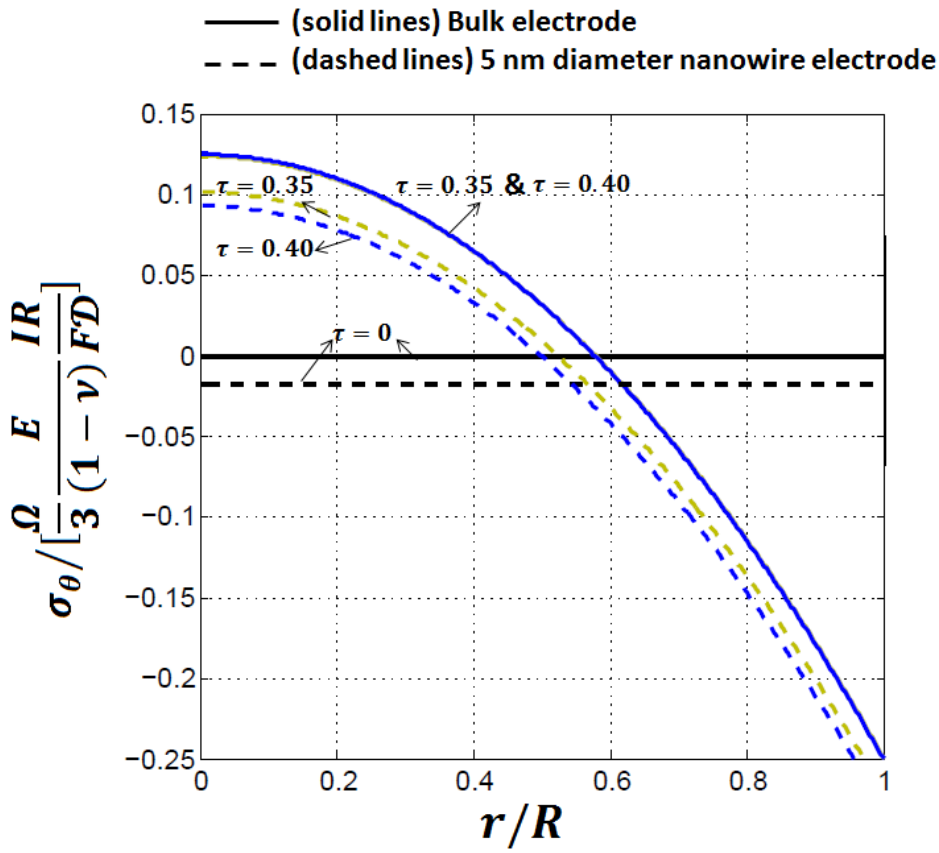

Figure 3.14: Tangential stress (Eq. 3.45) inside an electrode at radial locations and times. This is for the galvanostatic charging of the battery. Solid lines represents stresses in large electrode i.e. no surface effects are considered (S_1 = 1, S_2 = 0). Dashed lines represent stresses in 5 nm diameter nanowire electrodes i.e. surface effect is significant ($S_1 = 0.9855$ and $\left(S_2/\left[\frac{\Omega}{3}\frac{E}{(1-\nu)}\frac{IR}{F\mathcal{D}}\right]\right) = -0.0174$).

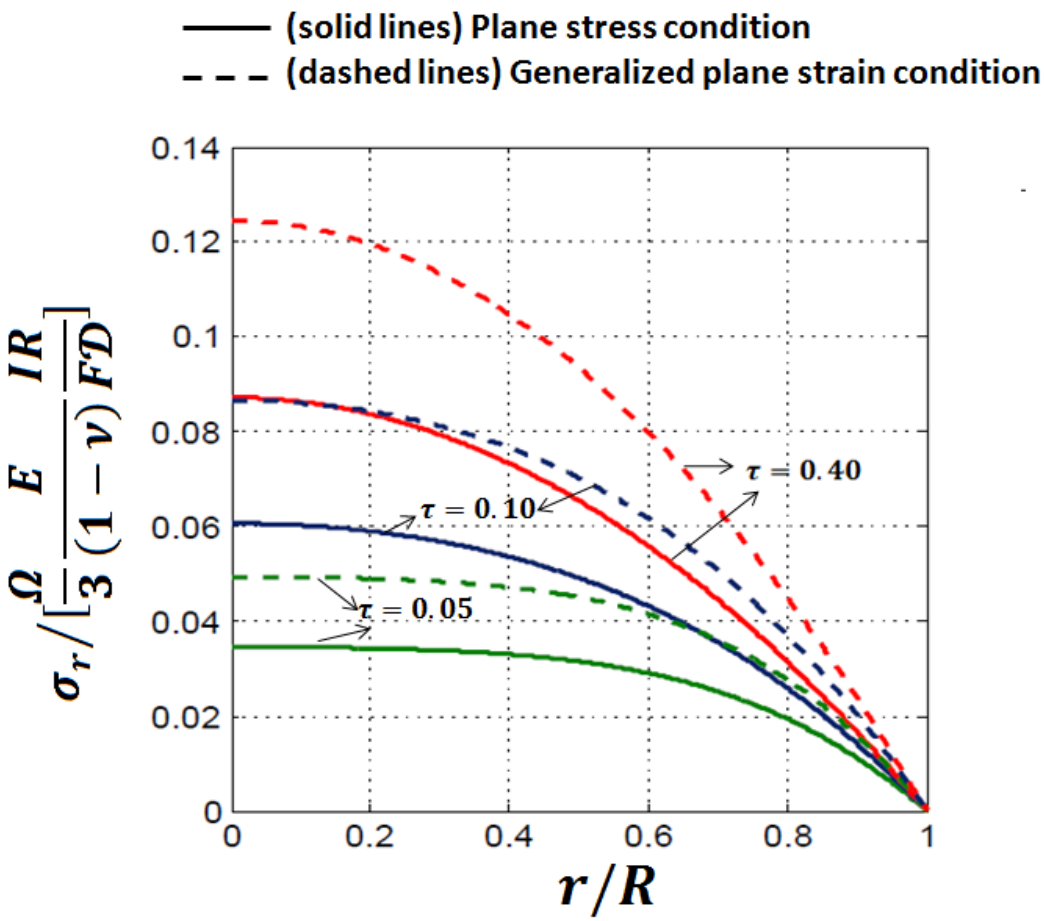

Figure 3.15: Radial stress (Eq. 3.44) inside an electrode at different radial locations and times. This is for the galvanostatic charging of the battery. Solid lines represent plane stress condition. Dashed lines represent generalized plane strain condition. No surface effects are considered.

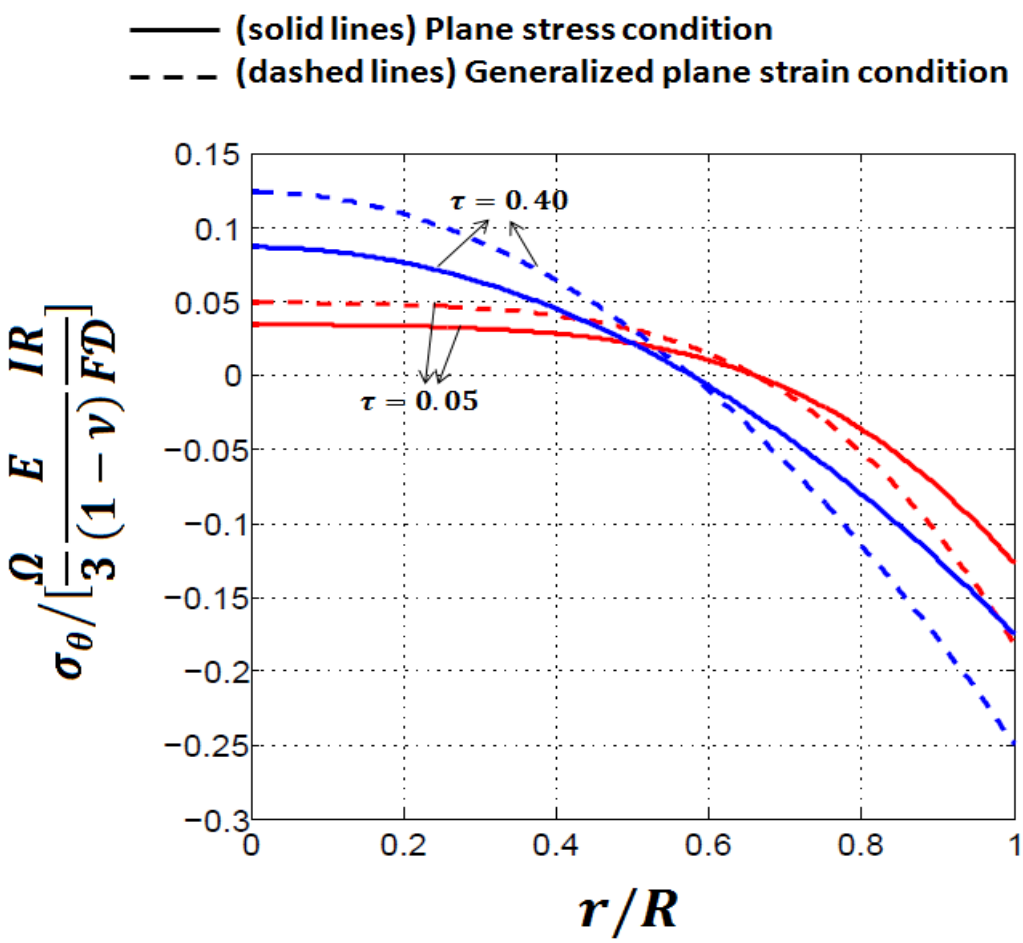

Figure 3.16: Tangential stress (Eq. 3.45) inside an electrode at different radial locations and times. This is for the galvanostatic charging of the battery. Solid lines represent plane stress condition. Dashed lines represent generalized plane strain condition. No surface effects are considered.

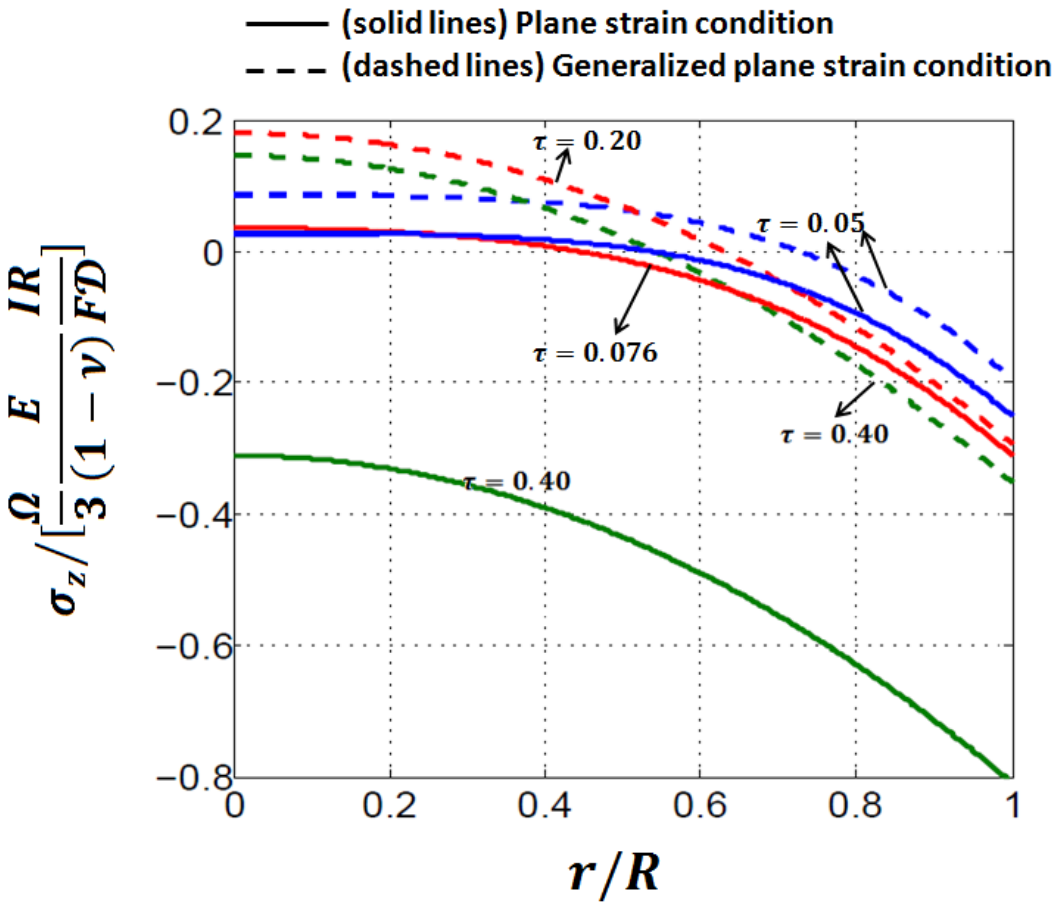

Figure 3.17: Axial stress (Eq. 3.46) inside an electrode at radial locations and times. This is for the galvanostatic charging of the battery. Solid lines represent the plane strain condition. Dashed lines represent the generalized plane strain condition. No surface effects are considered.

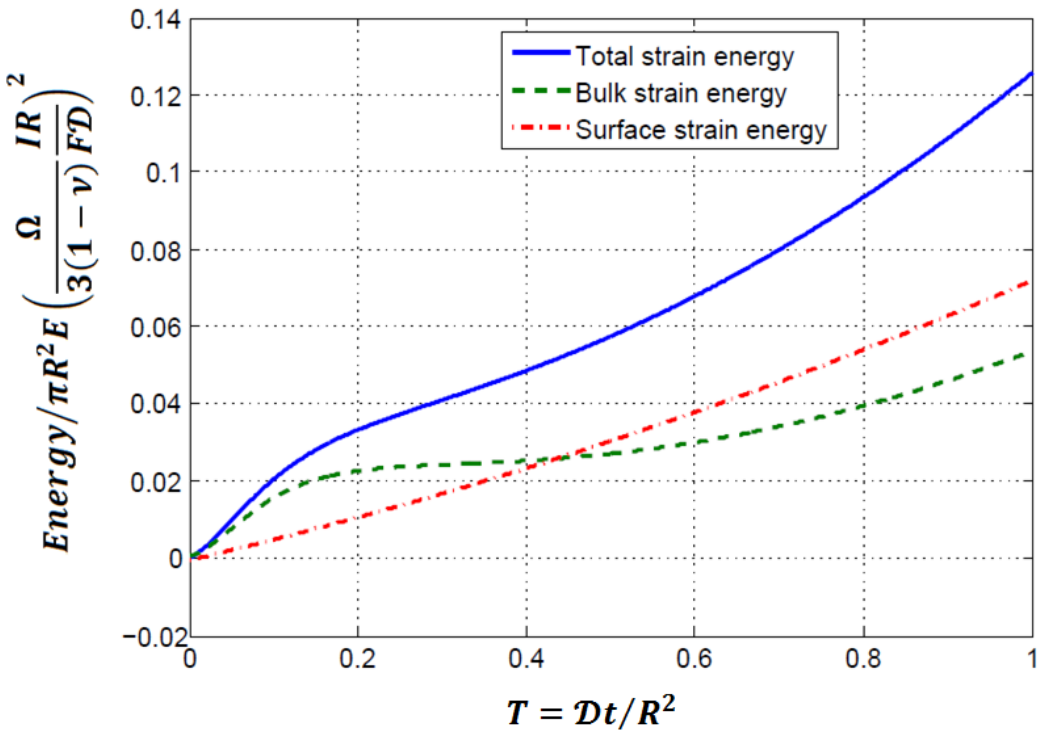

Figure 3.18: Bulk strain energy, surface strain energy, total strain energy with time for a 5-nm electrode subject to the generalized plane strain condition. This is for the galvanostatic charging of the battery.

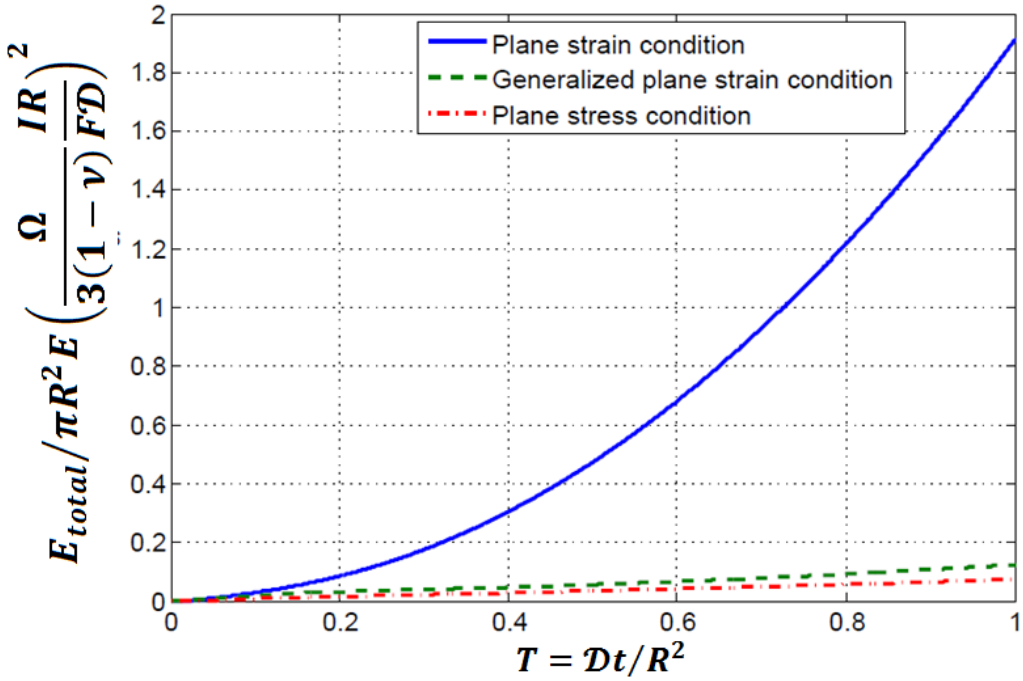

Figure 3.19: Total strain energy variation with time for a 5-nm electrode. All the three loading conditions are taken investigated, and it is clear that the total strain energy stored varies with the axial loading condition. This is for the galvanostatic charging of the battery.

CHAPTER 4

DESIGNING NANOTUBES AS DURABLE LITHIUM-ION BATTERY NEGATIVE ELECTRODES WITH TIO2 NANOTUBES AS AN EXAMPLE

4.1 Summary

The capacity of lithium ion battery fades upon electrochemical cycling due to coupled chemical and mechanical degradation. Diffusion induced stresses (DISs) upon charging and discharging are considered to be one of the major causes of mechanical degradation of electrodes. Different electrode particle geometries have shown different degradation behavior. Here, we present a mathematical model for understanding DISs in cylindrical tubular electrode elements. We understand the effect of the dimensions of tubes such as inner diameter, outer diameter and length of tube on fracture tendencies. Depending upon the dimensions of the tubular electrode element, it might undergo splitting along the length or it may open up as a result of mechanical stresses. Splitting of the tube would be more detrimental for battery applications since it results in the loss of electrical contact of the electrode material from a current collector. We develop a simple mathematical relation between the different tube dimensions for improved designing of the tubular electrode with which tube splitting can be minimized. We also develop a way to calculate critical current density for a given dimension of the tubular electrode beyond which the tube has high tendency of cracking.

Under the guidelines of the model, titania (TiO_2) nanotube electrodes were prepared and the cycling performance was evaluated. In accordance with the prediction, the tubes were found to be mechanically stable upon electrochemical cycling.

4.2 Introduction

With widespread applications in portable electronics such as cellphones, laptops and other electronic gadgets and the potential application for the automobile propulsion, lithium ion batteries (LIBs) have gained the attention of researchers worldwide. There is an immense effort by the research community for improvement in the durability and capacity of lithium ion batteries. The capacities of lithium ion batteries fade upon electrochemical cycling due to different degradation mechanisms. The mechanical degradation of electrodes prevents commercial use of high capacity material such as silicon and tin (*1, 2*). The diffusion induced stresses (DISs) resulting from lithium intercalation may lead to mechanical degradation of the battery electrode. Different electrode geometries such as spherical, cylindrical, tubular, thin films *etc.*, upon electrochemical cycling, show variation in degradation behavior. There is an immense interest in porous electrodes since they offer the following advantages: First, the porous structure offers a short Li diffusion length in the solid phase and high accessibility for the transport of electrolyte ions into the material framework, thus potentially decreasing the polarization and possibly increasing the rate of charging and discharging. Second, the large surface area provided by this porous structure increases the electrode/electrolyte contact area and decreases the local current density. Third, the tubular structure can effectively accommodate the expansion/contraction occurring during the lithium ion insertion / removal process (*3*).

In fact, a large number of studies have demonstrated the good mechanical stability of an array of nanotubes, when used as the anode for lithium ion batteries (*4*, *5*). However, the effects of wall thickness, tube length or the ratio of inner to the outer diameter of the tubes on the durability of tubular electrodes has not been directly elucidated in the above reports.

In this chapter, we develop a mathematical model to understand the DISs behavior and the fracture tendency of tubular electrodes. We understand the dependence of fracture tendency of the tubular electrode on the dimensions of the tube. In accordance with the model, we fabricate aligned TiO_2 nanotubes with controlled pore size and wall thickness by anodizing pure Ti foils in a neutral fluoride solution comprising $(NH_4)_2SO_4$ and NH_4F as the electrolyte. The use of neutral fluoride solutions allows the fabrication of TiO_2 nanotubes with a thin wall by reducing the dissolution rate of oxide layers (*6*, *7*). Electrochemical performance of the TiO_2 nanotube arrays as LIB electrodes is examined by means of galvanostatic cycling and excellent capacity retention is observed for TiO_2 tubes of the designed dimensions.

4.3 Experimental section

Qingliu Wu (Chemical and Material Engineering Department, University of Kentucky) used the anodization technique to prepare TiO_2 nanotube electrodes from pure Ti foils (99.6%, Strem Chemicals) with a thickness of 0.025 mm (*8*). The electrochemical characterization part is done by co-author Juchuan Li (Chemical and Material Engineering Department, University of Kentucky).

The electrochemical performance of TiO_2 nanotube arrays was tested in CR2025 coin cells using the anodized TiO_2 foils as the working electrodes (WE), and pure Li metal foils as the counter electrodes (CE). The cells were fabricated in an Ar-filled glove box (MBraun) where the oxygen and moisture levels were below 0.1 ppm. The electrolyte was 1 M $LiPF_6$ salt dissolved in an equal-volume mixture of ethylene carbonate and dimethyl carbonate (Novolyte). Coin cells were galvanostatically cycled between 1.0 and 2.7 V at a rate of C/3 controlled by a multi-channel potentiostat (VMP3, Bio-Logic) Qingliu employed X-ray diffraction (XRD) analysis using Cu K_α (λ=1.5406Å) radiation to determine the TiO2 film crystal structure. Measurements were conducted directly on the thin films in Bragg-Brentano geometry using a Bruker D8 Advance diffractometer. Scanning Electron Microscope (SEM) (Hitachi S-4300 microscope at 3 kV) characterization is done by co-author Juchuan Li for observation of tubes before and after cycling.

4.4 Analysis of the fracture tendency for tubular electrode

The mechanical degradation such as cracking and fracture of the electrodes is one of the main obstacles preventing the commercial application of advanced LIB electrodes. Lithium diffusion into electrode materials results in diffusion-induced stresses (DISs), which cause mechanical degradation of the electrode materials, and leads to the loss of electric conduction. Recent publications utilized the analogy between thermal stresses and DISs to calculate the stress field evolution during electrochemical cycling (*9*). We use a similar approach to calculate DISs in LIB electrode elements with tubular geometry. The analysis is used to design TiO_2 nanotubes with high mechanical stability for LIB electrode applications.

For cylindrically symmetric tubes with inner radius of a and outer radius of R, the concentration of Li atoms at a particular position and time can be defined with the diffusion equation in a cylindrical coordinate system by

$$\frac{\partial C}{\partial t} = \mathcal{D}\left(\frac{\partial^2 C}{\partial r^2} + \frac{1}{r}\frac{\partial C}{\partial r}\right) \tag{4.1}$$

where C is the molar concentration of Li, and D is the Li diffusion coefficient inside the electrode material. We assume that a constant flux diffusion occurs at the inner surface of the tubes, which represents a constant current cycling in this work and the case of small modified Biot number under constant potential conditions (*10*), and there is no flux going out from the outer surface. Hence, the boundary conditions of diffusion are

$$C(r,0) = C_0\,, \qquad for\ a \le r \le R \tag{4.1a}$$

$$D\left.\frac{dC(r,t)}{dr}\right|_{r=a} = \frac{I}{F}, \quad for\ t \ge 0 \tag{4.1b}$$

$$D\left.\frac{dC(r,t)}{dr}\right|_{r=R} = 0, \quad for\ t \ge 0 \tag{4.1c}$$

where F is Faraday's constant. Equation (4.1) can be transferred to dimensionless form with the definitions $x = \frac{r}{R}$, $\tau = \frac{\mathcal{D}t}{R^2}$, and $y = [C(r,t) - C_0]\frac{F\mathcal{D}}{IR}$.

We assume that the electrode material is an isotropic, linearly elastic solid. Using the analogy between thermal stresses (*11, 12*) and DISs (*13, 14*), the stress-stain relationships for the radial, tangential and axial components are

$$\varepsilon_i - \alpha C = \frac{1}{E}\left(\sigma_i - \nu(\sigma_j + \sigma_k)\right) \tag{4.2}$$

Here ε_i and σ_i represent strain and stress in 'i' direction, respectively. i, j and k represent the principal directions in a cylindrical coordinate system. α is the partial molar volume of lithium atoms. Since the mechanical equilibrium is established much faster than the atomic diffusion process in solid, we treat this as a static equilibrium problem. In the absence of any body force, the equation for the static mechanical equilibrium in the bulk of a tube is given by (*12*):

$$\frac{d\sigma_r}{dr} + \frac{\sigma_r - \sigma_\theta}{r} = 0 \tag{4.3}$$

Let u denote the radial displacement. For small displacement u, strains are given as: $\varepsilon_{rr} = \frac{du}{dr}$, and $\varepsilon_{\theta\theta} = \frac{u}{r}$.

For a tubular electrode with inner radius a and outer radius R, the radial stress on the free surface is zero, *i.e.*, $\sigma_r(a) = 0$ and $\sigma_r(R) = 0$. The radial and tangential stresses can be calculated as:

$$\sigma_r = \frac{\Omega E}{3(1-\nu)}\left[-\frac{1}{r^2}\int_a^r C(r)rdr + \frac{1}{R^2-a^2}\left(1-\frac{a^2}{r^2}\right)\int_a^R C(r)rdr\right] \tag{4.4}$$

$$\sigma_\theta = \frac{\Omega E}{3(1-\nu)}\left[\frac{1}{r^2}\int_a^r C(r)rdr + \frac{1}{R^2-a^2}\left(1+\frac{a^2}{r^2}\right)\int_a^R C(r)rdr + C(r)\right] \tag{4.5}$$

In practice, tubular electrodes are long tubes grown on a substrate and thus one of the ends of the tube is always attached to the substrate. The other end is free to expand. Changes in stress condition at the fixed end have effect on the stress distribution near that end. But according to Saint-Venant's principle (*15*), the effects on stress due by the fixed end are expected to diminish with distance from the fixed end. Since the other end is free

to expand, we can assume that the long tube with a fixed end is under the generalized plane strain condition.

In generalized plain strain condition, the ends of the tube are free of external force *i.e.*, $F_z = \int_0^R 2\pi r \sigma_z dr = 0$. Under this condition, the axial stress is given as (*16*):

$$\sigma_z = \sigma_r + \sigma_\theta \tag{4.6}$$

where $C_{avg}(r) = \frac{2}{r^2 - a^2} \int_a^r C(r')r'dr'$ is the average concentration within radius r per unit length of the tubular electrode.

Based on the concentration profiles, we compute all the principal stresses at different radial positions as a function of time. It is found that the radial stresses are tensile only during lithiation, while the tangential and axial stresses are tensile at the outer surface of the tube during lithiation, and are tensile at the inner surface of the tube during delithiation. The maximum tensile axial and tangential stresses are several times larger than the maximum radial stress (Figure 4.1, a and f); hence the tubes are more prone to cracking as a result of the axial and tangential stress, rather than the radial stress. The maximum axial stress is about four times larger during delithiation than it is during lithiation (Figure 4.1, b and f), which indicates that the tubular electrode would be more prone to cracking during delithiation than during lithiation.

During crack propagation, the strain energy stored in materials is transferred to the surface energy associated with generated cracks. Following Cheng and Verbrugge (*12*), the bulk strain energy density, $e(r)$, accumulated as a result of elastic deformation of the isotropically deformed tube, can be calculated as:

$$e(r) = \frac{1}{2E}\left(\sigma_r^2 + \sigma_\theta^2 + \sigma_z^2\right) - \frac{\nu}{E}\left(\sigma_r\sigma_\theta + \sigma_\theta\sigma_z + \sigma_z\sigma_r\right) \tag{4.7}$$

where σ_i represents the principal stress in "i" direction in the cylindrical coordinate system. E and ν are the Young's modulus and Poisson's ratio of the electrode material, respectively. The total bulk strain energy can be obtained by integrating the strain energy density over the entire electrode material volume.

$$E_{bulk} = \int_a^R e(r) \cdot h \cdot r dr \tag{4.8}$$

The bulk strain energy of the tube in dimensionless form ($\prod_{strain}$) is:

$$\prod_{strain} = \frac{E_{bulk}}{E\pi R^2 h(\frac{\Omega \quad IR}{3(1-\nu)F\mathcal{D}})^2} = \int_{(a/R)}^{1}[\left(\xi_r^2 + \xi_\theta^2 + \xi_z^2\right) - 2\nu(\xi_r\xi_\theta + \xi_\theta\xi_z + \xi_z\xi_r)\,]xdx$$

(4.9)

where E_{bulk} is the strain energy, Ω is the partial volume of lithium, and $\xi_i = \frac{\sigma_i}{[\frac{\Omega \quad E \quad IR}{3\,(1-\nu)F\mathcal{D}}]}$ is the dimensionless stress. For a crack to propagate, the fracture energy E_f should exceed the surface energy of newly created cracks, *i.e.*

$$E_f = \gamma_{surface} \cdot A_s \tag{4.10}$$

Here $\gamma_{surface}$ is the surface energy per unit area, and A_s is the area of new surfaces. If the fracture is a result of tangential/hoop stress, we assume that a crack of height h along the axis of tube is created (Figure 4.2). We call such cracking "tangential cracking". The fracture energy for such a crack is:

$$E_{f,tangential} = \gamma_{surface} \cdot 2(R-a)h \tag{4.11}$$

Similarly, if the fracture is a result of the axial stress, we assume that the tube is broken into two pieces, each with a length smaller than the original value (Figure 4.a.2). We call such a cracking "axial cracking". Fracture energy in this case is given by:

$$E_{f,axial} = \gamma_{surface} \cdot 2\pi(R^2 - a^2) \tag{4.12}$$

The fracture energy can be normalized with a parameter similar to what we used to the bulk strain energy (in equation 4.3b):

$$\prod_{fracture} = \frac{E_f}{E\pi R^2 h(\frac{\Omega \quad IR}{3(1-\nu)F\mathcal{D}})^2} \tag{4.13}$$

The fracture tendency can be defined as the ratio between maximum strain energy to fracture energy (*17*) as:

$$Fracture\ tendency = \frac{Stored\ strain\ energy}{fracture\ energy\ required} = \frac{\prod_{strain}}{\prod_{fracture}} \tag{4.14}$$

If the fracture energy required for axial cracking is less than that required for tangential cracking, the tube would be more prone to axial cracking than tangential cracking and *vice versa*. The effect of the fracture tendency on cracking can be divided into two categories depending upon the length of the tube.

Case 1: Long tubes; *i.e.*, $h > \pi(R + a)$

The relatively long tubes are more prone to axial cracking. The axial fracture energy is normalized as:

$$\prod_{faxial} = \frac{\gamma_{surface} \cdot 2\pi(R^2 - a^2)}{E\pi R^2 h(\frac{\Omega \quad IR}{3(1-\nu)F\mathcal{D}})^2} = \frac{2\gamma_{surface}}{E(\frac{\Omega \quad IR}{3(1-\nu)F\mathcal{D}})^2}\frac{1}{h}\left(1 - \frac{a^2}{R^2}\right) = \frac{K}{I^2(R)^2}\frac{1}{h}\left(1 - \frac{a^2}{R^2}\right) \tag{4.15}$$

Here, we define $K \equiv \frac{2\gamma_{surface}}{E(\frac{\Omega}{3(1-\nu)}\frac{1}{F\mathcal{D}})^2}$, which is a constant for a specific material at a given current density. The dimensionless axial fracture energy depends on the current, the radius of the tube R, the length of the tube h, and the ratio a/R.

Case 2: Short tubes *i.e.*, $h < \pi(R + a)$

The relatively shorter tubes are more prone to tangential cracking. The tangential fracture energy is normalized as:

$$\prod_{ftangential} = \frac{\gamma_{surface} \cdot 2(R-a)h}{E\pi R^2 h(\frac{\Omega}{3(1-\nu)}\frac{IR}{F\mathcal{D}})^2} = \frac{2\gamma_{surface}}{E(\frac{\Omega}{3(1-\nu)}\frac{IR}{F\mathcal{D}})^2}\frac{1}{\pi R}\left(1-\frac{a}{R}\right) = \frac{K}{I^2}\frac{1}{\pi R^3}\left(1-\frac{a}{R}\right) \quad (4.16)$$

The dimensionless fracture energy depends on the current, radius of the tube R, the ratio a/R, but is independent of the tube length h.

Among these two modes of cracking, axial cracking might be more detrimental to LIB electrodes, since it leads to electrical isolation of the electrode material and thus results in capacity fading. On the other hand, pure tangential (hoop) cracking results in opening up of the tube in two parts which may still retain contact with the substrate/current collector (Figure 4.2).

4.5 Designing tubular electrodes based on DIS and fracture tendency

The dimensions of a tubular electrode, including the length, the outer and the inner radii, affect the fracture tendency strongly. The fracture tendencies of nanotubes during delithiation for different a/R ratios of tubes and fixed tube length and local current densities (1 mA cm^{-2}) are compared in Figure 4.3a. For calculations, we used material properties of TiO_2.

The solid lines represent the tangential fracture tendency and the dashed lines represent the axial fracture tendency (Figure 4.3a). It is seen that both tangential and axial fracture tendencies decrease with increase in a/R ratio. However, large a/R is equivalent to small tube thickness, and subsequently a small amount of active material per unit volume of electrode. On the other hand, small a/R ratio (a/R close to 0) gives a denser film of active materials; the effect of axial diffusion in terms of stresses is strong. Diffusion boundary conditions are changed, and DISs and fracture tendencies are different from the current case. At the same time, an increase in a/R leads to a decrease in active material volume fraction in the electrodes and thus a decrease in volumetric energy density.

Also, for a given a/R ratio of the tube, as the outer radius increases, both the fracture tendencies increase (Figure 4.3a). At the same time, a smaller tube diameter implies a small diffusion length and in turn better battery power. In the current work, we tune the porosity of TiO_2 nanotube electrodes with dimensions falling into a “safe” region.

The effect of tube lengths on fracture tendencies for a nanotube with fixed radius is plotted in Figure 4.3b. In agreement with Equations (4.5) and (4.10), the tangential fracture energy is found to be independent of tube length; at the same time, the axial fracture tendency increases with increase in the tube length. Thus, short tubes are less prone to cracking. In LIBs, fracture tendencies should be much smaller than 1 for stable cycling performance.

In the current work, TiO_2 nanotubes with three different dimensions are studied, whose outer radii are 32, 53, and 70 nm, with a/R ratios 0.47, 0.62 and 0.5 respectively, and tube lengths are 355, 540, and 351 nm, respectively.

For all three cases, the tubes are more prone to axial fractures, i.e., Case 1 above. The tube length is large enough to allow us to neglect the end effects from the substrate.

Fracture tendencies of TiO_2 nanotubes are calculated using Equations (4.3) and (4.8)-(4.10). The local current density of TiO_2 nanotubes in this work is 6.2 x 10^{-3}, 5.1 x 10^{-3}, and 13 x 10^{-3} mA cm^{-2} for tubes with diameters 32, 53, and 70 nm, respectively (See Appendix A). The diffusion coefficient of lithium inside TiO_2 tubes (*18*) is 2×10^{-8} m^2s^{-1}. We find that the values of fracture tendencies for TiO_2 nanotubes in electrochemical cycling are calculated to be 4.9 x 10^{-9}, 5.2 x 10^{-9} and 7.5 x 10^{-8}. These values of fracture tendencies for these nanotubes are really low as compared to the values of fracture tendencies reported for nanowires in Deshpande *et al.* (*17*) which were of the order of 10^{-2} for different material. Based on these calculations, it is reasonable to conclude that there is little probability for cracking to occur during cycling. Experimentally, co-worker Juchuna Li found that, there is no visible crack or other damage on the surface of the films, and tubular structures are well preserved after 200 cycles and also maintain contact with the Ti metal substrates. Thus, this study shows that TiO_2 nanotubes have good capacity retention and stable cycling performance. The total capacity fading is less than 6% between the 10th and 200th cycle for samples with diameters 70 and 53 nm and is 12.5% for the sample with tube diameter 32 nm.

In addition to the dimensions of the tube, the cracking tendency is also related to the current density during charging and discharging (Equations 4.9 and 4.10). The effect of current density on the fracture tendency is plotted in Figure 4.4 for a representative tube geometry (height h =351 nm, radius r=50 nm and a/R=0.5). For nanotubes with any given geometry, fracture tendency increases with an increase in current density.

We define the critical current density as the current density at which the fracture tendency reaches unity. The value of critical current density decreases with increasing radius of tubes. For the given example, the fracture tendency exceeds unity at a current density of 6.7 mA cm^{-2}. The local current density depends upon the surface area of tubes available for the diffusion of lithium, and thus the surface roughness. For increased local current density, for example, 2 mA cm^{-2}, the fracture tendencies are less than 0.1 and it is reasonable that TiO_2 will not suffer mechanical degradation. Thus, the cycling performance of TiO_2 nanotubes will be good, even at higher current density or higher cycling rates than what were used in these experiments. However, effects from lithium diffusion, polarization, and side reactions should be considered when setting charging and discharging rates and current densities.

We approximately calculate the current densities for the tubes to be 6.2×10^{-3}, 5.1×10^{-3}, and 13×10^{-3} mA cm^{-2}, respectively (Appendix A). The critical current densities required for a crack to generate are 9.6, 7.1, and 4.7 mA cm^{-2}, respectively. Thus, the current densities used in the experiments are much lower than the critical values and give low fracture tendencies, and the materials are stable upon electrochemical cycling leading to high capacity retention.

4.6 Results and discussion

Based on the simulation results of fracture tendencies derived from the Diffusion Induced Stress (DIS) model, we conclude:

1. Electrodes with hollow tubular structures are more prone to cracking during delithiation than the lithiation process since the tubes are subjected to much larger tensile stress in the tangential direction during delithiation as compared to stresses during lithiation.
2. All stresses including radial, tangential and axial stress can be reduced by decreasing the wall thickness of the tubes.
3. Consistent with this, both tangential and axial fracture tendencies decrease with an increasing ratio of inner to outer radius of the tubes (a/R) regardless of the length and the radius of the tubes.
4. If the a/R ratio and height of the tubes are kept constant, both the fracture tendencies decrease with decreasing radius of the tubes. Hence smaller tube diameter tends to prolong the life of the electrode.
5. An axial fracture may be more detrimental for battery applications as it results in electrical isolation of the active material. Here, we provide general guidelines for the tube design in order to minimize axial cracking.

Appendix A

Number of tubes in electrode substrate area = $N \cong \frac{(\pi \cdot 0.7^2)\ \mathrm{cm}^2}{\text{area of a tube}} = \frac{(\pi \cdot 0.7^2)}{\pi \cdot (32 \cdot 10^{-7})^2}$

$$= 4.788 \cdot 10^{10}$$

Surface area of tubes for diffusion (inner surface area) $= 2\pi ahN$

$$= 2\pi \cdot 15 \cdot 10^{-7} \cdot 355 \cdot 10^{-7} \cdot 4.788 \cdot 10^{10} = 16.01\ \mathrm{cm}^2$$

The real surface might be rougher than the ideal case.

Real surface area of tubes for lithium conduction $= \frac{\text{calulated surface area}}{\text{roughness factor}}$

$$= \frac{16.01\ \mathrm{cm}^2}{V_\rho}$$

Effective current density $= \frac{\text{current}}{\text{surface area}} = \frac{10\mu A}{16.01\ \mathrm{cm}^2} = \frac{0.62}{V_\rho}\mu A\ \mathrm{cm}^{-2}$

For ideal tubes, $V_\rho = 1$

Effective current density = $0.62\mu A\ \mathrm{cm}^{-2}$

Similarly the effective current densities for the other two tubes are calculated to be 5 .1 x 10^{-3}, and 13 x 10^{-3} mA cm^{-2}.

4.7 References

1. R. A. Huggins, *Advanced Batteries: Materials Science Aspects*. (Springer, 2009).
2. M. N. Obrovac, L. Christensen, D. Ba Le, J. R. Dahn, Alloy Design for Lithium-Ion Battery Anodes. *Journal of The Electrochemical Society* **154**, A849 (2007).
3. J. B. Goodenough, "Basic energy needs for electrical energy storage- Report of the Basic Energy Sciences Workshop for Electrical Energy Storage" (July, 2007).
4. L. B. Hu *et al.*, Silicon-Carbon Nanotube Coaxial Sponge as Li-Ion Anodes with High Areal Capacity. *Advanced Energy Materials* **1**, 523 (Jul, 2011).
5. H.-T. Fang *et al.*, Comparison of the rate capability of nanostructured amorphous and anatase TiO_2 for lithium insertion using anodic TiO_2 nanotube arrays. *Nanotechnology* **20**, 225701/1 (2009).
6. Q. Cai, M. Paulose, O. K. Varghese, C. A. Grimes, The effect of electrolyte composition on the fabrication of self-organized titanium oxide nanotube arrays by anodic oxidation. *Journal of Materials Research* **20**, 230 (2005).
7. J. M. Macak, H. Tsuchiya, L. Taveira, S. Aldabergerova, P. Schmuki, Smooth anodic TiO_2 nanotubes. *Angewandte Chemie, International Edition* **44**, 7463 (2005).
8. Q. Wu, *Synthesis and energy applications of oriented metal oxide nanoporous films*. PhD dissertaion (University of Kentucky, 2011).
9. J. Christensen, J. Newman, A mathematical model of stress generation and fracture in lithium manganese oxide. *J. Electrochem. Soc.* **153**, A1019 (2006).

10. Y.-T. Cheng, M. W. Verbrugge, Diffusion-Induced Stress, Interfacial Charge Transfer, and Criteria for Avoiding Crack Initiation of Electrode Particles. *Journal of the Electrochemical Society* **157**, A508 (2010).

11. H. S. Carslaw, J. C. Jaeger, *Conduction of heat in solids*. J. C. Jaeger, Ed., (Clarendon Press, Oxford, ed. second, 1959).

12. S. Timoshenko, J. N. Goodier, *Theory of elasticity*. (New York, McGraw-Hill, 1951).

13. S. Prussin, Generation and distribution of dislocations by solute diffusion. *J. Appl. Phys.* **32**, 1876 (1961).

14. S. J. Harris, R. D. Deshpande, Y. Qi, I. Dutta, Y. T. Cheng, Mesopores inside electrode particles can change the Li-ion transport mechanism and diffusion-induced stress. *Journal of Materials Research* **25**, 1433 (Aug, 2010).

15. J. Crank, *The Mathematics of Diffusion*. (Oxford University Press, USA, 1980).

16. R. Hetnarski, R. Eslami, *Thermal Stresses -- Advanced Theory and Applications (Solid Mechanics and Its Applications)*. (Springer, 2008).

17. R. Deshpande, Y. Qi, Y.-T. Cheng, Effects of Concentration-Dependent Elastic Modulus on Diffusion-Induced Stresses for Battery Applications. *J. Electrochem. Soc.* **157**, A967 (2010).

18. K. Zaghib, M. Simoneau, M. Armand, M. Gauthier, Electrochemical study of Li4Ti5O12 as negative electrode for Li-ion polymer rechargeable batteries. *Journal of Power Sources* **81-82**, 300 (1999).

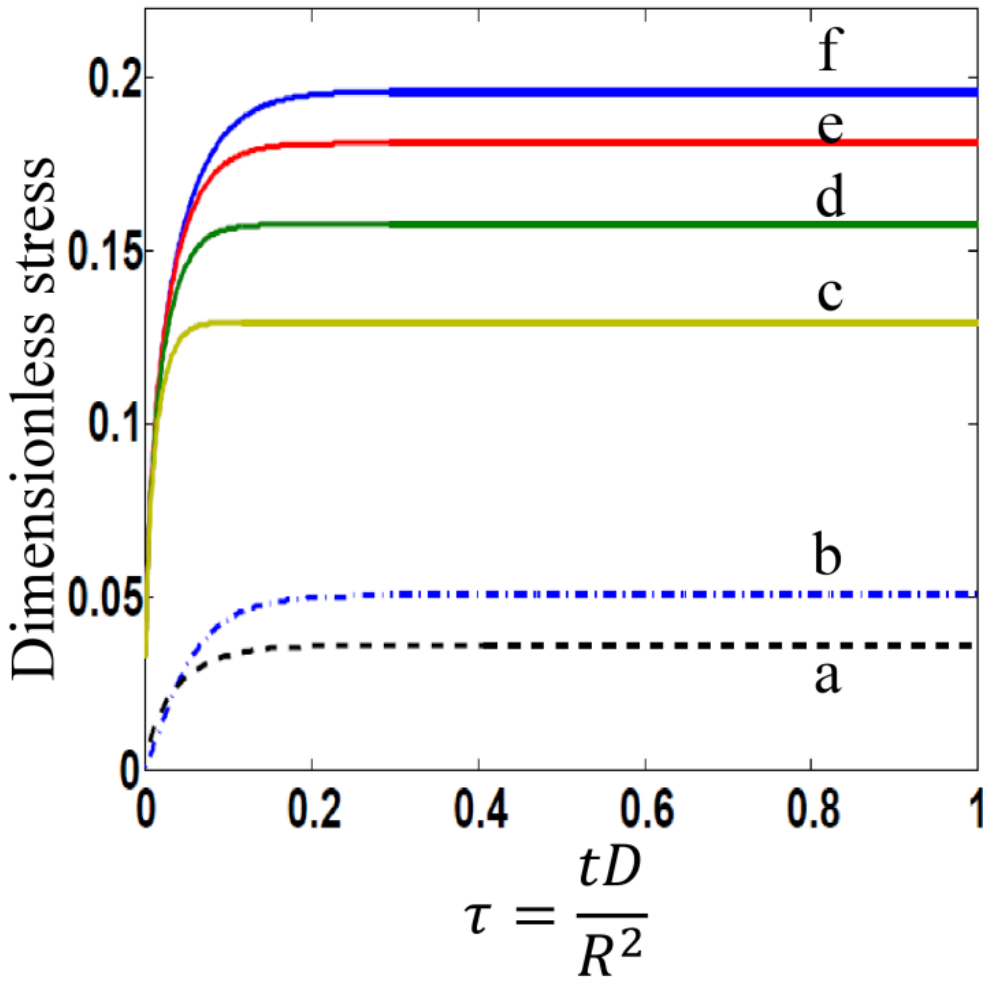

Figure 4.1: Comparison between the maximum stress that the tubular electrode experiences (a) in the radial direction during delithiation (lithium extraction), and (b) in the tangential direction during lithiation (lithium insertion) and (c, d, e, and f) delithiation. The ratio of inner radius to outer radius of tube (a/R) for curves (a, b, and f) = 0.3, for curve (e) 0.4, for curve (d) 0.5, and for curve (c) 0.6.

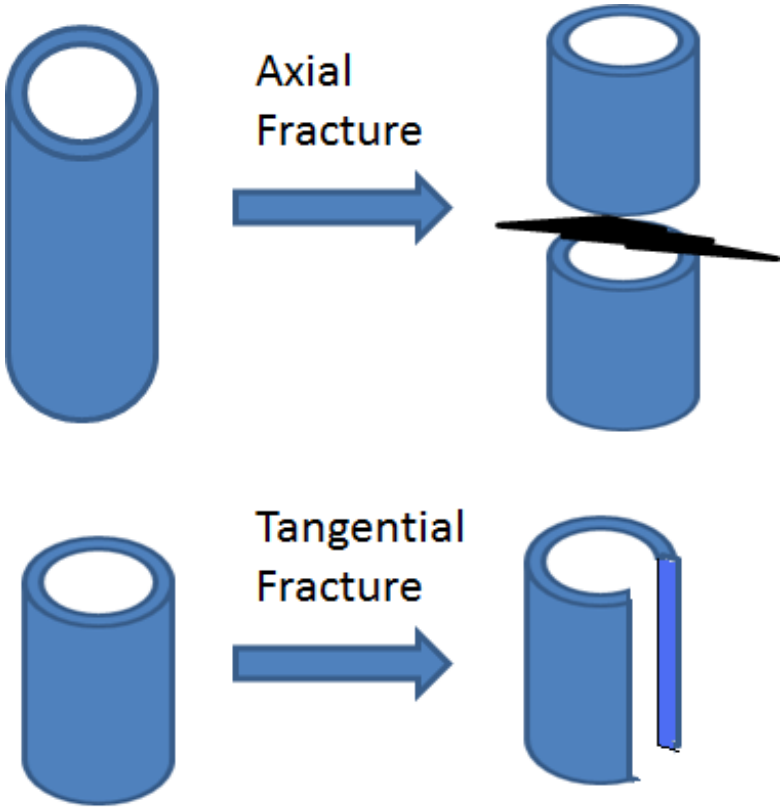

Figure 4.2**:** Schematic illustrating tubular electrode undergoing axial and tangential fracture during charge/discharge operation.

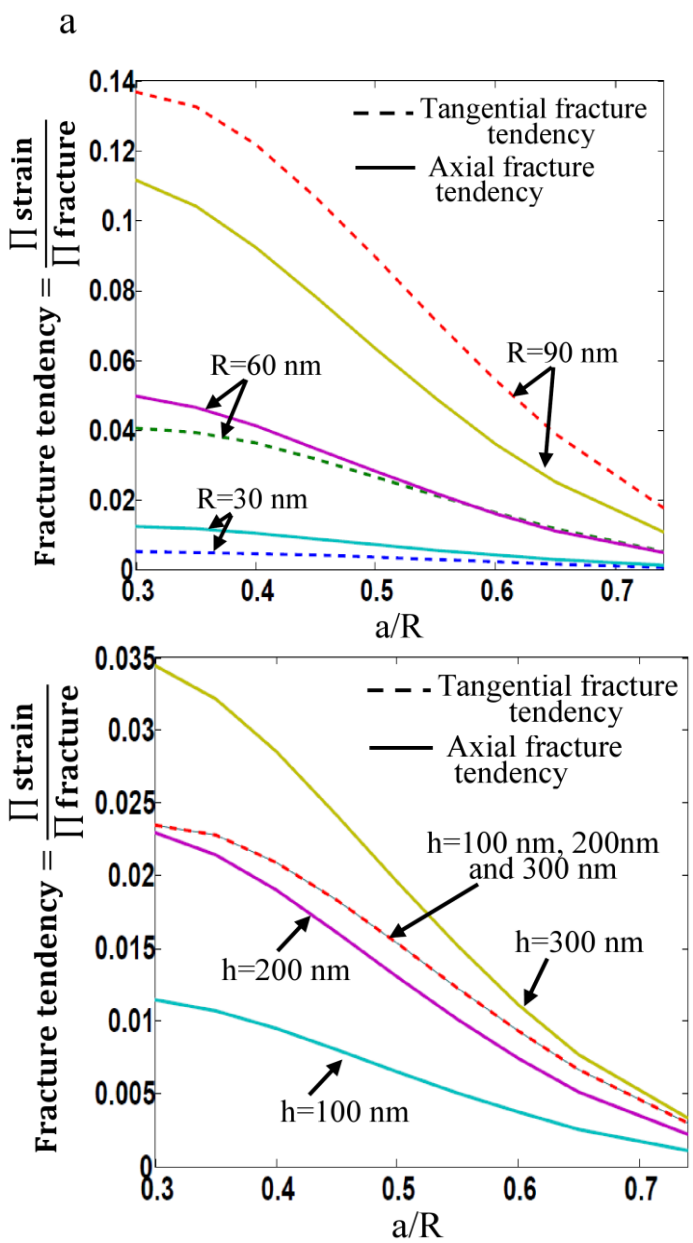

Figure 4.3: Fracture tendency as a function of the ratio of the inner radius to outer radius of tubes (*a/R*) assuming current density $I = 1\ mA\ cm^{-2}$ and (a) height of the tube fixed at $h = 300\ nm$ or (b) radius of the tube fixed at $R = 50\ nm$.

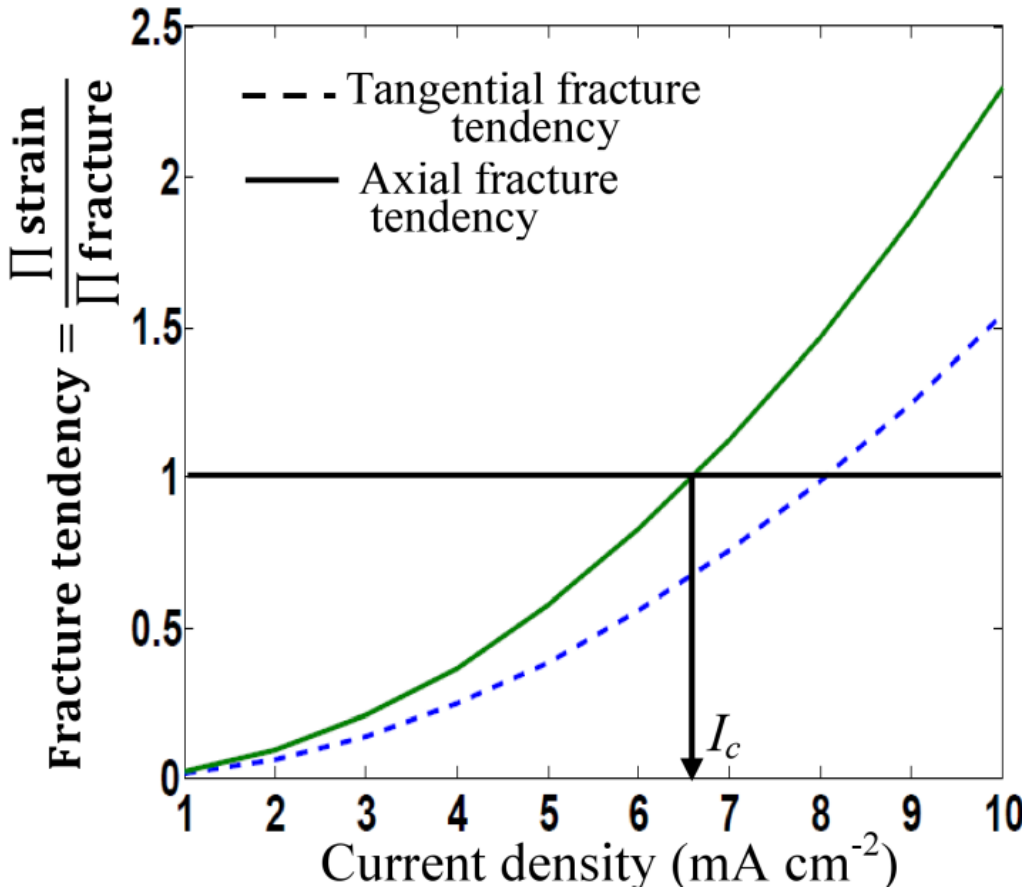

Figure 4.4: Fracture tendency as a function of current density for a given set of dimensions of the tube (height h =351 nm, radius r=50 nm and a/R=0.5). The solid line represent tangential fracture tendency and the dashed line represent axial fracture tendency.

CHAPTER 5

EFFECT OF CONCENTRATION-DEPENDENT ELASTIC MODULOUS ON DIFFUSION INDUCED STRESSES FOR BATTERY APPLICATIONS

This chapter is based on work published as:

R. Deshpande, Y. Qi, Y.-T. Cheng, Effects of Concentration-Dependent Elastic Modulus on Diffusion-Induced Stresses for Battery Applications. *Journal of The Electrochemical Society* **157**, A967 (2010).

It's reproduced by permission of The Electrochemical Society.

5.1 Summary

Most of the lithium ion battery electrodes experience a large volume changes associated with Li concentration changes within the host particles during charging and discharging. Electrode failure, in the form of fracture or decrepitation, can occur as a result of repeated volume changes. It has been recently found that many electrode materials such as graphite, silicon (Si) and lithium iron phosphate ($LiFePO_4$) change their elastic properties upon lithiation. However, previous diffusion-induced stress (DIS) models have not considered this relationship. We developed a mathematical model with the assumption of homogeneous isotropic cylindrical electrode particle to describe the effect of concentration-dependent Young's modulus on the DISs in battery electrodes. The proposed DIS model considers both increase and decrease in Young's modulus as a function of change in concentration of the lithium solute.

The model shows that the concentration dependence of Young's modulus has a significant effect on peak stress and stress evolution in the electrode particles. We show that insertion and removal are not symmetric in stress profiles. In conclusion, Li stiffening is beneficial to avoid surface cracking during de-lithiation, and moderate Li softening is beneficial to avoid particle cracking from the center during lithiation.

5.2 Introduction

Improving the energy capacity and the cycle life of the lithium ion battery is currently one of the prime focuses of research worldwide. The commercially available batteries fail after certain number of charging discharging cycles. Chemical and mechanical degradation of the electrode are the major causes of electrode failure. The chemical degradation occurs due to instability of the electrolyte which results in irreversible capacity loss as a result of the solid electrolyte interface (SEI) formation. The mechanical degradation is a result of fracture and fatigue failure of the electrode material due to DISs upon cycling. One of the critical challenges in commercializing the advanced lithium-ion batteries is the capacity fading upon electrochemical cycling as a result of fracture and electrode decrepitation due to lithium insertion and removal. During battery operation, when lithium is inserted into (or extracted from) the active materials of both positive and negative electrodes, volume expansion (and contraction) occurs (*1*). For example, graphite, the most common negative electrode for Li-ion batteries, expands 10% of its volume when Li intercalates between the graphite sheets (*2*). Compared to graphite, Si can store ~10 times more Li but is associated with massive volume expansion, of the order of 300% (*3*).

Large volume expansion and the associated stress within electrodes can lead to fracture and failure of electrodes causing capacity loss of batteries. To help minimize stresses and thus increase the mechanical durability, several groups (*4-13*) have recently modeled diffusion-induced stresses in lithium ion battery electrodes. For example, Verbrugge and Cheng recently studied the evolution of stress and strain energy within a spherically-shaped electrode element under either galvanostatic or potentiostatic operation. The study also investigated the effects of surface energy and surface elasticity on the stress evolution in spherical electrodes. Wolfenstine *et al*. (*14*) demonstrated that using Young's modulus, fracture toughness and the volume change, a critical particle size to lower capacity fade could be estimated with analytical modeling. These models are based on equations of solid-state diffusion and continuum mechanics. However, many of the input parameters such as elastic constants, surface energy and stress, volume expansion coefficients and diffusion coefficients are not readily available. More specifically, the intrinsic mechanical properties of electrodes such as Young's modulus are assumed to be constant (independent of Li concentration). The assumptions discussed are not surprising as there are not many studies with experimental data showing change in material properties with lithiation.

One of the recent studies by Qi and coworkers (*15*) used density functional theory (DFT) with local-density approximation (LDA) method to demonstrate that the polycrystalline Young's modulus (E) of graphite increases linearly with Li concentration, and that it triples when graphite is fully lithiated to LiC_6.

Shenoy *et al*. (*16*) computed the bulk modulus for various Li-Si crystalline and amorphous structures and found that the modulus of Si decreases almost linearly with Li concentration, dropping to one third of its original value when $Li_{15}Si_4$ phase is formed. Varying mechanical properties upon lithiation has also been found in cathode materials, such as $LiFePO_4$.

Maxisch and Ceder (*17*) used DFT calculation with generalized gradient approximations (GGA+U) method to show that olivine (Li_xFePO_4) is anisotropic and that the directional bulk moduli change significantly during lithiation, although the average Young's modulus did not change much with lithiation. Thus, changing mechanical properties with Li concentration is a general phenomenon in electrode materials: some electrode materials such as graphite can be stiffened by Li, while some other materials such as Si can be softened by Li. The DFT results on both graphite and Si anode materials have shown that the Young's modulus of active materials can be approximated by a linear function of Li concentration and that the Poisson's ratio does not change much with Li concentration. In this chapter, we shall evaluate the stiffening and softening effect of lithiation on the stress evolution in an idealized, fiber-shaped electrode using a continuum level model for DISs.

5.3 Methods

5.3.1 Mechanics

Numerous studies in the literature employed the analogy between thermal stresses and DISs for investigating the DISs in the lithium ion battery electrodes. In this work, we use a similar approach to model the stresses in a cylindrical electrode particle to examine the effects of concentration dependent Young's modulus on the stress distribution in a cylindrical electrode. We assume that the electrode is isotropic, linearly elastic solid. Using the analogy between thermal stresses (*18, 19*) and DISs we can write,

$$\varepsilon_{rr} - \alpha C = \frac{1}{E}(\sigma_r - \nu(\sigma_\theta + \sigma_z)) \tag{5.1}$$

$$\varepsilon_{\theta\theta} - \alpha C = \frac{1}{E}(\sigma_\theta - \nu(\sigma_r + \sigma_z)) \tag{5.2}$$

$$\varepsilon_{zz} - \alpha C = \frac{1}{E}(\sigma_z - \nu(\sigma_r + \sigma_\theta)) \tag{5.3}$$

Here, E is Young's modulus, C is molar concentration, and α is a "concentration expansion" coefficient which can be obtained from the partial molar volume of the solute, which is 3α .

We assume that Young's modulus is a function of Li concentration present at a particular location and time, $E = f\big(C(r,t)\big)$, which depends on the electrode material. We further assume that the Poisson's ratio ν, does not vary with concentration.

Since atomic diffusion in solids is a much slower process than elastic deformation, mechanical equilibrium is established much faster than that of diffusion. Mechanical equilibrium is, therefore, treated as a static equilibrium problem (*18, 19*).

In the absence of any body force, the equation for static mechanical equilibrium in the bulk of a cylinder is given by following equation:

$$\frac{d\sigma_r}{dr} + \frac{(\sigma_r - \sigma_\theta)}{r} = 0 \tag{5.4}$$

Let u denote the radial displacement. Strain can be written as,

$$\varepsilon_{rr} = \frac{du}{dr}, \quad \varepsilon_{\theta\theta} = \frac{u}{r} \tag{5.5}$$

Since there is no displacement at the center, $u(0) = 0$. At $r = R$ (where R radius of the cylinder), the radial stress, $\sigma_r(R) = 0$. The axial boundary condition at the ends of the cylinder depends upon the loading of the electrode.

Here, we assume that there is no load on the two ends of the cylinder; i.e., $F_z = \int_0^R 2\pi r \sigma_z dr = 0$. This is the generalized plane strain condition. Under this condition, the axial stress is given as (*18*)

$$\sigma_z = \nu(\sigma_r + \sigma_\theta) + \alpha E(C_{avg}(R) - C(r,t)) \tag{5.6}$$

where $C(r,t)$ is the solute concentration at a particular radial location at a particular time and $C_{avg}(r) = \frac{2}{r^2}\int_0^r C(r')r'dr'$ is the average concentration within radius r per unit length of the cylindrical electrode.

Equations (5.2), (5.3), and (5.6) can be solved to obtain

$$\sigma_r = \frac{\nu}{1-\nu}\sigma_\theta + \frac{E}{1-\nu^2}\left[\varepsilon_{rr} + \alpha(\nu C_{avg}(R) - (1+\nu)C(r,t))\right] \tag{5.7}$$

$$\sigma_\theta = \frac{\nu}{1-\nu}\sigma_r + \frac{E}{1-\nu^2}\left[\varepsilon_{\theta\theta} + \alpha(\nu C_{avg}(R) - (1+\nu)C(r,t))\right] \tag{5.8}$$

Combining Equations (5.7) and (5.8)

$$\sigma_r = \frac{E}{1-2\nu}\left\{\frac{\nu}{1+\nu}\varepsilon_{\theta\theta} + \frac{1-\nu}{1+\nu}\varepsilon_{rr} - \alpha C(r,t) + \frac{\nu}{1+\nu}\alpha C_{avg}(R)\right\} \tag{5.9}$$

$$\sigma_\theta = \frac{E}{1-2\nu}\left\{\frac{\nu}{1+\nu}\varepsilon_{rr} + \frac{1-\nu}{1+\nu}\varepsilon_{\theta\theta} - \alpha C(r,t) + \frac{\nu E}{1+\nu}\alpha C_{avg}(R)\right\} \tag{5.10}$$

Using Equations (5.5), (5.9) and (5.10) in Equations (5.4), we have

$$E\frac{d^2u}{dr^2} + \left(\frac{dE}{dr} + \frac{E}{r}\right)\frac{du}{dr} + \left\{\frac{\nu}{1-\nu}\frac{dE}{dr} - \frac{E}{r}\right\}\frac{u}{r} - \frac{\alpha(1+\nu)}{1-\nu}\left[\left(C(r) - \frac{\nu}{(1+\nu)}C_{avg}(R)\right)\frac{dE}{dr} + E\frac{dC(r)}{dr}\right] = 0 \tag{5.11}$$

5.3.2 Diffusion in a cylinder

Within the cylindrical host material, the solute (lithium) concentration is governed by the diffusion equation:

$$\frac{\partial C}{\partial t} = \mathcal{D}\left(\frac{\partial^2 C}{\partial r^2} + \frac{1}{r}\frac{\partial C}{\partial r}\right) \tag{5.12}$$

We assume that the electrode surface is surrounded by an invariant lithium ion concentration C_R (reflecting facile electrochemical kinetics and a porous-electrode system dominated by solute-diffusion resistance (*10-12*)) and the initial lithium concentration inside the electrode is C_0. Also, the concentration at the center is finite. The initial and boundary conditions are,

$$C(r,0) = C_0\,, \qquad for\ 0 \le r \le R$$

$$C(R,t) = C_R \text{ and } C(0,t) = finite, \qquad for\ t \geq 0 \tag{5.13}$$

Equations (5.13) can be made dimensionless with the following:

$$x = \frac{r}{R},\ \ T = \frac{\mathcal{D}t}{R^2},\ \ y = \frac{C - C_0}{C_R - C_0} \tag{5.14}$$

The dimensionless concentration at different radial positions and time is depicted in Figure 5.1 for Li insertion. The dimensionless concentration profile is $(1 - y)$ for Li removal. The concentration profiles are thus "symmetric" with respect to $y = 0.5$ for insertion and removal.

5.3.3 Effects of concentration-dependent Young's modulus on DIS

Although the functional dependence of Young's modulus on Li concentration is specific to electrode material, we assume, in this work, a simple functional form to investigate the effects of concentration dependent Young's modulus on stresses. Specifically, we assume Young's modulus (E) of the electrode material with a particular concentration (C) to be a linear function of lithium ion concentration or the state of charge (SOC) present in the electrode (*15*) :

$$E = E_0 + kC \tag{5.15}$$

$$\frac{E}{E_0} = 1 + \frac{k}{E_0}\left(\frac{C - C_0}{C_R - C_0}\right) \tag{5.16}$$

$$\frac{E}{E_0} = 1 + k'y \tag{5.17}$$

where E_0 is the Young's modulus of the pure electrode material and $k\ (or\ k')$ is a constant. We assume that α is constant.

If the material is stiffened due to Li insertion, then $k > 0$; and if the material is softened by Li insertion, then $k < 0$. For example, from Qi *et al*. and Shenoy *et al*. (*16, 20*) we can deduce $k' \sim 3$ for graphite electrode material, and $k' \sim -0.7$ for silicon electrode material. Using a finite-difference method, we obtain $u(r,t)$ by solving Equations (5.11) with the boundary condition:

$$u(0) = 0$$

$$\sigma_r(R,t) = 0 \quad \text{for } t \geq 0 \tag{5.18}$$

The radial, tangential, and axial stresses can then be obtained using $u(r,t)$ and Equations (5.5), (5.9), and (5.10). In Figures 5.2, 5.3, 5.4, and 5.5, we plot the dimensionless radial and tangential stresses normalized by $\alpha E_0(C_R - C_0)/(1-\nu)$, i.e.,

$$\xi_r = \frac{\sigma_r}{[\frac{\alpha E_0}{(1-\nu)}(C_R - C_0)]}, \ \xi_\theta = \frac{\sigma_\theta}{[\frac{\alpha E_0}{(1-\nu)}(C_R - C_0)]}, \ \xi_z = \frac{\sigma_z}{[\frac{\alpha E_0}{(1-\nu)}(C_R - C_0)]} \tag{5.19}$$

for both insertion and removal at dimensionless time, $T = 0.01$ and $T = 0.076$, and several *k* values.

5.4 Results and discussions

5.4.1 Stress evolution

Figure 5.2 illustrates that, as the k' value increases, the radial stress increases in the case of insertion. The blue dash line in Figure 5.1 shows Li concentration at time $T = 0.01$ is still close to zero in a region near to the center $(x < 0.6)$. Interestingly, we note that, at time $T = 0.01$, the stress level in this un-lithiated core region can be very different depending upon the Young's Modulus of the lithiated shell.

Due to lithiation, the outer shell $(x > 0.6)$ expands, but to maintain the continuity of the expansion, the inner core is pulled mechanically. Apparently, the outer shell with higher Young's modulus can exert greater stress to the inner core than that with lower E.

As a result, the inner core is under higher tensile stress if the electrode material is stiffened $(k' > 0)$ due to Li insertion but under a lower tensile stress if it is softened $(k' < 0)$ by Li insertion. In this figure, we observe a similar behavior during removal.

Furthermore, it can be seen that the stress profiles for insertion and removal are no longer symmetric, though concentration profiles for insertion and removal are exact mirror images of each other (Figure 5.1). The higher the k' value, the less symmetric the stress profiles are for insertion and deinsertion.

We show in Figure 5.3, the radial stress profile at time $T = 0.076$. We chose this time because the radial stress has a maximum at the time of $T = 0.076$, if Young's modulus is concentration independent, i.e., $k' = 0$ (*12*). We have observed that not only the peak value of radial stress changes with change in Young's modulus but the time to reach the peak value also shifts. For comparison, we plot the radial stresses at the same time of $T = 0.076$ with different k' values. We observe that, with an increasing value of k', the magnitude of radial stress at $T = 0.076$ increases; and with a negative k', the magnitude of stress at $T = 0.076$ decreases. The location of the peak radial stress is at the center for all the k' values. The dimensionless stress is normalized by the host material modulus without Li insertion E_0.

If we consider near the center of the electrode at $y = 0.07$, the modulus for the different electrode changes from 93.7 to 114 due to different k values, however the variation of the tensile peak stress at the center is much larger range from 0.12 to 0.43 (about three fold increase). If we consider that the material fails due to tensile stress at the center, larger k' values will lead to higher stresses and thus material will become more prone to fracture. During insertion, the maximum value of tangential stress is compressive and is at the surface. Figure 5.4 compares the tangential stress at time $T = 0.01$ for different k' values.

This figure also shows that the tangential stress for insertion and removal are asymmetric. Here, not only the magnitude of the stresses is changed but the nature of the stress profiles is no longer symmetric during insertion and removal. For a particular time (here, $T = 0.01$), the maximum compressive stress at the surface increases as k' increases. The stress increase is mainly due to the modulus increase effect, if we normalize it by the modulus at $x = 1$, they are all about ~0.75, similar to that the stress computed with constant E. Another feature of the insertion is that the peak compressive stress decreases as k' decrease. The location of the maximum stress shifts from surface to just beneath the surface with decreasing k'. During insertion, there is a shift in the stresses in a region near the center before the region is lithiated at time $T = 0.01$. During removal, however, the value of the peak stress at the surface does not vary much. Because the Li concentration drops to zero on the surface during removal, the influence of concentration dependent modulus on stress generation is minimized. However, an important observation is that, during removal, as the k' value increases, the peak value of stress shifts towards the center.

In this figure, for $k' = 2$, we observe that, the peak tensile stress is not at the surface, but is located just beneath the surface. Previous analytic models, using a constant modulus value, have shown that the peak tensile tangential stress on the surface when delithiation process starts is the main reason for surface cracks (*15*). This is particularly important since the surface tends to have much higher density of defects which makes it more prone to cracking. By shifting the maxima, the cracking tendency of the electrode material decreases. We make similar observations in Figure 5.5 for time *T=0.076*.

5.4.2 Tendency of fracture

Since we are more interested in the damage of electrodes during Li diffusion, we discuss the tendency of fracture based on the stress field and elastic strain energy. If we consider Li concentration dependent material properties (modulus), the fracture energy should also vary with Li concentration. For example, the DFT predicted basal cleavage energy is for LiC_6 to be 1 J m^{-2} and 0.1 J m^{-2} for graphite. Li intercalation has increased the fracture energy about 10 times in Li-graphite. If we ignore a possible brittle to ductile transition due to Li insertion, we can assume that Li has a similar influence on fracture energy and fracture strength as it has on modulus. More specifically, if the material is stiffened by Li insertion, it will require larger energy and stress to break and vice versa. We can scale the fracture energy or fracture strength with modulus that changes with Li concentration. The fracture energy is twice of the surface energy. Both scale linearly with *E* and thus scales linearly with Li concentration. For example, based on Kelly's approximation(*21*), the surface energy can be written as

$$\gamma = Ea_0 / 10 = (E_0 + kC)a_0 / 10 , \tag{5.20}$$

where E is Young's modulus and a_0 is the equilibrium separation between two atomic planes.

In terms of stress criteria, the Griffith toughness of a mode I crack (where the crack opens under a tensile stress normal to the plane of the crack) is related to the theoretical strength, which is the stress required to pull apart two planes in a perfect solid(*22*). Using the theoretical strength, we have

$$\sigma_{\max} = \sqrt{E\gamma / a_0} = 0.3E = 0.3(E_0 + kC)\,, \tag{5.21}$$

here E is the Young's Modulus, γ is the surface energy of the newly-cleaved free surfaces, and a_0 is the equilibrium spacing between atomic planes. Thus both fracture energy and strength scales linearly with Li concentration.

Fracture is more likely to start from where the local stress is beyond the critical fracture strength, and its growth is mainly driven by the stored elastic energy. We now identify both strength- and energy-based criteria for fracture of electrodes.

During insertion, maximum radial tensile stress occurs at the center of the electrode. In Table 5.1, we first determine the time, T_p , at which the radial stress reaches maximum during insertion and the value of the peak tensile stress (at the center) as $\xi_r|_{max}$. The theoretical fracture strength was then computed based on the Li concentration at the center of the electrode, as σ_{max}. We then computed the ratio of peak tensile stress with respect to the theoretical fracture strength as $\xi_r|_{max}/\sigma_{max}$, as one measure of fracture tendency.

Then we computed the strain energy at time when peak stress is reached, as $\prod_{bulk}|_{T_p}$. The total bulk strain energy can be obtained by integrating the strain energy density over the entire volume.

Bulk strain energy per unit length of the cylinder in dimensionless form is

$$\prod_{bulk} = \frac{E_{bulk}}{\pi R^2 E_0^2 (\frac{\Omega(C_R - C_0)}{3 \quad (1-\nu)})^2} = \int_0^1 [(\xi_r^2 + \xi_\theta^2 + \xi_z^2) - 2\nu(\xi_r\xi_\theta + \xi_\theta\xi_z + \xi_z\xi_r)\,] \frac{E_0}{E} x dx \tag{5.22}$$

As discussed earlier, fracture energy is linearly proportional to E. Thus the other fracture tendency is the ratio between strain energy to fracture energy as

$$\prod_{bulk}/2\gamma = \prod_{bulk}/\frac{E(C)}{E_0} \tag{5.23}$$

Both fracture tendency criteria, namely $\xi_r|_{max}/\sigma_{max}$ and $\prod_{bulk}|_{T_p}/\frac{E(C)}{E_0}$ as a function of k' in Figure 5.6. It is clear that as k' value increases, it is more likely to fracture at the center during Li insertion due to tensile radial stress. In other words, lithium softening material might be less prone to cracking than lithium hardening material.

During removal, fracture is more likely to occur at the surface by a tangential stress. Regardless of the k' values, we observe that the tensile stress level was similar at the surface in Figure 5.4 and 5.5. However, with Li stiffening, there is a shift of the peak stress location from the surface to underneath the surface. Since there are fewer defects than on the top surface, we conclude that this shift with increasing k value may make the material more resistant to cracking, thus enhancing the durability of the electrode.

5.5 Conclusion

We developed a model for diffusion-induced stresses in insertion electrodes which takes into account the concentration dependence of Young's modulus. This model follows the convention of assuming the electrode particle to be a homogeneous isotropic particle (*10, 12, 13, 23*). Under such an assumption we could show that,

The stress profiles during lithiation and de-lithiation are asymmetric if Young's modulus is a function of concentration. This implies that the driving force and probability of cracking during insertion and removal is unequal.

If the electrode material has a lithiation stiffening tendency, during the de-lithiation process, there is a shift of the tensile tangential stress maximum from the surface of the material to just underneath the surface, which may reduce cracking failure since the number of defects present in the interior may be less than that at the surface of the electrode material.

During the lithiation process, when strain energy reaches a maximum, the peak radial stress value at the center of the electrode increases with lithiation stiffening. The strain energy analysis in comparison with fracture energy suggests that moderate lithiation softening can reduce the fracture tendency at the center of electrode.

A real electrode particle may not be homogeneous and isotropic, but, the model can provide semi-quantitative predictions about the stresses and their behavior for different material systems in general, with concentration dependent Young's modulus. Also it gives an idea about the general trends in fracture tendency for different variation in Young's Modulus on lithiation.

5.6 List of symbols

r, θ, z	cylindrical coordinates
γ	surface energy per unit area $(J\ m^{-2})$
Ω	partial molar volume of the solute $(m^3 mol^{-1})$
R	radius of the cylindrical electrode (m)
ν	Poisson's ratio
E	Young's modulus $(N\ m^{-2})$
u	radial displacement
σ_r	radial stress $(N\ m^{-2})$
σ_θ	tangential stress $(N\ m^{-2})$
σ_z	axial stress$(N\ m^{-2})$
ε_{rr}	radial strain
$\varepsilon_{\theta\theta}$	tangential strain
ε_{zz}	axial strain
$C(r, t)$	solute concentration at radius r at time t $(mol\ m^{-3})$

$C_{avg}(r)$	average concentration in the area of radius r $(mol\ m^{-3})$
$C_{avg}(R)$	average concentration in the area of radius R $(mol\ m^{-3})$
D	diffusion coefficient of the solute $(m^2 sec^{-1})$
t	time (*sec*)
x	dimensionless radius
T	dimensionless time
y	dimensionless concentration
ξ_r	dimensionless radial stress
ξ_θ	dimensionless tangential stress
ξ_z	dimensionless axial stress
E_{bulk}	strain energy per unit length stored due to bulk deformation ($J\ m^{-1}$)
$\prod_{bulk}$	dimensionless bulk strain energy
$E_{fracture}$	dimensionless fracture energy
T_p	dimensionless time at which radial stress reaches maximum tensile value at the center during insertion condition
C_{Li}	concentration at the center at a time when radial stress reaches its maximum during insertion condition

$\xi_r\|_{max}$	maximum tensile radial stress during insertion condition
σ_{max}	maximum theoretical strength
$\prod_{bulk}\|_{T_p}$	dimensionless strain energy at time T_p

5.7 References

1. R. A. Huggins, *Advanced Batteries: Materials Science Aspects*. (Springer, 2009).
2. J. R. Dahn, Phase diagram of LixC6. *Physical Review B* **44**, 9170 (1991).
3. L. Y. Beaulieu, T. D. Hatchard, A. Bonakdarpour, M. D. Fleischauer, J. R. Dahn, Reaction of Li with Alloy Thin Films Studied by In Situ AFM. *Journal of The Electrochemical Society* **150**, A1457 (2003).
4. Y. Li, Y.-T. Cheng, Studies of Metal Hydride Electrodes Using an Electrochemical Quartz Crystal Microbalance. *Journal of The Electrochemical Society* **143**, 120 (1996).
5. R. Huggins, W. Nix, Decrepitation model for capacity loss during cycling of alloys in rechargeable electrochemical systems. *Ionics* **6**, 57 (2000).
6. J. Christensen, J. Newman, A Mathematical Model of Stress Generation and Fracture in Lithium Manganese Oxide. *Journal of The Electrochemical Society* **153**, A1019 (2006).
7. J. Christensen, J. Newman, Stress generation and fracture in lithium insertion materials. *Journal of Solid State Electrochemistry* **10**, 293 (2006).

8. X. Zhang, W. Shyy, A. M. Sastry, Numerical Simulation of Intercalation-Induced Stress in Li-Ion Battery Electrode Particles. *Journal of The Electrochemical Society* **154**, A910 (2007).

9. X. Zhang, A. M. Sastry, W. Shyy, Intercalation-Induced Stress and Heat Generation within Single Lithium-Ion Battery Cathode Particles. *Journal of The Electrochemical Society* **155**, A542 (2008).

10. Y.-T. Cheng, M. W. Verbrugge, The influence of surface mechanics on diffusion induced stresses within spherical nanoparticles. *Journal of Applied Physics* **104**, 083521 (2008).

11. Y.-T. Cheng, M. W. Verbrugge, Automotive traction battery needs and the influence of mechanical degradation of insertion electrode particles. *Electrochemical Society Transactions* **16**, (2008, 2008).

12. Y.-T. Cheng, M. W. Verbrugge, Evolution of stress within a spherical insertion electrode particle under potentiostatic and galvanostatic operation. *Journal of Power Sources* **190**, 453 (2009).

13. R. Deshpande, Y.-T. Cheng, M. W. Verbrugge, Modeling diffusion-induced stress in nanowire electrode structures. *Journal of Power Sources* **195**, 5081 (2010).

14. J. Wolfenstine, A high ratio of the testing temperature to the melting temperature: a necessary but not sufficient condition for an alloy anode to exhibit low capacity fade. *Materials Letters* **57**, 3983 (2003).

15. Y. Qi, H. Guo, L. G. Hector, A. Timmons, *Journal of The Electrochemical Society*, (2010).

16. V. B. Shenoy, P. Johari, Y. Qi, Elastic softening of amorphous and crystalline Li-Si Phases with increasing Li concentration: A first-principles study. *Journal of Power Sources* **195**, 6825 (Oct, 2010).

17. T. Maxisch, G. Ceder, Elastic properties of olivine Lix FePO4 from first principles. *Physical Review B* **73**, 174112 (2006).

18. R. Hetnarski, R. Eslami, *Thermal Stresses -- Advanced Theory and Applications (Solid Mechanics and Its Applications)*. (Springer, 2008).

19. S. Timoshenko, J. N. Goodier, *Theory of elasticity, by S. Timoshenko and J.N. Goodier*. (New York, McGraw-Hill, 1951).

20. Y. Qi, H. Guo, J. L. G. Hector, A. Timmons, Threefold Increase in the Young's Modulus of Graphite Negative Electrode during Lithium Intercalation. *Journal of The Electrochemical Society* **157**, A558 (2010).

21. A. F. R. S. Kelly, *Strong solids, by A. Kelly*. Monographs on the physics and chemistry of materials (Clarendon Press, Oxford, 1973).

22. L. Le May, *Principles of mechanical metallurgy*. (Elsevier North-Holland, New york, 1981).

23. M. W. Verbrugge, Y.-T. Cheng, Stress and Strain-Energy Distributions within Diffusion-Controlled Insertion-Electrode Particles Subjected to Periodic Potential Excitations. *Journal of The Electrochemical Society* **156**, A927 (2009).

Table 5.1: Fracture tendency at *Tp*, which is the dimensionless time at which radial stress reaches maximum during insertion

$k'value$	Tp	c_{Li}	$\xi_r\|_{max}$	σ_{max}	$\xi_r\|_{max}/\sigma_{max}$ (Fracture tendency)	$\prod_{bulk}\|_{T_p}$	$\frac{\prod_{bulk}\|_{T_p}}{E_{fracture}}$
2.0	0.099	0.148	0.437	39.12	0.0112	0.0771	0.0595
1.5	0.094	0.130	0.387	35.84	0.0108	0.0714	0.0597
0.9	0.086	0.102	0.327	32.75	0.0100	0.0652	0.0598
0.0	0.076	0.073	0.233	30.00	0.0078	0.0542	0.0542
-0.4	0.073	0.061	0.188	29.23	0.0064	0.0517	0.0529
-0.9	0.068	0.048	0.048	28.71	0.0017	0.0829	0.0867

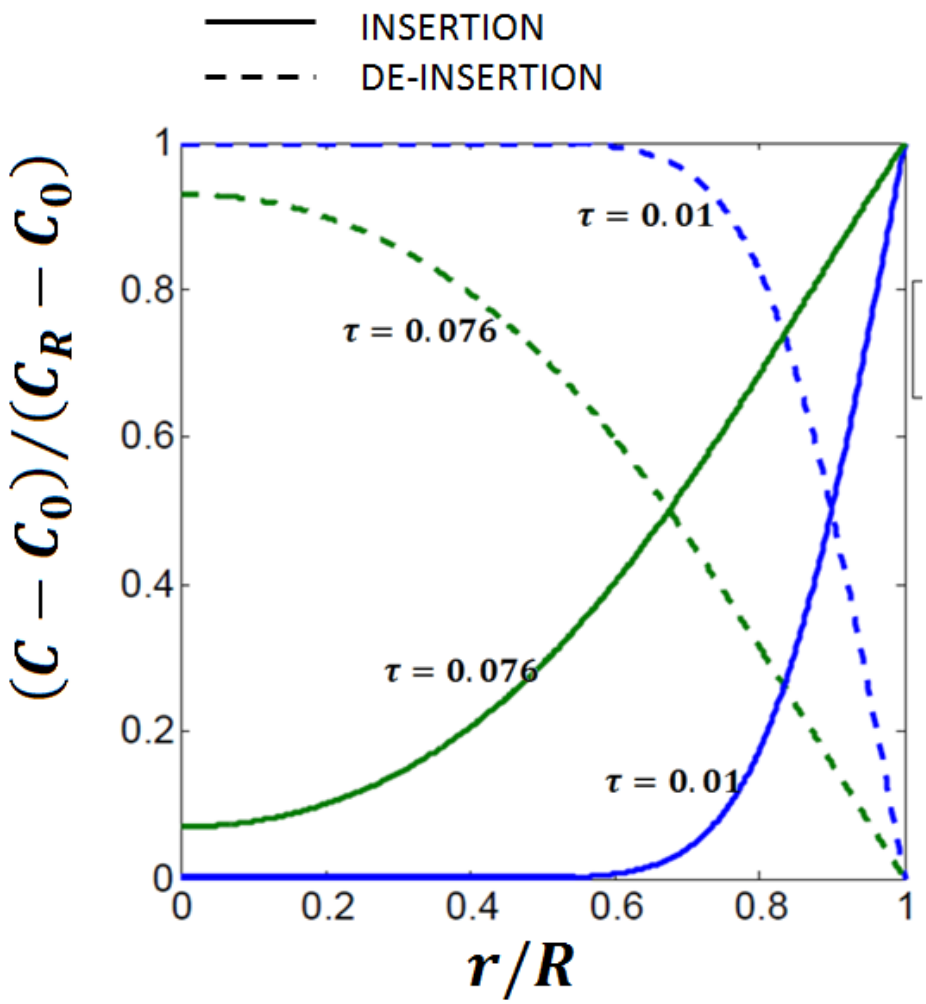

Figure 5.1: Lithium ion concentration inside an electrode at different radial locations at time T=0.01 and T=0.076 for insertion and de-insertion conditions.

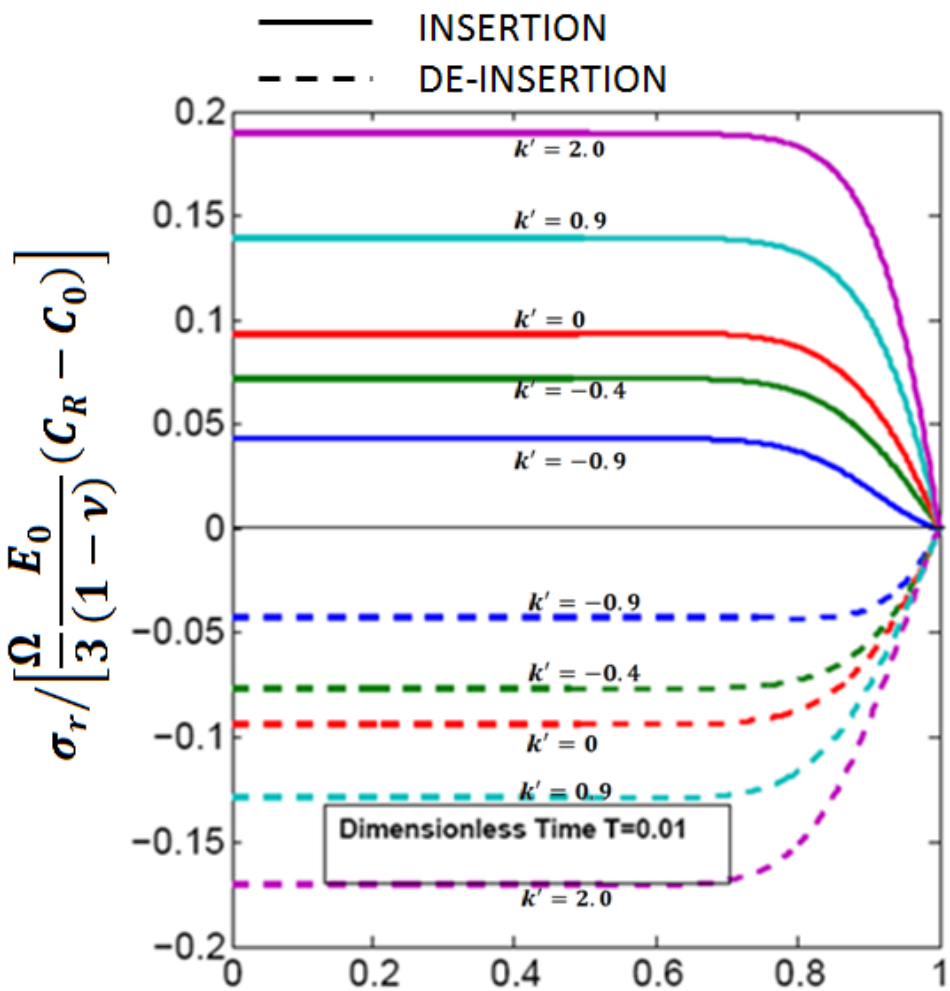

Figure 5.2: Radial stress inside an electrode at different radial locations at time $T = 0.01$ for insertion and de-insertion for different k' values.

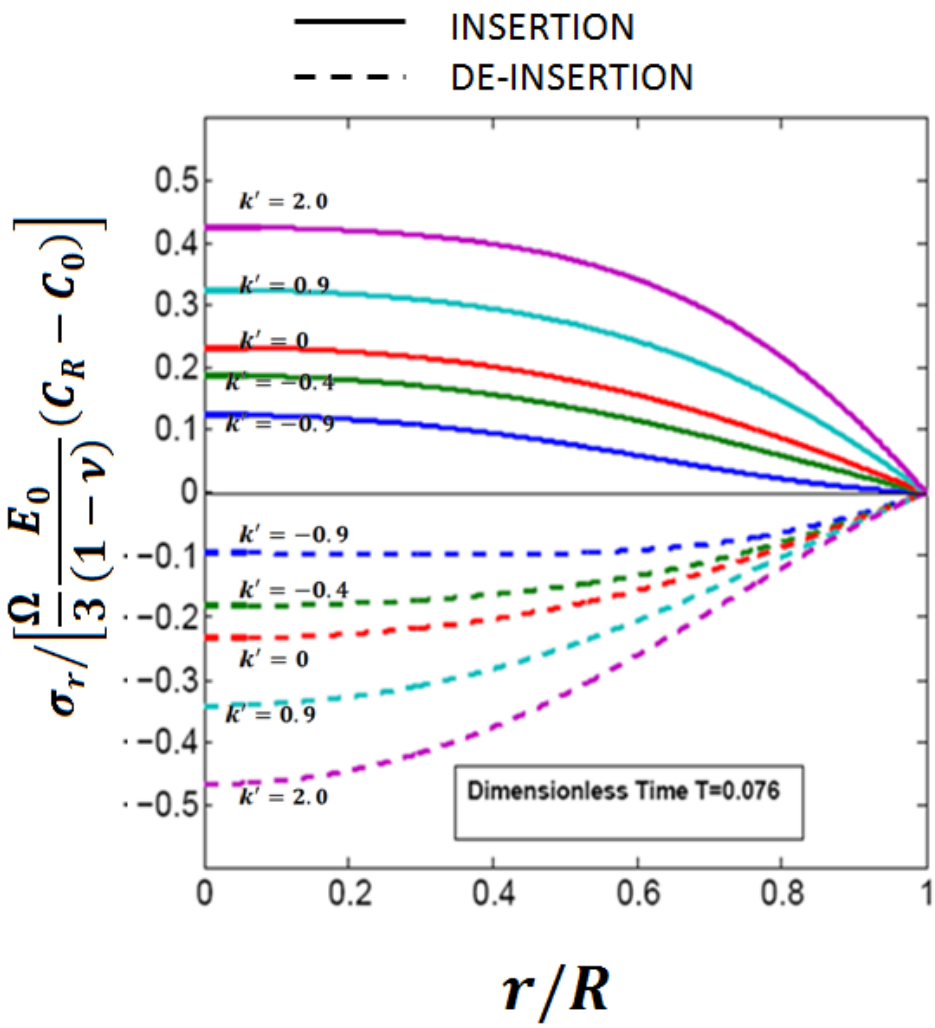

Figure 5.3: Radial stress inside an electrode at different radial locations at time $T = 0.076$ for insertion and de-insertion for different k' values.

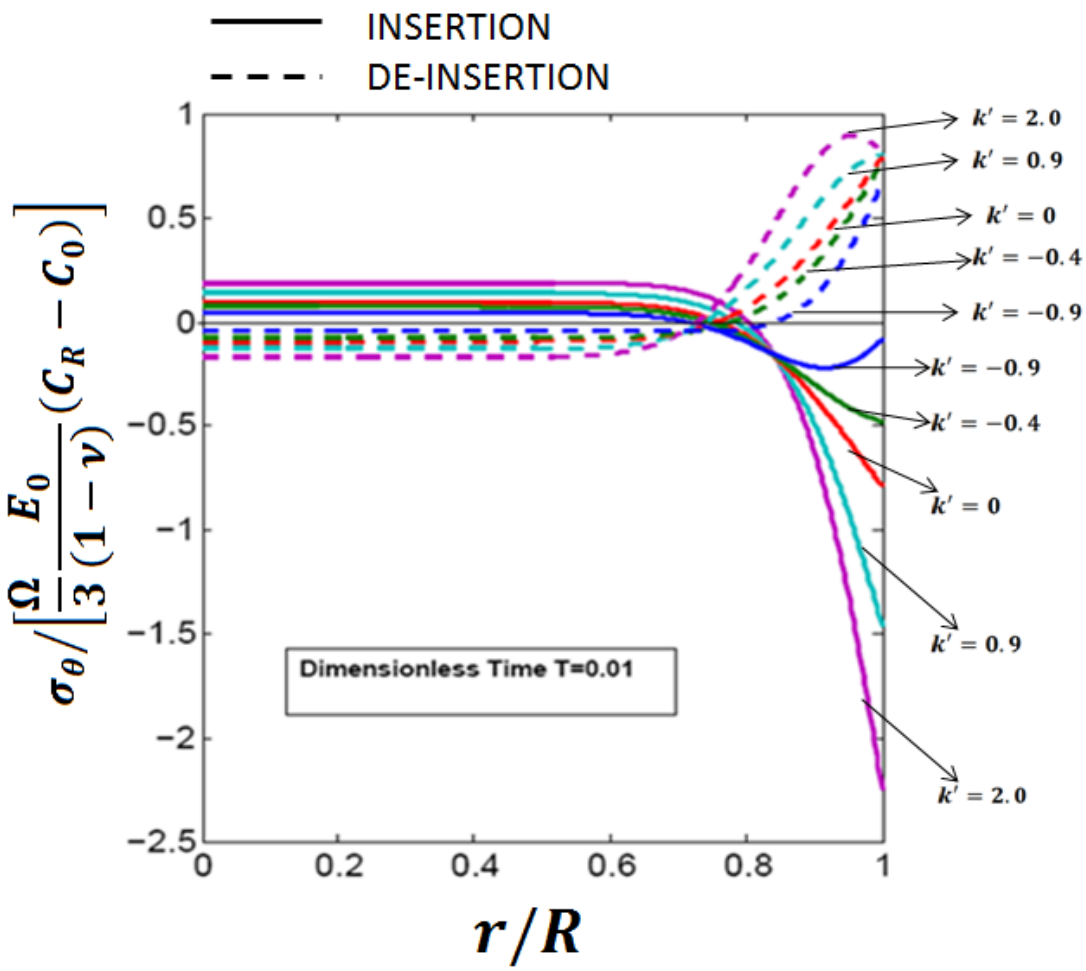

Figure 5.4: Tangential stress inside an electrode at different radial locations at time $T = 0.01$ for insertion and de-insertion for different k' values.

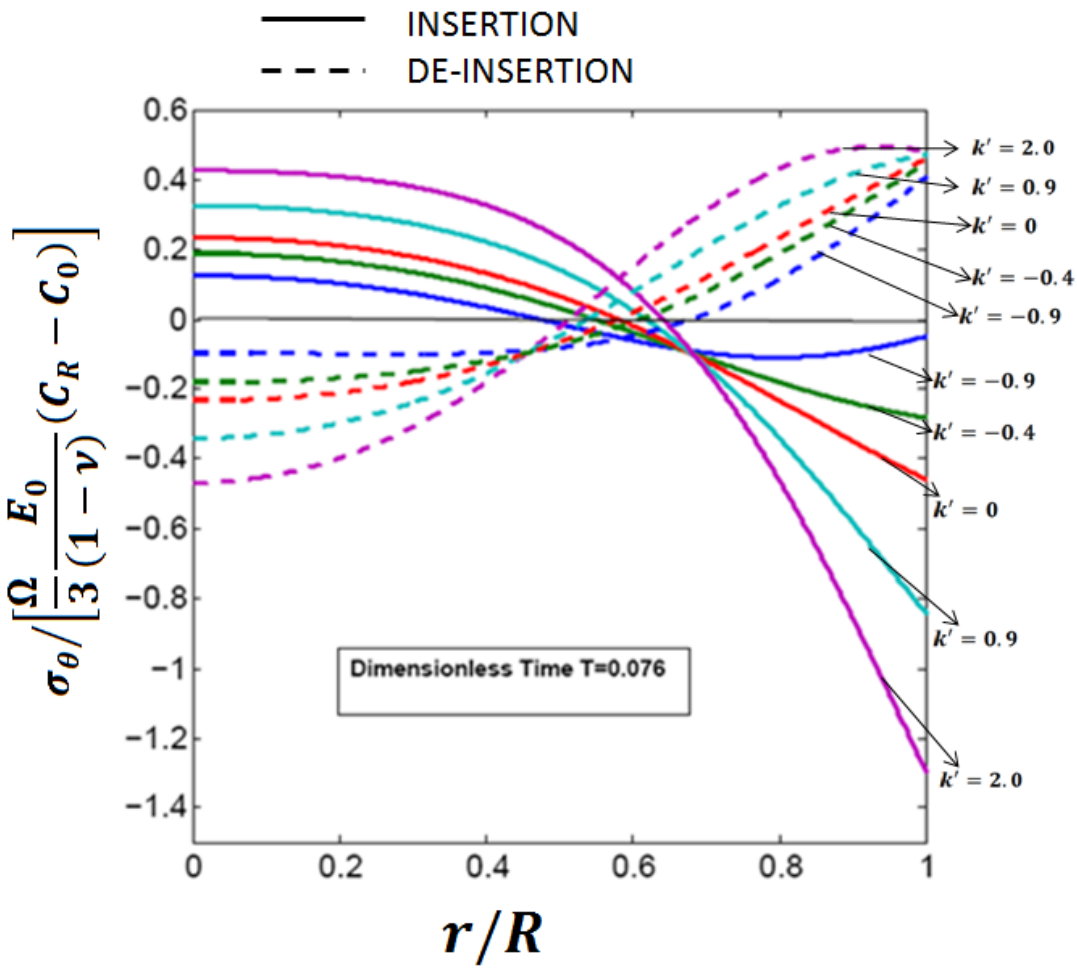

Figure 5.5: Tangential stress inside an electrode at different radial locations at time $T = 0.076$ for insertion and de-insertion for different k' values.

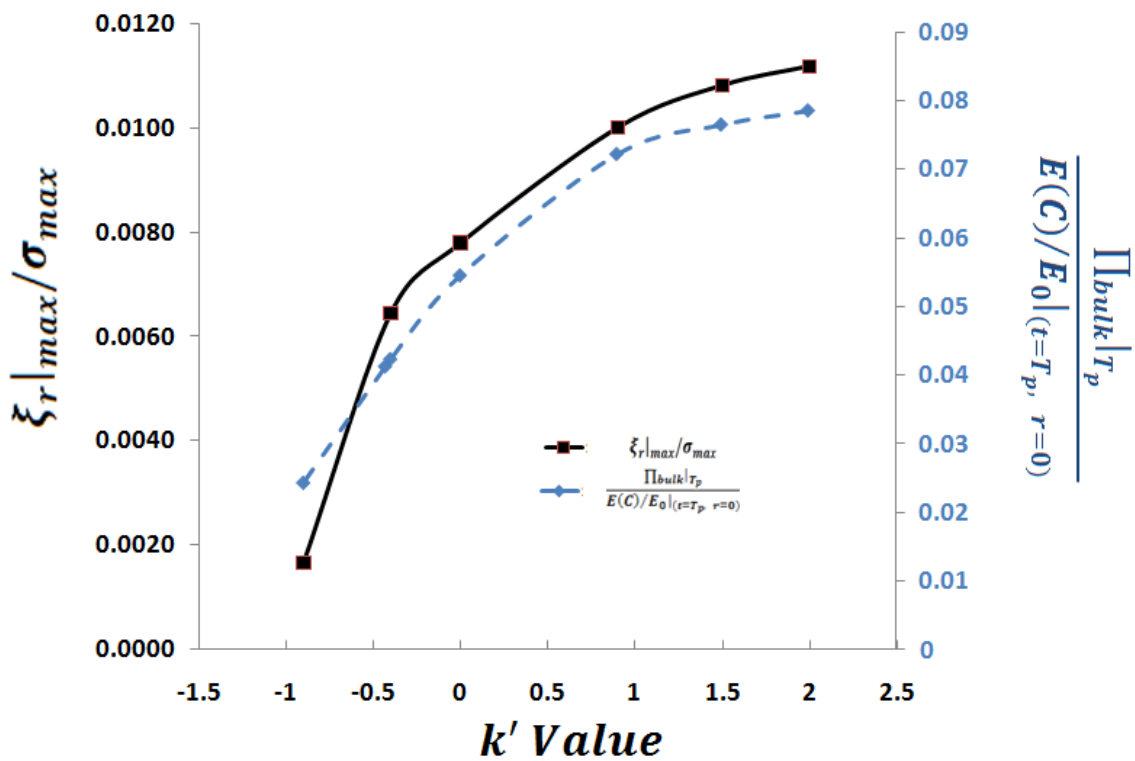

Figure 5.6: Variation of maximum stress normalized with strength, and strain energy normalized with fracture energy with *k'* value

CHAPTER 6

DIFFUSION INDUCED STRESSES AND STRAIN ENERGY IN A PHASE-TRANSFORMING SPHERICAL ELECTRODE PARTICLE

This chapter is based on work published as:

R. Deshpande, Y.-T. Cheng, M. W. Verbrugge, A. Timmons, Diffusion Induces Stresses and Strain Energy in a Phase Transforming Spherical Electrode Particle. *Journal of The Electrochemical Society* **158**, 1 (2011).

It's reproduced by permission of The Electrochemical Society.

6.1 Summary

Lithium insertion and removal in lithium ion battery electrodes can result in diffusion induced stresses (DISs) which may cause fracture and decrepitation of electrodes. Many lithium ion electrode materials undergo formation of two or more phases during lithium insertion or removal. In this chapter, we mathematically investigate the DISs in phase transforming electrodes using a core-shell structural model. We examine the concentration jumps at phase boundaries that result in stress discontinuities, which in turn can cause cracking. The influence of the mechanical properties of the two phases on stress evolution, stress discontinuity, and strain energy are clarified. The trends obtained with the model may be used to help tune electrode materials with appropriate interfacial and bulk properties so as to increase the durability of battery electrodes.

6.2 Introduction

Overcoming the mechanical degradation caused by diffusion induced stresses (DISs) is critical for advancement of lithium ion batteries (LIBs). Recently, several mathematical models have been developed along with experimental investigations to understand DISs in LIB electrodes. Christensen and Newman (*1, 2*), and Zhang *et al*.(*3, 4*) simulated intercalation induced stresses within single particles to capture the salient features of the governing electrochemistry and solid mechanics taking place in LIBs. A substantial body of literature is devoted to the modeling of LIBs using volume-averaged (macro-homogeneous) methods to simultaneously characterize the liquid and solid phase phenomena (*5-12*). García *et al.* (*13*) developed a numerical framework that describes the spatial distribution of electrochemical fields and stress distributions in porous electrode microstructures. Recently, we (*14-17*) have analyzed the effects of battery operating conditions and surface properties of nano-scaled electrodes on the stresses and strain energy. We have also proposed fracture criteria for insertion electrodes(*18*).

Many of these models assume that the electrode particle remains in single phase during lithium insertion and removal. However, it is well-known that lithium insertion often leads to the formation of different phases depending upon electrode materials and the state of charge (*19*). For example, graphite and $LiCoO_2$(*20*) electrodes are known to have distinct phases during lithium insertion. As lithium is inserted into the electrode, solid-solutions, inter-metallic compounds, and amorphous alloys may form so as to reduce the Gibbs free energy of the system. Often, the systems have multiple phases separated by moving phase boundaries during lithium insertion and removal.

For a spherical electrode particle, the diffusion and phase transformation processes have been modeled with the assumption that the two phases are situated in concentric spheres, i.e., a core-shell structure, with a moving boundary at the interface between the two distinct phases (*10*). During lithium insertion, the shell would be a lithium-rich phase and the core would be a lithium-poor phase (*vice-versa* for lithium removal). These shrinking core models are "sharp interface" (*21*) models with an abrupt change (jump) in the concentration at the phase boundary. The shrinking core model further assumes isotropic diffusion. There exist electrode materials, such as lithium-iron-phosphate, that are known to have unidirectional diffusion behavior for which the shrinking core model has been critiqued (*22*). But other electrode materials, such as silicon particles, are fairly isotropic in diffusion and can thus be assumed to follow the shrinking core model, which have been investigated by several authors. Han *et at*. (*23*) modeled the system with phase field model based on the Cahn–Hilliard equation to simulate both diffusion and diffusional phase transformations simultaneously. Several other authors have modeled diffusion inside the particle. In particular, Subramanian and White (*24, 25*) and Jagannathan (*26*) have provided analytic and numerical solutions of the diffusion equation for core-shell models to help understand the kinetics of phase boundary motion. More recently, Renganathan *et al*. (*27*) developed a numerical model with detailed consideration of the effect of phase change on stresses inside a two phase core-shell system. In this chapter, we analytically analyze DISs in the core-shell model of Subramanian and White (*24*). Our analytic treatment yields simple relationships between the stress discontinuity at the interface and various material properties for the two phase core-shell system.

6.3 Core-shell model

We consider an isotropic diffusion system with two phases (α and β) in a core-shell structure with a moving interface (*24*) as illustrated in Figure 6.1. Although the diffusion equation appropriate for the core-shell model has been studied by several authors, analytic solutions of stresses within the core-shell framework have not appeared in the literature. Analytic solutions, if attainable, can help elucidate the effects of sharp jump in the concentration at the interface of the two phases on DISs. In addition, several groups have provided evidence for changes in mechanical properties with phase transformations. Qi *et al*.(*28, 29*) showed that material properties change substantially upon lithium insertion. Deshpande *et al*.(*30*) considered the effects of concentration-dependent elastic properties on DISs in single phase systems.

6.4 Mathematical analysis

6.4.1. Mechanics

The bulk of the particle is assumed to initially be in the β phase. It transform to the α phase as a result of diffusion on delithiation (Figure 6.1). Both the α and β phases are assumed to be isotropic linear elastic solids. The constitutive relationship in the spherical coordinate system, for the radial and tangential components, are (*4, 15, 18*)

$$\varepsilon_r = \frac{1}{E_i}(\sigma_r - 2\nu_i\sigma_\theta) + \frac{1}{3}\Omega_i C$$

$$\varepsilon_\theta = \frac{1}{E_i}\left((1-\nu_i)\sigma_\theta - \nu_i\sigma_r\right) + \frac{1}{3}\Omega_i C \tag{6.1}$$

here, Young's modulus is E_i, Poisson's ratio is ν_i, the partial molar volume of the solute is Ω_i for the respective α and β phases ($i = \alpha$ or β), and the molar concentration is C.

Equation (6.1) is analogous to the constitutive law typically used for modeling thermal stress (*31, 32*) and has been used for modeling DISs (*33*), including stresses in battery electrodes (*4, 15-18*). We further assume that the elastic properties of any of the phases do not vary with the lithium composition variation in it and the influence on elastic properties from the interface between the two phases is negligible.

Because of the spherical symmetry, the radial and tangential strains, in the infinitesimal formulation of deformation, can be expressed as functions of radial displacement u as follows;

$$\varepsilon_r = \frac{du}{dr} \text{ and } \varepsilon_\theta = \frac{u}{r} \tag{6.2}$$

Since atomic diffusion in solids is a much slower process than elastic deformation, mechanical equilibrium is established much faster than that of diffusion. Mechanical equilibrium is, therefore, treated as a static equilibrium problem (*31, 32*). In the absence of any body force, the equation for static mechanical equilibrium in the bulk of a sphere is given by following equation[32] :

$$\frac{d\sigma_r}{dr} + \frac{2(\sigma_r - \sigma_\theta)}{r} = 0. \tag{6.3}$$

The solutions of this differential equation for a sphere $(a \le r \le R)$ for the case of constant E, ν, and Ω, are given by

$$\sigma_r = -\frac{\Omega E}{3(1-\nu)}\frac{2}{r^3}\int_a^r C(r)r^2dr + \left[\frac{EI_1}{(1-2\nu)} - \frac{E}{(1+\nu)}\frac{I_2}{r^3}\right],$$

$$\sigma_\theta = \frac{\Omega E}{3(1-\nu)}\frac{1}{r^3}\int_a^r C(r)r^2dr - \frac{\Omega EC(r)}{3(1-\nu)} + \left[\frac{EI_1}{(1-2\nu)} + \frac{E}{(1+\nu)}\frac{I_2}{r^3}\right].$$

The displacement $u(r)$ is given by

$$u(r) = \left(\frac{1+\nu}{1-\nu}\right)\frac{\Omega}{3r^2}\int_a^r C(r)r^2dr + rI_1 + \frac{I_2}{r^2} \tag{6.4}$$

The parameters, I_1 and I_2, can be obtained from the appropriate boundary conditions for both the α and β phases (see, Equation (6.6) below). For the α phase in the region of $r_i \le r \le R$, we have

$$\sigma_r = -\frac{2E_\alpha}{3(1-\nu_\alpha)}\left(1-\left(\frac{r_i}{r}\right)^3\right)\frac{\Omega_\alpha}{3}C^\alpha_{avg}(r) + \left[\frac{E_\alpha I_{1\alpha}}{(1-2\nu_\alpha)} - \frac{2E_\alpha}{(1+\nu_\alpha)}\frac{I_{2\alpha}}{r^3}\right],$$

$$\sigma_\theta = \frac{E_\alpha}{3(1-\nu_\alpha)}\left(1-\left(\frac{r_i}{r}\right)^3\right)\frac{\Omega_\alpha}{3}C^\alpha_{avg}(r) - \frac{E_\alpha\Omega_\alpha C(r)}{3(1-\nu_\alpha)} + \left[\frac{E_\alpha I_{1\alpha}}{(1-2\nu_\alpha)} + \frac{E_\alpha}{(1+\nu_\alpha)}\frac{I_{2\alpha}}{r^3}\right] \quad . \tag{6.5a}$$

Here, $C^\alpha_{avg}(r) = (3/(r^3 - r_i^3))\int_{r_i}^r C(r')r'^2dr'$ is the average concentration in α phase $(r_i \le r \le R)$

Because stress and displacement are finite at $r = 0$, we have, for the β phase within $0 \le r < r_i$,

$$\sigma_r = -\frac{2E_\beta}{3(1-\nu_\beta)}\frac{\Omega_\beta}{3}C^\beta_{avg}(r) + \frac{E_\beta I_{1\beta}}{(1-2\nu_\beta)},$$

$$\sigma_\theta = \frac{E_\beta}{3(1-\nu_\beta)}\frac{\Omega_\beta}{3}C^\beta_{avg}(r) - \frac{E_\beta\Omega_\beta C(r)}{3(1-\nu_\beta)} + \frac{E_\beta I_{1\beta}}{(1-2\nu_\beta)} \quad . \tag{6.5b}$$

Here $C_{avg}^{\beta}(r) = (3/r^3)\int_0^r C(r')r'^2 dr'$ is the average concentration in β phase $(0 \leq r \leq r_i)$.

Without considering the effects of surface energy and surface stresses, the normal stress at the free surface of the spherical particle is $\sigma_r(R) = 0$. Since, the normal component stresses and displacements are continuous at the interface between the α and β phases, we have

$$\sigma_r(r_i^{\alpha}) = \sigma_r\left(r_i^{\beta}\right) \text{ and } u(r_i^{\alpha}) = u\left(r_i^{\beta}\right). \tag{6.6}$$

Using these conditions, we can solve for the parameters $I_{1\alpha}$, $I_{2\alpha}$ and $I_{1\beta}$

$$I_{2\alpha} = r_i^3 \frac{\frac{2}{3}\left[\frac{(1-2\nu_\beta)E_\alpha}{(1-\nu_\alpha)E_\beta} - \frac{(1-2\nu_\alpha)}{(1-\nu_\alpha)}\right]\left(1-\left(\frac{r_i}{R}\right)^3\right)\frac{\Omega_\alpha}{3}C_{avg}^{\alpha}(R) + {}^{\Omega_\beta}/_{3}C_{avg}^{\beta}(r_i)}{1+2\frac{(1-2\nu_\beta)E_\alpha}{(1+\nu_\alpha)E_\beta}\left(1-\left(\frac{r_i}{R}\right)^3\right)+2\frac{(1-2\nu_\alpha)}{(1+\nu_\alpha)}\left(\frac{r_i}{R}\right)^3},$$

$$I_{1\alpha} = 2\frac{(1-2\nu_\alpha)}{(1+\nu_\alpha)}\frac{I_{2\alpha}}{R^3} + \frac{2(1-2\nu_\alpha)}{3(1-\nu_\alpha)}\left(1-\left(\frac{r_i}{R}\right)^3\right)\frac{\Omega_\alpha}{3}C_{avg}^{\alpha}(R), \tag{6.7}$$

$$I_{1\beta} = -\frac{2E_\alpha(1-2\nu_\beta)}{E_\beta(1+\nu_\alpha)}\left(1-\left(\frac{r_i}{R}\right)^3\right)\frac{I_{2\alpha}}{{r_i}^3} + \frac{2E_\alpha(1-2\nu_\beta)}{3E_\beta(1-\nu_\alpha)}\left(1-\left(\frac{r_i}{R}\right)^3\right)\frac{\Omega_\alpha}{3}C_{avg}^{\alpha}(R) + \frac{2(1-2\nu_\beta)}{3(1-\nu_\beta)}\left(\frac{r_i}{R}\right)^3\frac{\Omega_\beta}{3}C_{avg}^{\beta}(r_i)$$

Motivated by the discontinuities of properties at the interface between the α and β phases, we evaluate the stress jump at the interface in the tangential direction:

$$\Delta\sigma_\theta(r_i) = \sigma_\theta|_{r_i^+} - \sigma_\theta|_{r_i^-} = \left[\frac{E_\beta\Omega_\beta C_\beta(r_i)}{3(1-\nu_\beta)} - \frac{E_\alpha\Omega_\alpha C_\alpha(r_i)}{3(1-\nu_\alpha)}\right] + \left[\frac{E_\alpha I_{1\alpha}}{(1-2\nu_\alpha)} - \frac{E_\beta I_{1\beta}}{(1-2\nu_\beta)} + \frac{E_\alpha}{(1+\nu_\alpha)}\frac{I_{2\alpha}}{r_i^3} - \frac{E_\beta\Omega_\beta C_{avg}^{\beta}(r_i)}{3(1-\nu_\beta)}\right] \quad (6.8)$$

As an example, we calculated the concentration profiles for a specific case of lithium removal using the spherical core-shell model.

6.4.2. Diffusion in spherical core-shell

We assume a spherical particle of radius R in the β phase, with an initial uniform concentration C_β and a constant concentration C_R at the surface (reflecting facile electrochemical kinetics and a porous-electrode system dominated by solute-diffusion resistance (*14*, *15*)).

The concentration in the β phase remains constant, but the interface between the α and β phases, r_i, moves toward the center of the sphere as the β phase is consumed. Diffusion in the α phase is assumed to follow the diffusion equation with a constant diffusion coefficient $\mathcal{D}_\alpha$

$$\frac{\partial C}{\partial t} = \frac{\mathcal{D}_\alpha}{r^2}\left(\frac{\partial}{\partial r}\left(r^2\frac{\partial C}{\partial r}\right)\right), \quad (6.9)$$

with boundary condition

$$C(R,t) = C_R, \quad for\ t \geq 0,$$

$$C(r_i,t) = C_\alpha, \quad for\ t \geq 0, \quad (6.9a)$$

initial condition

$$C(r,t) = C_\beta, \quad at\ 0 \le r \le R \tag{6.9b}$$

and interface condition (*33*)

$$\left(C_\beta - C_\alpha\right)\frac{dr_i}{dt} = D_\alpha \left.\frac{\partial C}{\partial r}\right|_{r=r_i} \tag{6.9c}$$

The Equation set 6.9 can be cast in dimensionless form by using $\hat{C} = C/C_\alpha$, $x = r/R$, $x_i = r_i/R$ and $\tau = D_\alpha t/R^2$. We solve Equation set (6.9) to obtain the solution for concentration as follows (details in Appendix 1).

Of particular interest is when $C_R = 0$, we have

$$\hat{C}(x,\tau) = \frac{x_i}{(1-x_i)x} - \frac{x_i}{(1-x_i)} + \frac{2}{x}\sum_{n=0}^{\infty}\left[(c_0 - 1)\frac{x_i}{n\pi} - c_0\frac{(-1)^n}{n\pi}\right] sin\left(\frac{n\pi}{(1-x_i)}(x - x_i)\right) exp\left(-\left(\frac{n\pi}{(1-x_i)}\right)^2 \tau\right) \tag{6.10}$$

and

$$\left.\frac{d\hat{C}(x,\tau)}{dx}\right|_{r=r_i} = -\frac{1}{x_i(1-x_i)} + \frac{2}{x_i(1-x_i)}\sum_{n=0}^{\infty}[(c_0 - 1)x_i - (-1)^n c_0]\, exp\left(-\left(\frac{n\pi}{(1-x_i)}\right)^2 \tau\right)$$

(6.11)

where $c_0 = \hat{C}(x,0) = \frac{C_\beta}{C_\alpha}$.

Thus, we can locate the interface position using this Equation (6.9c) and Equation (6.11). From the concentration profile and interface position, we can calculate the parameters $I_{2\alpha}, I_{1\alpha}$ and $I_{2\beta}$ using Equation (6.7).

These parameters are used to calculate the radial and tangential stresses using Equation (6.5a) and Equation (6.5b). The tangential stress jump at the interface is obtained using Equation (6.8).

6.5 Results and discussions

In Figure 6.2 we plot the dimensionless concentration at various radial locations and at different dimensionless times. Within the core-shell model, we obtain the lithium ion concentration profile for the two phase system in a spherical electrode particle. We impose a sharp jump in concentration at the interface between the two phases with continuous movement of the interface towards the center. The interface location vs. time is plotted in Figure 6.3.

We define dimensionless stresses as follows;

$$\xi_i = \frac{\sigma_i}{\frac{\Omega_\alpha C_\alpha}{3}\frac{E_\alpha}{(1-\nu_\alpha)}}$$

Here, 'i' represents direction $r, \theta,$ or φ. We plot the dimensionless stresses ξ_i at different radial locations (x) and dimensionless times (τ) for a core-shell, spherical electrode particle in Figures 6.4 & 6.5. We now consider several cases of material parameters. First, we consider that both phases have the same mechanical properties *i.e.*, $E_\beta/E_\alpha = 1$ and $\Omega_\beta/\Omega_\alpha = 1$. This assumption enables us to analyze the effect of a sharp jump in concentration at the interface on the stress profiles.

Figure 6.4 shows the radial stress distribution in the two phase core-shell model. If we compare these results with the previously obtained results for single phase electrodes (Cheng and Verbrugge, Fig 1b and Fig 1c) (*15*), we find that, unlike previous single phase models, the core region of the two phase system has a uniform radial compressive stress. This can be a result of the uniform concentration in the core region. But we note that the magnitude of stress in the core region depends upon the interfacial location and not just the concentration of solute in the core region. The same can be observed for the tangential stresses (Figure 6.5).

We see (Figure 6.4) that, as the interface moves towards the center, the compressive radial stress increases until the β phase vanishes.

In general, the radial stress is always compressive and the tangential stress is tensile in the α phase during lithium removal. Since cracking is caused by tensile stress, the tangential stress plays more important role in surface cracking of the electrode particle. Furthermore, from Figure 6.5 we observe that there is a tangential stress discontinuity at the interface, which can cause crack initiation. More specifically, since the α phase region is under tension and the β phase region is under compression, there is a sharp change in

tangential stresses from compression to tension across the interface. This jump in stress levels may increase the tendency of cracking of the electrode material. In addition, the tangential stress has a maximum tensile value at lithium removal. The magnitude of the radial and tangential stress are the same at the center so that stress at the center is purely hydrostatic in compression. In comparison with the radial and tangential stresses of the single phase model (Cheng and Verbrugge, Figure 1b and Figure 1c) (*15*), we observe that the stress levels at any given time are significantly different in the two phase model even though we assume the same material properties of both the phases.

In Figure 6.6 we plot the maximum tangential stress jump as a function of C_β/C_α, assuming that other material properties of both phases are the same. We observe that as the ratio C_β/C_α increases, the stress jump across the interface increases. As discussed earlier, the increase in stress jump can be detrimental to the electrode and may lead to cracking. In real batteries, the coexistence of phases with large C_β/C_α should therefore be avoided. This may be accomplished by controlling the state of charge to avoid forming multiple phases with high C_β/C_α ratios.

Next, we consider the case when Poisson's ratio of both the phases is the same, i.e., $\nu_\alpha = \nu_\beta = \nu$. Equation (6.8), in dimensionless form, can then be written as

$$\Delta\xi_\theta(x_i) = \left|\xi_\theta|_{x_i^+} - \xi_\theta|_{x_i^-}\right| =$$

$$\bar{E}\bar{\Omega}\hat{C}_\beta(x_i) - 1 - \frac{\bar{E}\bar{\Omega}}{3}(1+2x_i^3)\hat{C}_{avg}^\beta(x_i) + \frac{2\left[\frac{1}{\bar{E}}-1\right]\frac{(1-2\nu)}{(1-\nu)}(1-x_i^3)\hat{C}_{avg}^\alpha(R)+3\bar{\Omega}\hat{C}_{avg}^\beta(x_i)}{\frac{2(1-2\nu)}{\bar{E}(1-\nu)}(1-x_i^3)+\frac{2(1-2\nu)}{(1-\nu)}x_i^3+\frac{(1+\nu)}{(1-\nu)}}, \qquad (6.12)$$

where $\bar{E} = E_\beta/E_\alpha$ and $\bar{\Omega} = \Omega_\beta/\Omega_\alpha$. We find that the maximum stress jump during lithium removal at the surface is obtained at the start of lithium removal. If we assume, $\bar{E} = 1$, the stress jump at the start of lithium removal is

$$\Delta\xi_\theta(x_i)|_{r_i\to R,\ \tau\to 0} = \left|\xi_\theta|_{x_i^+} - \xi_\theta|_{x_i^-}\right|_{max} \sim \left|\bar{\Omega}\hat{C}_\beta(x_i) - 1\right|. \tag{6.12a}$$

If $\bar{\Omega} = 1$, the maximum stress jump can be related to the concentration jump at the interface as follows

$$\Delta\xi_\theta(x_i)|_{r_i\to R,\ \tau\to 0} = \left|\xi_\theta|_{x_i^+} - \xi_\theta|_{x_i^-}\right|_{max} \sim \left|\hat{C}_\beta(x_i) - 1\right|. \tag{6.12b}$$

We observe that material properties such as the volume expansion coefficient and Young's modulus have a significant effect on stress behavior, as well as on the magnitude of stress discontinuity at the interface. We plot in Figure 6.7 the magnitude of maximum stress discontinuity as a function of the relative expansion coefficient $\Omega_\beta/\Omega_\alpha$ for different values of the relative Young's modulus E_β/E_α of the two phases. The ratio $C_\beta/C_\alpha = 2$ is held constant to observe the effects of $\Omega_\beta/\Omega_\alpha$ and E_β/E_α on the magnitude of the stress discontinuity.

We observe that for $C_\beta/C_\alpha = 2$, even if the two phases have the same partial molar volumes $\left(\Omega_\beta/\Omega_\alpha = 1\right)$, there can be a stress discontinuity at the interface, depending on the values of E_β/E_α. We observe that, for $\Omega_\beta/\Omega_\alpha > 1$, the stress discontinuity increases continuously with an increasing ratio of E_β/E_α. In contrast, if $\Omega_\beta/\Omega_\alpha \ll 1$ the stress discontinuity may increase or decrease with an increase in E_β/E_α. If $E_\beta/E_\alpha = 1$, there is no stress discontinuity at the interface when $\Omega_\beta C_\beta/\Omega_\alpha C_\alpha = 1$. This is in agreement

with Equation (12a). For other values of E_β/E_α, the minimum stress discontinuity is located near the value $\Omega_\beta/\Omega_\alpha$ such that $\Omega_\beta C_\beta/\Omega_\alpha C_\alpha = 1$, because $\Omega_\beta C_\beta/\Omega_\alpha C_\alpha = 1$ implies that both phases have the same expansion tendency. Thus, the minimum stress jump is around $\Omega_\beta/\Omega_\alpha = 0.5$ for $C_\beta/C_\alpha = 2$ (see, Figure 6.7).

6.6 Strain energy calculations

We calculate the bulk strain energy per unit volume, or the bulk strain energy density, $e(r)$, accumulated as a result of the elastic deformation for the isotropically deformed sphere as(*32*)

$$e(r) = \frac{1}{2E}\left(\sigma_r^2 + 2\sigma_\theta^2\right) - \frac{\nu}{E}\left(2\sigma_r\sigma_\theta + \sigma_\theta^2\right) . \tag{6.13}$$

The total bulk strain energy can be obtained by integrating the strain energy density over the entire volume. In the core-shell model, the total bulk energy is the sum of strain energies in both phases. The bulk strain energy of such an electrode particle in dimensionless form is

$$\Pi_{bulk} = \frac{W_{bulk}}{2\pi R^3 E_\alpha\left(\frac{\Omega_\alpha \quad C_\alpha}{3\ (1-\nu_\alpha)}\right)^2} = \int_0^{\left(r_i/R\right)} \frac{E_\alpha}{E_\beta}\left[\left(\xi_r^2 + 2\xi_\theta^2\right) - 2\nu_\beta\xi_\theta(2\xi_r + \xi_\theta)\right]x^2dx \ +$$

$$\int_{\left(r_i/R\right)}^{1}\left[\left(\xi_r^2 + 2\xi_\theta^2\right) - 2\nu_\alpha\xi_\theta(2\xi_r + \xi_\theta)\right]x^2dx \tag{6.14}$$

From the plot (Figure 6.8) of dimensionless strain energy versus time, we observe that the strain energy increases initially, reaches a peak value, and then decreases. The strain energy stored is transferred to surface energy during fracture; hence, strain energy can

drive crack propagation. We now analyze peak strain energy as a function of various parameters. The strain energy depends on the relative magnitude of material properties of the two phases. From Figure 8, we observe that, for a given value of E_β/E_α and C_β/C_α, the magnitude of the peak strain energy increases with increase in $\Omega_\beta/\Omega_\alpha$. We plot the maximum strain energy as a function of E_β/E_α for different C_β/C_α values (Figure 6.9) for a given value of $\Omega_\beta/\Omega_\alpha$. From Figure 6.9, we observe that strain energy increases with increase in C_β/C_α. For a given value of $\Omega_\beta/\Omega_\alpha$, the peak strain energy increases, reaches a maximum and then decreases slightly with increasing E_β/E_α, as shown in Figure 6.9. From Figure 6.5, we observe that the maximum tensile stress is reached at the surface at the start of lithium removal. At this moment, the stress discontinuity reaches a maximum. We analytically calculate the strain energy at the surface at the start of lithium removal

$$\frac{1}{\left[E_\alpha\left(\frac{\Omega_\alpha}{3}\frac{C_\alpha}{(1-\nu_\alpha)}\right)^2\right]} e(r)\Bigg|_{t\to 0, r\to R} = 2(1-\nu_\alpha)\xi_\theta^2 \;=\; 2(1-\nu_\alpha)\left(\bar{\Omega}\hat{C}_\beta(r_i)-1\right)^2 \;. \qquad (6.15)$$

This local strain energy density is responsible for crack initiation and propagation at the surface at the start of lithium removal. Thus, we find that the strain energy at the surface has a dependence on the Poisson's ratio of the α phase, as well as the ratio expansion tendencies of the two phases $\left(\bar{\Omega}\hat{C}_\beta = \Omega_\beta C_\beta/\Omega_\alpha C_\alpha\right)$.

For evaluating the magnitude of stresses and strain energy density, we consider an electrode particle of radius 1 micro-meter. We use the material properties of a similar order of magnitude as that used by Cheng and Verbrugge(*15*) for representative lithium ion electrode materials. The material properties of α phase are assumed to be $E_\alpha =$

$10GPa,\ \nu_\alpha = 0.3$ and $(\Omega_\alpha/3)C_\alpha = 0.08$. We assume the properties of β phase to be $E_\beta = 10GPa,\ \nu_\beta = 0.3$ and $(\Omega_\beta/3)C_\beta = 0.16$. This gives $\bar{\Omega}\hat{C}_\beta(r_i) = 2$. With these values and values from Figure 6.3, the tangential stress at the surface at dimensionless time $\tau = 0.001$ can be found to be $\xi_\theta = 1.9$ which corresponds to $0.724GPa$. Using the analysis from Deshpande *et al.*(*30*), we can approximate the theoretical strength of the material as $0.3E\ or\ 3GPa$. We find that the stress level is the same order of magnitude as the theoretical strength of the material.

Similarly, from Figure 6.9, the magnitude of dimensionless strain energy is found to be 0.3. Thus the total strain energy (W_{bulk}), calculated from Equation (6.14), is found to be $1.822 \cdot 10^{-10}J$. If we assume that the surface energy of the material is about $\gamma_{surface} = 5\,J\,m^{-2}$, the fracture energy to cut the particle into two pieces through the center, would be $E_{fracture} = 2\pi R^2\gamma_{surface} = 3.14 \cdot 10^{-11}J$. Thus, we find that the peak strain energy has a similar order of magnitude as the fracture energy.

This approximate analysis shows that both the stresses and the strain energy can be high enough to cause electrode fracture.

6.7 Summery and conclusions

The extraction of lithium from an electrode particle in the context of a core-shell geometry is modeled, yielding the solute (guest) concentration profile inside an electrode particle as well as stress distribution throughout the two phase particle.

At the interface between the two phases, α and β, the stress discontinuity is observed to depend upon the ratio of the equilibrium concentrations on the two phases: the larger the

equilibrium ratio C_β/C_α, the greater is the stress discontinuity. A phase transformation involving a large change in concentration should therefore be avoided by optimizing the operating condition to minimize electrode degradation. Furthermore, the maximum stress discontinuity occurs at the particle surface when the lithium removal process initiates (e.g., at the start of discharge for a graphitic negative electrode), suggesting surface as the fracture initiation sites.

The interfacial stress discontinuity also depends upon material properties of the two phases. For any ratio of moduli E_β/E_α, there is a value of the partial molar volume ratio $\Omega_\beta/\Omega_\alpha$ at which the stress discontinuity is a minimum. The minimum stress discontinuity occurs when $\Omega_\beta C_\beta/\Omega_\alpha C_\alpha = 1$; i.e., the expansion tendency of both phases is the same.

Alloying the electrode material with another inactive material may change mechanical properties of both the phases, such as the E_β/E_α value. Similarly, alloying may also change the partial molar values of solute in both the phases, i.e., the ratio $\Omega_\beta/\Omega_\alpha$. The systematic trends obtained from the two phase core-shell model suggest that by reducing E_β/E_α and also modifying the $\Omega_\beta/\Omega_\alpha$ in such a way that $\Omega_\beta C_\beta/\Omega_\alpha C_\alpha = 1$ would minimize stresses at interfaces.

As the lithium removal proceeds, strain energy stored within the particle, which can be released to drive crack propagation, increases initially, reaches a peak value, and then decreases gradually. We find that the local strain energy density depends upon the difference in expansion tendencies of the two phases and the local strain energy density scales with $\left(\Omega_\beta C_\beta - \Omega_\alpha C_\alpha\right)^2$.

$$\frac{\partial C}{\partial t} = \frac{\mathcal{D}_\alpha}{r^2}\left(\frac{\partial^2}{\partial r}\left(r^2\frac{\partial C}{\partial r}\right)\right),$$

(9)

with boundary condition

$$\hat{C}(1,\tau) = \frac{C_R}{C_\alpha} = c_1, \quad for\ t \geq 0,$$

$$\hat{C}(x_i,\tau) = 1, \quad for\ t \geq 0,$$

(9a)

initial condition

$$\hat{C}(x,0) = \frac{C_\beta}{C_\alpha} = c_0, \quad at\ 0 \leq r \leq R$$

(9b)

and interface condition[33]

$$\frac{dx_i}{dt} = k\left.\frac{\partial \hat{C}}{\partial x}\right|_{x=x_i}$$

(9c)

where $= \frac{1}{c_0 - 1}$.

The solution to the above partial-differential equation corresponds to[24]

$$\hat{C}(x,\tau) = -\frac{A}{x} + B + \frac{2}{x}\sum_{n=0}^{\infty} B_n \sin\left(\frac{n\pi}{1-x_i}(x-x_i)\right)\exp\left(-\left(\frac{n\pi}{1-x_i}\right)^2\tau\right)$$

(26)

where $A = \dfrac{1-c_1}{1-\dfrac{1}{x_i}}$, $B = \dfrac{1-c_1\dfrac{1}{x_i}}{1-\dfrac{1}{x_i}}$, and $B_n = (c_0-1)\dfrac{x_i}{n\pi} - (c_0-c_1)\dfrac{(-1)^n}{n\pi}$.

Of particular interest is when $c_1 = 0$ (i.e., $C_R = 0$).

Then $A = B = \dfrac{1}{1-\dfrac{1}{x_i}} = -\dfrac{x_i}{1-x_i}$ and $B_n = (c_0-1)\dfrac{x_i}{n\pi} - c_0\dfrac{(-1)^n}{n\pi}$.

We then have

$$\hat{C}(x,\tau)=\frac{x_i}{(1-x_i)x}-\frac{x_i}{1-x_i}+\frac{2}{x}\sum_{n=0}^{\infty}\left((c_0-1)\frac{x_i}{n\pi}-(c_0)\frac{(-1)^n}{n\pi}\right)\sin\left(\frac{n\pi}{1-x_i}(x-x_i)\right)\exp\left(-\left(\frac{n\pi}{1-x_i}\right)^2\tau\right) \tag{27}$$

and

$$\left.\frac{\partial\hat{C}}{\partial x}\right|_{x=x_i}=-\frac{1}{x_i(1-x_i)}+\frac{2}{x_i(1-x_i)}\sum_{n=0}^{\infty}\left((c_0-1)x_i-(-1)^n c_0\right)\exp\left(-\left(\frac{n\pi}{1-x_i}\right)^2\tau\right). \tag{28}$$

6.8 List of symbols

r, θ, φ	spherical coordinates
Ω_i	partial molar volume of the solute in phase 'i' ($m^3\ mol^{-1}$)
R	radius of the spherical electrode particle (m)
r_i	radial location of interface form the center of particle (m)
ν_i	Poisson's ratio of phase 'i'
E_i	Young's modulus of phase 'i' ($N\ m^{-2}$)
u	radial displacement (m)
σ_r	radial stress ($N\ m^{-2}$)
σ_θ	tangential stress ($N\ m^{-2}$)
σ	mean stress ($N\ m^{-2}$)

σ_{shear}	shear stress $(N\ m^{-2})$
ε_r	radial strain
ε_θ	tangential strain
$C(r,t)$	solute concentration at radius r at time t $(mol\ m^{-3})$
C_α	equilibrium concentration of solute in α phase $(mol\ m^{-3})$
C_β	equilibrium concentration of solute in β phase $(mol\ m^{-3})$
D_α	diffusion coefficient of the solute in α phase $(m^2\ sec^{-1})$
t	Time
x	dimensionless radius
x_i	dimensionless radial location of interface
τ	dimensionless time
$\hat{C}$	dimensionless concentration
ξ_r	dimensionless radial stress
ξ_θ	dimensionless tangential stress
$\Delta\xi_\theta(r_i)$	dimensionless tangential stress jump at the interface
e(r)	local strain energy density $(J\ m^{-3})$

W_{bulk}	total strain energy stored due to bulk deformation (J)
$\prod_{bulk}$	dimensionless bulk strain energy
$\prod_{bulk}\|_{max}$	maximum strain energy stored
$\gamma_{surface}$	surface energy $(J\ m^{-3})$
$E_{fracture}$	fracture energy $(J\ m^{-2})$

6.9 References

1. J. Christensen, J. Newman, A Mathematical Model of Stress Generation and Fracture in Lithium Manganese Oxide. *Journal of The Electrochemical Society* 153, A1019 (2006).

2. J. Christensen, J. Newman, Stress generation and fracture in lithium insertion materials. *Journal of Solid State Electrochemistry* 10, 293 (2006).

3. X. Zhang, A. M. Sastry, W. Shyy, Intercalation-Induced Stress and Heat Generation within Single Lithium-Ion Battery Cathode Particles. *Journal of The Electrochemical Society* 155, A542 (2008).

4. X. Zhang, W. Shyy, A. M. Sastry, Numerical Simulation of Intercalation-Induced Stress in Li-Ion Battery Electrode Particles. *Journal of The Electrochemical Society* 154, A910 (2007).

5. M. Doyle, T. F. Fuller, J. Newman, Modeling of Galvanostatic Charge and Discharge of the Lithium/Polymer/Insertion Cell. *Journal of The Electrochemical Society* 140, 1526 (1993).

6. T. F. Fuller, M. Doyle, J. Newman, Simulation and Optimization of the Dual Lithium Ion Insertion Cell. *Journal of The Electrochemical Society* 141, 1 (1994).

7. M. Doyle, J. Newman, A. S. Gozdz, C. N. Schmutz, J.-M. Tarascon, Comparison of Modeling Predictions with Experimental Data from Plastic Lithium Ion Cells. *Journal of The Electrochemical Society* 143, 1890 (1996).

8. R. Darling, J. Newman, Modeling a Porous Intercalation Electrode with Two Characteristic Particle Sizes. *Journal of The Electrochemical Society* 144, 4201 (1997).

9. D. R. Baker, M. W. Verbrugge, Temperature and Current Distribution in Thin-Film Batteries. *Journal of The Electrochemical Society* 146, 2413 (1999).

10. V. Srinivasan, J. Newman, Discharge Model for the Lithium Iron-Phosphate Electrode. *Journal of The Electrochemical Society* 151, A1517 (2004).

11. S. Devan, V. R. Subramanian, R. E. White, Analytical Solution for the Impedance of a Porous Electrode. *Journal of The Electrochemical Society* 151, A905 (2004).

12. D. Dees, E. Gunen, D. Abraham, A. Jansen, J. Prakash, Electrochemical Modeling of Lithium-Ion Positive Electrodes during Hybrid Pulse Power Characterization Tests. *Journal of The Electrochemical Society* 155, A603 (2008).

13. R. E. Garcia, Y.-M. Chiang, W. C. Carter, P. Limthongkul, C. M. Bishop, Microstructural Modeling and Design of Rechargeable Lithium-Ion Batteries. *Journal of The Electrochemical Society* 152, A255 (2005).

14. Y.-T. Cheng, M. W. Verbrugge, Evolution of stress within a spherical insertion electrode particle under potentiostatic and galvanostatic operation. *Journal of Power Sources* 190, 453 (2009).

15. Y.-T. Cheng, M. W. Verbrugge, The influence of surface mechanics on diffusion induced stresses within spherical nanoparticles. *Journal of Applied Physics* 104, 083521 (2008).

16. M. W. Verbrugge, Y.-T. Cheng, Stress and Strain-Energy Distributions within Diffusion-Controlled Insertion-Electrode Particles Subjected to Periodic Potential Excitations. *Journal of The Electrochemical Society* 156, A927 (2009).

17. R. Deshpande, Y.-T. Cheng, M. W. Verbrugge, Modeling diffusion-induced stress in nanowire electrode structures. *Journal of Power Sources* 195, 5081 (2010).

18. Y.-T. Cheng, M. W. Verbrugge, Application of Hasselman's Crack Propagation Model to Insertion Electrodes. *Electrochemical and Solid-State Letters* 13, A128 (2010).

19. C. K. Chan, R. Ruffo, S. S. Hong, R. A. Huggins, Y. Cui, Structural and electrochemical study of the reaction of lithium with silicon nanowires. *Journal of Power Sources* 189, 34 (2009).

20. Q. Zhang, R. E. White, Moving Boundary Model for the Discharge of a LiCoO[sub 2] Electrode. *Journal of The Electrochemical Society* 154, A587 (2007).

21. D. M. Anderson, G. B. McFadden, A. A. Wheeler, A phase-field model with convection: sharp-interface asymptotics. *Physica D: Nonlinear Phenomena* 151, 305 (2001).

22. L. Laffont *et al.*, Study of the LiFePO4/FePO4 Two-Phase System by High-Resolution Electron Energy Loss Spectroscopy. *Chem. Mater.* 18, 5520 (2006).

23. B. C. Han, A. Van der Ven, D. Morgan, G. Ceder, Electrochemical modeling of intercalation processes with phase field models. *Electrochimica Acta* 49, 4691 (2004).

24. V. R. Subramanian, H. J. Ploehn, R. E. White, Shrinking Core Model for the Discharge of a Metal Hydride Electrode. *Journal of The Electrochemical Society* 147, 2868 (2000).

25. V. R. Subramanian, R. E. White, New separation of variables method for composite electrodes with galvanostatic boundary conditions. *Journal of Power Sources* 96, 385 (2001).

26. K. Jagannathan, Approximate Solution Methods for Solid-State Diffusion in Phase-Change Electrodes. *Journal of The Electrochemical Society* 156, A1028 (2009).

27. S. Renganathan, G. Sikha, S. Santhanagopalan, R. E. White, Theoretical Analysis of Stresses in a Lithium Ion Cell. *Journal of The Electrochemical Society* 157, A155 (2010).

28. Y. Qi, H. Guo, L. G. Hector, A. Timmons, *Journal of The Electrochemical Society*, (2010).

29. Y. Qi, V. Shenoy, P. Johari, *Journal of Power Sources*, (2010).

30. R. Deshpande, Y. Qi, Y.-T. Cheng, Effects of Concentration-Dependent Elastic Modulus on Diffusion-Induced Stresses for Battery Applications. *Journal of The Electrochemical Society* 157, A967 (2010).

31. R. Hetnarski, R. Eslami, *Thermal Stresses -- Advanced Theory and Applications (Solid Mechanics and Its Applications)*. (Springer, 2008).

32. S. Timoshenko, J. N. Goodier, *Theory of elasticity, by S. Timoshenko and J.N. Goodier*. (New York, McGraw-Hill, 1951).

33. J. Crank, *The Mathematics of Diffusion*. (Oxford University Press, USA, 1980).

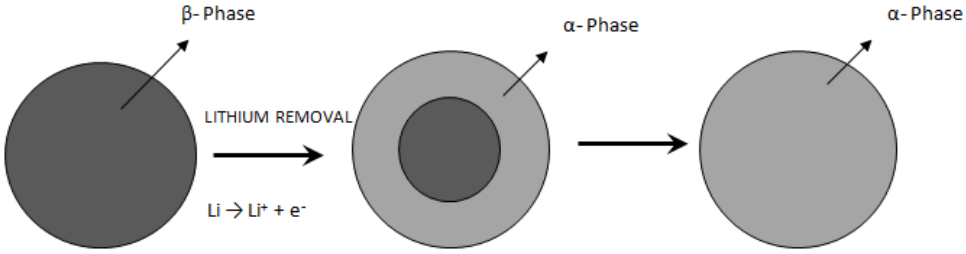

Figure 6.1: A cartoon diagram indicating that, initially, before lithium removal the electrode is completely β Phase (a), which convert to a two phase system with β core and α shell (b), and finally the whole particle is α phase (c).

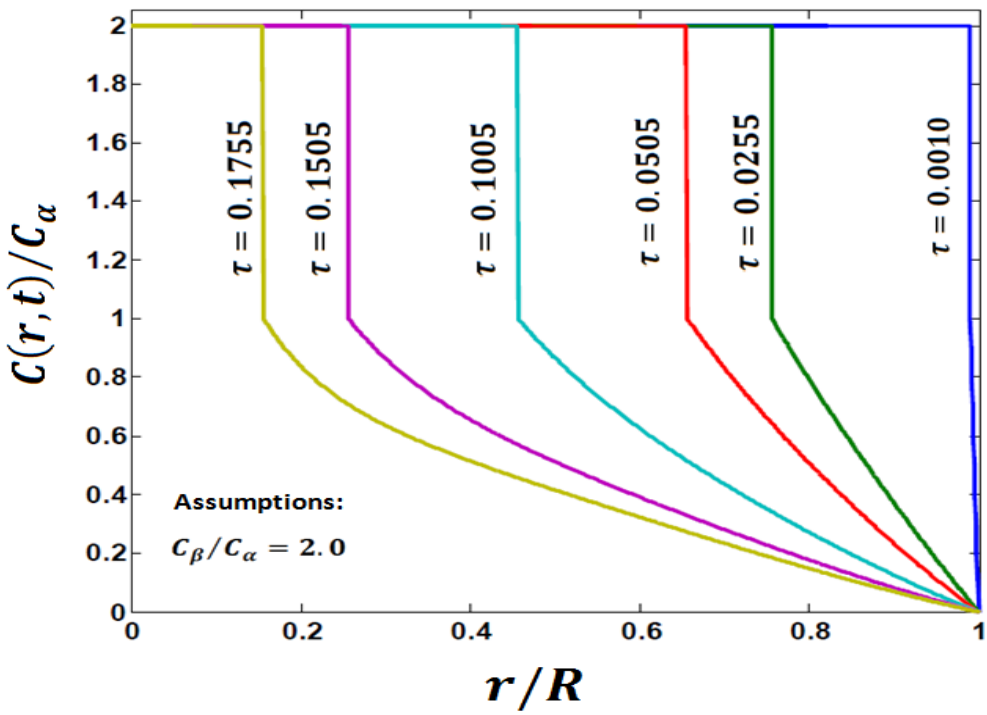

Figure 6.2: A plot of the lithium ion concentration inside an electrode particle at different radial locations and times for during lithium removal $\left(C_\beta/C_\alpha = 2\right)$. At the interface there is sharp jump in concentration. Here the magnitude of the jump in concentration is decided by the ratio of C_β/C_α between the two phases.

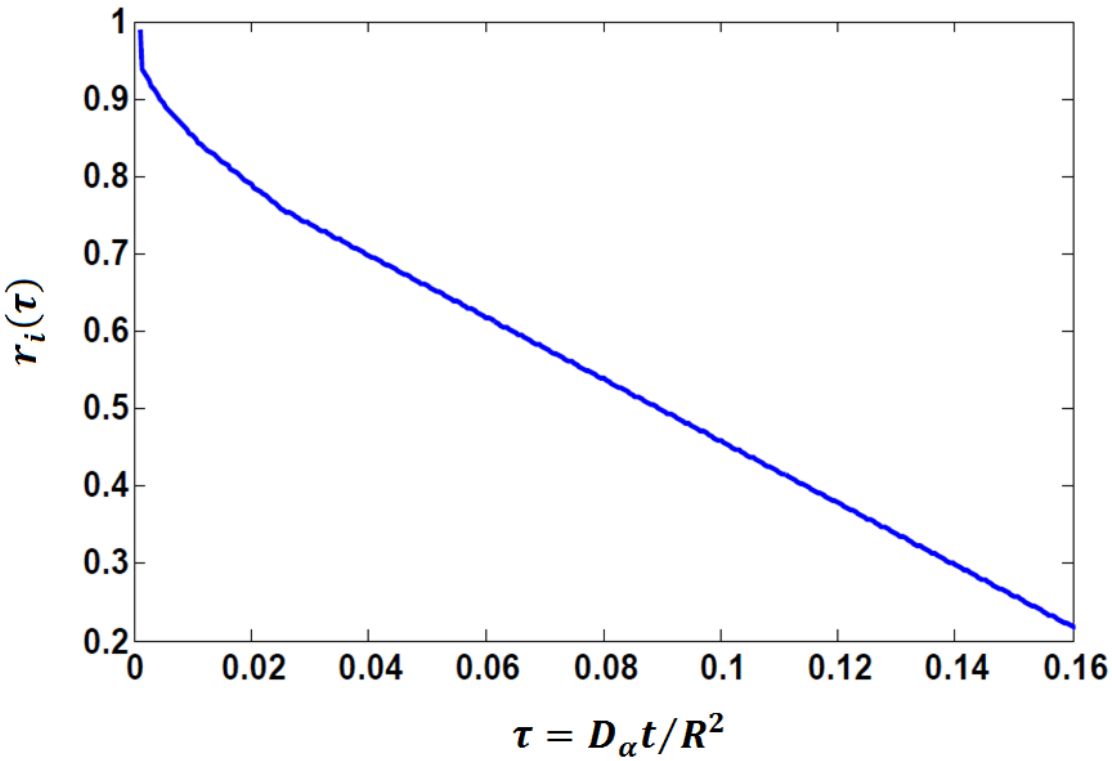

Figure 6.3: A plot of the interface location along the radius at different times $\left(C_\beta/C_\alpha = 2 \right)$. As the lithium removal proceeds, β phase transforms into α phase, and the interface moves towards the particle center. After a certain period of lithium removal, β phase completely diminishes and the particle becomes a single phase particle.

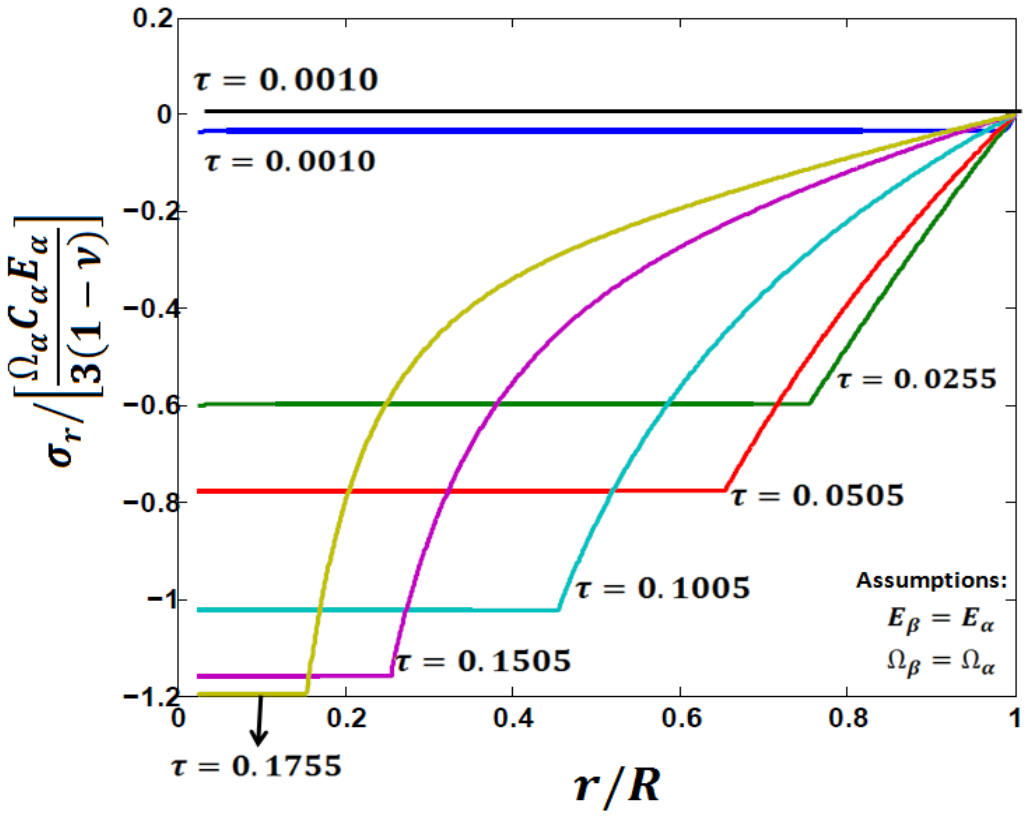

Figure 6.4: A plot of the radial stress inside an electrode particle at different radial locations at different times.

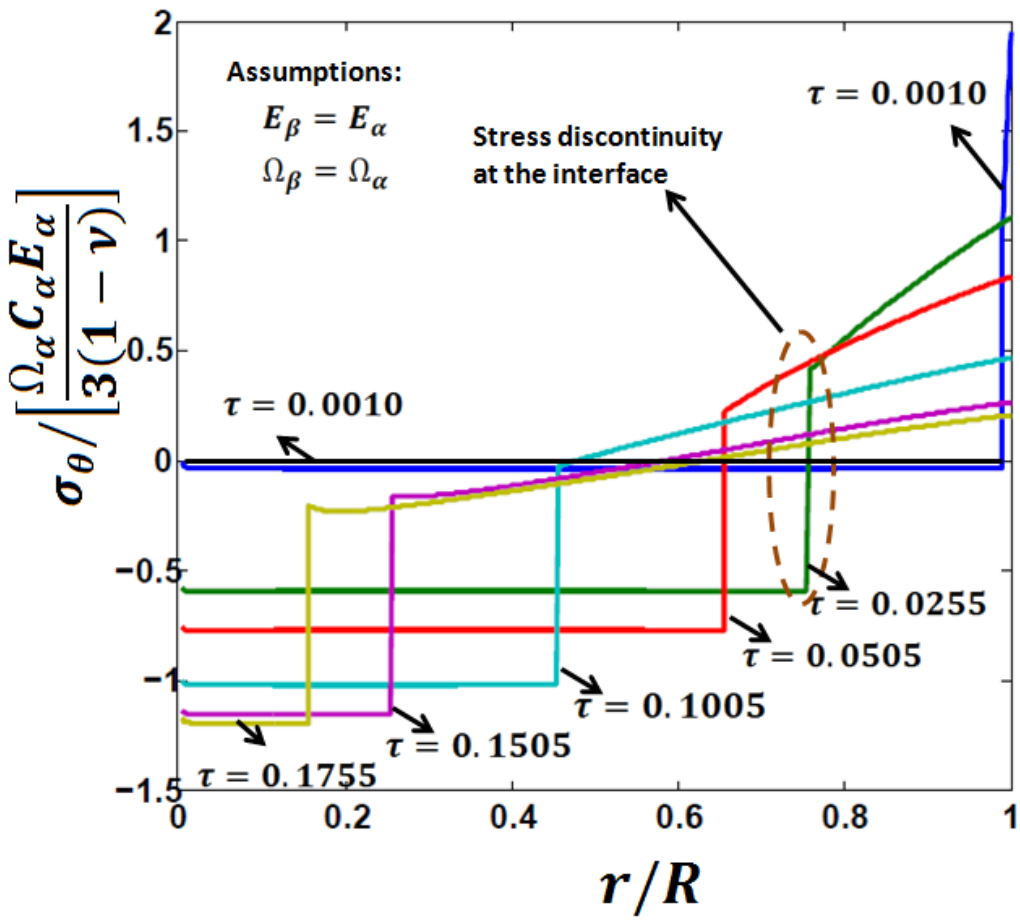

Figure 6.5: A plot of the tangential stress inside an electrode particle at radial locations and times.

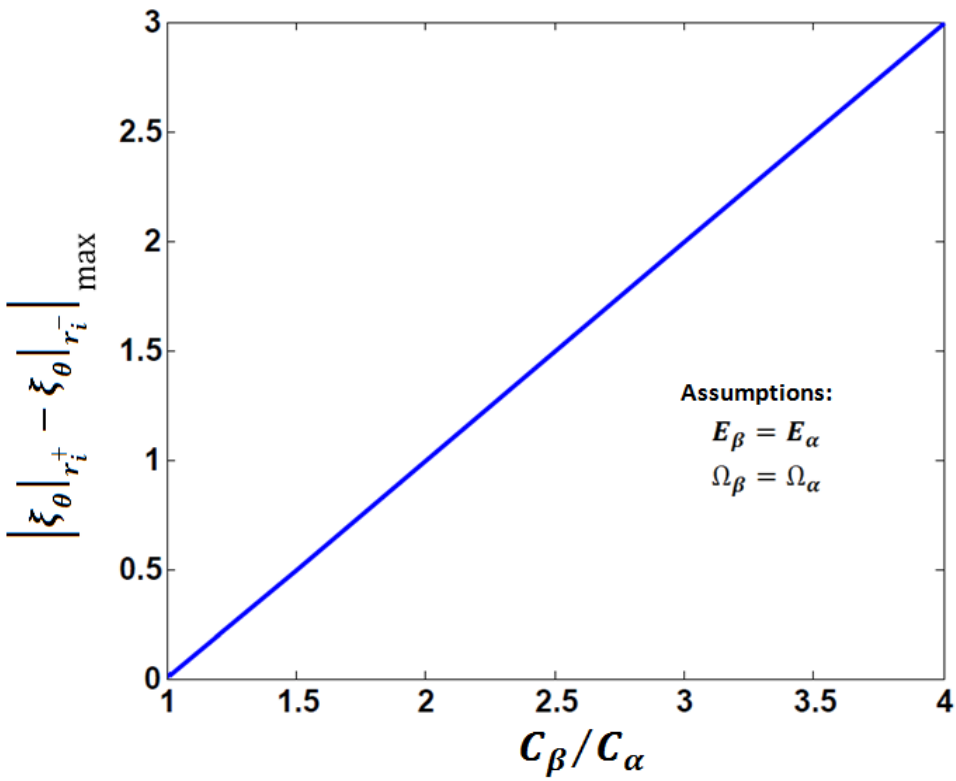

Figure 6.6: A plot of the maximum stress jump (tangential) at the interface as a function of C_β / C_α assuming the same material properties for both phases. If the material properties such as partial molar volume and Young's modulus of both phases are the same, as $C_\beta / C_\alpha \to 1$, then stress discontinuity at the interface vanishes.

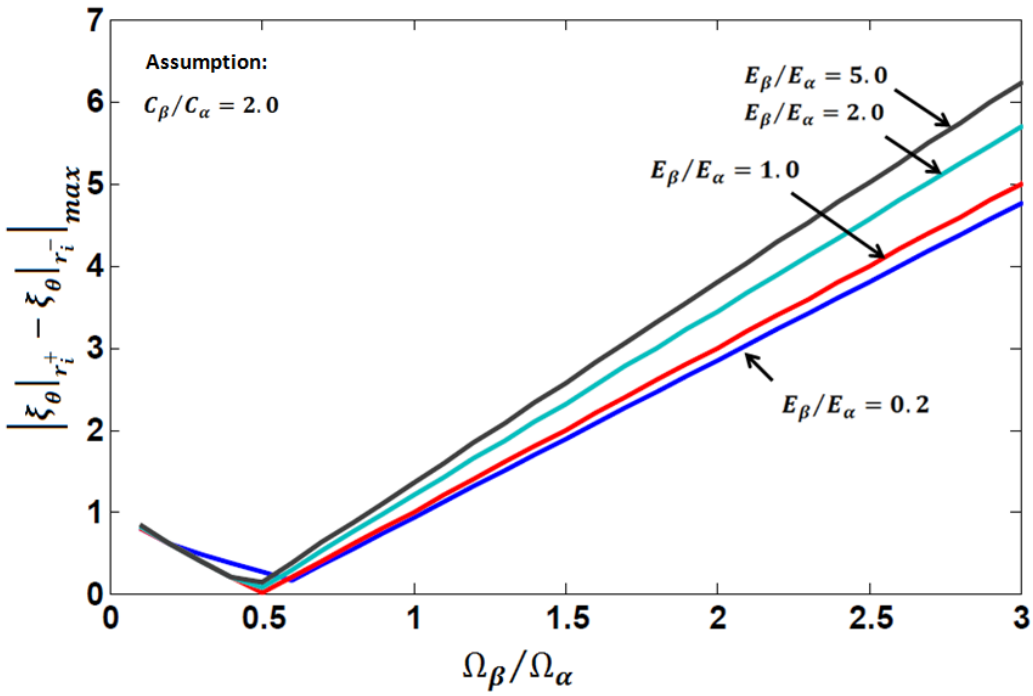

Figure 6.7: A plot of the maximum stress jump (tangential) at the interface as a function of the relative partial molar volume of two phases $\Omega_\beta/\Omega_\alpha$ for different values of relative Young's modulus E_β/E_α of the two phases, for $C_\beta/C_\alpha = 2$.

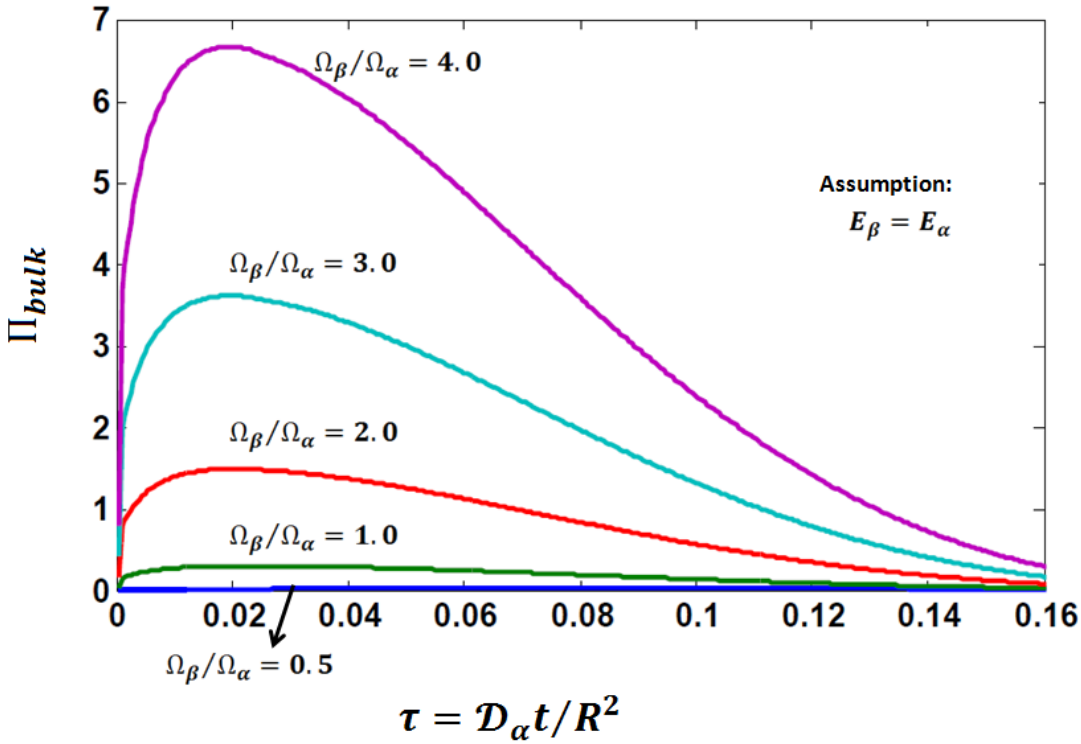

Figure 6.8: Variation of strain energy with time in an electrode particle. Different curves represent strain energy variation for different magnitudes of $\Omega_\beta/\Omega_\alpha$. For these curves, $E_\beta/E_\alpha = 1$ and $C_\beta/C_\alpha = 2$.

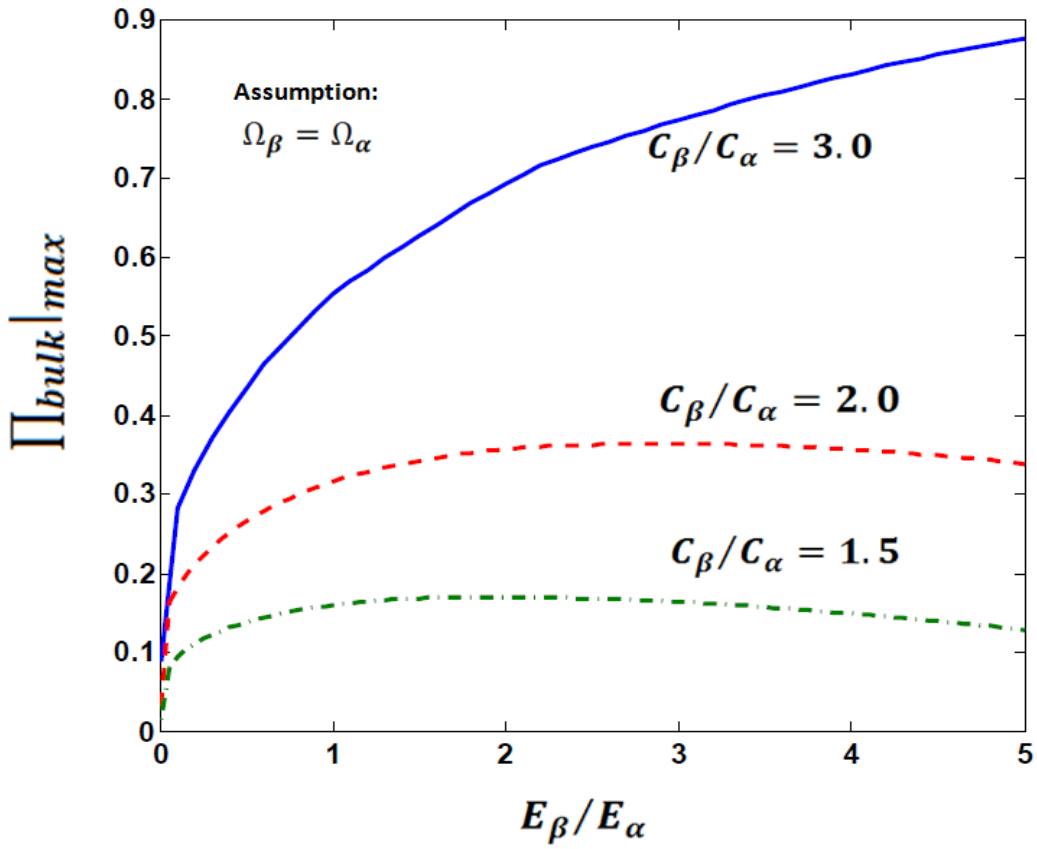

Figure 6.9: Peak strain energy variation with different values of E_β/E_α. The different curves represent such a variation in peak strain energy for different C_β/C_α ratios. Here $\Omega_\beta/\Omega_\alpha = 1$.

CHAPTER 7

EFFECT OF MESOPORES INSIDE ELECTRODE PARTICLES ON DIFFUSION INDUCED STRESS

This chapter is based on work published as:

S. J. Harris, R. D. Deshpande, Y. Qi, I. Dutta, Y. T. Cheng, Mesopores inside electrode particles can change the Li-ion transport mechanism and diffusion-induced stress. *Journal of Materials Research* **25**, 1433 (Aug, 2010)

It's reproduced by permission of Materials Research Society.

7.1 Summary

One of the major mechanisms behind capacity fading of the lithium ion batteries is mechanical degradation of electrode particles. A large number of articles explaining the transport and stress behavior of lithium inside the single electrode particles have been published. These single electrode particle models assume the electrode particles to be homogeneous and isotropic. In this chapter, experimentally we show that numerous internal pores or cracks are present in both the positive (Lithium cobalt oxide ($LiCoO_2$)) and negative (graphite) electrode particles, which is consistent with previously published data. We present a simple mathematical model to show that the presence of free surfaces, even from small internal cracks or pores, both quantitatively and qualitatively, alters the internal stress distributions such that particles are prone to internal cracking rather than surface cracking that has been predicted previously.

The fracture tendency of particles depend largely on the internal microstructure of particles, about which little is known, rather than on the intrinsic mechanical properties of the particle materials. The widely used shrinking core model for explaining either stress maps or transport is questioned for particles with internal structure, which includes all secondary electrode particles.

7.2 Introduction

Understanding mechanical degradation of electrode particles has been the subject of intense attention among the modelers. Along with Huggins and Nix (*1*), several recent theoretical studies have modeled internal stresses generated during insertion and de-insertion of Li into electrode particles (*2-5*). These mathematical models are used to understand the stress behavior and predict the fracture, which is sometimes observed in degraded electrodes (*6-9*). Most of these models are based on the assumption of macro-homogeneity of the electrode particles (*10, 11*) to predict intra-particle Li concentration profiles and the associated stress fields. These models typically implicitly assume that active particles are internally solid, homogeneous and flawless, and are isotropic. These assumptions naturally lead to the shrinking core model for lithium transport between the outside and the center of the particles. With the shrinking core model, the diffusion of solute is radially inwards or outwards and local variations in Li concentration cause local phase transitions, with phase boundaries separating the inner core from outer shell (*11, 12*). However, there is little direct experimental evidence supporting the homogeneity of Li-ion battery electrode particles.

In fact, for anisotropic materials such as single crystal $LiFePO_4$ particles, it may not be appropriate to assume the shrinking core model (*10, 13-15*), and it has been experimentally shown that for this material, the shrinking core model is not valid (*16, 17*). At the same time, the shrinking core has been implicitly accepted as applying to secondary particles since they are made from randomly oriented primary particles (*2, 3*).

The shrinking core model is valid depending on the internal micro/nano-structure of the active electrode particles, but very little such information is available about the micro/nano-structure. Few articles have been published on the internal structure of material where specific Brunauer–Emmett–Teller (BET) area of graphite particles has been measured by Joho *et al*, and they suggested that the existence of mesopores (2-50 nm) inside graphite particles and surface area of these mesopores contribute significantly to the electroactive surface area and the irreversible capacity loss during the first cycle due to SEI formation. Stephen J Harris and coworkers (General Motors R & D, Warren, MI) took images which show a complex internal structure of electrode particles, including what appear to be cracks, pores, and grain boundaries. These observations are consistent with a previous study using a focused ion beam on graphite particles that also observed internal cracks (*18*). With this understanding, we present simple calculations showing that the free surfaces from even small internal mesopores substantially alter the Li diffusion transport and the internal stress distributions. Our calculations assume cylindrical symmetry, which is more appropriate for layered materials such as graphite than the previously assumed spherical symmetry.

We point out that the fracture tendency of particles may well depend more on the internal microstructure of particles, about which little is known, than on the intrinsic mechanical properties of their constituent materials. With this model we illustrate the importance of including the real microstructure of electrode particles in future battery performance and failure modeling.

7.3 Experimental procedure

Stephen J Harris and coworkers (General Motors R & D, Warren, MI) performed the experimental part. Positive (LiCoO2) and negative (graphite) electrodes were removed from a newly purchased LR1865AH Lishen (Tianjin, China) 3.7V 18650 laptop batteries. High resolution scanning electron microscope (SEM) images of the deposited surface layers and particle size measurements were obtained using a Carl Zeiss NVision 40 Crossbeam® workstation with a LEO Gemini® field emission column. A beam energy of 3kV and WD of ~ 3.5 mm was used for SEM images. Energy dispersive spectroscopy (EDS) analysis was done using Apollo 40 SDD (EDAX Corp. Mahwah, NJ, USA) detector and a beam energy of 15kV. For details please refer Harris *et al.* (*19*).

7.4 Results

With an EDS phosphorus map, it is observed that electrolyte salt, $LiPF_6$ is present and it essentially outlines the pores inside 10 micron graphite particles. With a high resolution SEM images considerable anisotropy of the grains was observed. Also it could be observed that the graphite particles are comprised of smaller grains resulting in grain boundaries and pores. Similar observations were made for the $LiCoO_2$ particles. Details of these observations are reported in Harris *et al.* (*19*).

Analogous data have been published previously by Zhang *et al.* (*18*), who used a focused ion beam to expose the particle interiors. Because a focused ion beam is expected to cause much less surface damage on a scale of microns than a microtome, their observations of internal cracks/pores are particularly relevant here (*20*). However, similar types of cracks were also observed in the investigation done here. A typical propagation of a hairline crack and transgranular pore within a graphite particle could be observed. Pores of different sizes were observed in the graphite particles varying from surface defects to transgranular cracks. The presence of grain boundaries, cracks, and pores inside electrode particles suggests that if the electrolyte has access to the interior of such particles, then Li^+ ion transport could take place by grain boundary/pore diffusion as well as by bulk diffusion. Zhang *et al*. (*18*) observed that internal crack/pore surfaces were coated with solid electrolyte interphase (SEI) layer, showing that electrolyte and, therefore, lithium ions did in fact infiltrate into the particles. According to Joho's measurement, it is the surface area including the mesopores inside graphite particles that correlates with Li loss due to SEI formation, not the external surface area of the particle. Clearly, the mesopore surfaces inside these particles contribute a large portion to the total electroactive surface.

With this understanding of the microstructure, we use analytical modeling to show that the presence of complex internal structure can impact the amplitude and nature of the internal stresses caused by lithium insertion and removal. For real particles, we expect that the presence of several free surfaces at different orientations will have a profound effect, both quantitative and qualitative, on the internal stress and strain fields as well as on internal Li transport mechanisms.

7.5 Analysis for diffusion induced stress (DIS)

In order to calculate how the stress field evolves during lithium insertion in a particle, recent papers have used the analogy between thermal stresses and diffusion induced stresses (DISs) (*3, 5*). In this chapter, we use a slightly different approach to model stresses, where we take the electrode particle to be cylindrical with a coaxial pore in order to find the impact of small internal mesopore on the stress distributions.

In our model lithium insertion occurs only from the (prismatic) edges and not from top and bottom (basal) planes of the particle. This assumption of anisotropic particles and anisotropic insertion provides a better model for the transport processes in layered materials such as graphite and LiCoO2 grains than would the assumption of spherical particles, assumed in previous work. The mesopore diameter we consider is 1% of the (cylindrical) particle diameter, corresponding to $1\text{x}10^{-4}$ volume fraction. For an electrode particle of 10 μm diameter, the mesopore size would be 100 nm.

For our cylindrically symmetric particles, the concentration of lithium at a particular radius can be defined with a diffusion equation in a cylindrical co-ordinate system

$$\frac{\partial C}{\partial t} = \mathcal{D}\left(\frac{\partial^2 C}{\partial r^2} + \frac{1}{r}\frac{\partial C}{\partial r}\right) \tag{7.1}$$

where C is the molar concentration and D is diffusion coefficient of Li inside the electrode particle. Let us assume that the electrode is surrounded by a constant lithium ion concentration C_R. For a cylindrical electrode particle, we assume a finite concentration at the center where the initial lithium ion concentration inside the electrode is C_0.

Now assume that there is a single small mesopore, coaxial with the cylinder, with radius a. This mesopore may or may not be accessible to electrolyte. Thus, we can have following boundary conditions for concentration conditions of diffusion equation (7.1)

i. Solid electrode, no mesopore:

$$C(r,0) = C_0\,, \qquad for\ 0 \le r \le R\ \ ;$$

$$C(R,t) = C_R\,, \qquad for\ t \ge 0\ \ ;$$

$$C(0,t) = finite, \qquad for\ t \ge 0\ . \tag{7.2a}$$

ii. Pre-existing coaxial mesopore of radius a, filled with electrolyte

$$C(r,0) = C_0\,, \qquad for\ 0 \le r \le R;$$

$$C(R,t) = C_R\,, \qquad for\ t \ge 0\ ;$$

$$C(a,t) = C_R\,, \qquad for\ t \ge 0\ \ . \tag{7.2b}$$

Solving equation (7.1) with the above boundary conditions yields the concentration profiles, from which we can model the stress evolution inside each particle. We assume the electrodes are made from an isotropic, linearly elastic solid. Although we will find below that this assumption cannot be used to give accurate predictions for stresses inside a real particle, we believe that it is sufficiently good to give an estimate of the impact that the presence of a free surface would have on the local stress field. Using the analogy between thermal stresses (*21*) and DISs we can write the radial strain as

$$\varepsilon_{rr} - \frac{\Omega}{3}C = \frac{1}{E}(\sigma_r - \nu(\sigma_\theta + \sigma_z)) \tag{7.3}$$

Similarly, the tangential strain and axial strain are defined as

$$\varepsilon_{\theta\theta} - \frac{\Omega}{3}C = \frac{1}{E}(\sigma_\theta - \nu(\sigma_r + \sigma_z)) \quad , \tag{7.4}$$

and

$$\varepsilon_{zz} - \frac{\Omega}{3}C = \frac{1}{E}(\sigma_z - \nu(\sigma_r + \sigma_\theta)) \quad . \tag{7.5}$$

Here, E is Young's modulus of the electrode and Ω is partial molar volume of the solute. Since atomic diffusion in solids is a much slower process than elastic deformation, mechanical equilibrium is established on a time scale short compared to that for diffusive processes, and we treat this as a static equilibrium problem (*21*).

In the absence of any body force, the equation for static mechanical equilibrium in the bulk of a cylinder is given by

$$\frac{d\sigma_r}{dr} + \frac{(\sigma_r - \sigma_\theta)}{r} = 0 \quad . \tag{7.6}$$

Let u denote the radial displacement. Strain can be given as

$$\varepsilon_{rr} = \frac{du}{dr} \quad , \varepsilon_{\theta\theta} = \frac{u}{r} \ . \tag{7.7}$$

We will now assume that there is no stress applied in the z direction, $i.e., \sigma_z = 0$. Thus the electrode expands freely on z direction, and we have plane stress.

For a solid electrode particle, there is no displacement at the center, *i.e.*, $u(0) = 0$. For an electrode particle with a pre-existing void of radius a at the center, the radial stress on the free surface is zero, *i.e.*, $\sigma_r(a) = 0$.

For all electrodes, we also have $\sigma_r(R) = 0$ at $r = R$ (radius of the cylinder). Solving equation (7.6) using the above conditions, the radial stress distribution inside electrode are:

$$\sigma_r = \frac{\Omega}{3} E \left[-\frac{1}{r^2} \int_a^r C(r) r dr + \frac{1}{R^2 - a^2} \left(1 - \frac{a^2}{r^2}\right) \int_a^R C(r) r dr \right] \tag{7.8}$$

where, when a = 0, we have the solid electrode case without pre-existing mesopores. The dimensionless stress, radial position, time, and concentration can be represented as,

$$\xi_j = \frac{\sigma_j}{[\frac{\Omega}{3} E (C_R - C_0)]}, \quad x = \frac{r}{R}, \quad T = \frac{\mathcal{D}t}{R^2}, \quad and \;\; y = \frac{C - C_0}{C_R - C_0}, \text{ respectively} \tag{7.9}$$

Here, j is r, θ or z depending upon the direction of stress we are looking at.

We first determine the dimensionless concentrations at various radial positions and times using the diffusion equation (7.1) and the 2 sets of boundary conditions, *i, and ii,* listed in Equation (7.2). Then, based on the three concentration profiles, we compute radial and tangential stresses at different radial positions as a function of time.

Effects of an internal mesopore on the concentration profiles and on the corresponding radial stress field evolution inside particles are shown in Figures 7.1 *(a)*, and 7.1 *(b)* for the boundary conditions listed in (*i)*, a solid electrode without any mesopore*;* and *(ii)* an electrode with pre-existing coaxial mesopore of radius a=0.01, filled with electrolyte. For case *(i)*, the maximum of the radial stress is reached at the center of the cylinder, but even a small hole at center shifts the maximum stress location away from the center.

When we compare Figures 7.1 (*a)* and 7.1 *(b)*, we find that not only is there a shift in magnitude and location of the radial stress peak value, but even the sign of the stress changes. Figures 7.1 *(a)* and 7.1 *(b)* represent stress distributions for insertion of lithium in the electrode. Opposite conclusions would hold for the de-insertion case. Thus, a large region under compression in the homogeneous electrode during de-insertion would be in tension in the presence of a small mesopore (a=0.01) when it is filled with electrolyte. These effects are primarily due to the presence of free surfaces.

As with the radial stress case, the tangential stress σ_θ and the axial stress σ_z also show differences due to the presence of a mesopore, whether or not it is filled with electrolyte. Figure 7.2 shows tangential stresses for the de-insertion case, with and without a mesopore filled with electrolyte.

For a mesopore not accessible to the electrolyte, we find that the maximum tensile tangential stress is at the inner surface of the mesopore and has 1.96 times higher magnitude than the maximum stress for the electrode with no mesopore case. Our calculations also show that the maximum tensile tangential stress has only a weak dependence on the mesopore radius.

Following Cheng and Verbrugge (*22*), we calculated the bulk strain energy per unit volume, or bulk strain energy density, $W(r)$ accumulated as a result of the elastic deformation for the isotropically deformed cylinder as (*21*)

$$W(r) = \frac{1}{2E}\left(\sigma_r^2 + \sigma_\theta^2 + \sigma_z^2\right) - \frac{\nu}{E}\left(\sigma_r\sigma_\theta + \sigma_\theta\sigma_z + \sigma_z\sigma_r\right) \tag{7.10}$$

The total bulk strain energy can be obtained by integrating the strain energy density over the entire volume. Bulk strain energy per unit length of the wire in dimensionless form is

$$\prod_{bulk} = \frac{W_{bulk}}{\pi R^2 E\left(\frac{\Omega}{3}(C_R - C_0)\right)^2} = \int_{(a/R)}^{1} \left[\left(\xi_r^2 + \xi_\theta^2 + \xi_z^2\right) - 2\nu(\xi_r\xi_\theta + \xi_\theta\xi_z + \xi_z\xi_r)\right] x dx \tag{7.11}$$

When $a = 0$, we have a solid electrode, and when $a > 0$, we have a mesopore.

Figure 7.3 shows that for an electrode with a mesopore accessible to the electrolyte, the peak dimensionless strain energy is a little over half when compared with homogeneous solid electrode. The drastic change in magnitude of strain energy, demonstrate the significant effect that even a single mesopore can have on strain energy. Based on Griffith's energy criterion, the large drop in strain energy caused by free surfaces could mean a reduction in the probability of fracture for any given state of lithiation condition. On the other hand, mesopores will also affect the fracture strength of the particle and increase the stress intensity factor in complex ways. Thus, predictions of both particle strength and internal particle stress levels will have to rely heavily on knowledge of the internal microstructure of the particles for accurate results.

7.6 Discussion and conclusions

The shrinking core model, which has been widely assumed in battery analysis for calculating transport rates and stress evolution (*3-5, 10, 11, 23, 24*), depends on at least two assumptions as it is commonly applied. The first assumption is that the particles are isotropic, at least in terms of Li-transport and modulus.

It has been shown that the shrinking core model is not appropriate for the highly anisotropic single crystal material $LiFePO_4$. This same conclusion would also appear to hold for the highly anisotropic individual grains in graphite and $LiCoO_2$ particles. The second assumption is that transport of Li from the exterior to the interior of electrode particles is controlled by a single process, generally assumed to be bulk diffusion. We believe that our observation, together with analogous results from Zhang *et al*. (*18*), also cast doubt on the accuracy of this second assumption, for both positive and negative electrode materials.

If $\xi_{max}$is the yield stress for the electrode material, the stress required to fracture it when there is a preexisting mesopore is ξ_{max}/K . Here, K is the stress intensity factor which depends upon the geometry of the mesopore and direction of applied stress, but is typically around 2 for small holes (*25*). If we define the cracking tendency as the ratio of maximum tensile stress to the yield stress, we find that during insertion the electrode with pre-existing mesopore has at least 1.96×K ~ 4 times higher cracking tendency. Our calculations are based on the idealized assumption that the mesopore is cylindrical in nature, but they clearly indicate that the shrinking core model, with its isotropic electrode assumption, would substantially underestimate the cracking tendency.

Similarly, during de-insertion, the isotropic solid electrode model predicts a compressive tangential stress at the center of cylinder and maximum tensile tangential stress at the surface. This indicates that the electrode has a higher cracking tendency at its surface. On the other hand if the electrode has an electrolyte-accessible pre-existing mesopore, we find that the tangential stress is tensile at both the outer and inner surface of the electrode particle.

Depending on the stress intensity factor (K value), the cracking tendency may well be higher at the crack tip. Such an electrode is prone to internal cracking rather than surface cracking, contrary to the prediction of the shrinking core model.

The presence of SEI in internal mesopores shows that there are processes apart from bulk diffusion—perhaps grain boundary/pore diffusion—by which Li^+ ions can penetrate into the particles. The relative importance of bulk diffusion and grain boundary/pore diffusion will depend on the particular chemistry/microstructure as well as the local state of lithiation. For example, material swelling from lithiation could deform mesopores and change their effectiveness as a pathway for Li^+ ion transport. To the extent that grain boundary/pore diffusion is significant, the distribution of the various lithiated phases (or stages) within the particles will depend primarily on how the interior surfaces are arranged and may not in general resemble a shell and core. A follow-on step could then be bulk diffusion into individual grains, which might be fast or slow compared to other internal transport mechanisms. Given the extreme anisotropy of the individual grains, it is unlikely that a shrinking core model would be valid for this step either.

Zhang *et al*.(*18*) suggested that formation of SEI on interior mesopore surfaces could be sufficiently severe to lead to battery degradation through loss of lithium. The validity of this hypothesis depends on the amount of interior surface area accessible to the electrolyte. Additional analysis of particle microstructure, perhaps best accomplished with additional focused ion beam experiments, will be required to address this suggestion.

But whether or not the internal mesopore/grain boundary surface area is large enough to substantially affect the amount of SEI initially or ultimately formed, our images and analysis suggest that for particles such as those examined here: (1) the internal stress distribution and internal transport can be calculated accurately only with knowledge of the internal particle microstructure and (2) the core shell model does not give accurate predictions for either.

7.7 List of symbols

r, θ, φ	spherical coordinates
Ω_{i}	partial molar volume of the solute in phase 'i' ($m^3\ mol^{-1}$)
R	radius of the spherical electrode particle (m)
r_i	radial location of interface form the center of particle (m)
ν_{i}	Poisson's ratio of phase 'i'
E_{i}	Young's modulus of phase 'i' $(N\ m^{-2})$
u	radial displacement (m)
σ_r	radial stress $(N\ m^{-2})$
σ_θ	tangential stress $(N\ m^{-2})$
σ	mean stress $(N\ m^{-2})$
σ_{shear}	shear stress $(N\ m^{-2})$
ε_r	radial strain
ε_θ	tangential strain
$C(r,t)$	solute concentration at radius r at time t $(mol\ m^{-3})$
C_α	equilibrium concentration of solute in α phase $(mol\ m^{-3})$

C_β	equilibrium concentration of solute in β phase $(mol\ m^{-3})$
D_α	diffusion coefficient of the solute in α phase $(m^2\ sec^{-1})$
t	Time
x	dimensionless radius
x_i	dimensionless radial location of interface
τ	dimensionless time
$\hat{C}$	dimensionless concentration
ξ_r	dimensionless radial stress
ξ_θ	dimensionless tangential stress
$\Delta\xi_\theta(r_i)$	dimensionless tangential stress jump at the interface
$e(r)$	local strain energy density $(J\ m^{-3})$
W_{bulk}	total strain energy stored due to bulk deformation (J)
$\prod_{bulk}$	dimensionless bulk strain energy
$\prod_{bulk}\|_{max}$	maximum strain energy stored
$\gamma_{surface}$	surface energy $(J\ m^{-3})$
$E_{fracture}$	fracture energy $(J\ m^{-2})$

7.8 References

1. R. Huggins, W. Nix, Decrepitation Model For Capacity Loss During Cycling of Alloys in Rechargeable Electrochemical Systems. *Ionics* **6**, 57 (2000).
2. Y.-T. Cheng, M. W. Verbrugge, The influence of surface mechanics on diffusion induced stresses within spherical nanoparticles. *Journal of Applied Physics* **104**, 083521 (2008).
3. J. Christensen, J. Newman, A Mathematical Model of Stress Generation and Fracture in Lithium Manganese Oxide. *Journal of the Electrochemical Society* **153**, A1019 (2006).
4. E. Garcia, Y. Chiang, W. Carter, P. Limthongkul, C. Bishop, Microstructural Modeling and Design of Rechargeable Lithium-Ion Batteries. *Journal of the Electrochemical Society* **152**, A255 (2005).
5. X. Zhang, W. Shyy, A. M. Sastry, Numerical Simulation of Intercalation-Induced Stress in Li-Ion Battery Electrode Particles. *Journal of The Electrochemical Society*, **154**, A910 (2007).
6. H. Gabrisch, J. Wilcox, M. Doeff, TEM Study of Fracturing in Spherical and Plate-like LiFePO4 Particles. *Electrochemical and Solid-State Letters* **11**, A25 (2008).

7. E. Markervich, G. Salitra, M. Levi, D. Aurbach, Capacity fading of lithiated graphite electrodes studied by a combination of electroanalytical methods, Raman spectroscopy and SEM. *Journa of Power Sources* **146**, 146 (2005).

8. Y. Itou, Y. Ukyo, Performance of LiNiCoO2 materials for advanced lithium-ion batteries. *Journal of Power Sources* **146**, 39 (2005).

9. T. Ohzuku, H. Tamura, K. Sawai, Monitoring of particle fracture by acoustic emission during charge and discharge of Li/MnO2 cells. *Journal of the Electrochemical Society* **144**, (1997).

10. V. Srinivasan, J. Newman, Discharge Model for the Lithium Iron-Phosphate Electrode. *Journal of the Electrochemical Society* **151**, A1517 (2004).

11. V. Srinivasan, J. Newman, Existence of path-dependence in the LiFePO4 electrode. *Electrochemical and Solid-State Letters* **9**, A110 (2006).

12. A. Andersson, J. Thomas, *Journal of Power Sources* **97**, 498 (2001).

13. C. Wang, A. M. Sastry, Mesoscale Modeling of a Li-ion Polymer Cell. *Journal of The Electrochemical Society*, **154**, A1035 (2007).

14. G. Singh, G. Ceder, M. Bazant, Intercalation dynamics in rechargeable battery materials: General theory and phase-transformation waves in LiFePO4. *Electrochimica Acta* **53**, 7599 (2008).

15. C. Delmas, M. Maccario, L. Croguennec, F. L. Cras, F. Weill, Lithium deintercalation in LiFePO4 nanoparticles via a domino-cascade model. *Nature Materials* **7**, 665 (2008).

16. G. Chen, X. Song, T. Richardson, Electron Microscopy Study of the LiFePO4 to FePO4 Phase Transition. *Electrochemical and Solid-State Letters* **9**, A295 (2006).

17. L. Laffont *et al.*, Study of the LiFePO4/FePO4 Two-Phase System by High-Resolution Electron Energy Loss Spectroscopy. *Chem. Mater.* **18**, 5520 (2006).

18. H. Zhang, F. Li, C. Liu, J. Tan, H. Cheng, New Insight into the Solid Electrolyte Interphase with Use of a Focused Ion Beam. *J. Phys. Chem. B* **109**, 22205 (2005).

19. S. J. Harris, R. D. Deshpande, Y. Qi, I. Dutta, Y. T. Cheng, Mesopores inside electrode particles can change the Li-ion transport mechanism and diffusion-induced stress. *Journal of Materials Research* **25**, 1433 (Aug, 2010).

20. J. R. Smith *et al.*, Evaluation of the relationship between cathode microstructure and electrochemical behavior for SOFCs. *Solid State Ionics* **180**, 90 (Feb, 2009).

21. R. Deshpande, Y.-T. Cheng, M. W. Verbrugge, Modeling diffusion-induced stress in nanowire electrode structures. *Journal of Power Sources* **195**, 5081 (2010).

22. Y.-T. Cheng, M. W. Verbrugge, Evolution of stress within a spherical insertion electrode particle under potentiostatic and galvanostatic operation. *Journal of Power Sources* **190**, 453 (2009).

23. R. Pollard, J. Newman, Mathematical Modeling of the Lithium-Aluminum, Iron Sulfide Battery. *Journal of the Electrochemical Society* **128**, 491 (1981).

24. Y. Cheng, M. Verbrugge, The influence of surface mechanics on diffusion induced stresses within spherical nanoparticles. *JOURNAL OF APPLIED PHYSICS* **104**, 83521 (2008).

25. R. C. Hibbler, *Mechanics of Materials*. (Prentice Hall, New Jersey, ed. Third Edition, 1997).

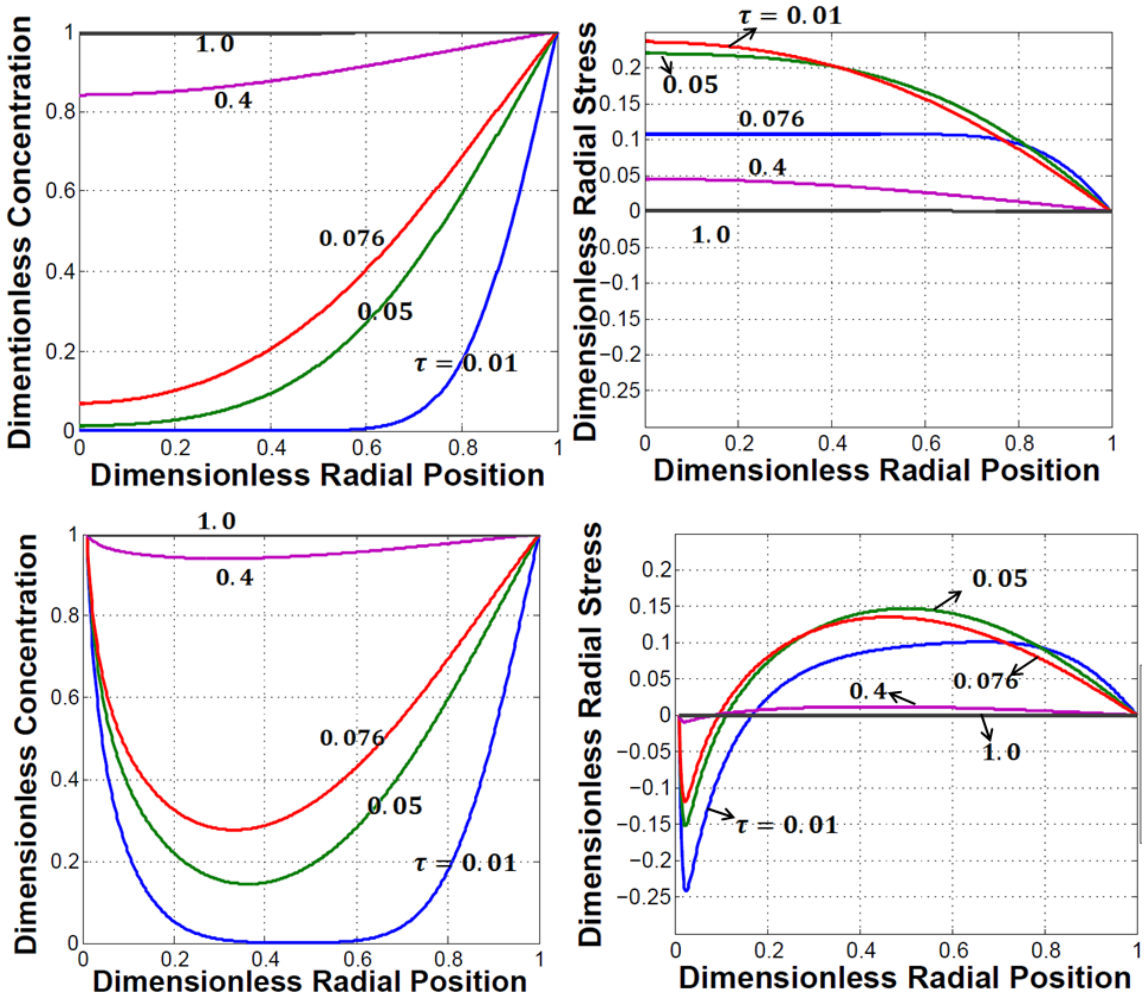

Figure 7.1: Li-concentration profiles and the radial stress distribution inside the particle subject to two different boundary conditions, (*i*) solid electrode particle (*ii*) an electrode particle with a pre-existing pore accessible to the electrolyte

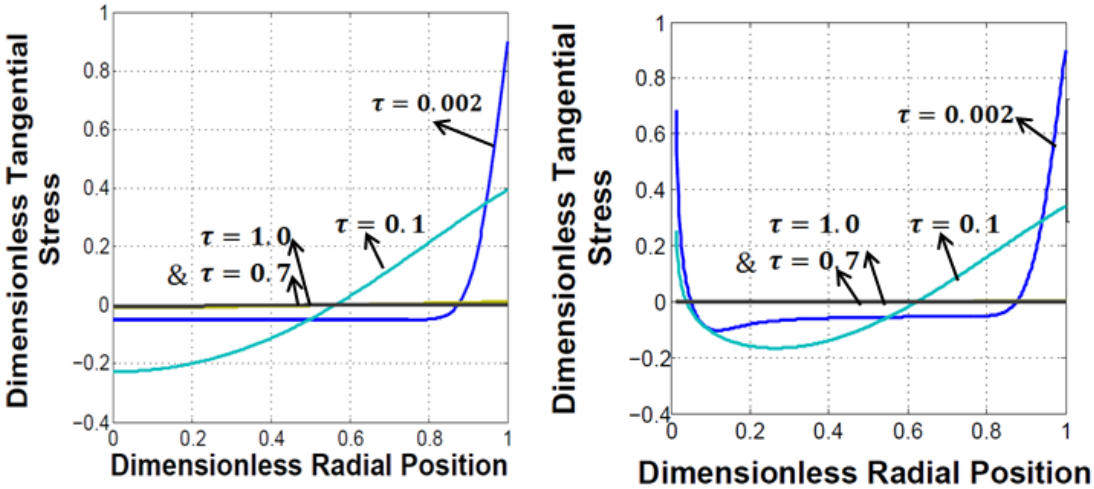

Figure 7.2: Dimensionless tangential stress at different radial location at different time (a) for solid homogeneous electrode, (b) for an electrode with a pre-existing pore accessible to the electrolyte during de-insertion.

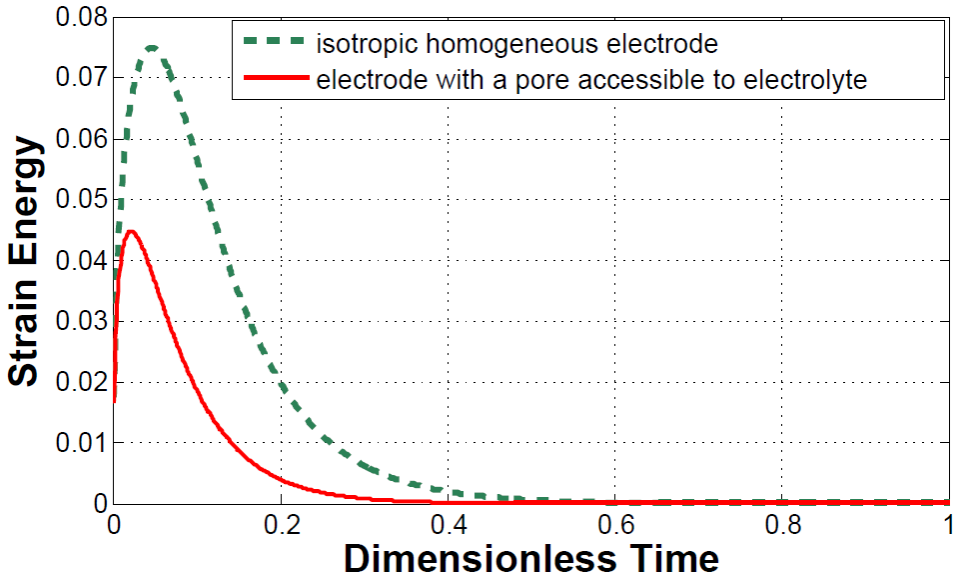

Figure 7.3: Strain energy evolution with diffusion time for a homogeneous particle (dotted line) and an electrode particle with a pre-existing pore accessible to the electrolyte.

CHAPTER 8

EFFECTS OF SOLID-ELECTROLYTE INTERPHASE (SEI) ON THE COUPLED MECHANICAL-CHEMICAL DEGRADATION OF LITHIUM ION BATTERY ELECTRODES

8.1 Summary

The coupled mechanical-chemical degradation of electrodes upon charging and discharging has been recognized as a major problem in lithium ion batteries. The instability of commonly employed electrolytes results in solid electrolyte interphase (SEI) formation. Although SEI formation contributes to irreversible capacity loss, the SEI layer is necessary, as it passivates the electrode-electrolyte interface from further solvent decomposition. Due to the volume changes and the associated stresses within the SEI layer and at the interface between the SEI layer and the underlying active electrode materials, the SEI layer may fracture, causing the growth of SEI on the newly exposed electrode surfaces. At the same time SEI affects the diffusion and mechanical stability of the electrode. Recently, several groups have used a strategy of having artificial SEI layers on electrode particles to improve performance and durability. In this chapter, through mathematical modeling, we provide an understanding of the effects of the properties and thickness of SEI on the stress and strain energy evolution inside an electrode particle and within the protective SEI layer. We calculate stresses at the interface between the electrode and the SEI. Our model can be used to help improve SEIs with desired mechanical properties and thickness to minimize irreversible losses caused by the coupled mechanical-chemical degradation processes.

8.2 Introduction

Lithium ion batteries (LIBs) are known to have high energy and power density, making them attractive for electric vehicle applications (*1*). However, electric vehicle applications demand LIBs with even greater energy and power density, as well as longer durability. Chemical and mechanical degradation of electrodes is one of the main reasons for capacity fade in LIBs (*2*). The chemical degradation occurs due to the instability of commonly used electrolytes at the operating potential, resulting in SEI formation (*3, 4*). The formation of SEI consumes active material and thus causes an irreversible loss in stored lithium. In spite of this, SEI formation is important since it passivates further reduction of the electrolyte and thus stabilizes the system (*5*). Several groups are studying SEI to unveil its formation mechanism and its mechanical and transport properties (*6, 7*). Tasaki *et al*. (*8, 9*) studied in detail the major components of SEI and their solubility in electrolytes. Electrolyte additives can be used to form a more stable SEI (*10*). Zhang *et al*.(*11*) explained the effect of different possible additives on SEI stabilization. There are also attempts to make a more stable artificial SEI layer of polymeric material such as poly(ethylene-co-acrylic acid) and sodium carboxymethyl cellulose with methods such as electro-painting (*12*). Surface modifications and surface coatings, such as metals, metal oxides and conductive polymers are shown to improve battery performance (*13*).

Diffusion of lithium inside the electrode particle upon charging and discharging results in diffusion induced stresses (DISs). DISs may result in degradation of electrode creating a new surface exposed to the electrolyte which results in new SEI formation.

Overcoming the mechanical degradation caused by the DISs is an important topic in lithium ion battery (LIB) research. DISs also affect stability of the SEI layer which determines rate of irreversible capacity loss with cycling. For understanding the mechanical degradation of the battery electrode, several groups (*2, 14-24*) have recently modeled DISs in lithium ion battery electrodes. The diffusion of lithium through the SEI might affect the diffusion profile and intern the stress profile inside the active core. Also, the SEI may provide additional mechanical stability to the active core, depending upon its mechanical properties. Most of the DIS models in the published literature did not account for these effects of the SEI on the DISs in the electrode particle

In this chapter, we explore the relationship between DISs and the different transport and mechanical properties of the SEI layer. An understanding of such a coupled chemical and mechanical degradation will help reveal the ideal mechanical properties of the SEI so that the fracture tendency of the electrode particle can be minimized. The results of this study may be used as a guideline for making an artificial SEI layer to improve electrode durability. Throughout this chapter “artificial SEI”, “coatings”, “stabilizing layer” are all referred to as SEI.

8.3 Mathematical analysis:

We assume that (1) the electrode particle is a spherical particle with a SEI layer formed uniformly around the particle (Fig. 8.1), (2) the particle and SEI are homogeneous and isotropic in mechanical and transport properties.

8.3.1. Mechanics:

To simplify the notion, the bulk active phase is referred to as the α phase and the SEI layer as SEI. Using the analogy between thermal stress and DIS, the stress-strain relationships expressed in the spherical coordinate system for the radial and tangential components are:

$$\varepsilon_r = \frac{1}{E_i}(\sigma_r - 2\nu_i\sigma_\theta) + \frac{1}{3}\Omega_i C$$

$$\varepsilon_\theta = \frac{1}{E_i}\left((1-\nu_i)\sigma_\theta - \nu_i\sigma_r\right) + \frac{1}{3}\Omega_i C \tag{8.1}$$

where Young's modulus is E_i, Poisson's ratio is ν_i, the partial molar volume of the solute is Ω_i for the respective α phase and SEI phase, molar concentration is C and the radial and tangential stresses are represented by σ_r and σ_θ. Eq. (8.1) is analogous to the constitutive law typically used for modeling thermal stress (*25, 26*) and has been used for modeling DISs (*27*), including stresses in battery electrodes (*18, 20, 23, 28, 29*). We further assume that the elastic properties of any of the phases do not vary with the lithium composition variation in it.

Because of the spherical symmetry, the radial and tangential strains, in the infinitesimal formulation of deformation, can be expressed as functions of radial displacement, u, as:

$$\varepsilon_{rr} = \frac{du}{dr} \quad , \varepsilon_{\theta\theta} = \frac{u}{r} \tag{8.2}$$

Since atomic diffusion in solids is a much slower process than elastic deformation, the mechanical equilibrium is established much faster than that of diffusion. The mechanical equilibrium is, therefore, treated as a static equilibrium problem.

In the absence of any body-force, the equation for static mechanical equilibrium in the bulk of a sphere is given by following equation,

$$\frac{d\sigma_r}{dr} + \frac{2(\sigma_r - \sigma_\theta)}{r} = 0 \tag{8.3}$$

The solutions of this differential equation for the case with constant E, ν and Ω, are given by:

$$\sigma_r = -\frac{\Omega E}{3(1-\nu)} \frac{2}{r^3} \int_a^r C(r) r^2 dr + \left[\frac{EI_1}{(1-2\nu)} - \frac{E}{(1+\nu)} \frac{I_2}{r^3}\right]$$

$$\sigma_\theta = \frac{\Omega E}{3(1-\nu)} \frac{1}{r^3} \int_a^r C(r) r^2 dr - \frac{\Omega E C(r)}{3(1-\nu)} + \left[\frac{EI_1}{(1-2\nu)} + \frac{E}{(1+\nu)} \frac{I_2}{r^3}\right]$$

and the displacement $u(r)$ is given by,

$$u(r) = \left(\frac{1+\nu}{1-\nu}\right) \frac{\Omega}{3r^2} \int_a^r C(r) r^2 dr + rI_1 + \frac{I_2}{r^2} \tag{8.4}$$

The constants I_1 and I_2 can be obtained from the appropriate boundary conditions for both the α phase and the SEI layer. Because stress and displacement are finite at $r = 0$, we have, for the α phase within $0 \leq r < r_i$,

$$\sigma_r = -\frac{2E_\alpha}{3(1-\nu_\alpha)} \frac{\Omega_\alpha}{3} C_{avg}^\alpha(r) + \frac{E_\alpha I_{1\alpha}}{(1-2\nu_\alpha)}$$

$$\sigma_\theta = \frac{E_\alpha}{3(1-\nu_\alpha)} \frac{\Omega_\alpha}{3} C_{avg}^\alpha(r) - \frac{E_\alpha \Omega_\alpha C(r)}{3(1-\nu_\alpha)} + \frac{E_\alpha I_{1\alpha}}{(1-2\nu_\alpha)} \tag{8.5}$$

Here, $C_{avg}^{\alpha}(r) = (3/r^3)\int_0^r C(r')r'^2 dr'$ is the average concentration in the α phase $(0 \leq r \leq r_i)$.

For the SEI layer in the region of $r_i \leq r \leq R$, we have:

$$\sigma_r = -\frac{2E_{SEI}}{3(1-\nu_{SEI})}\left(1-\left(\frac{r_i}{r}\right)^3\right)\frac{\Omega_{SEI}}{3}C_{avg}^{SEI}(r) + \left[\frac{E_{SEI}I_{1SEI}}{(1-2\nu_{SEI})} - \frac{2E_{SEI}}{(1+\nu_{SEI})}\frac{I_{2SEI}}{r^3}\right]$$

$$\sigma_\theta = \frac{E_{SEI}}{3(1-\nu_{SEI})}\left(1-\left(\frac{r_i}{r}\right)^3\right)\frac{\Omega_{SEI}}{3}C_{avg}^{SEI}(r) - \frac{E_{SEI}\Omega_{SEI}C(r)}{3(1-\nu_{SEI})} + \left[\frac{E_{SEI}I_{1SEI}}{(1-2\nu_{SEI})} + \frac{E_{SEI}}{(1+\nu_{SEI})}\frac{I_{2SEI}}{r^3}\right] \tag{8.6}$$

Here, $C_{avg}^{\alpha}(r) = (3/(r^3 - r_i^3))\int_0^r C(r')r'^2 dr'$ is the average concentration in the SEI layer $(r_i \leq r \leq R)$

Without considering the effects of surface energy and surface stresses, the normal stress at the free surface of the spherical particle is $\sigma_r(R) = 0$. Since the normal component of stresses and displacements are continuous at the interface between the α phase and SEI layer, $\sigma_r(r_i^{\alpha}) = \sigma_r(r_i^{SEI})$ and $u(r_i^{\alpha}) = u(r_i^{SEI})$, we can solve for constants I_{1SEI}, I_{2SEI} and $I_{1\alpha}$,

$$I_{1\alpha} = -\frac{2E_{SEI}(1-2\nu_\alpha)}{E_\alpha(1-\nu_{SEI})}\frac{3t}{R}\frac{I_{2SEI}}{r_i^3} + \frac{2\Omega_{SEI}E_{SEI}(1-2\nu_\alpha)}{9E_\beta(1-\nu_{SEI})}\frac{3t}{R}C_{avg}^{\alpha}(R) + \frac{2\Omega_\alpha(1-2\nu_\alpha)}{3(1-\nu_\alpha)}\left(1-\frac{3t}{R}\right)C_{avg}^{\alpha}(r_i)$$

$$I_{1SEI} = 2\frac{(1-2\nu_\alpha)}{(1+\nu_{SEI})}\frac{E_{SEI}}{E_\alpha}\frac{I_{2SEI}}{R^3} + \frac{2(1-2\nu_{SEI})}{3(1-\nu_{SEI})}\frac{3t}{R}\frac{\Omega_{SEI}}{3}C_{avg}^{SEI}(R)$$

$$I_{2SEI} = r_i^3 \frac{\frac{2}{3}\left[\frac{(1-2\nu_\alpha)E_{SEI}}{(1-\nu_{SEI})E_\alpha} - \frac{(1-2\nu_{SEI})}{(1-\nu_{SEI})}\right]\frac{3t}{R}\frac{\Omega_{SEI}}{3}C_{avg}^{SEI}(R) + {}^{\Omega_\alpha}/_{3}\, C_{avg}^{\alpha}(r_i)}{1 + 2\frac{(1-2\nu_\alpha)E_{SEI}}{(1+\nu_{sei})E_\alpha}\frac{3t}{R} + 2\frac{(1-2\nu_{SEI})}{(1+\nu_{SEI})}\left(1-\frac{3t}{R}\right)}$$

(8.7)

Here, t is the thickness of the SEI layer. We used the assumption that $t \ll R$ and thus the higher order terms of $\left({}^{t}/_{R}\right)$ were neglected.

As an example, we calculate the concentration profiles for a specific case of deinsertion using a spherical shell model.

8.3.2. Diffusion in a spherical core-shell:

Fickian diffusion of a solute in α-phase core, $0 \leq r < r_i$

$$\frac{\partial C^\alpha}{\partial T} = \frac{\mathcal{D}_\alpha}{r^2}\left(\frac{\partial}{\partial r}\left(r^2\frac{\partial C^\alpha}{\partial r}\right)\right) \tag{8.8}$$

Within the SEI, $r_i < r < R$

$$\frac{\partial C^{SEI}}{\partial T} = \frac{\mathcal{D}_{SEI}}{r^2}\left(\frac{\partial}{\partial r}\left(r^2\frac{\partial C^{SEI}}{\partial r}\right)\right) \tag{8.9}$$

The concentration at the surface of the SEI is denoted as C_R, and C_0^α and C_0^{SEI} are the concentrations of solute in the two phases when they are equilibrated.

At the interface ($r = r_i$) between the shell and the core, we assume equilibrium prevails and the flux is conserved

$$c^{\alpha} = Kc^{SEI} \quad \text{and} \quad \mathcal{D}_{\alpha}\frac{\partial c^{\alpha}}{\partial r} = \mathcal{D}_{SEI}\frac{\partial c^{SEI}}{\partial r} \tag{8.9a}$$

Let's consider a case of delithiation. We may assume, initially, $T = 0$, and both phases are equilibrated

$$c^{SEI} = c_0^{SEI}$$

$$c^{\alpha} = Kc_0^{SEI} \tag{8.9b}$$

At the particle surface $r = R$, the concentration is set

$$c^{SEI} = c_R \tag{8.9c}$$

The solution is well behaved at the center of the particle $r = 0$

$$\frac{\partial c^{\alpha}}{\partial r} = 0 \tag{8.9d}$$

Equation 8.9 can be made dimensionless with the following:

$$x = \frac{r}{R}, \quad \tau = \frac{D_{\alpha}T}{R^2}, \qquad y = \frac{C}{KC_0^{SEI}}, \qquad \xi = \frac{D_{SEI}}{D_{\alpha}}$$

Within the α-phase core, $0 < x < x_i$

$$\frac{\partial y^{\alpha}}{\partial \tau} = \frac{\partial^2 y^{\alpha}}{\partial x^2} + \frac{2}{x}\frac{\partial y^{\alpha}}{\partial x} \tag{8.10}$$

Within the SEI, $x_i < x < 1$

$$\frac{\partial y^{SEI}}{\partial \tau} = \xi\left(\frac{\partial^2 y^{SEI}}{\partial x^2} + \frac{2}{x}\frac{\partial y^{SEI}}{\partial r}\right) \tag{8.11}$$

At the interface $x = x_i$

$$y^{\alpha} = Ky^{SEI}$$

$$\frac{\partial y^{\alpha}}{\partial x} = \xi \frac{\partial y^{SEI}}{\partial x} \tag{8.11a}$$

Initially, $\tau = 0$

$$y^{SEI}(0, x_i < x < 1) = \frac{1}{K}$$

$$y^{\alpha}(0{,}0 < x < x_i) = 1 \tag{8.11b}$$

At the particle surface $x = 1$, the concentration is set

$$y^{SEI}(\tau > 0{,}1) = \frac{C_R}{KC_0^{SEI}} = y_R^{SEI} \tag{8.11c}$$

The solution is well behaved at the center of the particle $x = 0$

$$\frac{\partial y^{\alpha}}{\partial x}(\tau, 0) = 0 \tag{8.11d}$$

We solve this set of differential equation in three different ways.

a. Approximate solution:

Approximate solution methods for modeling diffusion in electrodes are useful in battery models to facilitate a one dimensional solution, and this provides computational advantages over the exact solution. The starting point in these approximations is a simplified expression for the concentration profile inside the spherical shell (*30*)

$$y^{SEI}(\tau, x_i < x < 1) = \frac{y_{SEI}^{0}(\tau)}{x} + y_{SEI}^{1}(\tau) \tag{8.12}$$

$y^0(\tau)$ and $y^1(\tau)$ are two unknowns and are functions of dimensionless time τ .

With the boundary conditions (8.11b) and (8.11c) we get,

$$y_{SEI}^0(\tau) = \frac{x_i}{1-x_i}\left[\frac{y^\alpha(\tau,x_i)}{k} - y_R^{SEI}\right]$$

$$y_{SEI}^1(\tau) = \frac{y^\alpha(\tau,x_i)}{k} - \frac{1}{1-x_i}\left[\frac{y^\alpha(\tau,x_i)}{k} - y_R^{SEI}\right] = -\frac{1}{1-x_i}\left[\frac{x_i y^\alpha(\tau,x_i)}{k} + y_R^{SEI}\right]$$

With these, we get the concentration profile in the SEI as,

$$y^{SEI}(\tau,x) = \frac{y^\alpha(\tau,x_i)}{k} + \left(\frac{1}{x} - \frac{1}{x_i}\right)\left(\frac{x_i}{1-x_i}\right)\left[\frac{y^\alpha(\tau,x_i)}{k} - y_R^{SEI}\right]$$

The interface condition for the α phase diffusion (Eq. 8.11b) now becomes a mixed boundary condition

$$\frac{\partial y^\alpha}{\partial x}(x_i) = \frac{\xi}{\delta}\frac{\partial y^{SEI}}{\partial z} = -\frac{\xi}{x_i(1-x_i)}\frac{1}{K}\left[y^\alpha(\tau,x_i) - K y_R^{SEI}\right] \tag{8.13}$$

With this condition, the diffusion equation (8.10) for the α phase can be directly solved to get concentration profile for both the phases. We use MATLAB partial differential equation solver ‘pdepe’ to solve equation (8.10) with condition (8.11d) and (8.13).

b. Linear perturbation analysis

We now assume that the appropriate characteristic length for the SEI is the SEI thickness, $R - r_i$ is, just as concentrations are scaled so as to be of order unity, the concentration gradients will also be of order unity for the majority of the diffusion process when the appropriate length scale for each region is employed in scaling.

Thus, we define;

$$z = \frac{r-r_i}{R-r_i} = \frac{R}{R-r_i}(x - x_i) = \frac{x-x_i}{\delta} \tag{8.14}$$

where $\delta = (R - r_i)/R$. Then

$$x = x_i + \delta z \tag{8.15}$$

Within the SEI, $0 < z < 1$

$$\delta^2 \frac{\partial y^{SEI}}{\partial \tau} = \xi \left(\frac{\partial^2 y^{SEI}}{\partial z^2} + \frac{2(\delta/x_i)}{1+z(\delta/x_i)} \frac{\partial y^{SEI}}{\partial z} \right) \tag{8.16}$$

We have assumed that for the duration of interest, all gradients have been scaled so as to be of order unity. In addition, we assume δ is an order unity quantity. Upon expanding the above equation about small δ, we obtain

$$\delta^2 \frac{\partial y^{SEI}}{\partial \tau} = \xi \left(\frac{\partial^2 y^{SEI}}{\partial z^2} + 2(\delta/x_i)[1 - z(\delta/x_i) + O(\delta)^2] \frac{\partial y^{SEI}}{\partial z} \right)$$

$$= \xi \left(\frac{\partial^2 y^{SEI}}{\partial z^2} + \frac{2}{x_i} \left[\delta - \frac{z}{x_i} \delta^2 + O(\delta)^3 \right] \frac{\partial y^{SEI}}{\partial z} \right)$$

$$\xi \left(\frac{\partial^2 y^{SEI}}{\partial z^2} + \frac{2}{x_i} \delta \frac{\partial y^{SEI}}{\partial z} \right) = \delta^2 \frac{\partial y^{SEI}}{\partial \tau} + \xi \left(\frac{2}{x_i} \left[\frac{z}{x_i} \delta^2 - O(\delta)^3 \right] \frac{\partial y^{SEI}}{\partial z} \right)$$

$$\xi \left(\frac{\partial^2 y^{SEI}}{\partial z^2} + \frac{2}{x_i} \delta \frac{\partial y^{SEI}}{\partial z} \right) = 0 + O(\delta)^2$$

We shall drop terms of $O(\delta)^2$ and higher order in δ, which leaves

$$\frac{\partial^2 y^{SEI}}{\partial z^2} + \frac{2}{x_i} \delta \frac{\partial y^{SEI}}{\partial z} = 0 \tag{8.17}$$

At the interface $x = x_i$ between the SEI and the core

$$y^{\alpha} = Ky^{SEI}$$

$$\frac{\partial y^{\alpha}}{\partial x} = \xi \frac{\partial y^{SEI}}{\partial x} \text{ or } \frac{\partial y^{\alpha}}{\partial x} = \frac{\xi}{\delta}\frac{\partial y^{SEI}}{\partial z} \tag{8.18}$$

At the particle surface $x = 1$, the concentration is set

$$y^{SEI}(\tau > 0,1) = \frac{C_R}{KC_0^{SEI}} = y_R^{SEI} \tag{8.19}$$

With these conditions, solving Eq. 8.15 we get, at the interface,

$$y^{SEI}(x_i) = \frac{\frac{y^{\alpha}(x_i)}{K}\left(1-e^{(2\delta/x_i)(1-z)}\right)-\frac{c_R}{Kc_0^{SEI}}\left(1-e^{-(2\delta/x_i)z}\right)e^{(2\delta/x_i)}}{\left(1-e^{2\delta/x_i}\right)} \tag{8.20}$$

The interface condition for the α phase diffusion now becomes a mixed boundary condition

$$\frac{\partial y^{\alpha}}{\partial x}(x_i) = \frac{\xi}{\delta}\frac{\partial y^{SEI}}{\partial z} = \frac{2\xi}{x_i}\frac{e^{2\delta/x_i}}{\left(1-e^{2\delta/x_i}\right)}\frac{1}{K}\left[y^{\alpha}(x_i) - \frac{c_R}{c_0^{SEI}}\right] \tag{8.21}$$

With this condition, the diffusion equation (8.10) for the α phase can be directly solved to get the concentration profile for both the phases. We use MATLAB partial differential equation solver 'pdepe' to solve equation (8.10) with condition (8.11d) and (8.21).

c. The COMSOL solution

The COMSOL multiphysics package can solve the coupled differential equations. To test the validity of the approximate solution, we solve the governing set of coupled diffusion equations with the 'transport of diluted species' module in the 'time dependent' mode in COMSOL, and compare the approximate solution with it.

Free tetrahedral mesh is used with 'fine' meshing size with physics controlled mode. This setting allows us to use mesh size of the shell and core according to their relative size and thus can be used for really thin shells.

We plot concentration at the interface of the shell side at any arbitrary time $(\tau = 0.4)$ for different thickness of the SEI for solutions obtained by all the three methods mentioned above (Figure 8.2a). From Figure 8.2a, we find that for thinner SEI, approximate solution and a linear perturbation analysis agree well with the COMSOL solution. These solutions deviate from the COMSOL solution as the relative SEI thickness (t/R) increases to greater than 0.01. To check the validity of the solutions at very short time, we plot the concentration at the interface as a function of time (for very short time) for a relative thickness $t/R = 0.005$ with all the three methods and find that all the three solutions match very well with each other at this small thickness (Figure 8.2b). Thus the solutions are valid if the thickness of the shell is small enough.

8.4 Results and discussion

We transform stresses to dimensionless form as follows

$$\bar{\sigma}_i = \frac{\sigma_i}{\frac{\Omega_\alpha K C_0^{SEI}}{3} \frac{E_\alpha}{(1-\nu_\alpha)}}$$

Here, 'i' represents direction $r, \theta,$ or φ. We plot dimensionless stresses $\bar{\sigma}_i$ at different radial locations (x) and dimensionless times (τ) for a core-shell, spherical electrode particle in Figures 8.3 & 8.4. We assume that the expansion coefficient of the SEI is negligible as compared to the expansion coefficient of the active material.

Figure 8.3 shows the radial stress distribution in the active material in the presence of the SEI surrounding the electrode particle. Here, as an example we assume the SEI thickness to be 1% of the particle radius $\left({}^{t}/_{R} = 0.01\right)$ and the SEI has the same Young's modulus $(E_{SEI}/E_{\alpha} = 1)$ and diffusion coefficient $(\xi = D_{SEI}/D_{\alpha} = 1)$ as the active core. We also assume the equilibrium concentration of the SEI to be the same as the equilibrium concentration of the active material $(K = C_0^{\alpha}/C_0^{SEI} = 1)$. We compare stresses for these particles-SEI core-shell structure with the previously obtained results for a spherical electrode particle without consideration of presence of the SEI (*20*). We find that, the maximum radial tensile stress is reached during insertion at the center of the particle but the magnitude of the maximum stress changes due to presence of the SEI. The radial stress in the SEI shell is always compressive during insertion. The final state of stress in the electrode particle is compressed state since the SEI layer constrains the expansion of active core part.

In Figure 8.4, we plot the tangential stress as a function of radial location and time during lithium removal. We find that, there is a sharp jump in the tangential stress at the interface of the SEI and the active electrode particle. We find the tangential stress reaches a maximum at the surface of the particle when the lithium removal is just started. When we compare the maximum tensile tangential stress at the core side of the interface with the results of a model of a spherical particle without any consideration of presence of SEI (*20*), we find presence of SEI in general decreases the maximum stress.

In Figure 8.5, we plot the variation of maximum tangential stress during de-insertion with the thickness of the SEI. As the thickness of the SEI increases, the maximum tangential stress in the core as well as the shell decreases.

Here we plot the variation of maximum stress for different values of equilibrium concentration ratio K. We find that, as the value of K increases, the maximum tangential stress on the core side decreases. The relative thickness $\left({}^{t}/_{R}\right)$ of the SEI can be increased by either increasing the SEI thickness (t) or by decreasing the particle radius (R).

Similar trends are observed for radial stress dependence on SEI thickness i.e. as the SEI thickness increases, maximum radial stress at the center decreases (not shown here).

Next, we fix the thickness of the SEI to 1% of the total radius of the particle and vary the stiffness of the SEI relative to the active core modulus. We maintain the other properties the same as before, *i.e.*, $D_{SEI}/D_{\alpha} = 1, C_0^{\alpha}/C_0^{SEI} = 1$. Figure 8.6 plots the variation in the maximum radial stress during insertion as a function of relative stiffness of SEI E_{SEI}/E_{α}. As the value of E_{SEI}/E_{α} increases, the maximum radial stress during insertion decreases. This is intuitively understandable since the stiffer SEI will impose more opposition to expansion, which would lead to an increase in the compressive stress and thus a decrease in the overall tensile stress.

Similarly, Figure 8.7 plots the variation in the maximum tangential stress during de-insertion as a function of the relative stiffness of the SEI E_{SEI}/E_{α}. As the value of E_{SEI}/E_{α} increases, the maximum tangential stress in the core region during de-insertion decreases. We plot the variation of the maximum tensile tangential stress with different values of ξ, *i.e.*, D_{SEI}/D_{α}. We find that as the diffusion coefficient of the SEI decreases,

the maximum stress in the core also decreases. This might be attributed to the lower concentration gradients in the active core due to the relatively slower diffusion in the SEI shell, thus in effect decreasing the electrochemical Biot number.

The magnitude of maximum tangential stresses (tensile) in the shell region, in fact, increases with increase in the stiffness of the SEI layer. However, with increase in the stiffness of the SEI shell, the strength of the shell also changes.

In terms of the stress criteria, the Griffith toughness of model I crack is related to the theoretical strength, which is the stress required to pull apart two planes in a perfect solid (*31*). Using the theoretical strength, we have

$$\sigma_{max} = \sqrt{E\gamma/a_0} \tag{8.22}$$

Hence, we define the fracture tendency as the ratio of maximum stress and the theoretical strength of the shell material. In Figure 8.8, we plot the fracture tendency of the SEI as a function of the stiffness of the SEI. We observe that the fracture tendency of the shell decreases with increase in SEI stiffness.

$$Fracture\ tendancy \propto \frac{Maximum\ stress}{Theoretical\ strength}$$

In general, an increase in stiffness and thickness of the SEI would decrease the maximum tensile stress the material experiences during either lithiation or de-lithiation. Also, decreasing the diffusion coefficient of the SEI decreases the maximum value of the tensile stress during either lithiation or de-lithiation.

8.5 Strain energy calculations

Following Cheng and Verbrugge (*22, 28*), we calculate the bulk strain energy per unit volume, or the bulk strain energy density, $e(r)$, accumulated as a result of the elastic deformation for the isotropically deformed sphere as (*26*)

$$e(r) = \frac{1}{2E}\left(\sigma_r^2 + 2\sigma_\theta^2\right) - \frac{\nu}{E}\left(2\sigma_r\sigma_\theta + \sigma_\theta^2\right) . \tag{8.23}$$

The total bulk strain energy can be obtained by integrating the strain energy density over the entire volume.

In the core-shell model, the total bulk energy is the sum of strain energies in both the phases. The bulk strain energy of such an electrode particle in dimensionless form is

$$\Pi_{bulk} = \frac{W_{bulk}}{2\pi R^3 E_\alpha\left(\frac{\Omega_\alpha \quad C_0^\alpha}{3 \ (1-\nu_\alpha)}\right)^2} = \int_0^{\left(r_i/R\right)} \left[\left(\xi_r^2 + 2\xi_\theta^2\right) - 2\nu_\alpha\xi_\theta(2\xi_r + \xi_\theta)\right]x^2dx \ +$$

$$\int_{\left(r_i/R\right)}^1 \frac{E_{SEI}}{E_\alpha}\left[\left(\xi_r^2 + 2\xi_\theta^2\right) - 2\nu_{SEI}\xi_\theta(2\xi_r + \xi_\theta)\right]x^2dx \tag{8.24}$$

When we plot (Figure 8.9) the strain energy versus time, we observe that the strain energy increases initially, reaches a peak value, and then decreases A finite amount of energy is stored in the particle at the end of lithiation since the final state of the particle is not stress-free after complete lithiation. The stored strain energy may transform to surface energy by fracture; hence, strain energy can drive crack propagation The energy stored in the particle at the end of previous lithiation might lead to detrimental effects since there is large tangential stress at the start of lithiation. In Figure 8.10 & 8.11, we plot the variation of maximum strain energy as a function of SEI thickness and SEI stiffness.

We see that the maximum strain energy does not change much. However, the energy stored at the end of lithiation increases more rapidly with an increase in either SEI thickness or SEI stiffness. Also from Figure 8.11, we observe that if the SEI layer has very high relative stiffness, the strain energy stored at the end of lithiation is the maximum strain energy stored by the particle during the process of lithiation.

Thus, considering strain energy stored as a driving force for fracture, there should be a limit for the stiffness and thickness of the SEI to minimize the fracture tendency of the particle.

8.6 Conclusions

We developed a model for that couples mechanical and chemical degradation of electrode particle. Diffusion-induced stresses in insertion electrodes are affected by the properties of the SEI such as thickness, stiffness, diffusion coefficient, and equilibrium concentration. This model follows the convention of assuming the electrode particle to be an homogeneous isotropic particle. Under such an assumption we show the following:

1. Effect on stresses:
    - The radial stress (tensile) during lithiation and tangential stress (tensile) during delithiation decreases due to presence of the SEI.
    - The SEI constrains the expansion of the active electrode particle on lithiation. Hence, the active core is under compression at the end of lithiation.
    - There is discontinuity in tangential stress across the interface between the SEI and the active electrode particle.

- The maximum radial stress (tensile) during lithiation and tangential stress (tensile) during de-lithiation decreases lineally with an increase in stiffness or thickness of the SEI.
- The maximum radial stress (tensile) during lithiation and tangential stress (tensile) during de-lithiation decreases with decrease in diffusion coefficient or equilibrium concentration of solute in the SEI.
- The fracture tendency in terms of stresses in the SEI layer also decreases with an increase in either stiffness or thickness of the SEI layer.

Thus, a stiffer and thicker SEI can be helpful in decreasing the overall stresses of the electrode particle.

The SEI thickness can be increased by increasing the thickness of the coating or for by decreasing the size of the electrode particles and thus increasing the dimensionless thickness t/R .

2. Effects on strain energy:
    - Maximum strain energy and strain energy at the end of lithiation are affected by the properties of SEI
    - There is small increase in maximum stress energy with increasing stiffness.
    - The strain energy stored at the end of lithiation increases rapidly with an increase in either thickness or stiffness of the SEI. This might be detrimental since strain energy stored could be relieved by creating new fracture surfaces and resulting in cracking of the particle.

Hence, the stiffness or thickness of the SEI should be optimized taking into account both the stress and the strain energy.

Although actual electrode particles may not be homogeneous and isotropic(*24*), the model developed in this work can provide semi-quantitative predictions about the stresses and their behavior for various electrode/SEI systems.

8.7 List of symbols

r, θ, φ	spherical coordinates
Ω_{i}	partial molar volume of the solute in phase 'i' (m^3/mol)
R	radius of the spherical electrode particle (m)
t	thickness of SEI
r_i	radial location of interface between active core and SEI form the center of particle (m)
ν_{i}	Poisson's ratio of phase 'i'
E_{i}	Young's modulus of phase 'i' (N/m^2)
u	radial displacement (m)
σ_r	radial stress (N/m^2)
σ_θ	tangential stress (N/m^2)
σ_{shear}	shear stress (N/m^2)
ε_{rr}	radial strain
$\varepsilon_{\theta\theta}$	tangential strain
$C(r,t)$	solute concentration at radius r at time t (mol/m^3)
C_0^{SEI}	equilibrium concentration of solute in SEI layer (mol/m^3)

C_0^α	initial concentration of solute in active core phase (mol/m^3)
K	ratio of equilibrium concentrations at the interface C_0^α/C_0^{SEI}
C_R	concentration of the solute on the particle surface (mol/m^3)
$\mathcal{D}_{SEI}$	diffusion coefficient of the solute in SEI phase (m^2/sec)
D_α	diffusion coefficient of the solute in α phase (m^2/sec)
T	time
x	dimensionless radius
x_i	dimensionless radial location of interface
τ	dimensionless time
y	dimensionless concentration
ξ_i	dimensionless stress in i direction
ξ_θ	dimensionless tangential stress
e(r)	local strain energy density (J/m^3)
W_{bulk}	total strain energy stored due to bulk deformation (J)
$\prod_{bulk}$	dimensionless bulk strain energy
$\prod_{bulk}\|_{max}$	maximum dimensionless strain energy stored

8.8 Reference:

1. J. M. Tarascon, M. Armand, Issues and challenges facing rechargeable lithium batteries. *Nature* **414**, 359 (2001).
2. R. Deshpande, Y. Qi, Y.-T. Cheng, Effects of Concentration-Dependent Elastic Modulus on Diffusion-Induced Stresses for Battery Applications. *Journal of The Electrochemical Society* **157**, A967 (2010).
3. D. Aurbach, Review of selected electrode-solution interactions which determine the performance of Li and Li ion batteries. *Journal of Power Sources* **89**, 206 (2000).
4. E. Markervich, G. Salitra, M. Levi, D. Aurbach, Capacity fading of lithiated graphite electrodes studied by a combination of electroanalytical methods, Raman spectroscopy and SEM. *Journa of Power Sources* **146**, 146 (2005).
5. E. Peled, D. Golodnitsky, C. Menachem, D. Bar-Tow, An Advanced Tool for the Selection of Electrolyte Components for Rechargeable Lithium Batteries. *Journal of The Electrochemical Society* **145**, 3482 (1998).
6. S. S. Zhang, K. Xu, T. R. Jow, EIS study on the formation of solid electrolyte interface in Li-ion battery. *Electrochimica Acta* **51**, 1636 (2006).
7. V. A. Sethuraman, L. J. Hardwick, V. Srinivasan, R. Kostecki, Surface structural disordering in graphite upon lithium intercalation/deintercalation. *Journal of Power Sources* **195**, 3655 (2010).

8. K. Tasaki *et al.*, Solubility of Lithium Salts Formed on the Lithium-Ion Battery Negative Electrode Surface in Organic Solvents. *Journal of The Electrochemical Society* **156**, A1019 (2009).

9. K. Tasaki, S. J. Harris, Computational Study on the Solubility of Lithium Salts Formed on Lithium Ion Battery Negative Electrode in Organic Solvents. *J. Phys. Chem. C* **114**, 8076 (May, 2010).

10. Y. Ein-Eli, A new perspective on the formation and structure of the solid electrolyte interface at the graphite anode of Li-ion cells. *Electrochem. Solid State Lett.* **2**, 212 (May, 1999).

11. S. S. Zhang, A review on electrolyte additives for lithium-ion batteries. *Journal of Power Sources* **162**, 1379 (Nov, 2006).

12. S. Menkin, D. Golodnitsky, E. Peled, Artificial solid-electrolyte interphase (SEI) for improved cycleability and safety of lithium-ion cells for EV applications. *Electrochemistry Communications* **11**, 1789 (2009).

13. L. J. Fu *et al.*, Surface modifications of electrode materials for lithium ion batteries. *Solid State Sci.* **8**, 113 (Feb, 2006).

14. Y. Li, Y.-T. Cheng, Studies of Metal Hydride Electrodes Using an Electrochemical Quartz Crystal Microbalance. *Journal of The Electrochemical Society* **143**, 120 (1996).

15. R. Huggins, W. Nix, Decrepitation model for capacity loss during cycling of alloys in rechargeable electrochemical systems. *Ionics* **6**, 57 (2000).

16. J. Christensen, J. Newman, A Mathematical Model of Stress Generation and Fracture in Lithium Manganese Oxide. *Journal of The Electrochemical Society* **153**, A1019 (2006).

17. J. Christensen, J. Newman, Stress generation and fracture in lithium insertion materials. *Journal of Solid State Electrochemistry* **10**, 293 (2006).

18. X. Zhang, W. Shyy, A. M. Sastry, Numerical Simulation of Intercalation-Induced Stress in Li-Ion Battery Electrode Particles. *Journal of The Electrochemical Society* **154**, A910 (2007).

19. X. Zhang, A. M. Sastry, W. Shyy, Intercalation-Induced Stress and Heat Generation within Single Lithium-Ion Battery Cathode Particles. *Journal of The Electrochemical Society* **155**, A542 (2008).

20. Y.-T. Cheng, M. W. Verbrugge, The influence of surface mechanics on diffusion induced stresses within spherical nanoparticles. *Journal of Applied Physics* **104**, 083521 (2008).

21. Y.-T. Cheng, M. W. Verbrugge, Automotive traction battery needs and the influence of mechanical degradation of insertion electrode particles. *Electrochemical Society Transactions* **16**, (2008, 2008).

22. Y.-T. Cheng, M. W. Verbrugge, Evolution of stress within a spherical insertion electrode particle under potentiostatic and galvanostatic operation. *Journal of Power Sources* **190**, 453 (2009).

23. R. Deshpande, Y.-T. Cheng, M. W. Verbrugge, Modeling diffusion-induced stress in nanowire electrode structures. *Journal of Power Sources* **195**, 5081 (2010).

24. S. Harris, R. Deshpande, Y. Qi, Y. T. Cheng, I. Dutta, Mesopores inside electrode particles can change the Li-ion transport mechanism and diffusion-induced stress. *J. Mater. Res.* **25**, (August, 2010).

25. R. Hetnarski, R. Eslami, *Thermal Stresses -- Advanced Theory and Applications (Solid Mechanics and Its Applications)*. (Springer, 2008).

26. S. Timoshenko, J. N. Goodier, *Theory of elasticity, by S. Timoshenko and J.N. Goodier*. (New York, McGraw-Hill, 1951).

27. J. Crank, *The Mathematics of Diffusion*. (Oxford University Press, USA, 1980).

28. Y.-T. Cheng, M. W. Verbrugge, Application of Hasselman's Crack Propagation Model to Insertion Electrodes. *Electrochemical and Solid-State Letters* **13**, A128 (2010).

29. M. W. Verbrugge, Y.-T. Cheng, Stress and Strain-Energy Distributions within Diffusion-Controlled Insertion-Electrode Particles Subjected to Periodic Potential Excitations. *Journal of The Electrochemical Society* **156**, A927 (2009).

30. K. Jagannathan, Approximate Solution Methods for Solid-State Diffusion in Phase-Change Electrodes. *Journal of The Electrochemical Society* **156**, A1028 (2009).

31. L. Le May, *Principles of mechanical metallurgy*. (Elsevier North-Holland, New york, 1981).

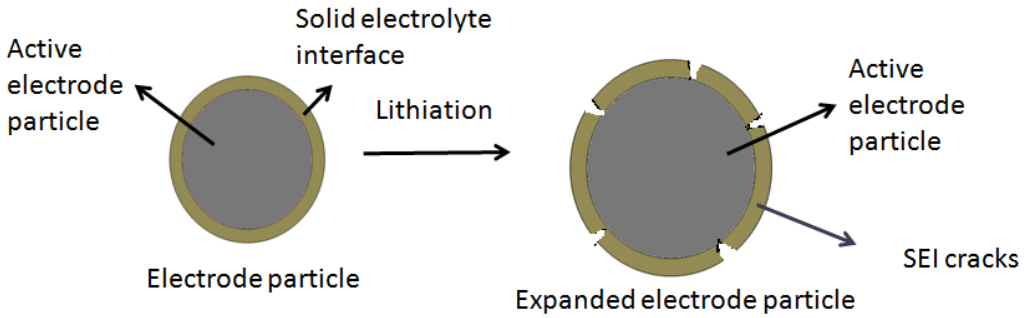

Figure 8.1: A schematic diagram indicating that, initially, before lithiation particle/ SEI layer makes a shell surrounding the active material core.

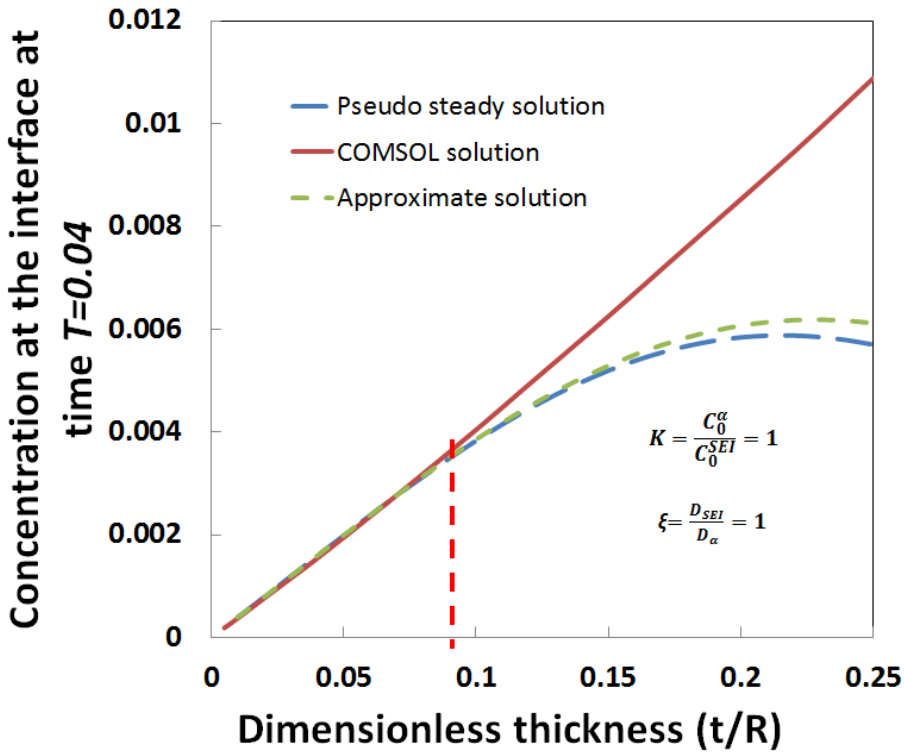

Figure 8.2: a. A plot showing the interface concentration (shell side) of the solute during de-insertion at a time $\tau = 0.4$ for different SEI thicknesses calculated using COMSOL, approximate solution and pseudo steady solution

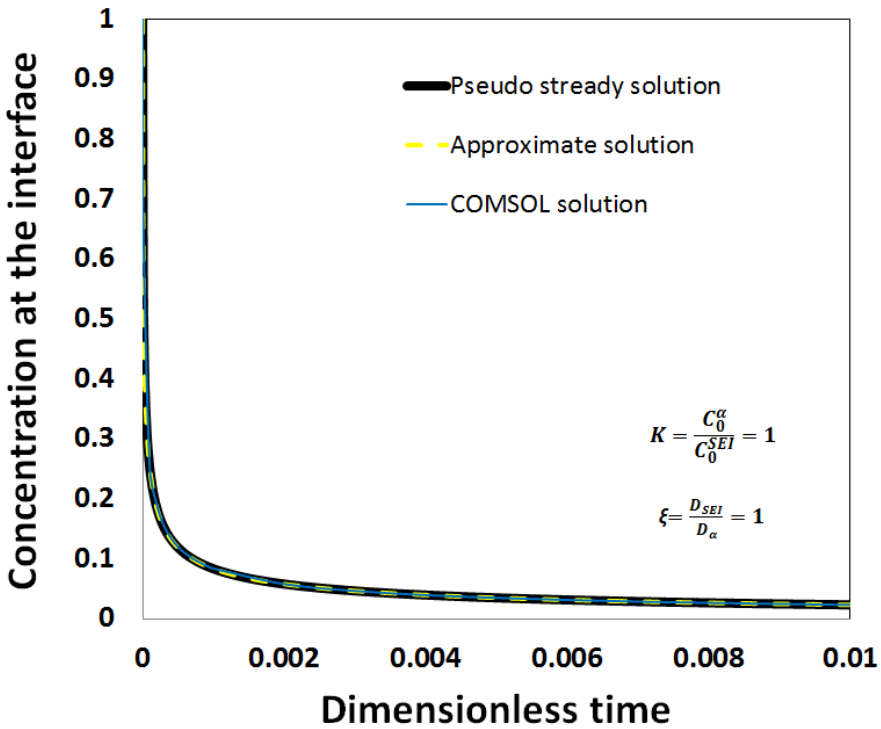

Figure 8.2: b. A plot showing the interface concentration (shell side) of the solute during de-insertion as a function of time for different SEI thicknesses calculated using COMSOL, approximate solution and pseudo steady solution

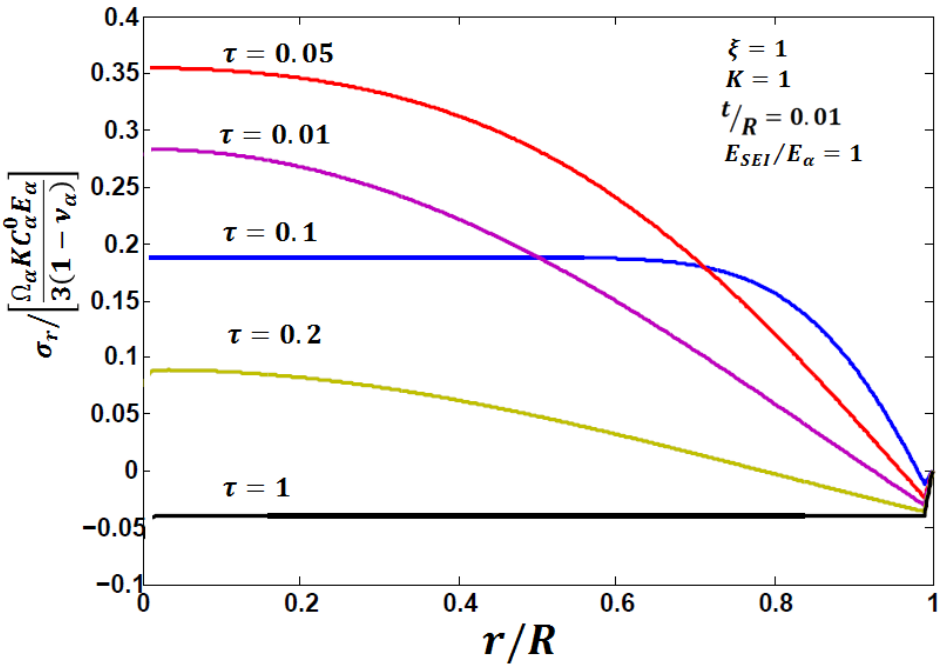

Figure 8.3: A plot of the radial stress during lithiation inside an electrode particle at different radial locations at different times in presence of SEI

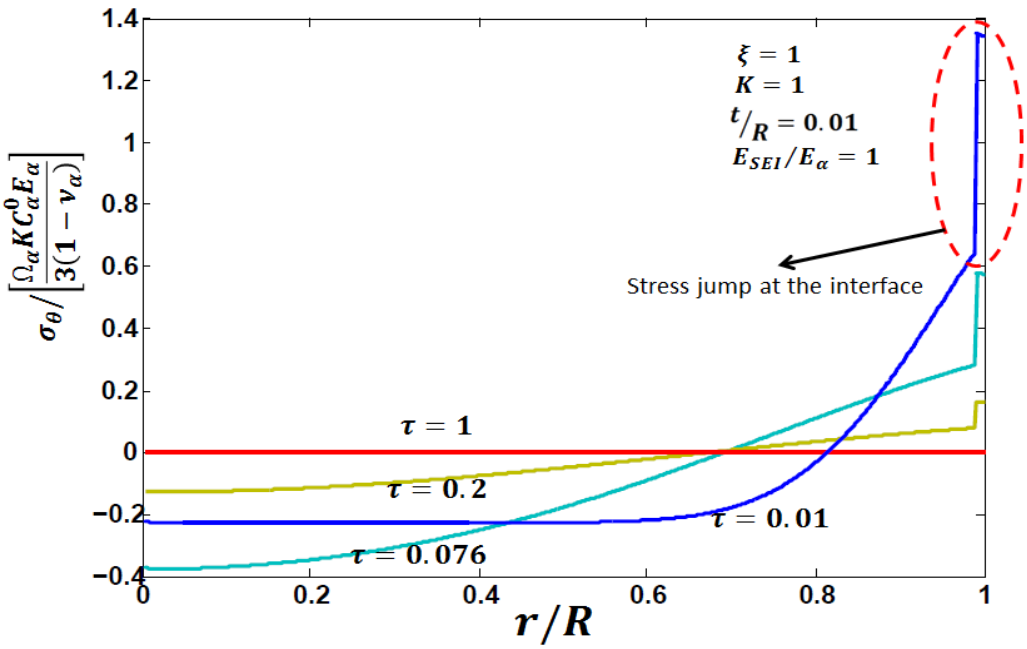

Figure 8.4: A plot of the tangential stress during de-lithiation inside an electrode particle at radial locations and times in presence of SEI. There is a jump in the stress at the interface between SEI and active core.

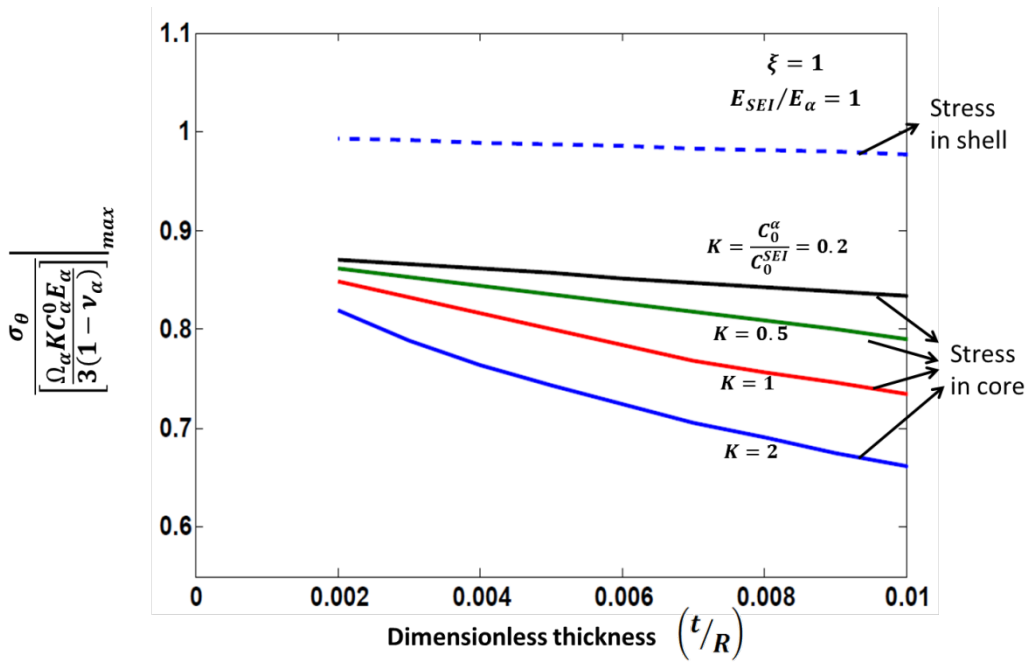

Figure 8.5: A plot of the maximum tangential stress inside an electrode particle during delithiation as a function of change in SEI thickness for different values of relative equilibrium concentration of SEI (K) with $E_{SEI}/E_\alpha = 1$ and $\xi = D_{SEI}/D_\alpha = 1$.

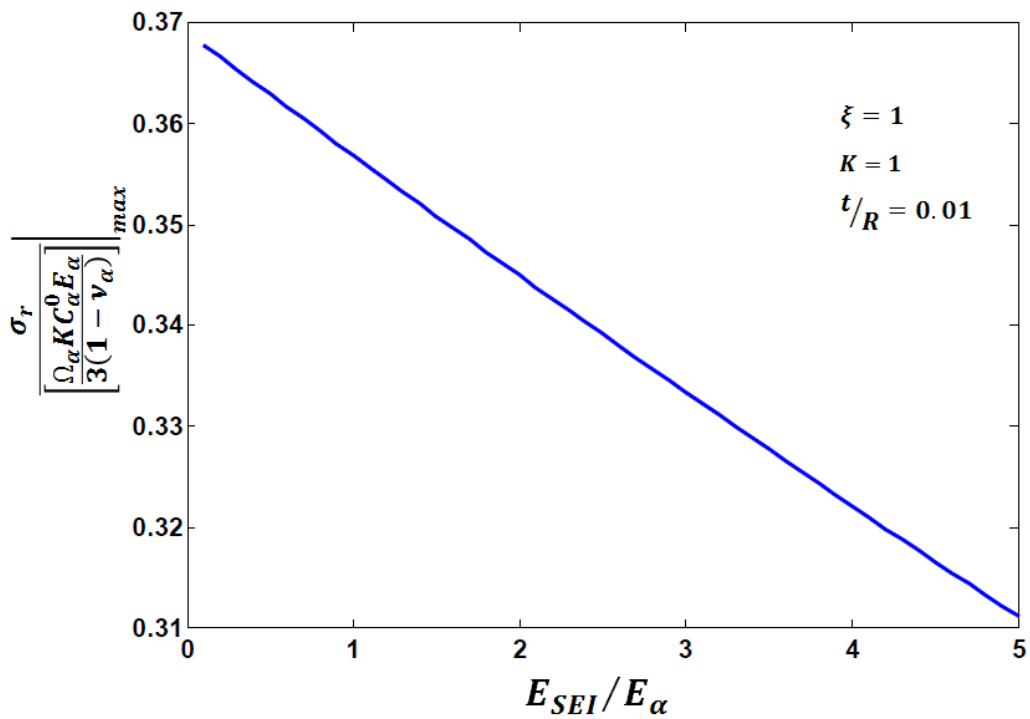

Figure 8.6: A plot of the maximum radial stress inside an electrode particle during lithiation as a function of change in SEI stiffness with $t/R = 0.01$.

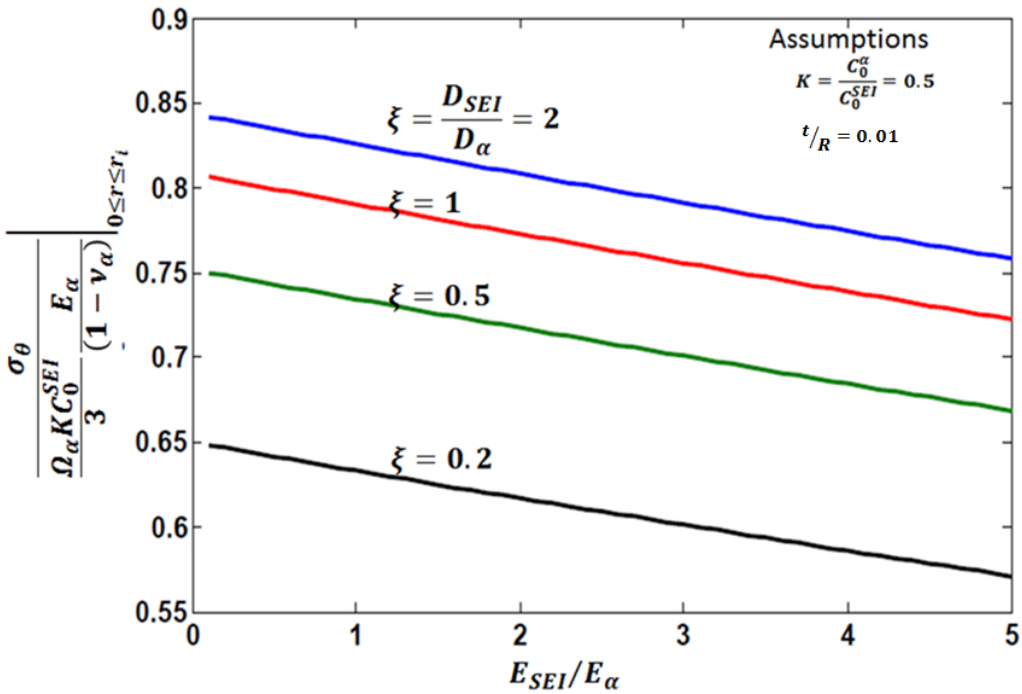

Figure 8.7: A plot of the maximum tangential stress inside an active core part of the electrode particle during delithiation as a function of change in SEI stiffness for different values of relative diffusion coefficient of SEI (ξ) with $t/R = 0.01$ and $C_0^\alpha/C_0^{SEI} = 1$.

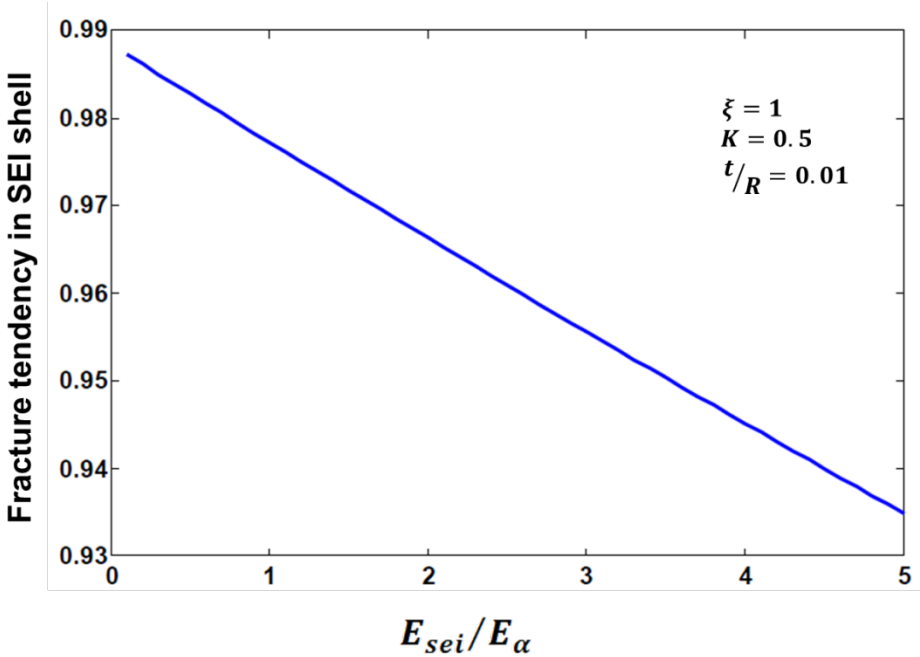

Figure 8.8: A plot of the fracture tendency inside SEI layer part of the electrode particle during lithiation as a function of change in SEI stiffness with $t/R = 0.01$, $C_0^{\alpha}/C_0^{SEI} = 1$ and $D_{SEI}/D_{\alpha} = 1$.

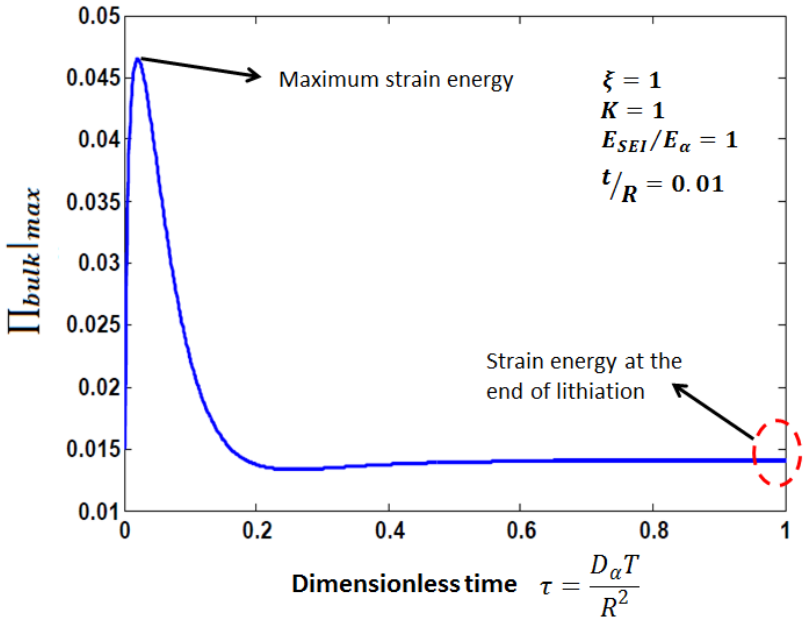

Figure 8.9: Variation of dimensionless strain energy stored with time during lithiation in presence of SEI. We assumed thickness $t/R = 0.01$, $E_{SEI}/E_\alpha = 1$, $C_0^\alpha/C_0^{SEI} = 1$ and $D_{SEI}/D_\alpha = 1$.

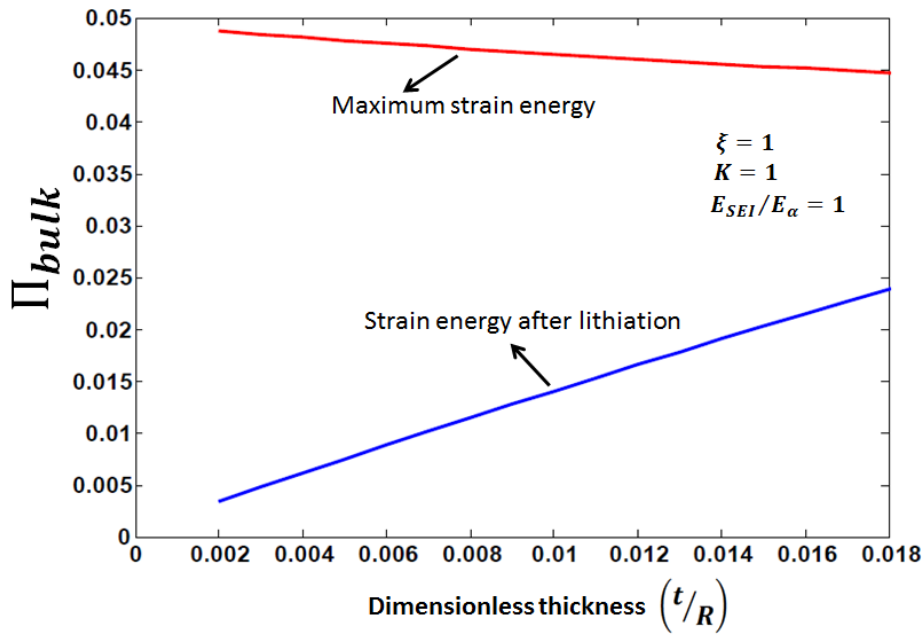

Figure 8.10: A plot of peak strain energy variation with different values of relative thickness (t/R) of SEI (dotted red line). Also, a plot of strain energy stored at the end of lithiation variation with different values of relative thickness (t/R) of SEI (blue line). We assume $E_{SEI}/E_{\alpha} = 1$, $C_0^{\alpha}/C_0^{SEI} = 1$ and $D_{SEI}/D_{\alpha} = 1$.

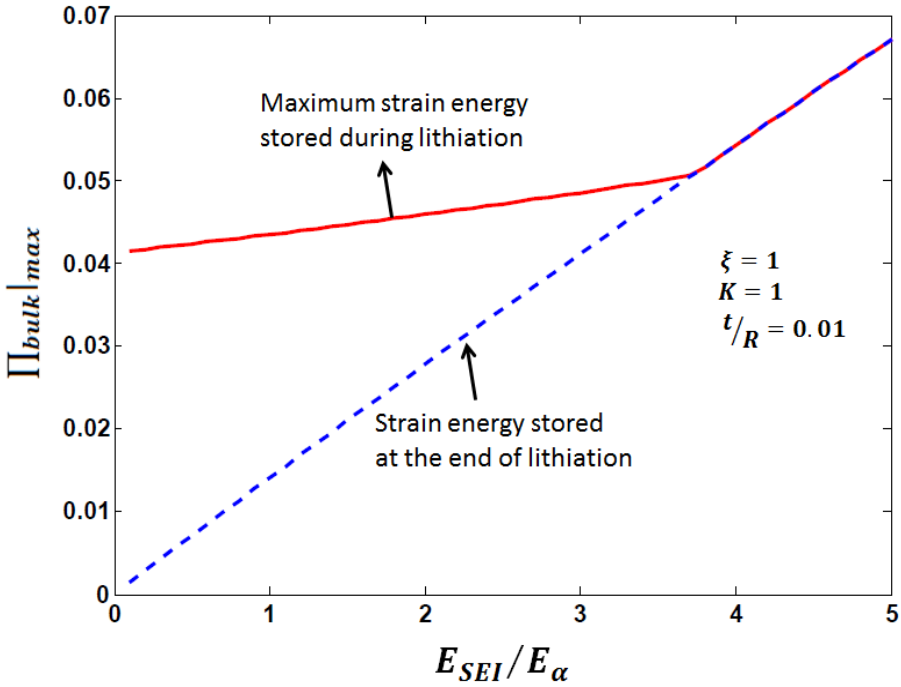

Figure 8.11: A plot of peak strain energy variation with different values of relative stiffness (E_{SEI}/E_{α}) of SEI (dotted red line). Also, a plot of strain energy stored at the end of lithiation variation with different values of relative thickness (t/R) of SEI (blue line). We assume $t/R = 0.01$, $C_0^{\alpha}/C_0^{SEI} = 1$ and $D_{SEI}/D_{\alpha} = 1$.

CHAPTER 9

BATTERY CYCLE LIFE PREDICTION WITH COUPLED CHEMICAL DEGRADATION AND FATIGUE MECHANICS

9.1 Summary

The coupled mechanical-chemical degradation of electrodes upon electrochemical cycling has been recognized as a major reason of capacity fading in lithium ion batteries. The instability of commonly employed electrolytes at the operating potentials results in electrolyte reduction on the negative electrode surface, thus a solid electrolyte interphase (SEI) is formed. Although the SEI layer is necessary, as it passivates the electrode-electrolyte interface from further solvent decomposition, the SEI formation contributes to the irreversible capacity loss. The SEI formation results in capacity loss due to the chemical degradation. Lithium diffusion in the electrode particles results in 'diffusion induced stresses' (DISs). DISs may lead to the mechanical degradation thus resulting in capacity loss due to electrode cracking, fracture, pulverization or structural changes. In this chapter, with experimental evidence, we propose a model explaining a loss of active lithium from the system as a major mechanism of capacity fading of the commercial lithium iron phosphate ($LiFePO_4$) lithium ion battery. The pre-existing cracks on the electrode surface grow gradually upon cycling due to the DISs, causing the formation of a new SEI on the newly exposed electrode surfaces. Because lithium is consumed in SEI formation, the irreversible capacity loss continues with cycling. Along with the new SEI formation, growth in thickness of the existing SEI with time results in additional loss of active material.

In this study, we provide a simple mathematical model, which uses Paris' law formulation from fatigue mechanics in combination with chemical degradation to predict the capacity fading for $LiFePO_4$ lithium ion batteries. We compare the predicted capacities at different cycle number at different operating temperatures with the experimental data of A123 batteries.

9.2 Introduction

With the potential use of lithium ion batteries for the propulsion purpose in automobile industry, the cycle life prediction of the commercial lithium ion batteries has become of utmost importance. Battery capacity decays upon electrochemical cycling as a result of several degradation mechanisms such as the irreversible lithium loss due to solid electrolyte interphase (SEI) formation, electrode particle cracking, electrode particle isolation *etc*. Among these degradation mechanisms, the chemical degradation, as a result of SEI formation, has been widely recognized as a major cause of loss of active lithium content (*1-3*). The 'calendar life' of a lithium ion battery is associated with the chemical degradation. Spotnitz *et al.* (*4*) give a nice review of different capacity fading experiments and models predicting the calendar life of a battery. Some of the models such as that of Bloom *et al.* (*5*) are purely empirical and might not describe the physics behind the degradation. Many of the other life prediction models in the literature such as that of Christensen and Newman (*6*) consider the chemical degradation as a major source of capacity fading and thus predict the calendar life of the battery (*6-13*). Broussely *et al.* (*14*) attempted to understand the capacity loss of batteries at different temperatures with controlled experiments and put forward a simple mathematical model which predicts the calendar life.

Ning *et al.* (*15*) developed a computer simulation based on the solvent reduction on the electrode-electrolyte interface as a major source of lithium loss. Safari *et al* (*7, 8*) used a different approach and took fatigue mechanics into account for battery life prediction. Ramadass *et al.* (*16*) developed a capacity fade prediction model for Li-ion cells based on a semi-empirical approach. Santhanagopalan *et al.* (*17*) has a nice review of the cycle life prediction models. Along with the chemical degradation, mechanical degradation is also a major reason of capacity fading which is not paid enough attention by the reported life cycle prediction models. The mechanical degradation of batteries occurs due to diffusion induced stresses (DISs) as a result of the lithium insertion and removal from the electrode particles. A good number of articles in the literature discuss the mechanical stresses in single electrode particles (*18-21*). Recently, through different mathematical models we investigated the effects of different operating conditions, different electrode particle sizes, particle shapes, phase transformations *etc.* on the DISs (*22-26*). In this chapter we couple the mechanical degradation with chemical degradation to develop a simple model to predict the lithium ion battery life.

$LiFePO_4$ based lithium ion battery has been considered as one of most promising candidates for large scale applications in the automotive and space industries because of its excellent chemical and thermal stability and low cost (*27-31*). Liu *et al.* (*32*) established lithium loss as a major mechanism for capacity fading of the battery. Wang *et al.* (*33*) presented a semi-empirical model for life cycle prediction. A phenomenological life model combining the chemical degradation with mechanical degradation to predict capacity fading is still needed.

We cycle the commercial A123 batteries at different temperatures with the potentiostatic and galvanostatic conditions. We monitor the capacity fade as a function of number of cycles. Here, with cycling experiments and model results, we again confirm the lithium loss as a major the aging mechanism of $LiFePO_4$ lithium ion battery cells using both destructive physical analysis and non-destructive electrochemical analysis. We propose a mathematical model to describe the lithium loss phenomena which results from coupled chemical and mechanical degradation. We find that the model predicts the battery life with fair accuracy. In addition, we regenerate the voltage and differential voltage curves for the batteries at different cycle number and find that they are in nice agreement with the experimental voltage curves. Furthermore, we degenerate the cell voltage curve into the individual electrode voltages, to understand the individual electrode behavior with cycling. To the best of our knowledge this is the first attempt to couple chemical degradation with mechanical degradation for the cycle life prediction of lithium ion batteries.

9.3 Theory

We assume the thin film electrode consist of a large number of spherical particles with a uniform size. Freshly exposed surfaces give rise to the SEI formation during the subsequent charge due to reduction of the electrolyte in the presence of high lithium contents within the carbon host. For example, the ethylene carbonate solvent can be reduced in the presence of lithiated carbon (*3*).

$2[Li\text{-}S] + 2e^- +$ 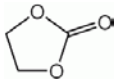 $\longrightarrow Li_2CO_3 + H_2C{=}CH_2 + 2S$

where the lithium carbonate leads to SEI formation, stabilization of the exposed surface, and a loss of lithium from the cell. The lithium guest species corresponds to [Li-S], where S is a vacant site within the host carbon (*34*). We assume the newly exposed surface is covered by a new SEI over the subsequent charge cycle, as described above relative to the formation of Li_2CO_3. We also assume that, the existing SEI gradually grows in thickness with time till it is stabilized at a certain thickness.

As a result of the DISs, the pre-existing cracks at the particle surface propagate upon electrochemical cycling. On each cycle the newly cracked surface is exposed to the electrolyte and thus results in SEI formation. Figure 9.1 represents the schematics of the lithium loss as proposed. The capacity loss of a commercial battery is associated with the lithium loss from the system.

9.4 Experimental

Our collaborators Ping Liu and John Wang at HRL Laboratories LLC (Malibu, CA 90265-4797) did the experimental part. The commercially available 2.2 Ah, 28650 cylindrical cells were purchased from A123 Systems in which the material chemistry is composed of $LiFePO_4$ cathode and carbon anode. The cycling was done at (C/2) rate, 90% depth of discharge (DOD) at three different temperatures (15, 45, 60°C). In defining the DOD and C rates, the cell is de-rated to 2 Ah. The cut-off voltages for the cycle test of all the cells were at 3.6 V and 2.0 V. The cells were charged to 3.6 V and held at 3.6 V until the current dropped below 0.1A for a maximum of 2 days.

For the cell characterization Wang *et al*. (*32*) is followed. For each of the cells tested, the cell capacity measured at a C/20 rate during characterization was used for the subsequent modeling work.

9.5 Experimental results and discussion:

With a reference electrode arrangement (*32*) we could generate potential vs. state of discharge (SOD) curves for individual electrodes of a commercial A123 battery, shown as solid lines in Figure 9.2. We find that, iron phosphate ($FePO_4$) electrode voltage is fairly constant for the entire SOD range (blue solid curve), on the other hand negative carbon electrode undergoes staging (red solid curve) and thus phase transformations (*35*) upon lithiation or delithiation. We also plot the dV /d(SOD) against the SOD for individual electrodes, in Figure 9.2 (symbols). We observe that the negative electrode dV/d(SOD) curve (red symbols) shows peaks for the graphite staging at the same time dV/d(SOD) curve for $FePO_4$ (blue symbols) is fairly constant and does not show any variation.

With the experimental setting as described above, we could monitor the capacity fading of A123 batteries upon electrochemical cycling. The cycling is done with 90% depth of discharge (DOD) and C/2 operating rate. We are informed that the formation cycles had already been done at the manufactures end. Hence, the first cycle tested in our laboratory is termed as cycle number ‘2’. Figure 9.3 shows the measured voltage against capacity curves for A123 battery at 45^0C at cycle number 2, 436 and 963. We find that, as we cycle the battery, the discharge voltage is reached quickly. Thus the capacity fading of the battery with cycling can be easily observed.

We calculate the differential voltage d(Voltage, V) /d(Capacity, Ah) for the full cell at different cycle number for that cell. We plot the experimentally obtained differential voltage against cell capacity (Ah) at different cycle numbers (Figure 9.4). There differential voltage curves for different cycle numbers have a similar peak pattern. Since, there are no peaks in the differential voltage curves of the $FePO_4$ electrodes, all the peaks in Figure 9.4 actually correspond to the graphite staging. The distance between any two peaks represents width of a stage. In other words it represents the amount of lithium that can be stored in a particular stage of graphite electrode. The differential voltage curves in Figure 9.4 are for the same cell cycled at different cycle numbers 2, 436 and 963. We find that the distance between any two peaks in all three cases remains the same, at the same time, the whole curve shifts to left on cycling decreasing the width of last graphite stage. A constant distance between the peaks over cycle implies that the amount of active carbon to store lithium is fairly constant upon cycling. At the same time, there is a shift of the differential voltage curves to the left which indicates the capacity loss is due to the loss of lithium from the system. Thus, these experimentally obtained differential voltage curves confirm our initial assumption that, the capacity loss in the commercial A123 batteries is due to the lithium loss in the SEI formation and most of the carbon is still active and contribute minimally to the total capacity loss.

9.6 Mathematical model:

We assume capacity loss in a battery is solely because of the irreversible lithium loss and the electrode material is intact and active for lithiation

The total lithium loss during cycling might be divided in following 4 sections

i. The lithium loss due to SEI formation on first cycle. This is related to the SEI formation on the surface of the spherical particle with the pre-existing cracks and a new surface formed on the propagation of cracks at the end of the first cycle.

ii. The lithium loss due to SEI formation on the newly formed surface due to crack propagation during subsequent cycles.

iii. The lithium loss due to the thickness growth of the SEI formed on the first cycle.

iv. The lithium loss due to the thickness growth of the new SEI formed in the subsequent cycles on the new surface exposed due to crack propagation.

The first cycle capacity loss is related to the particle surface area. The total rate of capacity loss after initial SEI formation cycles *i.e.* after first cycle can be calculated using mechanism (ii),(iii) and (iv) as:

$$\frac{dQ}{dN} = \frac{dQ}{dN_{SEI\ formation\ due\ to\ crack\ propagation}} + \frac{dQ}{dN_{SEI\ thickness\ growth\ on\ spherical\ surface}} + \frac{dQ}{dN_{SEI\ thickness\ growth\ on\ cracked\ surface}} \quad (9.1)$$

9.6.1 Loss of lithium due to SEI formation on the new surface formed due to crack propagation

The diffusion in the spherical particle for the galvanostatic charging condition can be described with the Fick's law of diffusion. Diffusion equation for transport inside a spherical electrode particle can be written as

$$\frac{\partial C}{\partial t} = \frac{D}{r^2}\left(\frac{\partial}{\partial r}\left(r^2 \frac{\partial C}{\partial r}\right)\right) \tag{9.2}$$

with initial and boundary conditions:

$$C(r,0) = C_0\,, \qquad for\ 0 \le r \le R$$

$$D\left.\frac{\partial C(r,t)}{\partial r}\right|_{r=R} = \frac{i}{F}, \qquad for\ t \ge 0$$

$$C(0,t) = finite, \qquad for\ t \ge 0 \tag{9.2a}$$

Here 'i' is the current over the particle surface.

The solution for galvanostatic condition is well-known (*36*): [1]

$$c(x,\tau) = c_0 + \frac{iR}{FD}\left[3\tau + \frac{1}{2}x^2 - \frac{3}{10} - \frac{2}{x}\sum_{n=1}^{\infty}\left(\frac{sin(\lambda_n x)}{{\lambda_n}^2 sin(\lambda_n)} exp\left(-{\lambda_n}^2\tau\right)\right)\right] \tag{9.3}$$

where $x = r/R\,, \tau = tD/R^2$, positive current densities i over the particle surface denote charge and $\lambda_n (n = 1,2,3, \dots)$ are the positive roots of $tan(\lambda_n) = \lambda_n$.

[1] The concentration $C(r,t)$ must be greater than zero and cannot exceed the concentration of available sites for the solute in the case of insertion electrodes, and this will place limits on the admissible values of the product It.

For thin film electrode with specific surface area a_s, thickness L and geometric area A, the current density 'i' can be calculated as

$$i = \frac{I_{cell}}{a_s(AL)_{PE}} \tag{9.4}$$

the specific surface a_s of the porous electrode is related to the radius R of the active spherical particles and overall their contribution to the solid phase porosity ε_{1a}, $a_s = 3\varepsilon_{1a}/R$. Hence,

$$i = \frac{I_{cell}R}{3\varepsilon_{1a}(AL)_{PE}} \tag{9.4a}$$

Cheng and Verbrugge (*36*) showed the maximum stress in a cell is at the surface of the electrode in the tangential direction at the beginning of delithiation. The magnitude of this stress is described as;

$$\sigma_\theta = -\frac{1}{3}\frac{E\Omega}{(1-\nu)}\left(\frac{iR}{FD}\right)\left[\frac{1}{5}(1-2x^2) + 2\sum_{n=1}^{\infty}\frac{exp(-\lambda_n^2\tau)}{\lambda_n sin(\lambda_n)}\left(\frac{sin(\lambda_n x)}{\lambda_n x} - \frac{sin(\lambda_n x) - (\lambda_n x)cos(\lambda_n x)}{\lambda_n^3 x^3}\right)\right] \tag{9.5}$$

We are interested in longer times; that is, the time for discharge $\tau_{dis} \gg \tau = tD/R^2$. Hence, the exponential terms in the stress equations tend to zero and summations can be neglected. Because the magnitude of the tangential stress σ_θ increases monotonically to an asymptote and is largest at the particle surface, we shall refer to the long-time asymptotic value of the surface tangential stress as $\sigma_{\theta,max}$.

Second, we restrict our attention to the cracks formed and growing at the particle surface. Since, the particle is taken to be isolated and we do not account for surface mechanics (e.g., surface tension) associated with nano size particles (*26*), the radial component of the stress at the surface is zero, and the tangential stress at the surface corresponds to

$$\sigma_{\theta,max} = -\frac{1}{15}\frac{E\Omega}{(1-\nu)}\left(\frac{iR}{FD}\right) = -\frac{1}{45}\frac{E\Omega}{(1-\nu)}\left(\frac{R^2}{FD}\right)\frac{I_{cell}}{\varepsilon_{1a}(AL)_{PE}} \tag{9.6}$$

The charge currents for the experiments in this work are C/20 which are quite low relative to those of discharge. Hence, in terms of stress over a cycle, the surface undergoes tensile stress during discharge in accordance with Equation 9.5 and relaxes during the majority of the charge cycles ($\sigma_{\theta,surface} = 0$ during charge). We employ the Paris' Law formulation to represent a surface crack of depth *a* growing with each charge-discharge cycle *N*,

$$\frac{da}{dN} = k\Delta K_I^m \tag{9.7}$$

where *k* and *m* are taken to be constants, and the difference in the mode I stress intensity factor K_I between the fully loaded state, corresponding to the steady-state constant current discharge, and the unloaded state (low current charge) is given by

$$\Delta K_I = \sigma_{\theta,max} b\sqrt{\pi a} \tag{9.8}$$

here, a is the depth of the crack. We assume that the electrode surface has pre-existing cracks of depth a_0 and the crack width 'w'. For the small surface crack we investigate,

$a \ll R$, and the constant b = 1.12 (*37*). Substituting Equations 9.6 and 9.8 into Equation 9.7, we obtain

$$\frac{da}{dN} = k\left[\sigma_{\theta,max} b\sqrt{\pi a}\right]^m \tag{9.9}$$

$$\frac{da}{dN} = k\left[-\frac{1}{45}\frac{E\Omega}{(1-\nu)}\left(\frac{R^2}{FD}\right)\frac{I_{cell}}{\varepsilon_{1a}(AL)_{PE}} b\sqrt{\pi a}\right]^m \tag{9.10}$$

$$a_0\frac{d\tilde{a}}{dN} = k\left[\sigma_{\theta,max} b\sqrt{\pi a}\right]^m = k\left[\sigma_{\theta,max} b\sqrt{\pi a_0}\right]^m \tilde{a}^{m/2} \tag{9.11}$$

$$\frac{d\tilde{a}}{d\tilde{N}} = \tilde{a}^{m/2} \tag{9.12}$$

here we define

$$\tilde{N} = k\left[\sigma_{\theta,max} b\sqrt{\pi}\right]^m {a_0}^{m/2-1} N = k\left[\sigma_{\theta,max} b\sqrt{\pi}\right]^m {a_0}^{\left(\frac{m-2}{2}\right)} N$$

and $\tilde{a} = a/a_0$

Integrating (9.12)

$$\int_1^{\tilde{a}} \frac{d\tilde{a}}{\tilde{a}^{m/2}} = \int_0^{\tilde{N}} d\tilde{N}$$

$$\tilde{a} = \left(1 + \frac{2-m}{2}\tilde{N}\right)^{\frac{2}{2-m}} \tag{9.13}$$

Equation 9.13 relates the crack depth with the number of cycles.

As the crack grows during discharge, a new surface of area $2l_{cr}(da)$ is exposed to the electrolyte. Here, l_{cr} is the length of the crack.

We take the number of cracks and the length of each crack to be the same throughout this particle life; that is, the cracks are all taken to be identical and grow in depth into the particle during each discharge half cycle. Hence, ρ_{cr} is defined as the surface crack density, i.e., the number of cracks per unit area of particle surface. We shall treat the surface density of the cracks as a constant, and it is determined by the initial number of cracks over the particle surface, $N_{cr} = 4\pi R^2 \rho_{cr}$. The total area associated with cracks is given by $A_{cr} = 8\pi R^2 \rho_{cr} a l_{cr}$. We can express the change in the total area associated with cracks for each discharge of cycle N as

$$\frac{dA_{cr}}{dN} = \frac{dA_{cr}}{da}\frac{da}{dN} = 8\pi R^2 l_{cr} \rho_{cr} k \left[\sigma_{\theta,max} b \sqrt{\pi a_0}\right]^m \tilde{a}^{m/2} \tag{9.14}$$

We assume the newly exposed surface is covered by a new SEI over the next charge cycle, as described above relative to the formation of Li_2CO_3.

SEI forms on the newly cracked surface as soon as it is exposed to the electrolyte, forming a layer of thickness L_{SEI}^0.

$$\frac{dQ}{dN}_{SEI\ formation\ due\ to\ crack\ propagation} = -\frac{n_{SEI} L_{SEI}^0 \rho_{SEI} F}{M_{SEI}} \frac{d(A_{cr})}{dN}$$

$$= -\frac{n_{SEI} F L_{SEI}^0 \rho_{SEI} 8\pi R^2 l_{cr} \rho_{cr}}{M_{SEI}} \left[\sigma_{\theta,max} b \sqrt{\pi a_0}\right]^m k \tilde{a}^{m/2}$$

(9.15)

9.6.2 Lithium loss due to increase in the thickness (L_{SEI}) of the initial SEI layer

Along with crack propagation, an increase in the thickness of the existing SEI upon cycling also contributes to the lithium loss from the cell. The increase in SEI thickness has been observed by several groups by increase in the resistance of the cell (*12*). We assume that SEI grows initially with the number of cycles and then stabilizes at a certain thickness. Most of the calendar life experiments and models assume that the thickness growth is time dependent and is proportional to square root of time (*4*). Since, the exact functional form of SEI growth during cycling is unknown; we assume SEI growth with the following equation

$$L_{SEI} = K_{th} N^{1/2} \tag{9.16}$$

Here K_{th} is a constant and is temperature dependent.

9.6.3 Lithium loss due to increase in the thickness (L_{SEI}) of the initial SEI layer.

First cycle is the SEI formation cycle. From the second cycle onwards, the SEI grows in thickness on the initial surface area of particle. Initial surface area of the spherical particle during the formation cycle would be the surface area of sphere with pre-existing cracks.

$$A_{initial} = spherical\ surface\ area$$
$$+ area\ associated\ with\ preexisting\ cracks\ on\ the\ surface$$

$$A_{initial} = 4\pi R^2 + 8\pi R^2 l_{cr} \rho_{cr} a_0 = 4\pi R^2 (1 + 2 l_{cr} \rho_{cr} a_0)$$

Hence, the rate of capacity loss upon cycling due to growth in thickness of SEI is;

$$\frac{dQ}{dN}_{SEI\ thickness\ growth\ on\ spherical\ surface} = -\frac{n_{SEI}F\rho_{SEI}}{M_{SEI}}A_{initial}\frac{dL_{SEI}}{dN}$$

$$= -\frac{n_{SEI}F\rho_{SEI}}{M_{SEI}}4\pi R^2(1+2l_{cr}\rho_{cr}a_0)\frac{dL_{SEI}}{dN}$$

(9.17)

Now, differentiating Equation 9.14 with respect to number of cycles we can get,

$$\frac{dL_{SEI}}{dN} = \frac{1}{2}K_{th}N^{-1/2} \tag{9.18}$$

$$\frac{dQ}{dN}_{SEI\ thickness\ growth\ on\ spherical\ surface} = -\frac{n_{SEI}F\rho_{SEI}}{M_{SEI}}4\pi R^2(1+2l_{cr}\rho_{cr}a_0)\frac{1}{2}K_{th}N^{-1/2}$$

(9.19)

9.6.4 Loss of lithium due to growth of SEI thickness in the cracked area.

There is an incremental increase in the new surface area each cycle. As soon as a new area is exposed to electrolyte SEI is formed on this area. The SEI formed in this cracked area grows in thickness in the subsequent cycles. On Nth cycle, the area of crack opened on first cycle would have undergone N-1 cycles, thus thickness growth related to N-1 cycles would occur on that area. Similarly, on Nth cycle, the crack area opened on second cycle would undergo N-2 cycles hence a thickness growth related to N-2 cycles. Capacity loss in the crack area on Nth cycle can be mathematically written as;

$$\frac{dQ}{dN}_{SEI\ thickness\ growth\ on\ cracked\ surface}$$

$$= -\left[\frac{n_{SEI}F\rho_{SEI}}{M_{SEI}}\left(\frac{dA_{cr}}{dN}\right)_1\left(\frac{dL_{SEI}}{dN}\right)_{N-1} + \frac{n_{SEI}F\rho_{SEI}}{M_{SEI}}\left(\frac{dA_{cr}}{dN}\right)_2\left(\frac{dL_{SEI}}{dN}\right)_{N-2}\right.$$

$$\left. + \cdots + \frac{n_{SEI}F\rho_{SEI}}{M_{SEI}}\left(\frac{dA_{cr}}{dN}\right)_{N-1}\left(\frac{dL_{SEI}}{dN}\right)_1\right]$$

$$\frac{dQ}{dN}_{SEI\ thickness\ growth\ on\ cracked\ surface} = -\frac{n_{SEI}F\rho_{SEI}}{M_{SEI}}\sum_{i=1}^{N-1}\left(\frac{dA_{cr}}{dN}\right)_i\left(\frac{dL_{SEI}}{dN}\right)_{N-i}$$

(9.19)

The capacity loss in the cracked area due to SEI growth in the subsequent cycles is given as,

$$\frac{dQ}{dN}_{SEI\ thickness\ growth\ on\ cracked\ surface}$$

$$= -\frac{n_{SEI}F\rho_{SEI}}{M_{SEI}}\sum_{i=1}^{N-1} 8\pi R^2 l_{cr}\rho_{cr}k\left[\sigma_{\theta,max}b\sqrt{\pi a_0}\right]^m \left(1\right.$$

$$\left. + \frac{2-m}{2}k\left[\sigma_{\theta,max}b\sqrt{\pi}\right]^m a_0^{\left(\frac{m-2}{2}\right)}(N-i)\right)^{\frac{m}{2-m}}\frac{1}{2}K_{th}(N-i)^{-1/2}$$

(9.20)

9.6.5 Total lithium loss after formation cycles

After the formation cycle, the rate of capacity loss in the subsequent cycles is given by Equation 9.1;

$$\frac{dQ}{dN} = \frac{dQ}{dN_{SEI\ formation\ due\ to\ crack\ propagation}} + \frac{dQ}{dN_{SEI\ thickness\ growth\ on\ spherical\ surface}} + \frac{dQ}{dN_{SEI\ thickness\ growth\ on\ cracked\ surface}}$$

(9.21)

$$\frac{dQ}{dN} = -\frac{n_{SEI}FL_{SEI}\rho_{SEI}8\pi R^2 l_{cr}\rho_{cr}}{M_{SEI}}\left[\sigma_{\theta,max}b\sqrt{\pi a_0}\right]^m k\left(1 + \frac{2-m}{2}k\left[\sigma_{\theta,max}b\sqrt{\pi}\right]^m a_0^{\left(\frac{m-2}{2}\right)}N\right)^{\frac{m}{2-m}}$$

$$-4\pi R^2\frac{n_{SEI}F\rho_{SEI}}{M_{SEI}}(1+2l_{cr}\rho_{cr}a_0)\frac{1}{2}K_{th}(N)^{-1/2}$$

$$-\frac{n_{SEI}F\rho_{SEI}}{M_{SEI}}\sum_{i=1}^{N-1}8\pi R^2 l_{cr}\rho_{cr}k\left[\sigma_{\theta,max}b\sqrt{\pi a_0}\right]^m\left(1 + \frac{2-m}{2}k\left[\sigma_{\theta,max}b\sqrt{\pi}\right]^m a_0^{\left(\frac{m-2}{2}\right)}(N-i)\right)^{\frac{m}{2-m}}\frac{1}{2}K_{th}(N-i)^{-1/2}$$

(9.22)

We get the fractional capacity loss by dividing the equation by Q_0. We define Q_0 as the capacity of the electrode after formation cycle i.e. capacity of the cell after first cycle. Now, since, we lose around 10% capacity in the formation cycle,

$$Q_0 = 0.9 * Q_0^{initial}$$

$$Q_0^{initial} = cell\ capacity = \frac{\left(sp\ capacity\ of\ graphite\ anode\ .{}^4/_3\pi R^3\rho_{graphite}\right)}{1.1} \quad (9.23)$$

we divide by 1.1 since, the graphite is 10% in excess.

Now for simplicity we write,

$$A = l_{cr}\rho_{cr}\left[\sigma_{\theta,max} b\sqrt{\pi a_0}\right]^m k,$$

$$B = \frac{n_{SEI} F \rho_{SEI} 4\pi R^2}{M_{SEI} Q_0}, \quad C = -\frac{2-m}{2} k\left[\sigma_{\theta,max} b\sqrt{\pi}\right]^m a_0^{\left(\frac{m-2}{2}\right)}$$

Here the parameters A, B and C are all positive. Typical value of m in fracture mechanics is in domain (2, 5).

$$\frac{d\breve{Q}}{dN} = -2BAL_{SEI}(1-CN)^{\frac{m}{2-m}} - B(1+2l_{cr}\rho_{cr}a_0)\frac{1}{2}K_{th}(N)^{-1/2}$$
$$- 2BA\sum_{i=1}^{N-1}\left(1-C(N-i)\right)^{\frac{m}{2-m}}\frac{1}{2}K_{th}(N-i)^{-1/2}$$

(9.24)

Integrating,

$$\breve{Q} - 1 = -\frac{2-m}{C}BA\left((1-CN)^{\frac{m}{2-m}} - (1-C)^{\frac{m}{2-m}}\right)$$
$$+ BK_{th}(1+2l_{cr}\rho_{cr}a_0)\left((N)^{1/2}-1\right)$$
$$- BAL_{final}K_{th}\int_1^N \sum_{i=2}^{N-1}\left(1-C(N-i)\right)^{\frac{-m}{m-2}}(N-i)^{-1/2}\,dN$$

(9.25)

We numerically integrate this equation to get the fractional capacity as a function of cycle number.

9.7 First cycle SEI formation lithium loss and estimation of L_{SEI}^{0}

(SEI thickness during the formation cycle)

During the first cycle SEI is formed on the initial surface of spherical particle with pre-existing cracks on the surface and also on the area of cracks grown in the first cycle. This SEI formation results in irreversible loss of approximately 10% in capacity

The graphite capacity is in 10% excess to that of cell capacity. The L_{SEI}^{0} can be calculated roughly with the assumption of 10% cell capacity loss in the first cycle which is used to form a SEI of the thickness L_{SEI}^{0}

$$Q_0^{initial} = cell\ capacity = \frac{(sp\ capacity.{}^{4}/_{3}\pi R^3 \rho_{graphite})}{1.1} \tag{9.26}$$

we divide by 1.1 since, the graphite is 10% in excess.

Now capacity lost in initial SEI formation is

$$Q_{lost} = A_{initial} \frac{n_{SEI} F L_{SEI}^{0} \rho_{SEI}}{M_{SEI}} \tag{9.27}$$

On the first cycle we assume that all the surface area of surface and pre-existing cracks at the surface would be covered with SEI of thickness L_{SEI}^{0}.

$$A_{initial} = 4\pi R^2 + 8\pi R^2 l_{cr} \rho_{cr} a_0 = 4\pi R^2 (1 + 2 l_{cr} \rho_{cr} a_0) \tag{9.28}$$

Hence,

$$Q_{lost} = A_{initial} \frac{n_{SEI} F L_{SEI}^{0} \rho_{SEI}}{M_{SEI}} \tag{9.29}$$

$$Q_{lost} = 4\pi R^2 (1 + 2 l_{cr} \rho_{cr} a_0) \frac{n_{SEI} F L_{SEI}^{0} \rho_{SEI}}{M_{SEI}} \tag{9.30}$$

For simplicity purpose we write,

$$B^0 = \frac{n_{SEI} F \rho_{SEI} 4\pi R^2}{M_{SEI} Q_0^{initial}}, \qquad A = l_{cr}\rho_{cr}\left[\sigma_{\theta,max} b\sqrt{\pi a_0}\right]^m k$$

$$C = -\frac{2-m}{2} k\left[\sigma_{\theta,max} b\sqrt{\pi}\right]^m a_0^{\left(\frac{m-2}{2}\right)}$$

$$\frac{Q_{lost}^{formation\ cycle}}{Q_0^{initial}} = (1 + 2 l_{cr}\rho_{cr} a_0) L_{SEI}^0 B^0 \tag{9.31}$$

This can be equated with the 10% of the cell capacity to calculate initial SEI thickness L_{SEI}^0.

$$L_{SEI}^0 = \frac{0.1}{(1 + 2 l_{cr}\rho_{cr} a_0)\ B^0} \tag{9.32}$$

9.8 Parameters and assumptions:

We assume the initial crack depth and length to be $a_0 = l_{cr} = 2\ nm$. We assume the initial crack density $\rho_{cr} = 10^9$ cracks on the surface of a spherical electrode particle. The particle size for the calculations is assumed to be 10 microns, which is consistent with the observation done by Verbrugge *et al.* (*34*). The porosity of the electrode film is taken to be 65% (*34*). The value of Paris' law constant m is assumed to be '2.5' which is consistent with the general observed values in fracture mechanics$(2 \leq m \leq 5)$. Crack propagation as well as SEI growth rate are thermally activated processes. Hence, we assume Paris' law constant k as well as thickness growth constant K_{th} follows the Arrhenius law;

$$k = k_0 e^{(-E_{a1}/RT)} \text{ and } K_{th} = K_{th}^0 e^{(-E_{a2}/RT)} \quad (9.33)$$

k_0 value for electrochemical crack propagation in graphite and K_{th}^0 value for the SEI growth rate in graphite is unknowns hence are a fitting parameter. With the capacity fading data at three different temperatures we could calculate the activation energy for crack propagation to be $13.08\, kcal\, mol^{-1}$ and for SEI thickness growth to be $5.65\, kcal\, mol^{-1}$. As discussed earlier, we assume that all the SEI formed upon crack propagation, mainly consist of Li_2CO_3, thus there is two mole lithium loss on every mole of Li_2CO_3 formed during cycling $(n = 2)$. Also we take molecular weight of Li_2CO_3 as molecular weight of SEI. Using these parameters in the equation we calculate the initial SEI thickness to be $L_{SEI}^0 = 2.85\, nm$. In these calculations this SEI thickness grows gradually 2.85 nm to around 5 nm to 10 nm in the subsequent 2000 cycles depending upon the operating temperature conditions.

9.9 Modeling results and discussions:

With the assumptions as stated above in the Equation (9.25) we could plot the capacity fading of the cells as a function of cycle number for different temperatures. In Figure 9.5, the dots represent the experimental data of the capacity of the cell and the solid lines represent the calculated capacity using the model. We find that, the predicted capacity is in nice agreement with the experimental data. This agreement suggests that, the model predicts the capacity fading quite well. For further confirmation of validity of the model, we regenerate the voltage vs. capacity curves (Figure 9.6) at different number of cycles. We use the SOD vs. potential charts of the individual electrodes as lookup tables to

regenerate these curves. We find that the calculated cell voltage profiles in Figure 9.6 match fairly well with the experimental curves in Figure 9.3.

We calculate the differential voltages for the full cell using the cell voltage plots in Figure 9.6 and thus we could regenerate the plots of differential voltages of the full cell against the capacity (Ah) for different cycle numbers (Figure 9.7). We compare these plots with the experimental plots in Figure 9.4 and find that they are in nice agreement with eachother. Again we observe that the distance between the differential voltage peaks remains the same as we cycle the battery. This is consistent with our assumption that, in a good commercial battery lithium loss due to the SEI formation with crack propagation and the SEI thickness growth is the main mechanism of capacity fading with the minimal loss of active graphite particles.

With the knowledge of the SOD of the individual electrodes, we could degenerate the full cell voltage plots into the individual electrode voltages (Figure 9.6). Thus we know the state of the individual electrodes with the cycling. With Figure 9.6 we understand that, as we cycle the electrode, for initial few cycles there is increase in the voltage of $FePO_4$ (against lithium reference electrode) electrode at the end of discharge, since it cannot be completely lithiated. And it goes back to pure $FePO_4$ state at the end of charge with the same voltage against lithium reference electrode in all the cycles.

Graphite electrode is always in pure graphite stage at the end of discharge. In a commercial battery, the graphite capacity is always around 10% in excess than the positive electrode capacity. Thus there is always some unused capacity of graphite at the end of charging even in the first cycle. As the lithium is lost upon cycling, the graphite

electrode cannot be completely lithiated thus reducing the width of last stage at the end of the charging. Upon cycling there is an increase in the unused graphite capacity. The graphite voltage curve shifts to left upon cycling which also shows up as shift in peaks in the differential voltage curves of the full cell (Figure 9.7).

9.10 Conclusions:

1. We could experimentally prove the assumption that the capacity fade in a commercial battery is mainly due to the irreversible lithium loss due the SEI formation and growth, with most of the carbon is still active and contributing minimally to the total capacity loss.
2. A mathematical model is proposed to explain the lithium loss during cycling combining the new SEI formation with cycling and the SEI thickness growth with time. Thus we combine the chemical degradation due to SEI growth with the crack propagation *i.e.* mechanical degradation to predict capacity loss. The model predictions are found to be in good agreement with experimentally obtained data.
3. Voltage vs. capacity curves and differential voltage curves for the full cell are regenerated with the model and are found to be in good agreement with the experimental curves. We could degenerate the cell voltage curves to the individual electrode voltages thus understanding the states of individual electrodes upon electrochemical cycling.
4. The model explains the physical phenomena that result in capacity fading in a commercial A123 battery with $LiFePO_4$/graphite electrodes and predicts the capacity the cells with cycling at different temperature pretty well.

9.11 References:

1. J. Yan *et al.*, Phenomenologically modeling the formation and evolution of the solid electrolyte interface on the graphite electrode for lithium-ion batteries. *Electrochimica Acta* **53**, 7069 (2008).
2. E. Markervich, G. Salitra, M. Levi, D. Aurbach, Capacity fading of lithiated graphite electrodes studied by a combination of electroanalytical methods, Raman spectroscopy and SEM. *Journa of Power Sources* **146**, 146 (2005).
3. D. Aurbach, Review of selected electrode-solution interactions which determine the performance of Li and Li ion batteries. *Journal of Power Sources* **89**, 206 (2000).
4. R. Spotnitz, Simulation of capacity fade in lithium-ion batteries. *Journal of Power Sources* **113**, 72 (Jan, 2003).
5. I. Bloom *et al.*, An accelerated calendar and cycle life study of Li-ion cells. *Journal of Power Sources* **101**, 238 (2001).
6. J. Christensen, J. Newman, A mathematical model for the lithium-ion negative electrode solid electrolyte interphase. *Journal of The Electrochemical Society* **151**, A1977 (2004).
7. M. Safari, M. Morcrette, A. Teyssot, C. Delacourt, Life-Prediction Methods for Lithium-Ion Batteries Derived from a Fatigue Approach I. Introduction: Capacity-

Loss Prediction Based on Damage Accumulation. *Journal of The Electrochemical Society* **157**, A713 (2010).

8. M. Safari, M. Morcrette, A. Teyssot, C. Delacourt, Life Prediction Methods for Lithium-Ion Batteries Derived from a Fatigue Approach II. Capacity-Loss Prediction of Batteries Subjected to Complex Current Profiles. *Journal of The Electrochemical Society* **157**, A892 (2010).
9. Q. Zhang, R. E. White, Calendar life study of Li-ion pouch cells. *Journal of Power Sources* **173**, 990 (Nov, 2007).
10. Q. Zhang, R. E. White, Calendar life study of Li-ion pouch cells - Part 2: Simulation. *Journal of Power Sources* **179**, 785 (May, 2008).
11. Q. Zhang, R. E. White, Capacity fade analysis of a lithium ion cell. *Journal of Power Sources* **179**, 793 (May, 2008).
12. R. P. Ramasamy, R. E. White, B. N. Popov, Calendar life performance of pouch lithium-ion cells. *Journal of Power Sources* **141**, 298 (2005).
13. R. P. Ramasamy, J.-W. Lee, B. N. Popov, Simulation of capacity loss in carbon electrode for lithium-ion cells during storage. *Journal of Power Sources* **166**, 266 (2007).
14. M. Broussely *et al.*, Main aging mechanisms in Li ion batteries. *Journal of Power Sources* **146**, 90 (Aug, 2005).
15. G. Ning, R. E. White, B. N. Popov, A generalized cycle life model of rechargeable Li-ion batteries. *Electrochimica Acta* **51**, 2012 (Feb, 2006).
16. K. Kumaresan, Q. Z. Guo, P. Ramadass, R. E. White, Cycle life performance of lithium-ion pouch cells. *Journal of Power Sources* **158**, 679 (Jul, 2006).

17. S. Santhanagopalan, Q. Guo, P. Ramadass, R. E. White, Review of models for predicting the cycling performance of lithium ion batteries. *Journal of Power Sources* **156**, 620 (2006).

18. J. Christensen, J. Newman, A Mathematical Model of Stress Generation and Fracture in Lithium Manganese Oxide. *Journal of The Electrochemical Society* **153**, A1019 (2006).

19. J. Christensen, J. Newman, Stress generation and fracture in lithium insertion materials. *Journal of Solid State Electrochemistry* **10**, 293 (2006).

20. X. Zhang, A. M. Sastry, W. Shyy, Intercalation-Induced Stress and Heat Generation within Single Lithium-Ion Battery Cathode Particles. *Journal of The Electrochemical Society* **155**, A542 (2008).

21. X. Zhang, W. Shyy, A. M. Sastry, Numerical Simulation of Intercalation-Induced Stress in Li-Ion Battery Electrode Particles. *Journal of The Electrochemical Society* **154**, A910 (2007).

22. R. Deshpande, Y.-T. Cheng, M. W. Verbrugge, Modeling diffusion-induced stress in nanowire electrode structures. *Journal of Power Sources* **195**, 5081 (2010).

23. R. Deshpande, Y. Qi, Y.-T. Cheng, Effects of Concentration-Dependent Elastic Modulus on Diffusion-Induced Stresses for Battery Applications. *Journal of The Electrochemical Society* **157**, A967 (2010).

24. S. J. Harris, R. D. Deshpande, Y. Qi, I. Dutta, Y. T. Cheng, Mesopores inside electrode particles can change the Li-ion transport mechanism and diffusion-induced stress. *Journal of Materials Research* **25**, 1433 (Aug, 2010).

25. R. Deshpande, Y.-T. Cheng, M. W. Verbrugge, A. Timmons, Diffusion Induces Stresses and Strain Energy in a Phase Transforming Spherical Electrode Particle. *Journal of The Electrochemical Society* **158**, 1 (2011).

26. Y.-T. Cheng, M. W. Verbrugge, The influence of surface mechanics on diffusion induced stresses within spherical nanoparticles. *Journal of Applied Physics* **104**, 083521 (2008).

27. A. K. Padhi, K. S. Nanjundaswamy, J. B. Goodenough, Phospho-olivines as positive-electrode materials for rechargeable lithium batteries. *J. Electrochem. Soc.* **144**, 1188 (Apr, 1997).

28. N. Ravet *et al.*, Electroactivity of natural and synthetic triphylite. *J. Power Sources* **97-98**, 503 (2001).

29. N. Recham *et al.*, Ionothermal Synthesis of Tailor-Made LiFePO4 Powders for Li-Ion Battery Applications. *Chem. Mat.* **21**, 1096 (Mar, 2009).

30. B. Kang, G. Ceder, Battery materials for ultrafast charging and discharging. *Nature* **458**, 190 (2009).

31. S. Y. Chung, J. T. Bloking, Y. M. Chiang, Electronically conductive phospho-olivines as lithium storage electrodes. *Nat. Mater.* **1**, 123 (Oct, 2002).

32. P. Liu *et al.*, Aging Mechanisms of $LiFePO_4$ Batteries Deduced by Electrochemical and Structural Analyses. *Journal of The Electrochemical Society* **157**, A499 (2010).

33. J. Wang *et al.*, Cycle-life model for graphite-LiFePO4 cells. *Journal of Power Sources* **196**, 3942 (2011).

34. M. W. Verbrugge, B. J. Koch, Electrochemical analysis of lithiated graphite anodes. *Journal of the Electrochemical Society* **150**, A374 (Mar, 2003).

35. R. A. Huggins, *Advanced Batteries: Materials Science Aspects*. (Springer, 2009).

36. Y.-T. Cheng, M. W. Verbrugge, Evolution of stress within a spherical insertion electrode particle under potentiostatic and galvanostatic operation. *Journal of Power Sources* **190**, 453 (2009).

37. L. B. R., *Fracture of Brittle Solids* Cambridge Solid State Science Series (Cambridge University Press, ed. 2nd edition, 1993).

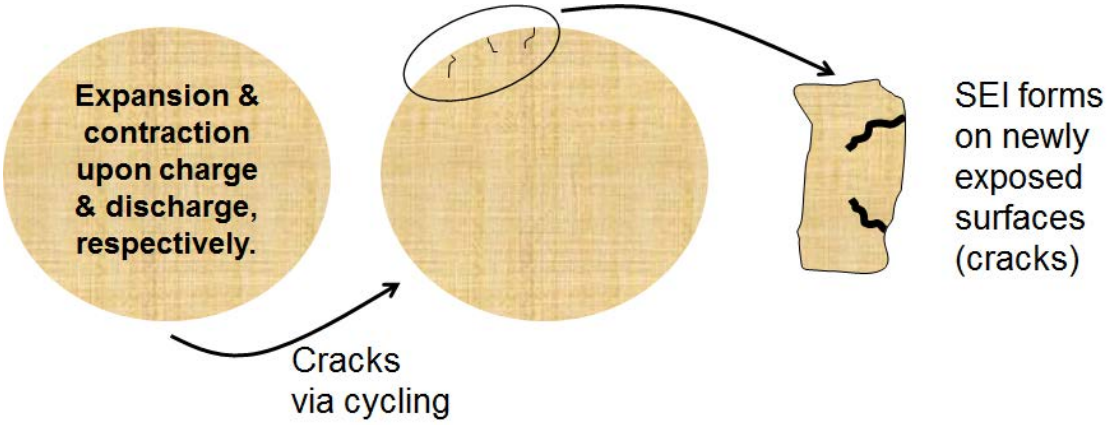

Figure 9.1: A cartoon diagram representing the schematics of the lithium loss as proposed. As a result of diffusion induced stresses (DISs), the cracks at the particle surface propagate with cycling, a new surface is exposed to electrolyte and results in SEI formation.

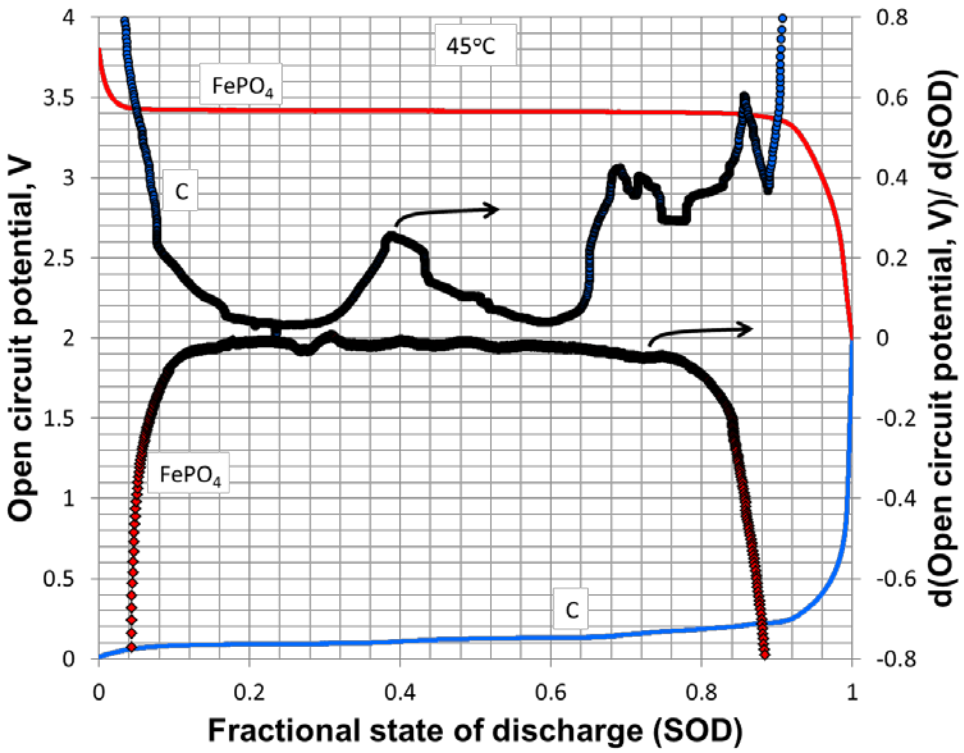

Figure 9.2: The solid curves are the plots potential vs. state of charge (SOD) curves for the individual electrodes of a commercial A123 battery. The dotted curves are the plots of dV /d(SOC) against SOC for the individual electrodes. We find that the negative electrode dV/d(SOC) curve (Blue symbols) shows peaks for the graphite staging at the same time dV/d(SOC) curve for $FePO_4$ have fairly constant and does not show any variation (Red symbols). In both plots, we use blue color for the negative electrode and red color for the positive electrode.

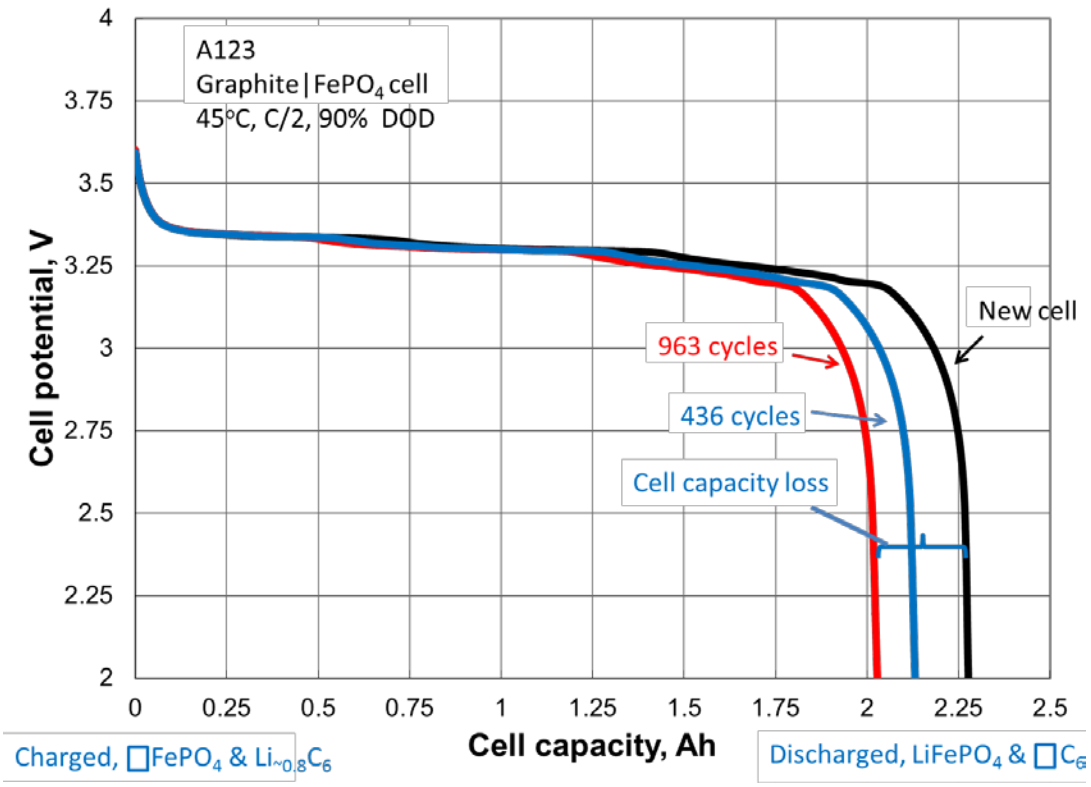

Figure 9.3: Plots of the measured voltage against the capacity for A123 battery at 45^0C at cycle numbers 2, 436 and 963.

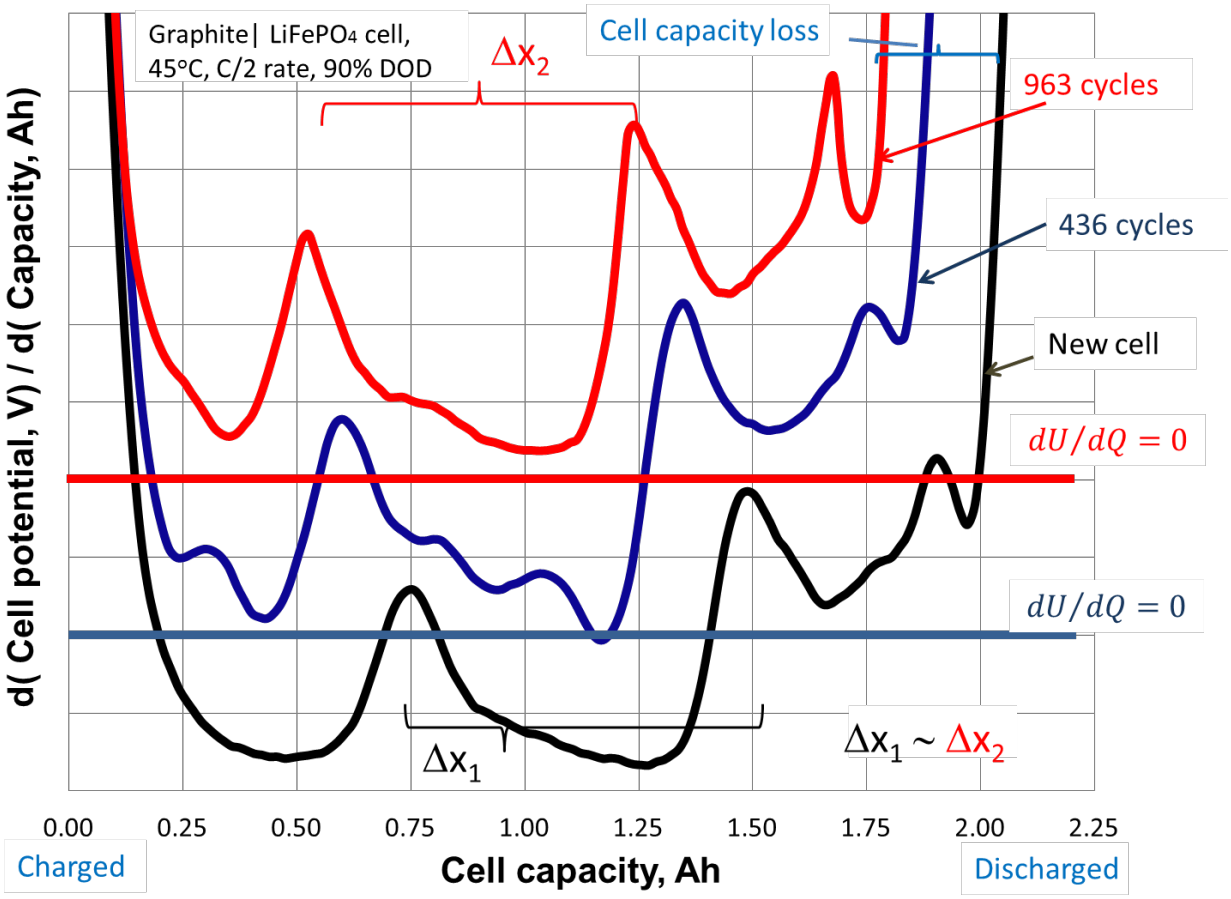

Figure 9.4: Plot of experimentally obtained differential voltages of the full cell against the cell capacity (Ah) for A123 battery at 45^0C at cycle numbers 2, 436 and 963.

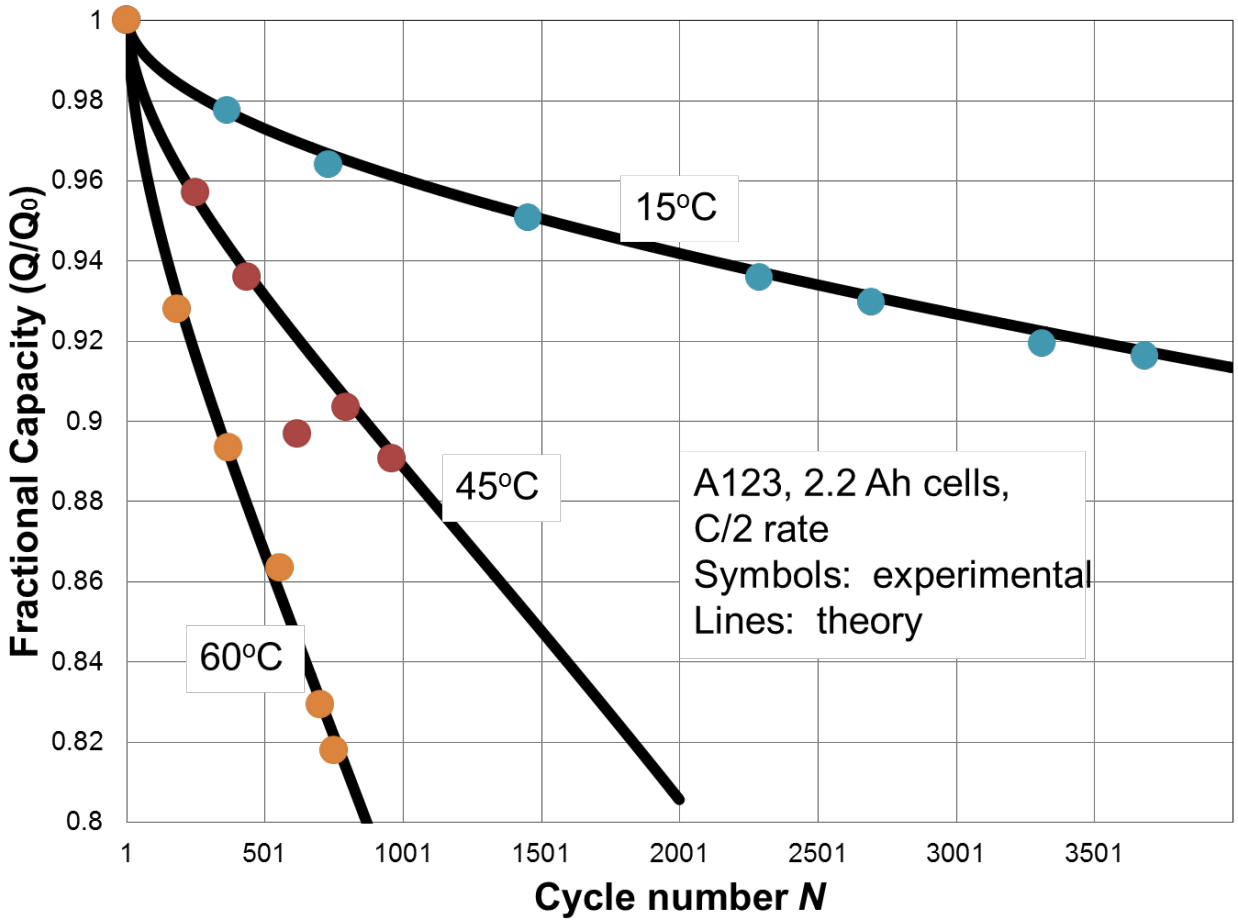

Figure 9.5: A plot of the capacity fading of the cell as a function of number of cycles for different temperatures. The dots represent the experimental data of the capacity of the cell and the solid lines represent the calculated capacity using the model.

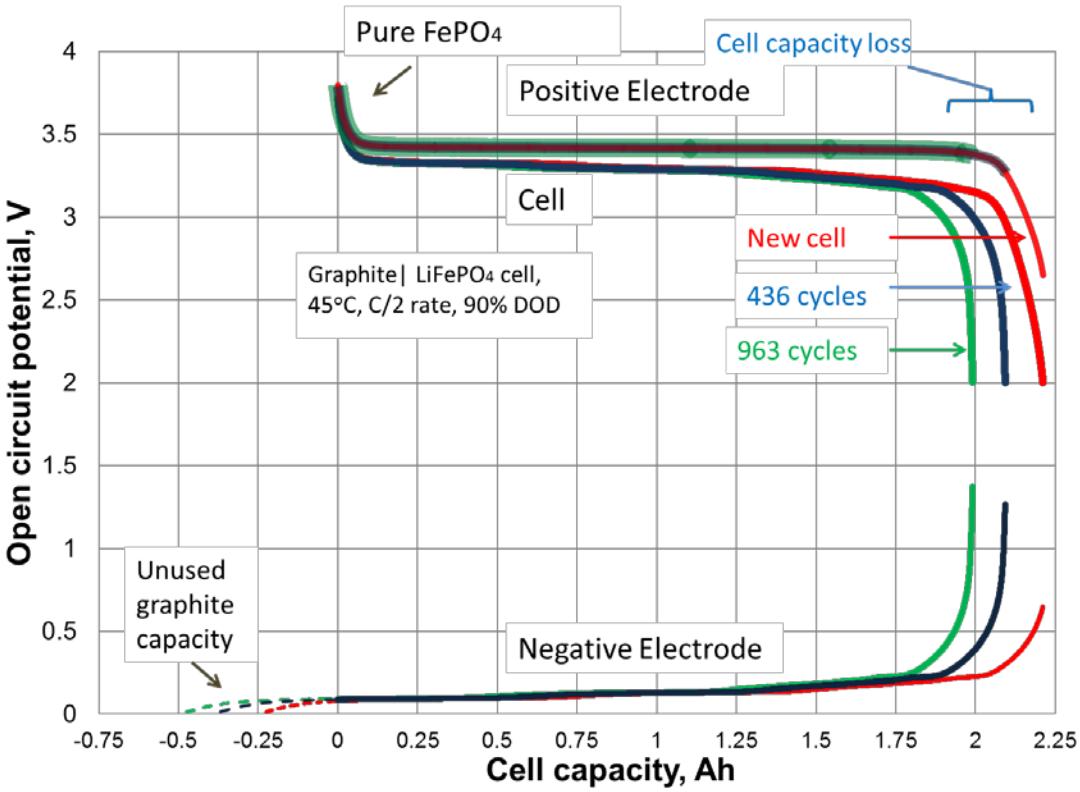

Figure 9.6: Plots of voltage (V) vs. capacity(Ah) at different number of cycles for the data calculated using the model. We degenerate the voltage cell voltage in to the voltage profiles for the individual electrode voltages against the cell capacity for different cycle numbers.

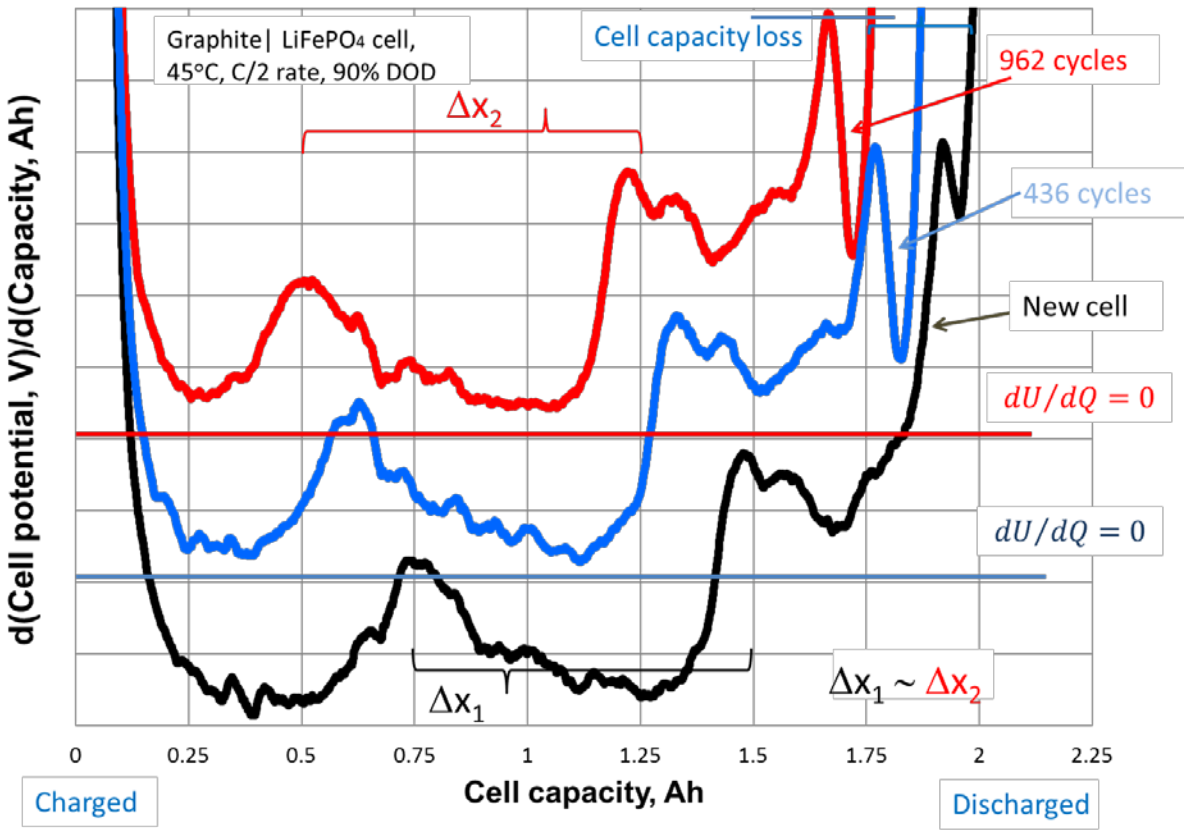

Figure 9.7: Plots of differential voltages (dV/dQ) against the Capacity (Ah) for different cycle numbers obtained using the proposed model for different cycle numbers.

CHAPTER 10

LIQUID METAL ALLOYS AS SELF-HEALING NEGATIVE ELECTRODES FOR LITHIUM ION BATTERIES

This chapter is based on work published as:

R. D. Deshpande, J. Li, Y.-T. Cheng, M. W. Verbrugge, Liquid Metal Alloys as Self-Healing Negative Electrodes for Lithium Ion Batteries. *Journal of The Electrochemical Society* **158**, A845 (2011).

It's reproduced by permission of The Electrochemical Society.

10.1 Summary

Improving the capacity and durability of electrode materials is one of the critical challenges lithium-ion battery technology is facing presently. Several promising anode materials, such as silicon (Si), germanium (Ge), and tin (Sn), have theoretical capacities several times larger than that of the commercially used graphite negative electrode. However, their applications are limited because of the short cycle life due to fracture caused by diffusion-induced stresses (DISs) and the large volume change during electrochemical cycling. In this chapter, we present a strategy to achieve high capacity and improved durability of electrode materials using low-melting point metallic alloys. With gallium (Ga) as an example, we show that at a temperature above the melting point of Ga, a reversible solid-liquid transition occurs upon lithiation (lithium insertion) and delithiation (lithium extraction) of Ga. As a result, cracks formed in the lithiated solid state can be "healed" once the electrode returns to liquid Ga after delithiation. This work indicates that cracking as a failure mode can be remedied using liquid metal electrodes.

10.2 Introduction

Lithium ion batteries (LIBs) with high energy capacity and long cycle life are employed to power numerous consumer electronic devices, portable tools, implantable medical devices, and more recently, hybrid electric vehicles (HEVs) and pure battery electric vehicles (BEVs) (*1*, *2*). Many elements react with Li to form binary alloys Li_xM (where M is, for example, Si(*3*), Ge(*4*), or Sn(*5*)). Their theoretical (Columbic) capacities are 3 to 12 times higher than that of graphite electrodes, as they host 2 to 4.4 Li atoms per M atom, in contrast to a single Li atom per 6 C atoms. These Li_xM alloys also show a discharge potential close to that of the Li/Li^+ reaction (*1*). These materials have, therefore, been considered as potential negative electrodes for the LIBs. However, low cycle life due to mechanical degradation (*6*, *7*) and current inefficiencies associated with undesired electrochemical reaction during cycling limit the application of these high capacity electrode materials in LIBs.

Different strategies such as alloying the Li-active materials with inactive elements, building nano-structural/ nano-porous electrodes, coating or having electrolyte additives for a stable SEI etc. are commonly used by different studies focusing on improving electrode durability in past 15 years. Alloying Li-active with inactive materials improves battery cycle life significantly, such as alloying Sn with Cu (*8*) , Co (*9*), or Ni (*10*). However, total gravimetric and volumetric energy densities are lowered because the inactive elements contribute to extra weight and volume.

Nano-structural electrodes, such as thin-film Si (*11*), Si nano-particles (*12*), Si nanowires (*3*) and TiO_2 nanowires (*13*), as well as porous transition metal oxides (*14, 15*), show improvement in cycle life compared to their bulk-material counterparts. However, nano-structuring reduces the volumetric capacity of electrodes because of the low packing density of nanowires, nanoparticles, and porous materials. Furthermore, nano-structured electrodes may suffer from increased irreversible capacity degradation due to excessive solid electrolyte interphase (SEI) formation (*16*), and other deleterious reactions with the electrolyte (leading to reduced current efficiency relative to the desired lithiation reaction), because of their large surface area to volume ratio. Last, conducting additives and chemical binders, such as carbon black and polyvinylidene fluoride (PVDF), have been shown to improve the cycle life at the cost of extra mass and volume occupied by the additives.

In this chapter, we demonstrate a strategy of achieving high capacity and durability using low-melting point, lithium active, liquid metals (LMs) as LIB negative electrodes. This idea is based on the premise that cracks formed in LMs during cycling can be self-healed by the liquid-solid-liquid transition. We examine the reversibility of lithiation of the LM pure Ga at 40 °C, as a negative electrode for a LIB. Ga hosts 2 Li atoms per Ga atom upon full lithiation, delivers a theoretical gravimetric capacity of 769 mAh g^{-1} by forming Li_2Ga alloy (*17*), and shows a discharge potential close to the Li/Li^+ reaction. It has been shown that LiGa alloys (*18*), CuGa alloys (*19*), and Ga confined in a carbon matrix (*20*) deliver capacities of about 200-400 mAh g^{-1} upon extended cycling.

10.3 Experimental

Commercial pure gallium (Ga) metal (99.99%, Alfa Aesar) was applied onto 0.025 mm thick 304-type stainless steel (SS) foils (Alfa Aesar) without any binder or conducting additive. The thickness of Ga film on SS substrate was controlled to be about 1 µm, and the mass of Ga was precisely measured by a microbalance (XS 205, Mettler Toledo). Samples were assembled into CR 2025-type coin cells (Hohsen) in an argon-filled glove-box (MBraun) with oxygen and moisture contents less than 0.1 ppm. Li metal foils (99.9%, Sigma Aldrich) were used as the counter electrode (CE). One piece of Celgard 3501 separator soaked in the electrolyte solution consisting of 1M $LiPF_6$ dissolved in a mixture of ethyl carbonate and dimethyl carbonate (EC/DMC, volumetric ratio 1:1) (Novolyte) was used in making the coin cells. Capillary cells were assembled with liquid gallium as the working electrode (WE) and lithium metal as the CE. Electrolyte solution was the same as for coin cells. The capillary was filled with liquid Ga from one end and solid lithium attached to a copper current collector was pushed in through the other end. The space between the electrodes was filled with the electrolyte (approximately 2 mm). Copper wires were used as current conductors. Both ends of the cell were sealed with Torr-seal (Varian). Electrolyte vapor was avoided from Torr-seal with a Teflon cap. The transparent glass body allowed direct observation of the color and texture changes in the Ga during lithiation and delithiation (Fig 10.3 a). Figure 10.3 b shows the conceptual picture of the capillary cell arrangement.

Cycling performance of coin cells was evaluated using a potentiostat (VersaSTAT 3, PAR). The cells were galvanostatically cycled between 2.0 V and 0.005 V at various rates.

During cycling, coin cells were kept in an environmental chamber (Test Equity) with precise temperature controlled at 40°C, according to the experimental needs. In this work charging refers to lithiation and discharging refers to delithiation.

Before characterization, the cycled cells were disassembled and the WE was washed by DMC (99%, Alfa Aesar). *Ex-situ* x-ray diffraction (XRD) was carried out using a D8 Discover (Bruker AXS) system with Cu Kα radiation (wavelength 1.54 nm). Samples were maintained at 40°C during XRD tests. For the capillary cell, the galvanostatic cycling was conducted with a current of 10 μA using a potentiostat (VersaSTAT 3, PAR). The optical observations were made under a model QX5 optical microscope (Prime Entertainment Company).

10.4 Results and discussion

The melting point of pure Ga is 29 °C. Electrochemical cycling tests in this work were held at 40 °C to ensure the liquid state of pure Ga. Different from the Ga-Li equilibrium phase diagram (*21*) and observations of Li in Ga at 415 °C (*17*), three intermetallic phases, Li_2Ga_7, LiGa, and Li_2Ga, form during the electrochemical reaction of Ga with Li at 40 °C. The potential-capacity profile in Figure 10.1 clearly shows four narrow single-phase regions, as well as two-phase regions (plateaus). The theoretical Coulombic capacity in going from Ga to Li_2Ga corresponds to 769 mAh per gram of Ga. The electrode used to generate the data of Figure 10.1 yielded a capacity of 700 mAh g^{-1} which is about 91% of the theoretical value, indicating that the vast majority of the Ga within the electrode was utilized for reaction with Li.

The hysteresis in the potential profile of Figure 10.1 is not well understood at this time; we suspect that although 50 hours were employed for each of the low-current-density charge and discharge experiments, irreversible phenomena still intrude on the results.

The thermodynamic relation used previously to describe staging phenomena during the lithiation of graphite (*22*) has been applied here to generate the curve labeled "Calculation" in Figure 10.1 for discharge at a low rate (C/50, corresponding to a 50-hr discharge). However, we note that while the thermodynamic relations derived and employed capture qualitatively the potential behavior, more work is needed to make the analysis quantitative. Deshpande et al (*23*) gives further details on these calculations.

X-ray diffraction (XRD) of Ga at 40 °C shows that before cycling Ga is liquid, as seen as a broad peak at 2θ=36° (Figure 10.2). During cycling, three reversible phases, including Li_2Ga_7, LiGa, and Li_2Ga form, as seen from XRD peak identification. After complete delithiation, Ga returns to its liquid state, indicated by the broad peak at 2θ=36° in the XRD profile. Thus, a reversible liquid-solid-liquid transition in Ga is confirmed upon lithiation and delithiation, corroborating the electrochemical results.

The capillary cell was observed in real time under microscope during lithiation and d-lithiation. Lithium-free liquid Ga appears glossy under the optical microscope (Figure 10.3c). After partial lithiation, a distinct gray layer of lithiated Ga above the unlithiated liquid Ga is observed. Un-lithiated liquid Ga could still be observed to be glossy as it was initially (Figure 10.3d). The partially lithiated gallium was completely delithiated: the glossy liquid Ga was completely recovered. Thus, the liquid-solid-liquid transition of gallium upon lithiation and delithiation was directly observed.

The co-author J C Li (Chemical and Materials Engineering, University of Kentucky) performed *ex-situ* SEM observation of the samples. The morphology changes of Ga at various stages of cycling were examined by *ex-situ* SEM.

With SEM, he could observe the solidified LM on lithiation, the cracks formed on partial delithiation and smooth liquid surface on complete delithiation. Deshpande *et al.* (*23*) gives further details about these observations.

Based on our XRD and electrochemical results, and the previous work of Saint *et al.* (*18*), the electrochemical reaction of liquid Ga with Li at 40 °C can be summarized to good approximation as

Lithiation: $$Ga(l) \xrightarrow{Li} Li_2Ga_7 \xrightarrow{Li} LiGa \xrightarrow{Li} Li_2Ga \quad (10.1)$$

Delithiation: $$Li_2Ga \xrightarrow{-Li} LiGa \xrightarrow{-Li} Li_2Ga_7 \xrightarrow{-Li} Ga(l) \quad (10.2)$$

The comparison of liquid gallium to solid gallium as electrode is studied in Deshpande *et al.*(*23*). The $GaLi_x$ compounds are solid at 40 °C. After the cell reaches the final plateau near 0.9 V, the electrode is a mixture of solid Li_2Ga_7 and liquid Ga. Because Li diffusion in liquid Ga is found to be much faster than in a solid, Li diffusion in solid Li_2Ga_7 is rate limiting at this stage. After reaching the liquid Ga single phase (starting at about 0.95 V), most of the electrode is liquid and Li diffusion is especially fast. Thus, the cell potential increases to the upper potential limit quickly.

The influence of discharge rates on the capacity is studied by co-author J C Li are reported in detail in Deshpande *et al.* (*23*). The discharging potential-capacity profiles of Ga LM in the second cycle with various rates are compared.

Even at a fast rate of 2C, Ga still delivers a considerable discharge capacity of 560mAh g^{-1}. The formation of LiGa delivers a capacity of 385 mAh g^{-1} and that of Li_2Ga delivers a capacity of 769 mAh g^{-1}, which is the theoretical maximum capacity of Ga.

The capacity versus cycle number for liquid Ga at 40°C is observed. A gradual decrease of capacity with cycling is apparent. Commercial lithium salt based electrolytes show fast Li diffusivity and moderate application temperature range compare to other types of electrolytes, such as ionic liquids and solid electrolytes. However, there is a drawback of SEI forming on electrode surface when the WE is charged (lithiated) to below 0.7 V vs. the Li/Li^+ reaction. The SEI consumes electrolyte, lithium, and electrode material. This SEI layer cannot be dissolved during the reversal electrochemistry process and contributes to irreversible capacity loss. For most of the negative materials, SEI formation completes in the first few cycles and facilitates the Li transportation during subsequent cycling. In this work, because the Ga electrode is in liquid state at the beginning of charging and returns to liquid at the end of discharging at each cycle, the SEI may come off the electrode surface and is no longer stable. Thus, a fresh SEI may form during every cycle and brings irreversible capacity loss. To commercially use liquid metal with low discharging potential, formation of SEI has to be avoided using other methods, such as using electrolytes that do not form SEI.

10.5 Conclusions

In this chapter, we demonstrate the concept of using low-melting point metal/alloys as lithium-ion battery electrodes. A conceptual picture, consistent with all of the experimental observations, is given in Figure 10.4 for self-healing liquid metal electrodes.

The liquid metal electrode undergoes crystallization upon lithiation and transforms to a solid electrode. On complete delithiation the solid phases are transformed to the liquid state.

Cracks are formed in the electrode mostly during delithiation and can be self-healed by the solid-to-liquid transformation. Along with that, the lithium transport in a liquid electrode is found to be faster than that in solid electrodes. This gives additional advantage to the liquid metal electrodes in terms of high power applications (*23*). Since many low melting point alloys exist and can potentially store large quantities of Li, the liquid metal approach demonstrated by liquid Ga may be generalized to many systems of technological significance.

10.6 References

1. R. A. Huggins, *Advanced Batteries: Materials Science Aspects*. (Springer, 2009).
2. M. Armand, J. M. Tarascon, Building Better Batteries. *Nature* **451**, 652 (Feb, 2008).
3. C. K. Chan *et al.*, High-Performance Lithium Battery Anodes using Silicon Nanowires. *Nat. Nanotechnol.* **3**, 31 (Jan, 2008).
4. B. Laforge, L. Levan-Jodin, R. Salot, A. Billard, Study of Germanium as Electrode in Thin-Film Battery. *Journal of The Electrochemical Society* **155**, A181 (2008).
5. M. Winter, J. O. Besenhard, Electrochemical lithiation of tin and tin-based intermetallics and composites. *Electrochimica Acta* **45**, 31 (1999).

6. Y. T. Cheng, M. W. Verbrugge, Evolution of Stress within a Spherical Insertion Electrode Particle under Potentiostatic and Galvanostatic Operation. *Journal of Power Sources* **190**, 453 (May, 2009).

7. Y. T. Cheng, M. W. Verbrugge, Diffusion-Induced Stress, Interfacial Charge Transfer, and Criteria for Avoiding Crack Initiation of Electrode Particles. *Journal of the Electrochemical Society* **157**, A508 (2010).

8. Y. Y. Xia, T. Sakai, T. Fujieda, M. Wada, H. Yoshinaga, Flake Cu-Sn alloys as Negative Electrode Materials for Rechargeable Lithium Batteries. *Journal of the Electrochemical Society* **148**, A471 (May, 2001).

9. A. D. W. Todd, R. E. Mar, J. R. Dahn, Tin-Transition Metal-Carbon Systems for Lithium-Ion Battery Negative Electrodes. *Journal of the Electrochemical Society* **154**, A597 (2007).

10. J. Hassoun, S. Panero, B. Scrosati, Electrodeposited Ni-Sn Intermetallic Electrodes for Advanced Lithium Ion Batteries. *Journal of Power Sources* **160**, 1336 (Oct, 2006).

11. J. Graetz, C. C. Ahn, R. Yazami, B. Fultz, Highly Reversible Lithium Storage in Nanostructured Silicon. *Electrochem. Solid State Lett.* **6**, A194 (Sep, 2003).

12. H. Kim, M. Seo, M. H. Park, J. Cho, A Critical Size of Silicon Nano-Anodes for Lithium Rechargeable Batteries. *Angew. Chem.-Int. Edit.* **49**, 2146 (2010).

13. G. Armstrong, A. R. Armstrong, P. G. Bruce, P. Reale, B. Scrosati, TiO_2(B) Nanowires as An Improved Anode Material for Lithium-Ion Batteries Containing $LiFePO_4$ or $LiNi_{0.5}Mn_{1.5}O_4$ Cathodes and A Polymer Electrolyte. *Adv. Mater.* **18**, 2597 (Oct, 2006).

14. H. C. Shin, J. Dong, M. L. Liu, Porous Tin Oxides Prepared using an Anodic Oxidation Process. *Adv. Mater.* **16**, 237 (Feb, 2004).

15. S. J. Bao, Q. L. Bao, C. M. Li, Z. L. Dong, Novel Porous Anatase TiO_2 Nanorods and their High Lithium Electroactivity. *Electrochemistry Communications* **9**, 1233 (May, 2007).

16. M. Winter, The Solid Electrolyte Interphase - The Most Important and the Least Understood Solid Electrolyte in Rechargeable Li Batteries. *Z. Phys. Chemie-Int. J. Res. Phys. Chem. Chem. Phys.* **223**, 1395 (2009).

17. C. J. Wen, R. A. Huggins, Electrochemical Investigation of the Lithium-Gallium System. *Journal of the Electrochemical Society* **128**, 1636 (1981).

18. J. Saint, M. Morcrette, D. Larcher, J. M. Tarascon, Exploring the Li-Ga Room Temperature Phase Diagram and the Electrochemical Performances of the Li_xGa_y Alloys vs. Li. *Solid State Ion.* **176**, 189 (Jan, 2005).

19. K. T. Lee, Y. S. Jung, J. Y. Kwon, J. H. Kim, S. M. Oh, Role of Electrochemically Driven Cu Nanograins in $CuGa_2$ Electrode. *Chemistry of Materials* **20**, 447 (Jan, 2008).

20. K. T. Lee *et al.*, Liquid Gallium Electrode Confined in Porous Carbon Matrix as Anode for Lithium Secondary Batteries. *Electrochemical and Solid State Letters* **11**, A21 (2008).

21. B. Predel, *Group IV Physical Chemistry - Phase Equilibria, Crystallographic and Thermodynamic Data of Binary Alloys*. M. O, Ed., Electronic Materials and Semiconductors (Springer, 1998), vol. 5.

22. M. W. Verbrugge, B. J. Koch, Electrochemical analysis of lithiated graphite anodes. *Journal of the Electrochemical Society* **150**, A374 (Mar, 2003).

23. R. D. Deshpande, J. Li, Y.-T. Cheng, M. W. Verbrugge, Liquid Metal Alloys as Self-Healing Negative Electrodes for Lithium Ion Batteries. *Journal of The Electrochemical Society* **158**, A845 (2011).

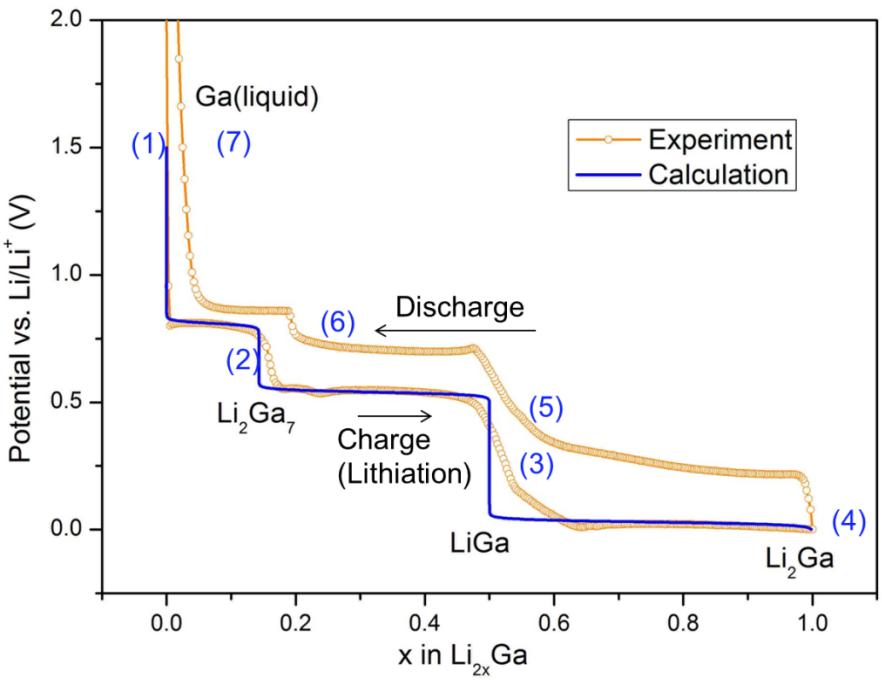

Figure 10.1: Galvanostatic voltage-capacity profile of Ga at 40 °C. The cycling rate was C/50. The numbers (1) – (7) correspond to different states for the XRD results in Fig. 10.2.

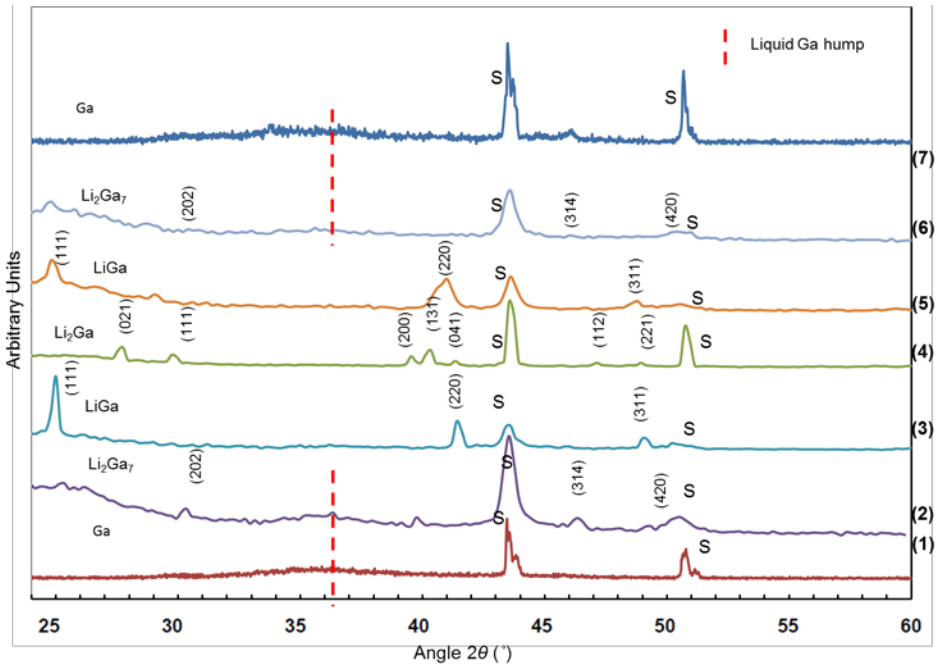

Figure 10.2: Ex-situ XRD results of the Ga electrode during electrochemical cycling. The numbers (1) – (7) refer to different states of Ga in a lithiation and delithiation cycle depicted in Fig. 10.1. The stainless steel substrate peaks are indicated with 'S'.

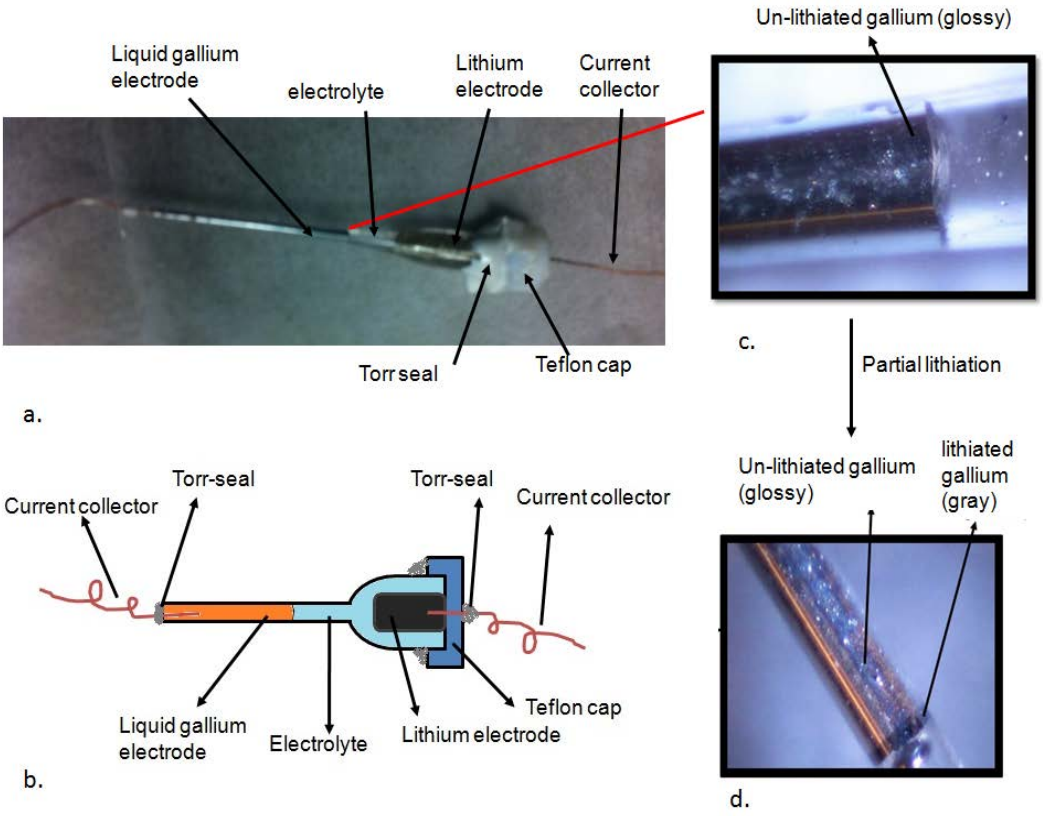

Figure 10.3: (a) A capillary cell with (b) its conceptual picture. (c) Magnified view of the surface near Ga electrode before lithiation and (d) after partial lithiation. The lithiated part is gray and delithiated part is glossy.

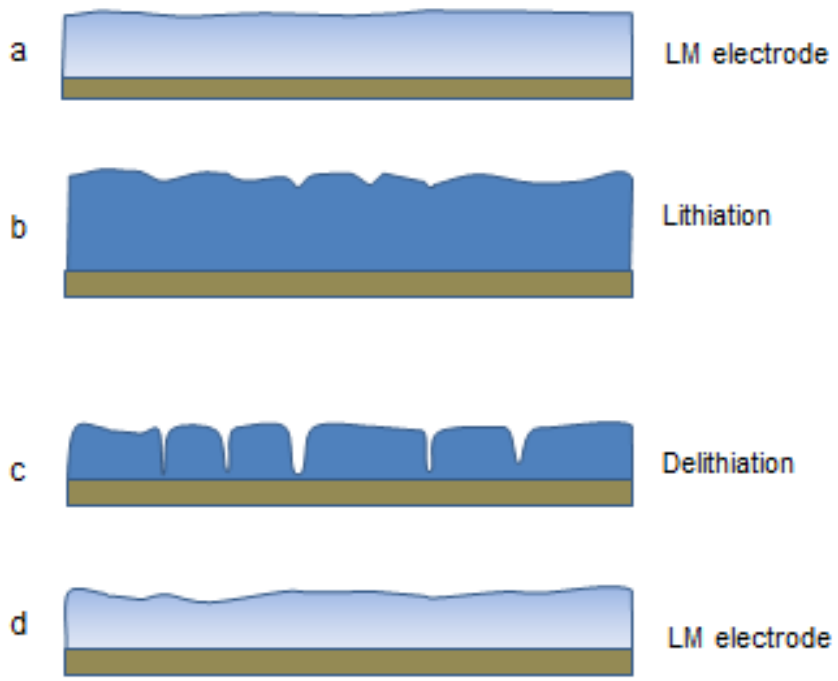

Figure 10.4: Schematic of morphology changes in liquid electrode during cycling. (a) Liquid metal electrode on a solid substrate before electrochemical cycling. (b) Liquid solidifies and expands during lithiation. (c) Cracking occurs in solid mainly during delithiation. (d) Electrode returns to the liquid state during delithiation. Cracks are self-healed by the solid-to-liquid phase transformation.

CHAPTER 11

IN SITU XRD OF LIQUID GALLIUM ELECTRODE AND AB-INITIO STUDY OF LITHIUM-GALLIUM PHASES

11.1 Summary

Lithium ion battery electrodes suffer chemical and mechanical degradation upon electrochemical cycling. Nano-scaled electrode materials, micro-porous electrode materials, active-inactive alloys and surface coated electrode particles are a few of the commonly used electrode designs for a longer electrode life. Recent studies show that liquid metal alloy can be used as a self-healing electrode for the lithium ion batteries. This electrode material undergoes liquid-solid-liquid transition upon electrochemical cycling, resulting in the self-healing of the cracks formed during delithiation process. With such an electrode, mechanical degradation could be minimized and longer cycle life may be achieved. To understand the crystallographic transformations, ab-initio study of lithium-gallium system is performed to regenerate the voltage profile for lithium-gallium system. *In-situ* X-ray diffraction (XRD) study to understand phase transformations in such a liquid electrode upon lithiation and delithiation could be really useful. In the presented work, we develop a method for *in-situ* XRD study of such a liquid metal electrode. We investigate the different phase transformations which the liquid gallium electrode undergoes during lithiation and delithiation. The cell design we developed for this study can be used to study many other electrode materials.

11.2 Introduction

The potential applications of lithium ion batteries for the automobile purpose have ignited a tremendous interest to improve the battery performance. For such an application, the battery needs to have high energy and power density along with good cycle life. The commercially available lithium ion batteries (LIBs) primarily use graphite as a negative electrode material which has a specific capacity of 371 mAhr g^{-1}(*1*). Materials such as tin, silicon are active for lithium storage with much higher specific capacity as compared to the currently used graphite material (*2, 3*). These high capacity materials are known to undergo a huge volumetric expansion and contraction upon lithiation and delithiation (*4*). The electrode material undergoes cracking, fatigue or structural changes due to the diffusion induced stresses (DISs) during charging and discharging (*5-7*). Recently, several mathematical models have been developed along with the experimental investigations to understand the DISs in LIB (*5, 8-14*). Under the guidelines of different mathematical models and with the use of novel experimental techniques, improved electrode designs such as nano-scale electrode material (*7*), porous electrode material (*15, 16*), electrode particles with artificial SEI or coatings (*17*) and alloying active and inactive material for electrodes (*18-20*) are employed. These approaches have shown some success in overcoming the mechanical degradation. Recently, we came up with a novel approach of using a liquid metal alloy as a self-healing electrode. We observed that the liquid metal electrode undergoes a reversible of liquid-solid-liquid transition upon lithiation and delithiation (*21*). Such self-healing liquid metal electrodes can have minimum mechanical degradation which makes them good candidates for durable - high energy battery applications.

Fundamental understanding of liquid-solid transition is important to understand the self-healing behavior of liquid metal electrode. *In-situ* XRD is one of the most powerful techniques for understanding crystallographic changes of electrode material. Traditionally, a beryllium window is used for such a study. For example, Courtney *et al.* (*22*) developed a cell design beryllium window for *in-situ* XRD study of silicon. Recently, Rhodes *et al.* (*23, 24*) has published an *in-situ* XRD study for cathode material such as $LiFePO_4$. They came up with a strategy of using a x-ray transparent polymer, 'Kapton', to seal the coin cell window. Using a Kapton tape window is much safer and cost effective as compared to a beryllium window for such a study. Using an approach similar to Rhodes *et al.* (*23, 24*), we designed a cell for *in-situ* XRD study of a liquid metal electrode. We study the lithiation and delithiation of liquid metal and the corresponding phase transformation using this technique.

First-principle calculation tools are widely used for fundamental understanding of various electrode materials. Courtney *et al.* (*25*) performed density functional theory (DFT) calculations to understand the voltage profile for Li-Sn system. We used DFT calculations with Vienna ab-initio simulation package (VASP) (*26*) for crystallographic understanding of different equilibrium phases of Li-Ga system. MedeA (*27*) is used as an interface for all VASP calculations. With these calculations, we regenerate the equilibrium voltage vs. state of charge (SOC) curve for lithium gallium system.

11.3 Computational methods

DFT calculations are performed using the Vienna ab-initio simulation package (VASP) with the Projector Augmented Wave (PAW) method and the Perdew–Burke–Ernzerhof (PBE) form of the generalized gradient approximation (GGA) for exchange and correlation. For crystalline phases, the structures of the alloys are obtained from crystal structure database (*28*). From convergence studies, we determined the kinetic energy cutoff in the plane wave expansion to be 367.5 eV. The electronic iterations convergence is 1×10^{-5}eV using the Normal (blocked Davidson) algorithm and reciprocal space projection operators. We use Gaussian smearing with a width of 0.2 eV. The gallium is liquefied using a super cell of 120 atoms by first raising the temperature to 500 K through ab initio molecular dynamics (AIMD) and optimizing the atomic positions with canonical ensemble (nVT), then taking several low energy configurations to further minimize at 0K with molecular dynamic simulation. A default planewave cutoff energy of 282.697 eV is used for this calculation, due to the size of the system. The optimized lattice parameters of the crystalline Li–Ga phases obtained from our calculations are summarized in Table 11.1. The number of irreducible k points used for each of the Li–Ga alloy phases, are also shown in this Table. The structural data in Table 11.1 are in consistence with the experimental studies and previous theoretical work.

11.4 Experimental

Commercially available pure gallium (Ga) metal (99.99%, Alfa Aesar) was applied onto a substrate without any binder or conducting additive. The substrate is specially designed according to the experimental requirements. The thickness of Ga film on the substrate was controlled to be about 1μm and the mass of Ga was precisely measured by a microbalance (XS 205, Mettler Toledo). Samples were assembled into a modified CR 2025-type coin cell (Hohsen) in an argon-filled glove-box (MBraun) with oxygen and moisture contents less than 0.1 ppm. The modifications to the cell were made in accordance with the experimental requirements and are described in the following sections. Li metal foils (99.9%, Sigma Aldrich) were used as the counter electrode (CE). One piece of Celgard 3501 separator soaked in the electrolyte solution consisting of 1M LiPF6 dissolved in a mixture of ethyl carbonate and dimethyl carbonate (EC/DMC, volumetric ratio 1:1) (Novolyte) was used in making the coin cells.

Charging and discharging of the coin cells was done using a potentiostat (VersaSTAT 3, PAR). During charging and discharging, coin cells were kept at 40 °C, with the precise temperature control according to the experimental needs. The temperature was maintained with a flexible silicone rubber fiberglass insulated heater (SRFG-101/10, Omega Engineering Inc) coupled with a thermostat. In this work, charging refers to lithiation and discharging refers to delithiation.

In-situ XRD was carried out using a BRUKER - General Area Diffraction Detector System (GADDS) with Cu Kα radiation (wavelength 1.54 nm) and beam diameter of 0.5 mm collimator. GADDS is assisted with a laser beam to pinpoint the location of the X-ray beam.

11.5 Cell design

Figure 11.1 shows the exploded view of a cell for the *in-situ* study of liquid gallium electrode. We drill a 10 mm hole in the CR 2025-type coin cell cap. A 14 mm diameter disk of 50 μm thick Kapton tape (Bertech, KPT2-1) was punched and affixed inside the can over the hole. A 36 μm thick metallized polyethylene terephthalate (Metallized-PET, Goodfellow) is used as a substrate for gallium electrode. Both the faces of this component were sputtered with a 400 nm thick film of titanium (Ti). Sputtering of Ti was performed at 75W, 25 mTorr, and 15 sccm of argon (EMSCOPE SC400). This Ti coating was used for improving electrical conductivity of the metalized PET. Using Ti coating for conductive coating is advantageous since Ti is inert with lithium, compatible with electrolytes and x-rays can go through a thin Ti coating without any interference. A gallium film covering a circular area of about 12 mm diameter was applied to the center of the substrate. A nickel ring was used to maintain good contact between the substrate and the cell cap. Direct contact of nickel ring with the gallium is avoided since, gallium reacts readily with nickel.

11.6 Simulations results and discussions

Figure 11.2 shows the different crystals of lithium gallium intermetallic phases that can be formed at equilibrium starting with a disordered liquid gallium structure. These crystals structure are obtained by minimizing the crystal energies. More specifically, we have considered Li_2Ga_7, LiGa, Li_5Ga_4, Li_3Ga_2, Li_2Ga as the equilibrium phases. Li_2Ga_7 phase has a tridiagonal R-3M crystal structure with lattice parameters of $a = 8.605$ Å and $c = 17.118$ Å. The Ga/Li ratio is about 3.5 ± 0.1. This phase can be considered as deficient Li_3Ga_7 phase which has a lower crystal energy (*29*).

Tillard-Charbonnel *et al*. studies of this phase in detail (*29*). They concluded that the deficiency of lithium allows this phase to conduct lithium easily because of the high mobility of lithium inside the cavity and through diffusion jump from one site to neighboring vacant site. The lithiation of Li_2Ga_7 phase results in formation of LiGa phase. LiGa is a cubic NaTl type structure with Fd3m symmetry. Each gallium atom can be observed to be co-ordinated to four equivalents. The structural parameter is calculated to be $a = 6.242$ Å which is close to the experimentally observed value of $a = 6.177$ Å (*30*). Li_5Ga_4 has crystal symmetry of p-3m1 with the lattice parameters $a = 4.375$ Å, $c = 8.257$ Å. The Ga/Li ratio is about 0.8. The Li_3Ga_2 phase has trigonal rhomboedric crystal with R-3M symmetry with the parameters calculated to be $a = 4.367$Å, $c = 13.857$Å which match very closely with the previously reported parameters of $a = 4.367$ Å, $c = 13.896$ Å (*31*). The final product of lithiation of gallium can be Li_2Ga which is an orthorhombic phase with cmcm symmetry and lattice parameters of $a = 4.539$ Å, $b = 9.509$ Å and $c = 4.358$ Å.

In Table 11.1 we list down the total energies of the different Li-Ga phases. We find that, the total energy of the total energy per mole of gallium decreases as the Li concentration increases which indicated that the lithiation of gallium is a thermodynamically favorable process. The calculated total energies of the different Li-Ga phases at equilibrium can be used to calculate the equilibrium voltages of any two-existing phases. The potential of a particular stage during lithiation can be obtained as tangent to the free energy of formation of the two coexisting phases (2)

$$V\ (V) = -\frac{dG_{formation}\ (eV)}{dn} \qquad (11.1)$$

We obtain the equilibrium voltage diagram for Li-Ga system.

For example, for the first phase formation;

$$7Ga\ (liq.) + 2Li \rightleftarrows\ Li_2Ga_7$$

$$Ga(liq.) + \frac{2}{7}Li \rightleftarrows\ \frac{1}{7}Li_2Ga_7$$

$$\Delta G_{formation} = \frac{1}{7}G_{Li_2Ga_7} - G_{Ga} - \frac{2}{7}G_{Li}$$

$$V\ (V) = \left(\tfrac{1}{7}G_{Li_2Ga_7} - G_{Ga} - \tfrac{2}{7}G_{Li}\right)/\left(\tfrac{2}{7} - 0\right) \qquad (11.2)$$

We found that at equilibrium there are five intermetallic phases possible for Li-Ga system. Figure 11.3 shows that the voltages obtained with DFT match closely with the experimentally obtained voltages.

A note should be made that, we have not considered the effects of the polarization and the over potentials. These factors might shift the voltage profile above or below the equilibrium potentials depending upon the experimental conditions. The voltage profile obtained with the DFT calculates show five stages corresponding to the co-existence of different phases. It should also be noted that the voltage plateaus for phase transitions between $LiGa \rightarrow Li_5Ga_4$ and $Li_5Ga_4 \rightarrow Li_3Ga_2$ are not distinguishable in the experimental voltage profile even at low charging rates of C/50. Slower charging might be needed for experimentally observing these phases during lithiation and delithiation. In the experimental voltage profile, a hysteresis is observed between lithiation and delithiation voltages.

One possible reason for the hysteresis is recognized as the differences in diffusion and interface kinetic rates during lithiation and delithiation. In the case of the lithiation, the lithium diffusion is through the lithium rich phase (lithium rich shell in a spherical particle during lithiation) from the surface to the lithium deficient phase. During delithiation, lithium diffuses through the lithium deficient phase (lithium deficient shell in a spherical particle during delithiation) from the lithium rich phase to the surface of the particle. The different diffusion and interface kinetic rates in the lithium rich and lithium deficient phases may result in the shifting of potential plateaus from equilibrium. It should be noted that, the voltage profile with DFT calculations is equilibrium profile without any consideration of the diffusion rates and interface kinetics.

With the DFT calculations, we could also obtain the densities of the different Li-Ga phases. These calculated densities are listed in Table 11.2. Interestingly we find that, liquid gallium has the maximum density (6.093 g cm^{-3}) among all the phases, and the density of the alloys decrease with increasing lithium content. Densities calculated for different phases are 4.56 g cm^{-3} for Li_2Ga_7, 4.19 g cm^{-3} for LiGa, 3.81 g cm^{-3} Li_5Ga_4, 3.49 g cm^{-3} for Li_3Ga_2 and 2.95 g cm^{-3} Li_2Ga. We calculate the volume of different Li-Ga phases per mole of gallium content. We find that, as the lithium content per mole of gallium in an alloy increases, the molar volume per mole of gallium increases. The molar volume of liquid Ga is 11.45 cm^3 which increases to 28.32 cm^3 per mole of Ga for Li_2Ga. We calculate the relative volume expansion (RVE) for different Li-Ga phases. The RVE can be defined as the change in volume of a material due to lithium addition relative to the virgin material volume.

In Figure 11.4, we plot the RVE for different Li-Ga phases against the mole of lithium per cc of liquid gallium in those phases. The partial molar volume of a solute can be defined as:

$$V_{solute}(cc\ per\ mol) = \frac{\Delta V\ (cc)}{\Delta n(mol)}$$

For Li-Ga system, we define,

$$V_{Li}(cc\ per\ mol) = \frac{V_{Li-Ga\ Phase} - V_{liquid\ Ga}}{\Delta n} \tag{11.3}$$

We rearrange this equation to get a relation in terms of the RVE

$$V_{Li}(cc\ per\ mol) = \frac{\left(V_{Li-Ga\ Phase} - V_{liquid\ Ga}\right)/V_{liquid\ Ga}}{\Delta n/V_{liquid\ Ga}}$$

$$= \frac{RVE}{moles\ of\ lithium\ per\ cc\ of\ liquid\ gallium} \tag{11.4}$$

Thus slope of the plot in Figure 11.4 gives the partial molar volume of lithium in liquid gallium. We calculate V_{Li} to be 7.93 cc per mole of the lithium inserted in the liquid gallium. We find that this value of the partial molar volume of lithium in liquid gallium is less than that for many other electrode materials such as Si, Sn, Zn, Ag and Al, in which Li is known to have a partial molar volume of 9.2 cc per mole of the lithium (*2, 32*). This indicates that, gallium would have relatively low expansion on lithiation than many other electrode materials.

11.7 Experimental results and discussions

Figure 11.5 shows the experimental setup for the *in-situ* XRD studies during electrochemical cycling of liquid gallium electrode cell. A laser pointer is used to locate the incident X-rays on the Kapton window. We could monitor the laser pointer location on the Kapton window with an optical microscope. Each XRD frame was obtained with a complete Y-scan along the Kapton window diameter. A Y-scan helps in minimizing the effects from crystal orientations and getting a complete diffraction ring pattern on the detector. XRD data were obtained every half an hour, each frame for about 10 mins, with 2θ angle varying from 30^0 to 70^0. We use a cell capsule for holding the coin cell together with the heating system (Figure 11.5). The Ti from the substrate appeared as a peak in all the scans and is used as a marker peak to understand the peak shifts upon electrochemical processes. We performed the electrochemistry in two parts.

The aim of the experiment was to understand the crystallographic changes upon lithiation and delithiation. We started with pre-lithiated gallium with Li_2Ga_7 as the starting phase and the starting voltage was about 0.7V (Figure 11.6a). We lithiated Li_2Ga_7, using a galvanostatic charging with a current of 100μA. The potential was allowed to drop to 10 mV before the cell is galvanostatically charged back to 0.7V. XRD scans were taken every half an hour. For the initial 2 to 2.5 hours of lithiation, Li_2Ga_7 phase peaks were dominating, with peak intensity diminishing as the time progressed (shown in Figure 11.6 a and b). After around 3 hours of lithiation, the LiGa peaks were dominant and the intensity of these peaks increased as the lithiation progressed to about 6.5 hour of lithiation when the second stage of lithiation of gallium is completed. At this point all the gallium is converted into LiGa phase demonstrated by clear and intense peaks in XRD.

On further lithiation of this phase, we get a continuously decreasing voltage profile indicating a single phase region. Thus, in this period, we observe a shift in the XRD peaks to the left. The peak shift to the left indicates that there is an expansion in LiGa crystals due to lithiation. A gradual peak shift is observed till the point when the potential is dropped to 10 mA.

Once the potential reached this state, galvanostatic delithiation started. With delithiation the peaks were observed to shift gradually to the right which indicates that the expanded crystals were returning to their original volume. Once the potential is increased to around 0.6V, the LiGa peaks appeared back at their normal position with no shifting.

We could clearly see that, with a large current density used in these experiments, the phase transformations $LiGa \rightarrow Li_5Ga_4$ and $Li_5Ga_4 \rightarrow Li_3Ga_2$ did not occur. Courtney *et al*. (*25*) has observed a similar phenomenon in case of lithiation of tin. This discrepancy may be due to an immiscibility gap so that the Li_5Ga_4, Li_3Ga_2 phases are unstable and undergo decomposition in LiGa and Li_2Ga phases.

Formation of the co-existing phases with a sharp phase boundary in any binary system is governed by the inter-diffusion rate and interface kinetics. The chemical non-equilibrium of the system drives the diffusion. If the process is diffusion controlled, two phases would co-exist with a moving phase boundary. These are discrete phases with continuous chemical potential and discontinuity in the concentration across the interface. On the other hand, if the interface kinetic processes cannot respond fast enough to the diffusion process, then metastable or amorphous phases are formed instead of discrete phases with a phase boundary (*33*). In case of lithiation of gallium in the experiments presented above, the operating currents are large leading to faster diffusion due to chemical non-

equilibrium. As compared to the fast diffusion processes the interface kinetics might be slower and thus the formation of equilibrium phases such as Li_5Ga_4 and Li_3Ga_2 is suppressed. Hence, there is no co-existence of two phases hence, no voltage plateau could be observed. Instead, fast lithiation results in the non-equilibrium single phase expansion of $LiGa$ phase leading to a continuous drop in voltage.

At the same time, the last phase of Li_2Ga did not appear till the voltage reached 10 mV. One possible explanation is that, the large currents led to deposition of lithium and results in polarization. Polarization shifts the voltage plateaus to lower voltages than the equilibrium voltage during lithiation. Hence, Li_2Ga phase did not appear even at a low voltage of 10 mV.

11.8 Conclusion

Using ab-initio calculations, we minimized the crystal energies of different possible equilibrium phases in Li-Ga binary system. These calculations helped us in understanding possible crystallographic transformations during lithiation process of liquid gallium. With the minimized free energy of the crystal of the different phases we could regenerate the equilibrium voltage profile for the Li-Ga binary system. On comparing the calculated voltage profile with the experimental voltage profile we found that $LiGa \rightarrow Li_5Ga_4$ and $Li_5Ga_4 \rightarrow Li_3Ga_2$ transformations were not distinguishable at C/50 rates. We could also calculate the densities of different Li-Ga phases and thus understood the volume changes occurring during lithiation of liquid gallium. We calculated the partial molar volume of lithium in liquid gallium and found it to be 7.95 cc per mole of lithium.

To understand the crystal transformation in more detail, we developed a method for *in-situ* XRD study of liquid gallium. This is the first *in-situ* XRD study of liquid gallium system. With the XRD study we observed the lithiation process of Li_2Ga_7. Transformation of Li_2Ga_7 to $LiGa$ phase could be observed as the lithiation proceeds. Upon further lithiation of $LiGa$ phase, $LiGa \rightarrow Li_5Ga_4$ and $Li_5Ga_4 \rightarrow Li_3Ga_2$ transformations were not observed, however, a single phase expansion of $LiGa$ phase was observed.

Such a combination of the DFT tools with the experimental methods such as *in-situ* XRD can help understanding of the battery electrodes and the different chemical transformations they undergo upon electrochemical cycling.

11.9 References

1. J. B. Goodenough, "Basic energy needs for electrical energy storage- Report of the Basic Energy Sciences Workshop for Electrical Energy Storage" (July, 2007).
2. R. A. Huggins, *Advanced Batteries: Materials Science Aspects*. (Springer, 2009).
3. M. N. Obrovac, L. Christensen, D. Ba Le, J. R. Dahn, Alloy Design for Lithium-Ion Battery Anodes. *Journal of The Electrochemical Society* **154**, A849 (2007).
4. L. Y. Beaulieu, T. D. Hatchard, A. Bonakdarpour, M. D. Fleischauer, J. R. Dahn, Reaction of Li with Alloy Thin Films Studied by In Situ AFM. *Journal of The Electrochemical Society* **150**, A1457 (2003).

5. Y. T. Cheng, M. W. Verbrugge, Evolution of Stress within a Spherical Insertion Electrode Particle under Potentiostatic and Galvanostatic Operation. *Journal of Power Sources* **190**, 453 (May, 2009).

6. Y. T. Cheng, M. W. Verbrugge, Diffusion-Induced Stress, Interfacial Charge Transfer, and Criteria for Avoiding Crack Initiation of Electrode Particles. *Journal of the Electrochemical Society* **157**, A508 (2010).

7. M.-H. Park *et al.*, Silicon Nanotube Battery Anodes. *Nano Letters* **9**, 3844 (2009).

8. Y.-T. Cheng, M. W. Verbrugge, The influence of surface mechanics on diffusion induced stresses within spherical nanoparticles. *Journal of Applied Physics* **104**, 083521 (2008).

9. Y.-T. Cheng, M. W. Verbrugge, Evolution of stress within a spherical insertion electrode particle under potentiostatic and galvanostatic operation. *Journal of Power Sources* **190**, 453 (2009).

10. M. W. Verbrugge, Y.-T. Cheng, Stress and Strain-Energy Distributions within Diffusion-Controlled Insertion-Electrode Particles Subjected to Periodic Potential Excitations. *Journal of The Electrochemical Society* **156**, A927 (2009).

11. Y.-T. Cheng, M. W. Verbrugge, Automotive traction battery needs and the influence of mechanical degradation of insertion electrode particles. *Electrochemical Society Transactions* **16**, (2008, 2008).

12. Y.-T. Cheng, M. W. Verbrugge, Application of Hasselman's Crack Propagation Model to Insertion Electrodes. *Electrochemical and Solid-State Letters* **13**, A128 (2010).

13. R. Deshpande, Y.-T. Cheng, M. W. Verbrugge, A. Timmons, Diffusion Induces Stresses and Strain Energy in a Phase Transforming Spherical Electrode Particle. *Journal of The Electrochemical Society* **158**, 1 (2011).

14. R. Deshpande, Y.-T. Cheng, M. W. Verbrugge, Modeling diffusion-induced stress in nanowire electrode structures. *Journal of Power Sources* **195**, 5081 (2010).

15. H.-C. Shin, J. A. Corno, J. L. Gole, M. Liu, Porous silicon negative electrodes for rechargeable lithium batteries. *Journal of Power Sources* **139**, 314 (2005).

16. H. C. Shin, J. Dong, M. L. Liu, Porous Tin Oxides Prepared using an Anodic Oxidation Process. *Adv. Mater.* **16**, 237 (Feb, 2004).

17. L. J. Fu *et al.*, Surface modifications of electrode materials for lithium ion batteries. *Solid State Sci.* **8**, 113 (Feb, 2006).

18. M. Winter, J. O. Besenhard, Electrochemical lithiation of tin and tin-based intermetallics and composites. *Electrochimica Acta* **45**, 31 (1999).

19. T. Tabuchi, N. Hochgatterer, Z. Ogumi, M. Winter, Ternary Sn-Sb-Co alloy film as new negative electrode for lithium-ion cells. *Journal of Power Sources* **188**, 552 (Mar, 2009).

20. O. Mao *et al.*, Active/inactive nanocomposites as anodes for Li-ion batteries. *Electrochem. Solid State Lett.* **2**, 3 (Jan, 1999).

21. R. D. Deshpande, J. Li, Y.-T. Cheng, M. W. Verbrugge, Liquid Metal Alloys as Self-Healing Negative Electrodes for Lithium Ion Batteries. *Journal of The Electrochemical Society* **158**, A845 (2011).

22. I. A. Courtney, J. R. Dahn, Electrochemical and in situ x-ray diffraction studies of the reaction of lithium with tin oxide composites. *Journal of The Electrochemical Society* **144**, 2045 (Jun, 1997).

23. K. Rhodes *et al.*, Novel cell design for combined in situ acoustic emission and x-ray diffraction study during electrochemical cycling of batteries. *Review of Scientific Instruments* **82**, (Jul, 2011).

24. K. Rhodes, R. Meisner, Y. Kim, N. Dudney, C. Daniel, Evolution of Phase Transformation Behavior in Li(Mn(1.5)Ni(0.5))O(4) Cathodes Studied By In Situ XRD. *Journal of The Electrochemical Society* **158**, A890 (2011, 2011).

25. I. A. Courtney, J. S. Tse, O. Mao, J. Hafner, J. R. Dahn, Ab initio calculation of the lithium-tin voltage profile. *Physical Review B* **58**, 15583 (1998).

26. J. Hafner, G. Kresse, D. Vogtenhuber, M. Marsman. (http://cms.mpi.univie.ac.at/marsweb/).

27. MedeA. (http://www.materialsdesign.com/medea/medea-vasp, 2011).

28. ICSD. (http://www.materialsdesign.com/medea/inorganic-crystal-structure-data-icsd).

29. M. Tillard-Charbonenel, C. Belin, J. L. Soubeyroux, The lithium-gallium intermetallic system: electrochemical and neutron powder diffraction study of lithium deficient phase Li_2Ga_7. *Eur. J. Solid State Inorg. Chem.* **t. 27**, 759 (1990).

30. J. Saint, M. Morcrette, D. Larcher, J. M. Tarascon, Exploring the Li-Ga Room Temperature Phase Diagram and the Electrochemical Performances of the Li_xGa_y Alloys vs. Li. *Solid State Ion.* **176**, 189 (Jan, 2005).

31. M. W., S. J., The crystal structure of Li_2Ga and Li_3Ga_2. *Z. Naturforsch.* **B 32**, 631 (1977).

32. A. Timmons, Dalhousie University (2007).

33. K. N. Tu, Interdiffusion in the thin-films. *Annu. Rev. Mater. Sci.* **15**, 147 (1985).

Table 11.1: The optimized lattice parameters of the different crystalline Li–Ga phases obtained from our calculations are summarized

Phase ($Li_{2x}Ga$)	**x**	**Space group**	**k points**	**a (Å)**	**b(Å)**	**c(Å)**	**Energy per cell per Ga atom (eV)**
Liquid Ga	0		2x1x2				-3.0202
Li_2Ga_7	0.143	disordered R-3MH	9x9x5	8.605	8.604	17.118	-3.8126
LiGa	0.5	Fd-3mO1	15x15x15	6.242	6.242	6.242	-5.5782
Li_5Ga_4	0.625	p-3m1	15x15x7	4.375	4.375	8.257	-6.1533
Li_3Ga_2	0.75	R-3MH	15x15x15	4.367	4.367	13.857	-6.6900
Li_2Ga	1	cmcm	13x13x13	4.539	9.509	4.358	-7.7253
Li			9x9x9	3.439	3.439	3.439	

Table 11.2: The calculation of Relative volume expansion of liquid Ga on lithiation using the densities calculated from the ab initio calculation

Phase (Li_nGa)	**Moles of lithium per cc of initial active material ($n/ V_{liquid\ Ga}$)**	**Density ($g\ cm^{-3}$)**	**Molecular weight (g)**	**Molar Volume (cm^3)**	**Volume per gallium (cm^3)**	**Relative volume expansion (Fractional) $dV/ V_{liquid\ Ga}$**
Ga	0.00	6.09	69.72	11.45	11.45	0.00
Li_2Ga_7	0.02	4.56	501.94	110.17	15.74	0.37
LiGa	0.09	4.19	76.66	18.31	18.31	0.60
Li_5Ga_4	0.11	3.81	313.60	82.42	20.60	0.80
Li_3Ga_2	0.13	3.49	160.27	45.94	22.97	1.01
Li_2Ga	0.17	2.95	83.61	28.32	28.32	1.47

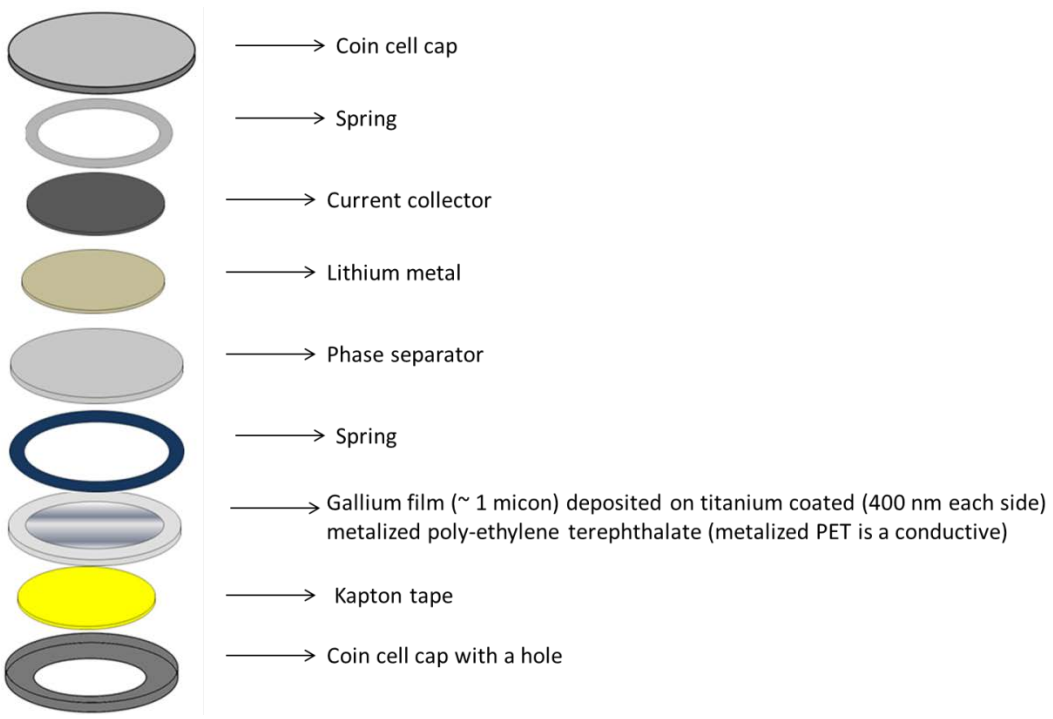

Figure 11.1: The exploded view of a cell for the in-situ study of liquid gallium electrode.

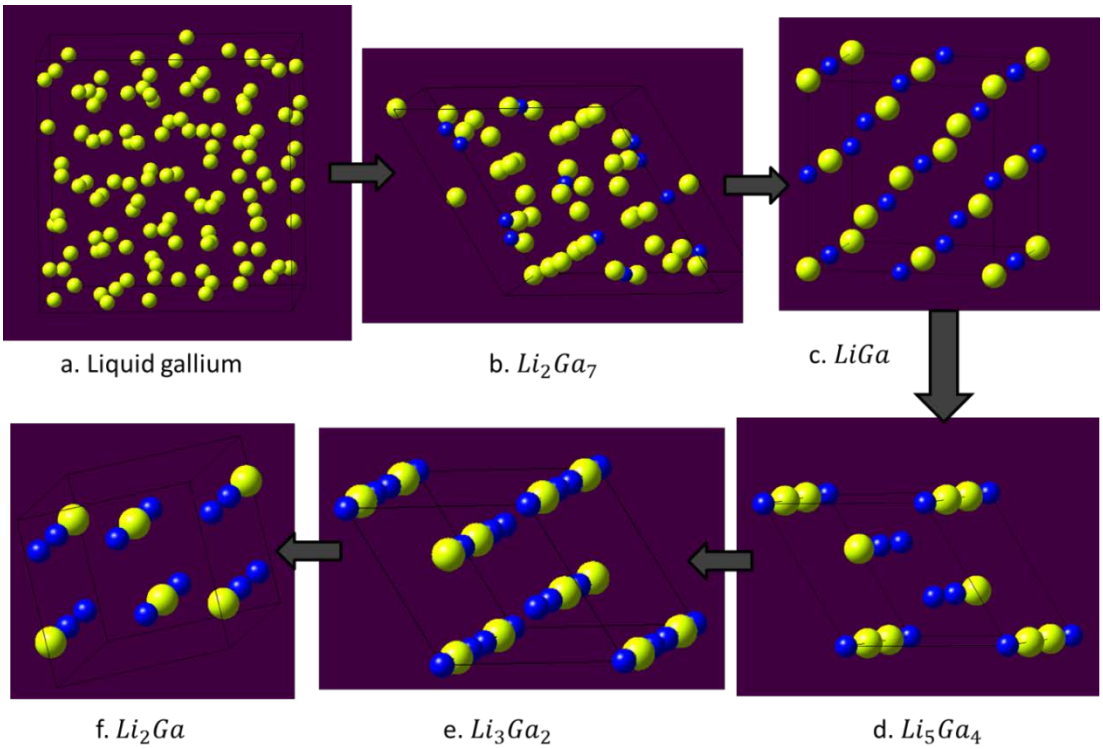

Figure 11.2: Optimized crystal structure different possible phases of the lithium-gallium system at equilibrium.

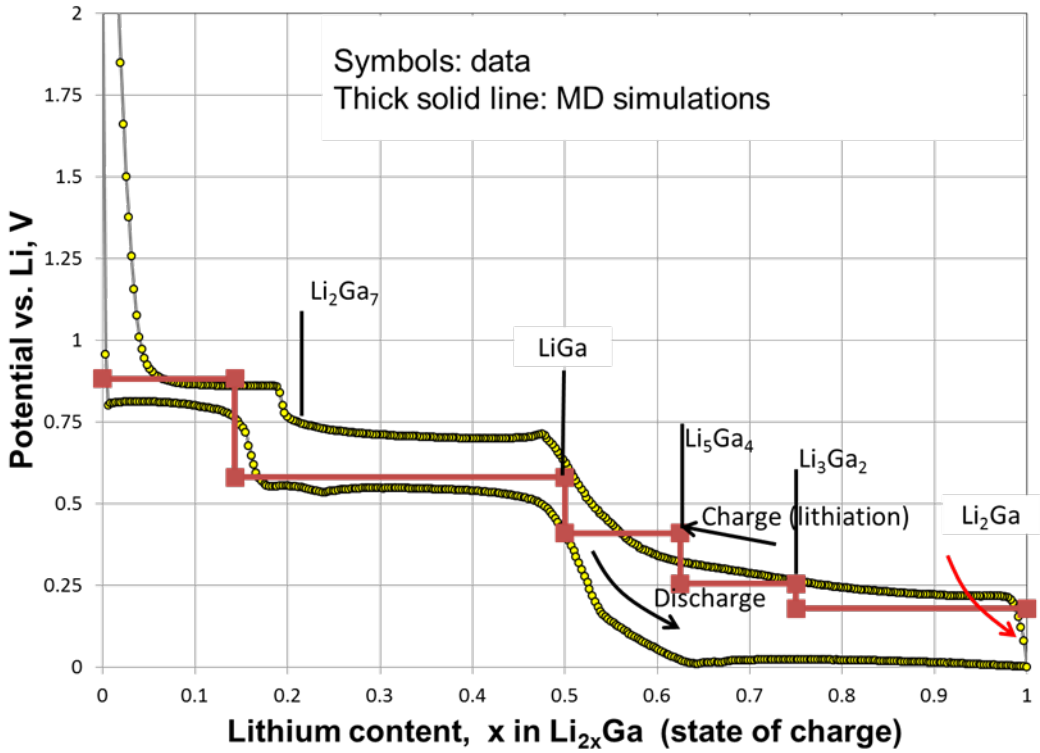

Figure 11.3: Voltage vs. SOC of liquid gallium electrode. The symbols are experimental data and solid lines are from MD calculations.

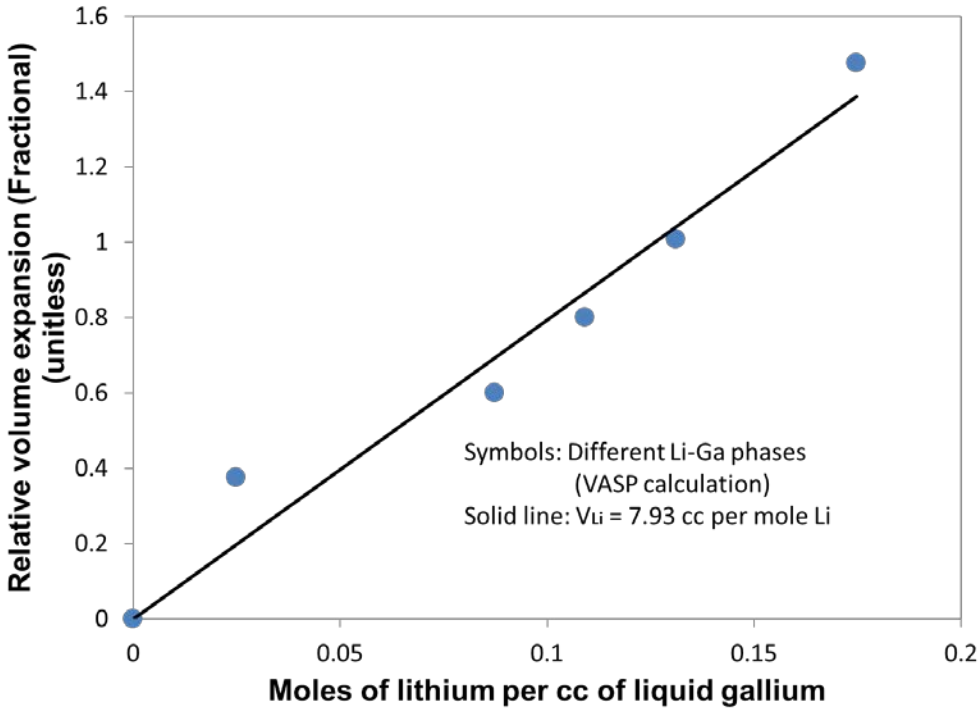

Figure 11.4: A plot of relative volume expansion (RVE) of different Li-Ga phases against the moles of lithium per cc of liquid gallium in those phases.

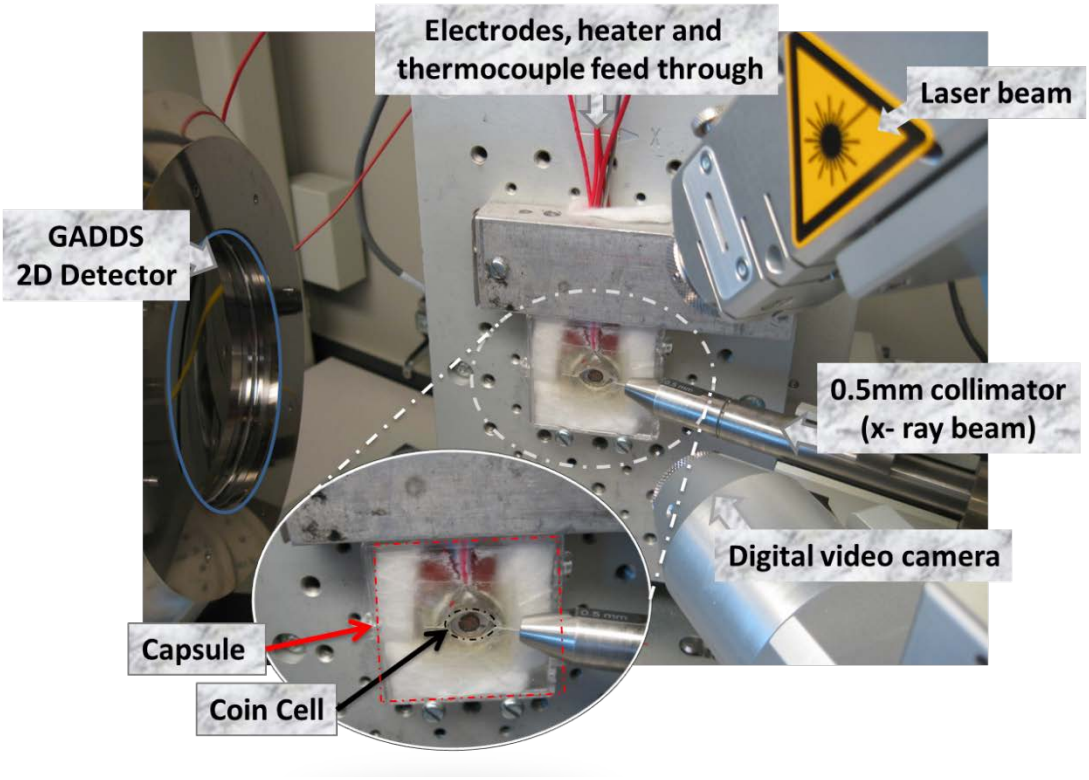

Figure 11.5: The experimental setup for the in-situ x-ray diffraction study of liquid gallium with heating arrangement. A cell capsule was used to hold the coin cell together with the heating system.

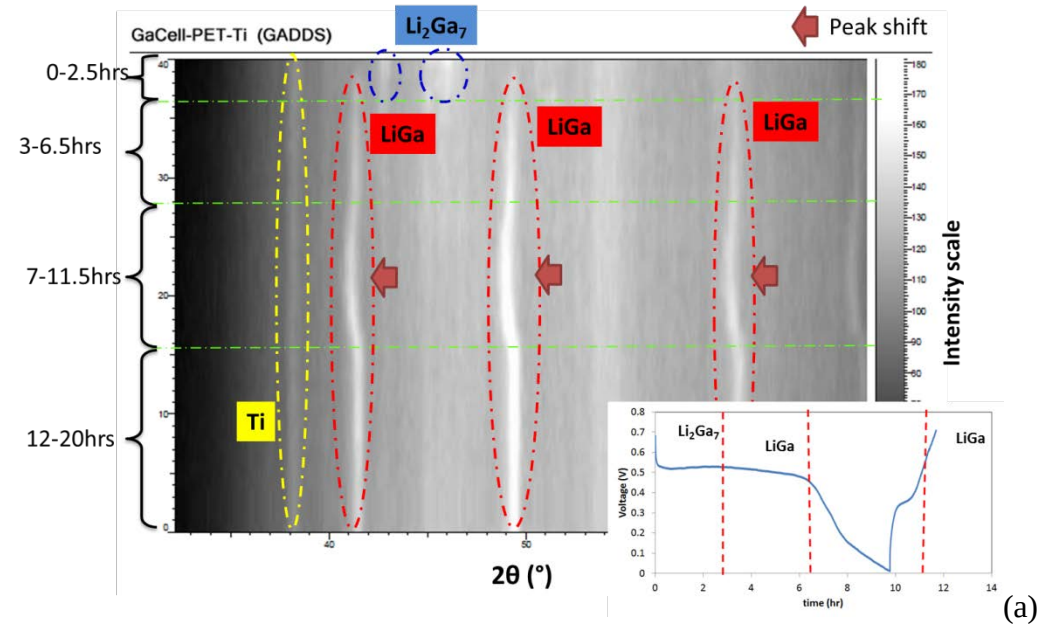

(a)

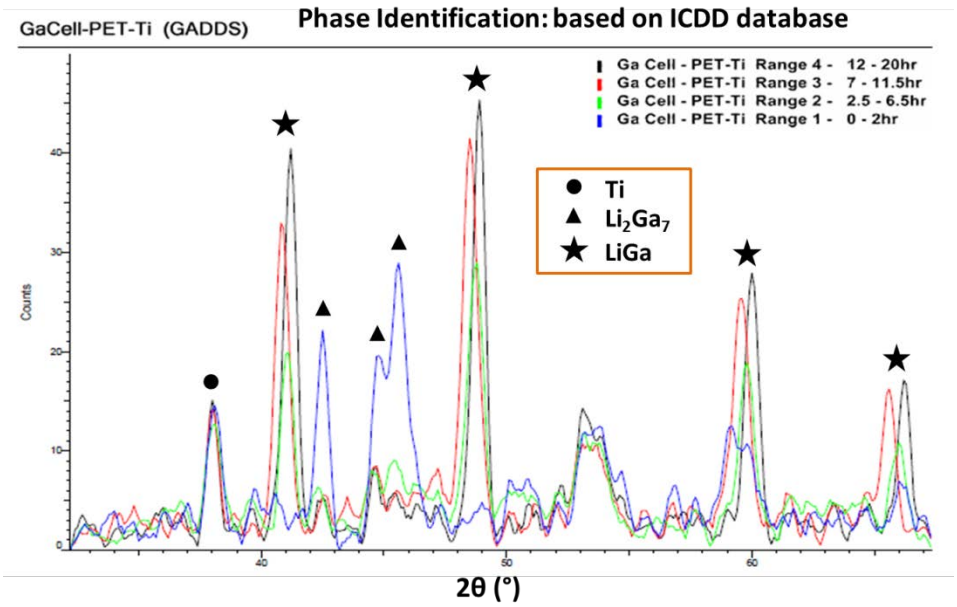

(b)

Figure 11.6: *In-situ* X-ray diffraction of lithiation and delithiation of Li_2Ga_7 (a) 2D peak intensity map as we lithiate and delithiate the Li_2Ga_7. (b) 1D peaks after integration at different time period.

CHAPTER 12

CONCLUSIONS

The commercially available lithium ion batteries do not match the requirements of the electric vehicle applications in terms of energy and power densities as well as the cycle life. This dissertation was focused on understanding the different mechanisms of the capacity fading of the lithium ion batteries and development of new electrode designs for the lithium ion batteries with high energy density, high power density and longer cycle life. With deep understanding of the multidisciplinary aspects of the lithium ion batteries, a meticulous study of the different mechanisms which result in the capacity fading of the batteries is done. The effects of electrode material properties, different electrode designs and operating conditions on the battery performance are investigated with established mathematical and experimental methods. With the fundamental understanding of the lithium ion battery operation, new mathematical and first principles simulation tools and experimental methods are developed for improving the electrode designs for durable high energy batteries.

Mechanical degradation of the lithium ion battery electrodes is one of the major mechanisms behind capacity loss of a lithium ion battery. While charging and discharging a battery, lithium insertion and extraction from the electrode particles result in 'Diffusion-induced stresses' (DISs) which may lead to the mechanical degradation of the active electrode materials. A part of this research was focused on understanding the DISs in battery electrodes with mathematical tools.

We mathematically modeled different mechanical, transport and electrochemical processes inside the battery with which we could co-relate DISs with local lithium ion concentration using the thermal stress analogy to the DISs. We studied the nature of these stresses and their dependence on various parameters such as battery operating conditions (constant current, constant potential), shape of electrode elements (spherical particles, cylindrical wires, tubes *etc.*), sizes of electrode element (nano, micro), mechanical and transport properties of the electrode material as well as the solid electrolyte interphase (SEI) properties.

Using mathematical formulations, we examined the nature of DISs in a cylindrical electrode particle on lithium insertion and extraction. It was found that the radial stress at the center initially increases, reaches a maximum at a particular time during lithiation and then decreases gradually until the electrode reaches saturation concentration. We found that the tangential stress is maximum just at the start of delithiation at the surface of the electrode particle. A simple mathematical relation could be established to correlate DISs with the material properties of electrode material. The DISs change qualitatively and quantitatively with the changing axial loading conditions for a cylindrical electrode. The effect of different axial loading conditions on the DISs is well incorporated in the model. To the best of our knowledge this was the first attempt in the published literature to understand the diffusion induced stresses in a cylindrical electrode element. We could also understand the effect of size of the particle on DISs. We found that, at the nano-scale, the surface properties such as surface tension and surface energy of the electrode have important roles to play in mitigating the diffusion induced stresses. Thus at nano-scale, the electrode material is less prone to cracking than at micro-scale.

The conclusions of the model explain the physics behind the improved cycle life of batteries with nanowire electrodes as observed in various experiments performed in the research community on the nanowire electrodes.

Along with nanowires, we also developed a mathematical model for understanding the stress distribution in a tubular electrode element. In case of tubular electrodes, there is more 'breathing space' for the electrode material to expand on lithiation. Thus the DISs in such a structure may be smaller as compared to those in the case of solid cylindrical electrode. With the model developed we understand that the tangential / axial stress reach maximum at the start of delithiation at the tube surface. It is observed that, the maximum tangential or axial stress is much larger than the maximum radial stress. Thus the tube is more prone to cracking due to the axial or tangential stress than the radial stress. Since, the maximum axial and tangential stresses have the same magnitude, the combination of surface energy required and strain energy stored would decide if the tube undergoes axial cracking (splitting of the tube) or tangential cracking (opening up of the tube). Splitting of the tube i.e. axial cracking is more detrimental for battery applications since it results in loss of electrical contact of the electrode material. We developed a co-relation between height and inner and outer radii of tubes which can be used to avoid axial cracking. Using guidelines from the model, TiO_2 nanotubes are prepared and are tested for cycle life in collaboration with my colleagues Juchuan Li and Qingliu Wu at the University of Kentucky. The experimental results show that such tubes show longer cycle life as predicted by the model.

With first principles calculations, researchers have found that there is a drastic change in the material properties of the electrode upon lithiation. Some of the materials soften on lithiation and some stiffen on lithiation. We developed a model to study the effects of lithium concentration dependent Young's modulus of the electrode material on the DIS behavior during lithiation and delithiation. To the best of our knowledge, this was the first mathematical model for DISs inside a battery electrode which takes into account the change in material properties with lithium concentration. We showed that the change in properties of the lithiated part affects stresses even in the unlithiated part. We calculated the fracture tendencies of different materials which undergo either stiffening or softening on lithiation, providing guidelines for minimizing it. The widely held assumption that the stress behavior during delithiation is exact reversal or a mirror image of that during lithiation is not valid for electrodes with concentration-dependent Young's modulus. Also, we observed that the magnitude of the stresses can also change drastically with composition-dependent Young's modulus. We found that the fracture tendency of the electrode due to radial stress decreases if the material is lithiation softening. At the same time, for lithiation stiffening material, the tangential stress maxima might shift from the surface to just below the surface. Since the defects are present at the surface, the shifting of peak stress location may result in decreasing fracture tendency.

In the battery community, it is well established that some of the electrode materials undergo the phase transformations during electrochemical charging/discharging, leading to a co-existence of two or more phases with moving phase boundaries. Common negative electrode materials such as graphite, tin and gallium are known to undergo such phase transformations.

We studied the concentration and stress profiles in such an electrode particle. With mathematical model we found that there is a stress jump at the interface. Such a stress jump at the inter-phase can cause crack initiation. We also analyzed the effect of material properties of the two phases on the stress jump and suggested some guidelines to tune the material properties to minimize the stress jump. It is found that, the stress jump can be minimized if the two co-existing phases have a similar expansion tendency.

In a real electrode particle numerous pre-existing cracks/ mesopores were observed. This contradicts the widely held assumption that the electrode particle is homogeneous and isotropic. A new mathematical model was proposed to show that the presence of free surfaces, from even a small internal crack or pore, could alter the internal stress distributions such that particles are prone to internal cracking instead of the surface cracking previously predicted. This was the first model in the literature which accounted for pre-existing cracks while understanding the diffusion induced stresses. We established that the fracture strength of particles depends largely on their internal microstructure, about which little is known, rather than on the intrinsic mechanical properties of the particle materials. This model establishes the significance of the fundamental understanding of the microstructure and its incorporation in the stress and transport models.

The operating voltage (vs. a lithium reference electrode) of the commonly used negative electrodes is lower than the lower limit of the stability voltage window of the commonly used electrolytes. Hence, the electrolytes undergo reduction on the negative electrode surface. It results in solid electrolyte interphase (SEI) formation on the surface of electrode and results in capacity fading of the battery due to the chemical degradation.

The SEI layer on the electrode particle affects the diffusion behavior or concentration profile of lithium atoms inside the host particle, which in turn results in change in the stress behavior. Different artificial SEI materials/coatings are used on the electrode particle in attempt to enhance the life of electrode. We mathematically co-relate the SEI properties with the diffusion induced stresses. The maximum radial stress (tensile) during lithiation and tangential stress (tensile) during de-lithiation decrease lineally with an increase in stiffness or thickness of the SEI and decrease in diffusion coefficient or equilibrium concentration of solute in the SEI. At the same time, the strain energy stored at the end of lithiation increases rapidly with an increase in either thickness or stiffness of the SEI. This might be detrimental since strain energy stored could be relieved by creating new fracture surfaces and resulting in cracking of the particle.

The chemical and mechanical degradation, in combination results in capacity fading of the lithium ion batteries. For automotive applications, prediction of battery life is of the utmost importance. Using the differential voltage technique we proved that lithium loss is the major mechanism behind the capacity loss in a commercial $LiFePO_4$/graphite lithium ion battery. The DISs result in gradual crack propagation each cycle exposing a new surface area to the electrolyte. A new SEI is formed on this surface consuming lithium from the system. Simultaneously, the thickness of SEI also increases with time, resulting in more capacity loss. With such a schematic model in mind, we developed a mathematical model that combines chemical and mechanical degradation capacity fading mechanism for the commercial batteries to predict battery life for a $LiFePO_4$ / graphite A123 battery at different operating temperatures.

The model predictions were compared with the experimental data. We were able to regenerate the voltage vs. capacity curves for different cycle number and degenerate the cell voltage curves into individual electrode voltages, thus at particular time during operation we could know the SOC of individual electrodes.

Different electrode designs and approaches such as nano-structural electrode particles, alloying of the active material with inactive material and coating electrode particles with artificial SEI have shown some improvement in the mechanical stability of the electrode material. To minimize the mechanical degradation and improve the energy density, we proposed a novel concept of using a liquid metal electrode as a self-healing electrode. Here we took gallium as a liquid electrode. We developed a method to prepare a thin film electrode of liquid metal with thickness of around 1 micron. For the experimental purpose, we operated the batteries at 40 ^{0}C, which is well above the melting point of Ga (29 ^{0}C). A new capillary cell design was developed for optical observation of such a liquid electrode. With different techniques such as XRD, optical observation and electrochemistry we demonstrated the reversibility of the liquid-solid-liquid transition of such a liquid metal electrode upon electrochemical cycling.

To get the crystal structure understanding of the different phases formed during lithiation of a gallium electrode, the density function theory (DFT) calculations on the different equilibrium phases of Li-Ga system using Vienna ab-initio simulation package (VASP) were implemented. We optimized the crystal energies of different possible equilibrium phases of Li-Ga system which we used to regenerate the equilibrium potential vs. state of charge (SOC) curve for the liquid gallium electrode. With this calculation we could get five equilibrium Li-Ga phases.

To further investigate the crystallographic changes in liquid metal electrode, a method for *in-situ* X-ray diffraction study of such an electrode was developed. With this technique we observed the different phase transformation the liquid gallium electrode undergoes during lithiation and delithiation. It was found that with the experimentally used current rate two of the equilibrium phases Li_5Ga_4 and Li_3Ga_2 cannot be formed.

In this work we performed detailed investigation of DISs in lithium ion battery electrodes. Various factors that affect the DISs are studied with mathematical models and solving them analytically. Analytical solutions are useful for understanding the physics behind different processes in LIBs. Effects of size of the nanowire electrode on DISs, effects of co-existence of two phases on DISs, effects of change in material properties on DISs, effects of the presence of SEI on DISs, effects of pre-existing pores on fracture tendency in LIB electrodes had never been investigated before these studies. These factors are shown to have a large effect on the nature of DISs during battery operation which in turn decides the mechanical degradation of lithium ion battery electrodes. A phenomenological model with coupled chemical and mechanical degradation for cycle life prediction has been proposed for the first time in the battery literature through this work. We also proposed a concept of using liquid electrode for avoiding mechanical degradation which is fundamentally different from the existing approaches of electrode engineering for mechanical stability. This approach opened up a new direction for potential improvement in advanced lithium ion batteries. The capillary cell and *in-situ* XRD cell designed for liquid electrode are novel cell designs for liquid electrode studies and can potentially be used to understand this new family of liquid metal electrodes.

The different DISs models proposed in this dissertation can be used as foundation for detailed analysis of the physical processes that result in mechanical degradation in the LIB electrodes. Various assumptions made in the presented models can be gradually relaxed depending upon the electrode material for more accurate analysis for specific electrode systems. For example, most of the models presented here assume that the strain in the electrode particle is infinitesimally small within the elastic limits. This assumption may not be valid for advanced electrode materials such as Silicon which is known to have 300% volume expansion on complete lithiation. For such a material, consideration of finite volume expansion and plastic deformation due to high shear stress might lead to more accurate conclusions. In this work we assumed that the diffusion follows Fick's law, neglecting the effects of hydrostatic stresses and concentration of solute on diffusion. As a next step, consideration of these effects might lead to more realistic concentration profiles which determine stress profiles. The presented models give general guidelines for the electrode material selection and design. More accuracy can be reached using exact properties of different advanced electrode materials. The life cycle model we proposed has several assumptions such as number of pre-existing cracks; initial crack lengths etc. which would need more experimental data to verify the accuracy. For mechanical stability of the electrodes we proposed the use of liquid electrode to avoid mechanical degradation with the example of liquid gallium as electrode material. Gallium is not commercially attractive since it is expensive. Several other liquid metal alloys are active for lithium storage and can be investigated with the techniques we developed in the present study. Furthermore, different combinations of active electrode material and liquid metal electrode can be investigated in further studies.

Thus, this dissertation was focused on understanding and improvement of the lithium ion batteries with mathematical modeling, computer simulations and experimental tools. With several experimental techniques, including ball milling, cryo-milling, x-ray diffraction, optical microscopy, cyclic voltammetry, potentiostatic and galvanostatic cycling and electro-impedance spectroscopy, several mathematical tools such as MATLAB, COMSOL and *Mathematica* and molecular simulation tools such as VASP the preset goals were achieved.

BIBLIOGRAPHY

1 Anderson, D. M., McFadden, G. B. & Wheeler, A. A. A phase-field model with convection: sharp-interface asymptotics. *Physica D: Nonlinear Phenomena* **151**, 305-331 (2001).

2 Andersson, A. & Thomas, J. *Journal of Power Sources* **97**, 498 (2001).

3 Arico, A. S., Bruce, P., Scrosati, B., Tarascon, J. M. & Van Schalkwijk, W. Nanostructured materials for advanced energy conversion and storage devices. *NATURE MATERIALS* **4**, 366-377, doi:10.1038/nmat1368 (2005).

4 Armand, M. & Tarascon, J. M. Building Better Batteries. *Nature* **451**, 652-657, doi:10.1038/451652a (2008).

5 Armstrong, G., Armstrong, A. R., Bruce, P. G., Reale, P. & Scrosati, B. TiO_2(B) Nanowires as An Improved Anode Material for Lithium-Ion Batteries Containing $LiFePO_4$ or $LiNi_{0.5}Mn_{1.5}O_4$ Cathodes and A Polymer Electrolyte. *Adv. Mater.* **18**, 2597-2600, doi:10.1002/adma.200601232 (2006).

6 Aurbach, D. Review of selected electrode-solution interactions which determine the performance of Li and Li ion batteries. *Journal of Power Sources* **89**, 206-218 (2000).

7 Aydinol, M. K., Kohan, A. F., Ceder, G., Cho, K. & Joannopoulos, J. Ab initio study of lithium intercalation in metal oxides and metal dichalcogenides. *Physical Review B* **56**, 1354-1365, doi:10.1103/PhysRevB.56.1354 (1997).

8 Baker, D. R. & Verbrugge, M. W. Temperature and Current Distribution in Thin-Film Batteries. *Journal of The Electrochemical Society* **146**, 2413-2424 (1999).

9 Bao, S. J., Bao, Q. L., Li, C. M. & Dong, Z. L. Novel Porous Anatase TiO_2 Nanorods and their High Lithium Electroactivity. *Electrochem. Commun.* **9**, 1233-1238, doi:10.1016/j.elecom.2007.01.028 (2007).

10 Beaulieu, L. Y., Hatchard, T. D., Bonakdarpour, A., Fleischauer, M. D. & Dahn, J. R. Reaction of Li with Alloy Thin Films Studied by In Situ AFM. *Journal of The Electrochemical Society* **150**, A1457-A1464 (2003).

11 Bloom, I. *et al.* An accelerated calendar and cycle life study of Li-ion cells. *Journal of Power Sources* **101**, 238-247, doi:10.1016/s0378-7753(01)00783-2 (2001).

12 Boukamp, B. A., Lesh, G. C. & Huggins, R. A. All-Solid Lithium Electrodes with Mixed-Conductor Matrix. *Journal of The Electrochemical Society* **128**, 725-729 (1981).

13 Broussely, M. *et al.* Main aging mechanisms in Li ion batteries. *Journal of Power Sources* **146**, 90-96, doi:10.1016/j.jpowsour.2005.03.172 (2005).

14 Cai, Q., Paulose, M., Varghese, O. K. & Grimes, C. A. The effect of electrolyte composition on the fabrication of self-organized titanium oxide nanotube arrays by anodic oxidation. *J. Mater. Res.* **20**, 230-236 (2005).

15 Carslaw, H. S. & Jaeger, J. C. *Conduction of heat in solids*. second edn, (Clarendon Press, 1959).

16 Ceder, G. *et al.* Identification of cathode materials for lithium batteries guided by first-principles calculations. *Nature* **392**, 694-696, doi:10.1038/33647 (1998).

17 Chan, C. K. *et al.* High-performance lithium battery anodes using silicon nanowires. *Nat Nano* **3**, 31-35, doi:http://www.nature.com/nnano/journal/v3/n1/suppinfo/nnano.2007.411_S1.html (2008).

18 Chan, C. K. *et al.* High-Performance Lithium Battery Anodes using Silicon Nanowires. *Nat. Nanotechnol.* **3**, 31-35, doi:10.1038/nnano.2007.411 (2008).

19 Chan, C. K., Ruffo, R., Hong, S. S., Huggins, R. A. & Cui, Y. Structural and electrochemical study of the reaction of lithium with silicon nanowires. *Journal of Power Sources* **189**, 34-39 (2009).

20 Chan, C. K., Zhang, X. F. & Cui, Y. High Capacity Li Ion Battery Anodes Using Ge Nanowires. *Nano Letters* **8**, 307-309, doi:10.1021/nl0727157 (2007).

21 Chen, G., Song, X. & Richardson, T. Electron Microscopy Study of the LiFePO4 to FePO4 Phase Transition. *Electrochemical and Solid-State Letters* **9**, A295 (2006).

22 Chen, L. B., Lu, N., Xu, C. M., Yu, H. C. & Wang, T. H. Electrochemical performance of polycrystalline CuO nanowires as anode material for Li ion batteries. *Electrochimica Acta* **54**, 4198-4201 (2009).

23 Cheng, Y. & Verbrugge, M. The influence of surface mechanics on diffusion induced stresses within spherical nanoparticles. *JOURNAL OF APPLIED PHYSICS* **104**, 83521 (2008).

24 Cheng, Y. T. & Verbrugge, M. W. Evolution of Stress within a Spherical Insertion Electrode Particle under Potentiostatic and Galvanostatic Operation. *Journal of Power Sources* **190**, 453-460, doi:10.1016/j.jpowsour.2009.01.021 (2009).

25 Cheng, Y. T. & Verbrugge, M. W. Diffusion-Induced Stress, Interfacial Charge Transfer, and Criteria for Avoiding Crack Initiation of Electrode Particles.

Journal of the Electrochemical Society **157**, A508-A516, doi:10.1149/1.3298892 (2010).

26 Cheng, Y.-T. & Verbrugge, M. W. The influence of surface mechanics on diffusion induced stresses within spherical nanoparticles. *Journal of Applied Physics* **104**, 083521-083526 (2008).

27 Cheng, Y.-T. & Verbrugge, M. W. Automotive traction battery needs and the influence of mechanical degradation of insertion electrode particles. *Electrochemical Society Transactions* **16** (2008).

28 Cheng, Y.-T. & Verbrugge, M. W. Evolution of stress within a spherical insertion electrode particle under potentiostatic and galvanostatic operation. *Journal of Power Sources* **190**, 453-460 (2009).

29 Cheng, Y.-T. & Verbrugge, M. W. Diffusion-Induced Stress, Interfacial Charge Transfer, and Criteria for Avoiding Crack Initiation of Electrode Particles. *J. Electrochem. Soc.* **157**, A508-A516 (2010).

30 Cheng, Y.-T. & Verbrugge, M. W. Application of Hasselman's Crack Propagation Model to Insertion Electrodes. *Electrochemical and Solid-State Letters* **13**, A128-A131 (2010).

31 Chen-Min Li, J. Physical chemistry of some microstructural phenomena. *Metallurgical and Materials Transactions A* **9**, 1353-1380, doi:10.1007/bf02661808 (1978).

32 Christensen, J. & Newman, J. A mathematical model for the lithium-ion negative electrode solid electrolyte interphase. *Journal of The Electrochemical Society* **151**, A1977-A1988, doi:10.1149/1.1804812 (2004).

33 Christensen, J. & Newman, J. A Mathematical Model of Stress Generation and Fracture in Lithium Manganese Oxide. *Journal of The Electrochemical Society* **153**, A1019-A1030 (2006).

34 Christensen, J. & Newman, J. Stress generation and fracture in lithium insertion materials. *Journal of Solid State Electrochemistry* **10**, 293-319 (2006).

35 Chung, S. Y., Bloking, J. T. & Chiang, Y. M. Electronically conductive phospho-olivines as lithium storage electrodes. *Nature Materials* **1**, 123-128, doi:10.1038/nmat732 (2002).

36 Courtney, I. A. & Dahn, J. R. Electrochemical and in situ x-ray diffraction studies of the reaction of lithium with tin oxide composites. *Journal of The Electrochemical Society* **144**, 2045-2052, doi:10.1149/1.1837740 (1997).

37 Courtney, I. A., Tse, J. S., Mao, O., Hafner, J. & Dahn, J. R. Ab initio calculation of the lithium-tin voltage profile. *Physical Review B* **58**, 15583-15588 (1998).

38 Crank, J. *The Mathematics of Diffusion*. (Oxford University Press, USA, 1980).

39 Cuenot, S., Frétigny, C., Demoustier-Champagne, S. & Nysten, B. Surface tension effect on the mechanical properties of nanomaterials measured by atomic force microscopy. *Physical Review B* **69**, 165410 (2004).

40 Cui, L.-F., Ruffo, R., Chan, C. K., Peng, H. & Cui, Y. Crystalline-Amorphous Core−Shell Silicon Nanowires for High Capacity and High Current Battery Electrodes. *Nano Letters* **9**, 491-495, doi:10.1021/nl8036323 (2008).

41 Cui, L.-F., Yang, Y., Hsu, C.-M. & Cui, Y. Carbon−Silicon Core−Shell Nanowires as High Capacity Electrode for Lithium Ion Batteries. *Nano Letters* **9**, 3370-3374, doi:10.1021/nl901670t (2009).

42 Dahn, J. R. Phase diagram of LixC6. *Physical Review B* **44**, 9170 (1991).

43 Darling, R. & Newman, J. Modeling a Porous Intercalation Electrode with Two Characteristic Particle Sizes. *Journal of The Electrochemical Society* **144**, 4201-4208 (1997).

44 Dees, D., Gunen, E., Abraham, D., Jansen, A. & Prakash, J. Electrochemical Modeling of Lithium-Ion Positive Electrodes during Hybrid Pulse Power Characterization Tests. *Journal of The Electrochemical Society* **155**, A603-A613 (2008).

45 Delmas, C., Maccario, M., Croguennec, L., Cras, F. L. & Weill, F. Lithium deintercalation in LiFePO4 nanoparticles via a domino-cascade model. *NATURE MATERIALS* **7**, 665 (2008).

46 Deshpande, R., Cheng, Y.-T. & Verbrugge, M. W. Modeling diffusion-induced stress in nanowire electrode structures. *Journal of Power Sources* **195**, 5081-5088 (2010).

47 Deshpande, R., Cheng, Y.-T., Verbrugge, M. W. & Timmons, A. Diffusion Induces Stresses and Strain Energy in a Phase Transforming Spherical Electrode Particle. *Journal of The Electrochemical Society* **158**, 1-7, doi:10.1149/1.3565183 (2011).

48 Deshpande, R., Qi, Y. & Cheng, Y.-T. Effects of Concentration-Dependent Elastic Modulus on Diffusion-Induced Stresses for Battery Applications. *Journal of The Electrochemical Society* **157**, A967-A971 (2010).

49 Deshpande, R. D., Li, J., Cheng, Y.-T. & Verbrugge, M. W. Liquid Metal Alloys as Self-Healing Negative Electrodes for Lithium Ion Batteries. *Journal of The Electrochemical Society* **158**, A845-A849, doi:10.1149/1.3591094 (2011).

50 Devan, S., Subramanian, V. R. & White, R. E. Analytical Solution for the Impedance of a Porous Electrode. *Journal of The Electrochemical Society* **151**, A905-A913 (2004).

51 Doyle, M., Fuller, T. F. & Newman, J. Modeling of Galvanostatic Charge and Discharge of the Lithium/Polymer/Insertion Cell. *Journal of The Electrochemical Society* **140**, 1526-1533 (1993).

52 Doyle, M., Newman, J., Gozdz, A. S., Schmutz, C. N. & Tarascon, J.-M. Comparison of Modeling Predictions with Experimental Data from Plastic Lithium Ion Cells. *Journal of The Electrochemical Society* **143**, 1890-1903 (1996).

53 Dunand, D. C. & Zwigl, P. Hydrogen-induced internal-stress plasticity in titanium. *Metallurgical and Materials Transactions a-Physical Metallurgy and Materials Science* **32**, 841-843, doi:10.1007/s11661-001-0100-3 (2001).

54 Ein-Eli, Y. A new perspective on the formation and structure of the solid electrolyte interface at the graphite anode of Li-ion cells. *Electrochemical and Solid State Letters* **2**, 212-214 (1999).

55 Fang, H.-T. *et al.* Comparison of the rate capability of nanostructured amorphous and anatase TiO2 for lithium insertion using anodic TiO2 nanotube arrays. *Nanotechnology* **20**, 225701/225701-225701/225707 (2009).

56 Fu, L. J. *et al.* Surface modifications of electrode materials for lithium ion batteries. *Solid State Sci.* **8**, 113-128, doi:10.1016/j.solidstatesciences.2005.10.019 (2006).

57 Fuller, T. F., Doyle, M. & Newman, J. Simulation and Optimization of the Dual Lithium Ion Insertion Cell. *Journal of The Electrochemical Society* **141**, 1-10 (1994).

58 Gabrisch, H., Wilcox, J. & Doeff, M. TEM Study of Fracturing in Spherical and Plate-like LiFePO4 Particles. *Electrochemical and Solid-State Letters* **11**, A25 (2008).

59 Garcia, E., Chiang, Y., Carter, W., Limthongkul, P. & Bishop, C. Microstructural Modeling and Design of Rechargeable Lithium-Ion Batteries. *Journal of The Electrochemical Society* **152**, A255 (2005).

60 Garcia, R. E., Chiang, Y.-M., Carter, W. C., Limthongkul, P. & Bishop, C. M. Microstructural Modeling and Design of Rechargeable Lithium-Ion Batteries. *Journal of The Electrochemical Society* **152**, A255-A263 (2005).

61 Goodenough, J. B. Basic energy needs for electrical energy storage- Report of the Basic Energy Sciences Workshop for Electrical Energy Storage. (July, 2007).

62 Graetz, J., Ahn, C. C., Yazami, R. & Fultz, B. Highly Reversible Lithium Storage in Nanostructured Silicon. *Electrochemical and Solid State Letters* **6**, A194-A197, doi:10.1149/1.1596917 (2003).

63 Hafner, J., Kresse, G., Vogtenhuber, D. & Marsman, M. *VASP*.

64 Han, B. C., Van der Ven, A., Morgan, D. & Ceder, G. Electrochemical modeling of intercalation processes with phase field models. *Electrochimica Acta* **49**, 4691-4699 (2004).

65 Harris, S., Deshpande, R., Qi, Y., Cheng, Y. T. & Dutta, I. Mesopores inside electrode particles can change the Li-ion transport mechanism and diffusion-induced stress. *J. Mater. Res.* **25** (August, 2010).

66 Harris, S. J., Deshpande, R. D., Qi, Y., Dutta, I. & Cheng, Y. T. Mesopores inside electrode particles can change the Li-ion transport mechanism and diffusion-induced stress. *J. Mater. Res.* **25**, 1433-1440, doi:10.1557/jmr.2010.0183 (2010).

67 Hassoun, J., Panero, S. & Scrosati, B. Electrodeposited Ni-Sn Intermetallic Electrodes for Advanced Lithium Ion Batteries. *Journal of Power Sources* **160**, 1336-1341, doi:10.1016/j.jpowsour.2006.02.068 (2006).

68 Herring, C. *Structure and properties of solid surface*. page 5 (University of Chicago press, 1953).

69 Hetnarski, R. & Eslami, R. *Thermal Stresses -- Advanced Theory and Applications (Solid Mechanics and Its Applications)*. (Springer, 2008).

70 Hibbler, R. C. *Mechanics of Materials*. Third Edition edn, (Prentice Hall, 1997).

71 Hosono, E., Kudo, T., Honma, I., Matsuda, H. & Zhou, H. Synthesis of Single Crystalline Spinel LiMn2O4 Nanowires for a Lithium Ion Battery with High Power Density. *Nano Letters* **9**, 1045-1051, doi:10.1021/nl803394v (2009).

72 Hosono, E. *et al.* Synthesis of single crystalline electro-conductive Na0.44MnO2 nanowires with high aspect ratio for the fast charge-discharge Li ion battery. *Journal of Power Sources* **182**, 349-352 (2008).

73 Hu, L. B. *et al.* Silicon-Carbon Nanotube Coaxial Sponge as Li-Ion Anodes with High Areal Capacity. *Advanced Energy Materials* **1**, 523-527, doi:10.1002/aenm.201100056 (2011).

74 Huggins, R. & Nix, W. Decrepitation Model For Capacity Loss During Cycling of Alloys in Rechargeable Electrochemical Systems. *Ionics* **6**, 57 (2000).

75 Huggins, R. A. *Advanced Batteries: Materials Science Aspects*. (Springer, 2009).

76 ICSD. *Inorganic crystal structure data*.

77 Itou, Y. & Ukyo, Y. Performance of LiNiCoO2 materials for advanced lithium-ion batteries. *Journal of Power Sources* **146**, 39 (2005).

78 Jagannathan, K. Approximate Solution Methods for Solid-State Diffusion in Phase-Change Electrodes. *Journal of The Electrochemical Society* **156**, A1028-A1033 (2009).

79 Jung, Y. S. *et al.* Enhanced Stability of LiCoO(2) Cathodes in Lithium-Ion Batteries Using Surface Modification by Atomic Layer Deposition. *Journal of The Electrochemical Society* **157**, A75-A81, doi:10.1149/1.3258274 (2010).

80 Jung, Y. S. *et al.* Ultrathin Direct Atomic Layer Deposition on Composite Electrodes for Highly Durable and Safe Li-Ion Batteries. *Adv. Mater.* **22**, 2172-+, doi:10.1002/adma.200903951 (2010).

81 Kang, B. & Ceder, G. Battery materials for ultrafast charging and discharging. *Nature* **458**, 190-193, doi:10.1038/nature07853 (2009).

82 Kang, K. S., Meng, Y. S., Breger, J., Grey, C. P. & Ceder, G. Electrodes with high power and high capacity for rechargeable lithium batteries. *Science* **311**, 977-980, doi:10.1126/science.1122152 (2006).

83 Kelly, A. F. R. S. *Strong solids, by A. Kelly*. (Clarendon Press, 1973).

84 Kil, K. C. *et al.* Enhanced Electrochemical Properties of LiFePO(4) Electrodes with Carboxylated Poly(vinyl difluoride) in Lithium-Ion Batteries: Experimental and Theoretical Analysis. *J. Phys. Chem. C* **115**, 16242-16246, doi:10.1021/jp205233h (2011).

85 Kim, H. & Cho, J. Superior Lithium Electroactive Mesoporous Si@Carbon Core−Shell Nanowires for Lithium Battery Anode Material. *Nano Letters* **8**, 3688-3691, doi:10.1021/nl801853x (2008).

86 Kim, H., Seo, M., Park, M. H. & Cho, J. A Critical Size of Silicon Nano-Anodes for Lithium Rechargeable Batteries. *Angew. Chem.-Int. Edit.* **49**, 2146-2149, doi:10.1002/anie.200906287 (2010).

87 Ko, S.-C., Lee, S. & Chou, Y. T. Chemical stresses in a square sandwich composite. *Materials Science and Engineering: A* **409**, 145-152 (2005).

88 Kumaresan, K., Guo, Q. Z., Ramadass, P. & White, R. E. Cycle life performance of lithium-ion pouch cells. *Journal of Power Sources* **158**, 679-688, doi:10.1016/j.jpowsour.2005.08.058 (2006).

89 Laffont, L. *et al.* Study of the LiFePO4/FePO4 Two-Phase System by High-Resolution Electron Energy Loss Spectroscopy. *Chem. Mater.* **18**, 5520 (2006).

90 Laforge, B., Levan-Jodin, L., Salot, R. & Billard, A. Study of Germanium as Electrode in Thin-Film Battery. *Journal of The Electrochemical Society* **155**, A181-A188 (2008).

91 Le May, L. *Principles of mechanical metallurgy*. (Elsevier North-Holland, 1981).

92 Lee, K. T. *et al.* Liquid Gallium Electrode Confined in Porous Carbon Matrix as Anode for Lithium Secondary Batteries. *Electrochemical and Solid State Letters* **11**, A21-A24, doi:10.1149/1.2823262 (2008).

93 Lee, K. T., Jung, Y. S., Kwon, J. Y., Kim, J. H. & Oh, S. M. Role of Electrochemically Driven Cu Nanograins in $CuGa_2$ Electrode. *Chem. Mat.* **20**, 447-453, doi:10.1021/cm702181m (2008).

94 Lee, S., Wang, W. L. & Chen, J. R. Diffusion-induced stresses in a hollow cylinder:: Constant surface stresses. *Materials Chemistry and Physics* **64**, 123-130 (2000).

95 Leung, K. & Budzien, J. L. Ab initio molecular dynamics simulations of the initial stages of solid-electrolyte interphase formation on lithium ion battery graphitic anodes. *Physical Chemistry Chemical Physics* **12**, 6583-6586 (2010).

96 Lewis, R. B., Timmons, A., Mar, R. E. & Dahn, J. R. In Situ AFM Measurements of the Expansion and Contraction of Amorphous Sn-Co-C Films Reacting with Lithium. *Journal of The Electrochemical Society* **154**, A213-A216, doi:10.1149/1.2429042 (2007).

97 Li, Y. & Cheng, Y.-T. Studies of Metal Hydride Electrodes Using an Electrochemical Quartz Crystal Microbalance. *Journal of The Electrochemical Society* **143**, 120-124 (1996).

98 Li, Y., Lv, X. & Li, J. High performance binderless TiO[sub 2] nanowire arrays electrode for lithium-ion battery. *Applied Physics Letters* **95**, 113102-113103 (2009).

99 Liu, P. *et al.* Aging Mechanisms of $LiFePO_4$ Batteries Deduced by Electrochemical and Structural Analyses. *Journal of The Electrochemical Society* **157**, A499-A507, doi:10.1149/1.3294790 (2010).

100 Macak, J. M., Tsuchiya, H., Taveira, L., Aldabergerova, S. & Schmuki, P. Smooth anodic TiO2 nanotubes. *Angewandte Chemie, International Edition* **44**, 7463-7465 (2005).

101 Mao, O. *et al.* Active/inactive nanocomposites as anodes for Li-ion batteries. *Electrochemical and Solid State Letters* **2**, 3-5, doi:10.1149/1.1390715 (1999).

102 Markervich, E., Salitra, G., Levi, M. & Aurbach, D. Capacity fading of lithiated graphite electrodes studied by a combination of electroanalytical methods, Raman spectroscopy and SEM. *Journa of Power Sources* **146**, 146 (2005).

103 Maxisch, T. & Ceder, G. Elastic properties of olivine Lix FePO4 from first principles. *Physical Review B* **73**, 174112 (2006).

104 MedeA. *MedeA*, 2011).

105 Menkin, S., Golodnitsky, D. & Peled, E. Artificial solid-electrolyte interphase (SEI) for improved cycleability and safety of lithium-ion cells for EV applications. *Electrochem. Commun.* **11**, 1789-1791 (2009).

106 Miller, R. E. & Shenoy, V. B. Size-dependent elastic properties of nanosized structural elements. *Nanotechnology* **11**, 139-147, doi:Doi:10.1016/j.jpowsour.2010.04.044
(2000).

107 Ning, G., White, R. E. & Popov, B. N. A generalized cycle life model of rechargeable Li-ion batteries. *Electrochimica Acta* **51**, 2012-2022, doi:10.1016/j.electacta.2005.06.033 (2006).

108 Obrovac, M. N., Christensen, L., Ba Le, D. & Dahn, J. R. Alloy Design for Lithium-Ion Battery Anodes. *Journal of The Electrochemical Society* **154**, A849-A855 (2007).

109 Ohzuku, T., Tamura, H. & Sawai, K. Monitoring of particle fracture by acoustic emission during charge and discharge of Li/MnO2 cells. *Journal of The Electrochemical Society* **144** (1997).

110 Padhi, A. K., Nanjundaswamy, K. S. & Goodenough, J. B. Phospho-olivines as positive-electrode materials for rechargeable lithium batteries. *Journal of the Electrochemical Society* **144**, 1188-1194 (1997).

111 Park, M.-H. *et al.* Silicon Nanotube Battery Anodes. *Nano Letters* **9**, 3844-3847, doi:10.1021/nl902058c (2009).

112 Peled, E., Golodnitsky, D., Menachem, C. & Bar-Tow, D. An Advanced Tool for the Selection of Electrolyte Components for Rechargeable Lithium Batteries. *Journal of The Electrochemical Society* **145**, 3482-3486 (1998).

113 Peled, E., Menachem, C., BarTow, D. & Melman, A. Improved graphite anode for lithium-ion batteries - Chemically bonded solid electrolyte interface and nanochannel formation. *Journal of The Electrochemical Society* **143**, L4-L7, doi:10.1149/1.1836372 (1996).

114 Pollard, R. & Newman, J. Mathematical Modeling of the Lithium-Aluminum, Iron Sulfide Battery. *Journal of The Electrochemical Society* **128**, 491 (1981).

115 Predel, B. *Group IV Physical Chemistry - Phase Equilibria, Crystallographic and Thermodynamic Data of Binary Alloys*. Vol. 5 (Springer, 1998).

116 Prussin, S. Generation and Distribution of Dislocations by Solute Diffusion. *Journal of Applied Physics* **32**, 1876-1881 (1961).

117 Qi, Y., Guo, H., Hector, J. L. G. & Timmons, A. Threefold Increase in the Young's Modulus of Graphite Negative Electrode during Lithium Intercalation. *Journal of The Electrochemical Society* **157**, A558-A566 (2010).

118 Qi, Y., Guo, H., Hector, L. G. & Timmons, A. *Journal of The Electrochemical Society* (2010).

119 Qi, Y., Shenoy, V. & Johari, P. *Journal of Power Sources*, doi:Doi:10.1016/j.jpowsour.2010.04.044 (2010).

120 R., L. B. *Fracture of Brittle Solids* 2nd edition edn, (Cambridge University Press, 1993).

121 Ramasamy, R. P., Lee, J.-W. & Popov, B. N. Simulation of capacity loss in carbon electrode for lithium-ion cells during storage. *Journal of Power Sources* **166**, 266-272, doi:10.1016/j.jpowsour.2006.12.086 (2007).

122 Ramasamy, R. P., White, R. E. & Popov, B. N. Calendar life performance of pouch lithium-ion cells. *Journal of Power Sources* **141**, 298-306, doi:10.1016/j.jpowsour.2004.09.024 (2005).

123 Ravet, N. *et al.* Electroactivity of natural and synthetic triphylite. *Journal of Power Sources* **97-98**, 503-507 (2001).

124 Recham, N. *et al.* Ionothermal Synthesis of Tailor-Made LiFePO4 Powders for Li-Ion Battery Applications. *Chem. Mat.* **21**, 1096-1107, doi:10.1021/cm803259x (2009).

125 Renganathan, S., Sikha, G., Santhanagopalan, S. & White, R. E. Theoretical Analysis of Stresses in a Lithium Ion Cell. *Journal of The Electrochemical Society* **157**, A155-A163 (2010).

126 Rhodes, K. *et al.* Novel cell design for combined in situ acoustic emission and x-ray diffraction study during electrochemical cycling of batteries. *Review of Scientific Instruments* **82**, doi:10.1063/1.3607961 (2011).

127 Rhodes, K., Meisner, R., Kim, Y., Dudney, N. & Daniel, C. Evolution of Phase Transformation Behavior in Li(Mn(1.5)Ni(0.5))O(4) Cathodes Studied By In Situ XRD. *Journal of The Electrochemical Society* **158**, A890-A897, doi:10.1149/1.3596376 (2011).

128 Safari, M., Morcrette, M., Teyssot, A. & Delacourt, C. Life-Prediction Methods for Lithium-Ion Batteries Derived from a Fatigue Approach I. Introduction: Capacity-Loss Prediction Based on Damage Accumulation. *Journal of The Electrochemical Society* **157**, A713-A720, doi:10.1149/1.3374634 (2010).

129 Safari, M., Morcrette, M., Teyssot, A. & Delacourt, C. Life Prediction Methods for Lithium-Ion Batteries Derived from a Fatigue Approach II. Capacity-Loss Prediction of Batteries Subjected to Complex Current Profiles. *Journal of The Electrochemical Society* **157**, A892-A898, doi:10.1149/1.3432560 (2010).

130 Saint, J., Morcrette, M., Larcher, D. & Tarascon, J. M. Exploring the Li-Ga Room Temperature Phase Diagram and the Electrochemical Performances of the Li_xGa_y Alloys vs. Li. *Solid State Ionics* **176**, 189-197, doi:10.1016/j.ssi.2004.05.021 (2005).

131 Santhanagopalan, S., Guo, Q., Ramadass, P. & White, R. E. Review of models for predicting the cycling performance of lithium ion batteries. *Journal of Power Sources* **156**, 620-628, doi:10.1016/j.jpowsour.2005.05.070 (2006).

132 Schuh, C. & Dunand, D. C. Internal stress plasticity due to chemical stresses. *Acta Mater.* **49**, 3387-3400, doi:10.1016/s1359-6454(01)00272-5 (2001).

133 Sethuraman, V. A., Hardwick, L. J., Srinivasan, V. & Kostecki, R. Surface structural disordering in graphite upon lithium intercalation/deintercalation. *Journal of Power Sources* **195**, 3655-3660 (2010).

134 Sharma, P., Ganti, S. & Bhate, N. Erratum: ``Effect of surfaces on the size-dependent elastic state of nano-inhomogeneities" [Appl. Phys. Lett. [bold 82], 535 (2003)]. *Applied Physics Letters* **89**, 049901-049901 (2006).

135 Shenoy, V. B., Johari, P. & Qi, Y. Elastic softening of amorphous and crystalline Li-Si Phases with increasing Li concentration: A first-principles study. *Journal of Power Sources* **195**, 6825-6830, doi:10.1016/j.jpowsour.2010.04.044 (2010).

136 Shin, H. C., Dong, J. & Liu, M. L. Porous Tin Oxides Prepared using an Anodic Oxidation Process. *Adv. Mater.* **16**, 237-240, doi:10.1002/adma.200305660 (2004).

137 Shin, H. C. & Liu, M. L. Three-dimensional porous copper-tin alloy electrodes for rechargeable lithium batteries. *Advanced Functional Materials* **15**, 582-586, doi:10.1002/adfm.200305165 (2005).

138 Shin, H.-C., Corno, J. A., Gole, J. L. & Liu, M. Porous silicon negative electrodes for rechargeable lithium batteries. *Journal of Power Sources* **139**, 314-320 (2005).

139 Singh, G., Ceder, G. & Bazant, M. Intercalation dynamics in rechargeable battery materials: General theory and phase-transformation waves in LiFePO4. *Electrochimica Acta* **53**, 7599 (2008).

140 Smith, J. R. *et al.* Evaluation of the relationship between cathode microstructure and electrochemical behavior for SOFCs. *Solid State Ionics* **180**, 90-98, doi:10.1016/j.ssi.2008.10.017 (2009).

141 Song, J. Y., Wang, Y. Y. & Wan, C. C. Review of gel-type polymer electrolytes for lithium-ion batteries. *Journal of Power Sources* **77**, 183-197, doi:10.1016/s0378-7753(98)00193-1 (1999).

142 Spotnitz, R. Simulation of capacity fade in lithium-ion batteries. *Journal of Power Sources* **113**, 72-80, doi:10.1016/s0378-7753(02)00490-1 (2003).

143 Srinivasan, V. & Newman, J. Discharge Model for the Lithium Iron-Phosphate Electrode. *Journal of The Electrochemical Society* **151**, A1517-A1529 (2004).

144 Srinivasan, V. & Newman, J. Existence of path-dependence in the LiFePO4 electrode. *Electrochemical and Solid-State Letters* **9**, A110 (2006).

145 Subramanian, V. R., Ploehn, H. J. & White, R. E. Shrinking Core Model for the Discharge of a Metal Hydride Electrode. *Journal of The Electrochemical Society* **147**, 2868-2873 (2000).

146 Subramanian, V. R. & White, R. E. New separation of variables method for composite electrodes with galvanostatic boundary conditions. *Journal of Power Sources* **96**, 385-395 (2001).

147 Tabuchi, T., Hochgatterer, N., Ogumi, Z. & Winter, M. Ternary Sn-Sb-Co alloy film as new negative electrode for lithium-ion cells. *Journal of Power Sources* **188**, 552-557, doi:10.1016/j.jpowsour.2008.11.116 (2009).

148 Tarascon, J. M. & Armand, M. Issues and challenges facing rechargeable lithium batteries. *Nature* **414**, 359 (2001).

149 Tasaki, K. *et al.* Solubility of Lithium Salts Formed on the Lithium-Ion Battery Negative Electrode Surface in Organic Solvents. *Journal of The Electrochemical Society* **156**, A1019-A1027, doi:10.1149/1.3239850 (2009).

150 Tasaki, K. & Harris, S. J. Computational Study on the Solubility of Lithium Salts Formed on Lithium Ion Battery Negative Electrode in Organic Solvents. *J. Phys. Chem. C* **114**, 8076-8083, doi:10.1021/jp100013h (2010).

151 Thorne, J. S., Sanderson, R. J., Dahn, J. R. & Dunlap, R. A. Combinatorial Study of the Sn-Cu-C System for Li-Ion Battery Negative Electrode Materials. *Journal of The Electrochemical Society* **157**, A1085-A1091, doi:10.1149/1.3476311 (2010).

152 Tillard-Charbonenel, M., Belin, C. & Soubeyroux, J. L. The lithium-gallium intermetallic system: electrochemical and neutron powder diffraction study of

lithium deficient phase Li_2Ga_7. *Eur. J. Solid State Inorg. Chem.* **t. 27**, 759-769 (1990).

153 Timmons, A. *Visible changes in lithium-ion electrodes upon lithium insertion and removal* Degree of Doctor of Philosophy thesis, Dalhousie University (2007).

154 Timoshenko, S. & Goodier, J. N. *Theory of elasticity, by S. Timoshenko and J.N. Goodier*. (1951).

155 Timoshenko, S. & Goodier, J. N. *Theory of elasticity*. (1951).

156 Todd, A. D. W., Mar, R. E. & Dahn, J. R. Tin-Transition Metal-Carbon Systems for Lithium-Ion Battery Negative Electrodes. *Journal of The Electrochemical Society* **154**, A597-A604, doi:10.1149/1.2724741 (2007).

157 Tu, K. N. Interdiffusion in the thin-films. *Annu. Rev. Mater. Sci.* **15**, 147-176, doi:10.1146/annurev.ms.15.080185.001051 (1985).

158 Verbrugge, M. W. & Cheng, Y.-T. Stress and Strain-Energy Distributions within Diffusion-Controlled Insertion-Electrode Particles Subjected to Periodic Potential Excitations. *Journal of The Electrochemical Society* **156**, A927-A937 (2009).

159 Verbrugge, M. W. & Koch, B. J. Electrochemical analysis of lithiated graphite anodes. *Journal of The Electrochemical Society* **150**, A374-A384, doi:10.1149/1.1553788 (2003).

160 W., M. & J., S. The crystal structure of Li_2Ga and Li_3Ga_2. *Z. Naturforsch.* **B 32**, 631 (1977).

161 Wachtler, M., Winter, M. & Besenhard, J. O. Anodic materials for rechargeable Li-batteries. *Journal of Power Sources* **105**, 151-160, doi:10.1016/s0378-7753(01)00934-x (2002).

162 Wang, C. & Sastry, A. M. Mesoscale Modeling of a Li-ion Polymer Cell. *Journal of The Electrochemical Society*, **154**, A1035 (2007).

163 Wang, J. *et al.* Cycle-life model for graphite-LiFePO4 cells. *Journal of Power Sources* **196**, 3942-3948, doi:10.1016/j.jpowsour.2010.11.134 (2011).

164 Wang, W. L., Lee, S. & Chen, J. R. Effect of chemical stress on diffusion in a hollow cylinder. *Journal of Applied Physics* **91**, 9584-9590 (2002).

165 Way, B. M. & Dahn, J. R. THE EFFECT OF BORON SUBSTITUTION IN CARBON ON THE INTERCALATION OF LITHIUM IN LIX(BZC1-Z)6. *Journal of The Electrochemical Society* **141**, 907-912, doi:10.1149/1.2054856 (1994).

166 Wen, C. J. & Huggins, R. A. Electrochemical Investigation of the Lithium-Gallium System. *Journal of The Electrochemical Society* **128**, 1636-1641 (1981).

167 Winter, M. The Solid Electrolyte Interphase - The Most Important and the Least Understood Solid Electrolyte in Rechargeable Li Batteries. *Z. Phys. Chemie-Int. J. Res. Phys. Chem. Chem. Phys.* **223**, 1395-1406, doi:10.1524/zpch.2009.6086 (2009).

168 Winter, M. & Besenhard, J. O. Electrochemical lithiation of tin and tin-based intermetallics and composites. *Electrochimica Acta* **45**, 31-50 (1999).

169 Wolfenstine, J. A high ratio of the testing temperature to the melting temperature: a necessary but not sufficient condition for an alloy anode to exhibit low capacity fade. *Materials Letters* **57**, 3983-3986 (2003).

170 Wu, Q. *Synthesis and energy applications of oriented metal oxide nanoporous films*. (University of Kentucky, 2011).

171 Xia, Y. Y., Sakai, T., Fujieda, T., Wada, M. & Yoshinaga, H. Flake Cu-Sn alloys as Negative Electrode Materials for Rechargeable Lithium Batteries. *Journal of The Electrochemical Society* **148**, A471-A481 (2001).

172 Yan, J. *et al.* Phenomenologically modeling the formation and evolution of the solid electrolyte interface on the graphite electrode for lithium-ion batteries. *Electrochimica Acta* **53**, 7069-7078, doi:10.1016/j.electacta.2008.05.032 (2008).

173 Yang, F. Q. Interaction between diffusion and chemical stresses. *Mater. Sci. Eng. A-Struct. Mater. Prop. Microstruct. Process.* **409**, 153-159, doi:10.1016/j.msea.2005.05.117 (2005).

174 Yang, F. Q. & Li, J. C. M. Diffusion-induced beam bending in hydrogen sensors. *Journal of Applied Physics* **93**, 9304-9309, doi:10.1063/1.1569980 (2003).

175 Zaghib, K., Simoneau, M., Armand, M. & Gauthier, M. Electrochemical study of Li4Ti5O12 as negative electrode for Li-ion polymer rechargeable batteries. *J. Power Sources* **81-82**, 300-305 (1999).

176 Zhang, H., Li, F., Liu, C., Tan, J. & Cheng, H. New Insight into the Solid Electrolyte Interphase with Use of a Focused Ion Beam. *J. Phys. Chem. B* **109**, 22205 (2005).

177 Zhang, Q. & White, R. E. Calendar life study of Li-ion pouch cells. *Journal of Power Sources* **173**, 990-997, doi:10.1016/j.jpowsour.2007.08.044 (2007).

178 Zhang, Q. & White, R. E. Moving Boundary Model for the Discharge of a LiCoO[sub 2] Electrode. *Journal of The Electrochemical Society* **154**, A587-A596 (2007).

179 Zhang, Q. & White, R. E. Calendar life study of Li-ion pouch cells - Part 2: Simulation. *Journal of Power Sources* **179**, 785-792, doi:10.1016/j.jpowsour.2007.12.022 (2008).

180 Zhang, Q. & White, R. E. Capacity fade analysis of a lithium ion cell. *Journal of Power Sources* **179**, 793-798, doi:10.1016/j.jpowsour.2008.01.028 (2008).

181 Zhang, S. C. *et al.* A three-dimensional tin-coated nanoporous copper for lithium-ion battery anodes. *Journal of Power Sources* **196**, 6915-6919, doi:10.1016/j.jpowsour.2010.12.021 (2011).

182 Zhang, S. S. A review on electrolyte additives for lithium-ion batteries. *Journal of Power Sources* **162**, 1379-1394, doi:10.1016/j.jpowsour.2006.07.074 (2006).

183 Zhang, S. S., Xu, K. & Jow, T. R. EIS study on the formation of solid electrolyte interface in Li-ion battery. *Electrochimica Acta* **51**, 1636-1640 (2006).

184 Zhang, X., Sastry, A. M. & Shyy, W. Intercalation-Induced Stress and Heat Generation within Single Lithium-Ion Battery Cathode Particles. *Journal of The Electrochemical Society* **155**, A542-A552 (2008).

185 Zhang, X., Shyy, W. & Sastry, A. M. Numerical Simulation of Intercalation-Induced Stress in Li-Ion Battery Electrode Particles. *Journal of The Electrochemical Society* **154**, A910-A916 (2007).

186 Zhang, X. L. & Zhou, C. Y. Study on cracking of welding overlay based on the theory of diffusion-induced stress. *Acta Metall. Sin.-Engl. Lett.* **24**, 75-80 (2011).

187 Zwigl, P. & Dunand, D. C. Internal-stress plasticity in titanium by cyclic alloying/dealloying with hydrogen. *Journal of Materials Processing Technology* **117**, 409-417, doi:10.1016/s0924-0136(01)00801-9 (2001).

VITA

Rutooj Deelip Deshpande was born on September 17, 1986 in Nanded, Maharashtra, India. He completed Bachelors in Chemical Engineering with First Class from the Institute of Chemical Technology (formerly known as UDCT), Mumbai, India, in May 2008. He joined Department of Chemical and Materials Engineering at the University of Kentucky in August 2008 as a PhD candidate.

HONORS AND AWARDS

- American Ceramic Society (ACerS) sponsored 'Graduate Excellence in Materials Science (GEMS)- Diamand Awards' at MS&T annual meeting, 2011.
- NSF-sponsored student travel award, ASME-IMECE Meeting, Denver, November 2011.
- Graduate Student Travel Scholarship, University of Kentucky, July 2010
- Electrochemical Society Travel Award, Electrochemical Society (ECS) Spring Meeting 2010, Vancouver, Canada.
- Graduate Student Travel Scholarship, University of Kentucky, July 2009

PUBLICATIONS

- R. Deshpande, Y.-T. Cheng, M. W. Verbrugge, Modeling diffusion-induced stress in nanowire electrode structures. *Journal of Power Sources* **195**, 5081 (2010).

- R. Deshpande, Y. Qi, Y.-T. Cheng, Effects of Concentration-Dependent Elastic Modulus on Diffusion-Induced Stresses for Battery Applications. *Journal of The Electrochemical Society* **157**, A967 (2010).
- R. Deshpande, Y.-T. Cheng, M. W. Verbrugge, A. Timmons, Diffusion Induces Stresses and Strain Energy in a Phase Transforming Spherical Electrode Particle. *Journal of The Electrochemical Society* **158**, 1 (2011).
- R. D. Deshpande, J. Li, Y.-T. Cheng, M. W. Verbrugge, Liquid Metal Alloys as Self-Healing Negative Electrodes for Lithium Ion Batteries. *Journal of The Electrochemical Society* **158**, A845 (2011).
- S. J. Harris, R. D. Deshpande, Y. Qi, I. Dutta, Y. T. Cheng, Mesopores inside electrode particles can change the Li-ion transport mechanism and diffusion-induced stress. *Journal of Materials Research* **25**, 1433 (Aug, 2010).

CONFERENCE PRESENTATIONS

Rutooj has presented papers and posters at several national and regional meetings including AIChE (American Institute of Chemical Engineers) Annual Meetings (Nashville, 2009; Salt Lake City, 2010), MRS (Materials research Society) Fall Meeting, Boston (2009, 2010), ECS (Electrochemical Society) Meeting (Vancouver, Spring, 2010; Boston, Fall, 2011), KIEC (Kentucky Innovation and Entrepreneurship Conference)